Many-Body Cavity Quantum Electrodynamics and Spin Dynamics with an Ensemble of Rare-Earth Ions

Thesis by
Mi Lei

In Partial Fulfillment of the Requirements for the
Degree of
Doctor of Philosophy

CALIFORNIA INSTITUTE OF TECHNOLOGY
Pasadena, California

2024
Defended February 14, 2024

Mi Lei
ORCID: 0009-0001-5484-7982

ACKNOWLEDGEMENTS

In this thesis, the interactions between different parts are one of the central themes. Throughout my PhD journey, I have been fortunate to meet many wonderful people and experience positive human-human interactions. Here, I would like to acknowledge the people I have interacted with during the past six and a half years.

First and foremost, I want to thank my advisor, Andrei Faraon, for all the support, encouragement, and guidance he has provided. I was trying to switch gears to quantum optics from a background in condensed matter physics and classical optics when I joined graduate school. I can still feel the happiness from the moment when Andrei accepted me as a graduate student in the first place and gave me the chance to make that transition. Andrei is always willing to give us the freedom and space to explore what we are interested in, while also providing guidance at the proper time. During the years, thank you for providing all the academic chances and opportunities, and for offering help and encouragement when I was feeling down in life.

Now, I would like to express my gratitude to three people I have been closely working with.

Ioana Craiciu was my mentor during the early stage of my PhD. I could not count how many thank-yous I should say to her for all the mentoring and friendship she has given me, from work to life. I remember first meeting Ioana in March 2017 during my visiting days at Caltech. I thought it would be so nice to work with someone like her, and then, here we are. She was always patient in teaching me every skill we need in labs and highly respected my opinion as a junior graduate student. She always gave me the chance to try things by myself and allowed me to make mistakes. Furthermore, she is also a role model for me in terms of how to be a nice person. I've learned a lot of interpersonal skills from her as well. Thank you for all the fun and exciting moments in the labs, for the sincere chats about life, and for picking up my late-night calls.

Riku Fukumori joined our project in 2021. We work well together as a team with our complementary skills and knowledge. It is nice to have someone who cares about details as much as you do for the project. I felt a bit lost when I was working by myself after Ioana graduated, and Riku helped me "get out of the pit of incompetence," quoting Andrei's words. I enjoy all of the discussions we have to figure out every

puzzle. Thank you for tirelessly running simulations to test the random thoughts we have. Thank you for your hard work, good insights, and contributions to the projects.

Joonhee Choi started collaborating with us in 2021 when we were trying to identify the missing noise operators in the equations. He is very knowledgeable and insightful, always providing new opinions and excitement from another point of view. Meanwhile, he always grasps our random thoughts quickly and is willing to pedagogically teach us some new knowledge. I enjoy every meeting we have, which often starts with a quick question and turns into hours of discussion. For me personally, thank you for encouraging me to stay in academia and providing guidance when I was anxious about my future.

The rest of the Faraon group is also amazing.

Firstly, I want to thank my cohort peers: Tian Xie, Tianzhe (Terry) Zheng, Greg Roberts and Andrei Ruskuc. Our time overlaps the most in the lab. In the early stages of our PhD, we took classes together, exchanged knowledge learned from our mentors, and explored nearby restaurants. Later in our PhD journey, we are all trying to figure out our next destinations. It has been a fun experience with you guys to go through the phase of transitioning from finding free food to finding a job. I wish you all a bright future.

Next, I want to thank the former group members: John Bartholomew, Jake Rochman, Jon Kindem and Chuting Wang. Thank you, John, for your solid knowledge of rare-earth ions and for covering various projects in the group. I remember the time you welcomed me as a new student to join the lab, and the time you went through my slides with me as a junior graduate when you missed my group meeting presentation. Thank you, Jake, for all the fabrication work you have done, and for sharing your industry experience with me when I was trying to find the next step after graduate school. I appreciate your kindness when you walked into my office and told me not to be afraid to ask you questions in my first year. Thank you, Jon, for mentoring me to build the laser in the lab as my very first project. Thank you, Chuting, for going to the gym and zoo together.

For the current group members, I want to thank Sophie Hermans for being good colleagues and friends. Thank you for caring about me and for those coffee chats. Thank you, Bilgehan Baspinar, for your friendship and our hike trips. Thank you to my office mates, Yiran (Suki) Gu, Jiahui Li, and Tianzhe (Terry) Zheng, for listening

to my whining and being flexible about the temperature of the office. Thank you, Chun-ju, for always being generous in lending us equipment. It is hard to list everyone since the Faraon group is growing. Thank you all for the time spent in the lab, as well as for all the skiing and hiking outside of the lab.

Beyond the lab, I have been lucky to know some great scientists and to receive help from them. Thank you to my defense committee, Manuel Endres, Andrei Faraon, Oskar Painter, Gil Refael, and Norman Yao, for your time and guidance. Also, thank you, Kerry Vahala and Nicholas Hutzler, for being on my candidacy committee. Thank you, Bihui Zhu, for the meetings and discussions we have had regarding the CIT and superradiance paper.

Outside of research, I am also lucky to have made some good friends. Thank you, Guannan Dong and Weiting Deng, for being my trusted friends. Thank you for picking up my late-night calls and being with me when I need you. Thank you, Laura Flower Kim, for being a supportive "big sister." From the trip to "The Big Bang Theory" taping to the mature advice you gave during my emotional times, I appreciate your kindness and friendship over the past years. Thank you, Xueyue (Sherry) Zhang, for sharing the periods of time on taking classes, attending conferences, and looking for postdocs. Thank you, Milo, my cat friend, for introducing me to the world of cats and for the time we spent together.

Last but not least, I would like to express my sincere gratitude to my dearest family, including my grandparents and my parents. My grandparents, unfortunately, have passed away, but their influence on me never ends. Growing up with them, I observed human qualities such as kindness, sincerity, honesty, and diligence. I believe their unconditional love will be with me forever, as they have never really left. My parents have always given me the greatest freedom to pursue whatever I wanted since I was able to make decisions. Especially my mom, thank you for always believing in me and loving me through the ups and downs.

ABSTRACT

Studying and controlling light-matter and matter-matter interactions is a central theme in quantum physics and provides the foundation for quantum applications. Rare-earth ions (REIs) doped in solids are promising candidates for engineering scalable quantum technologies, such as quantum memories and quantum transducers, and for exploring emerging fundamental phenomena. This is because REIs have highly stable optical and spin transitions at cryogenic temperatures, and as a solid-state platform, they are compatible for integrating with quantum devices using well-established semiconductor manufacturing techniques.

This thesis is centered on nanophotonic devices coupling to an ensemble of REIs. To explore the light-matter interaction, we build a light-matter interface by coupling an inhomogeneously broadened ensemble of ytterbium-171 doped in yttrium orthovanadate to a nanophotonic cavity with high cooperativity. In this many-body cavity quantum electrodynamics (cavity QED) system, we observe the appearance of a narrow transparency window in the cavity reflection spectrum under optical driving (collectively induced transparency, CIT). This phenomenon results from the destructive interference between pairs of two-level emitters across the inhomogeneous line and the saturation of resonant ions. Furthermore, coherent excitation of the system within this transparency window enables us to observe highly nonlinear optical emission, spanning from fast superradiance to slow subradiance. To study matter-matter interactions, we shift the focus to the strongly interacting spins. These spins feature clock transitions and pure spin exchange interactions, leading to comparable magnitudes of interaction strength and on-site disorder. We characterize and control the many-body dynamics via Hamiltonian engineering and population initialization. Furthermore, we observe the emergence of robust subharmonic oscillations under Floquet driving, providing evidence for the presence of a discrete time crystal.

The discoveries in many-body cavity QED enable new mechanisms for achieving slow light and frequency referencing, and they provide potential for superradiant lasers. Meanwhile, our studies on spin dynamics showcase REIs as a promising platform for the study of many-body physics, with potential applications in quantum sensing and quantum simulations. In general, our findings deepen the understanding for a disordered quantum system and offer valuable insights for development of quantum applications.

PUBLISHED CONTENT AND CONTRIBUTIONS

[1] Mi Lei, Rikuto Fukumori, Jake Rochman, Bihui Zhu, Manuel Endres, Joonhee Choi, and Andrei Faraon. "Many-body cavity quantum electrodynamics with driven inhomogeneous emitters." In: *Nature* (2023), pp. 1–6. DOI: 10.1038/s41586-023-05884-1.
M.L. planned the experiments, performed the measurements, analyzed the data, developed the theory of the collectively induced transparency, and wrote the manuscript.
M.L. and R.F. contributed equally to this work.

[2] Ioana Craiciu, Mi Lei, Jake Rochman, John G. Bartholomew, and Andrei Faraon. "Multifunctional on-chip storage at telecommunication wavelength for quantum networks." In: *Optica* 8.1 (2021), pp. 114–121. DOI: 10.1364/OPTICA.412211.
M.L. participated in building the experimental setup, performing the measurements, analyzing the data, developed the theory of high-order memory efficiencies, and provided input for the manuscript.
C.I. and M.L. contributed equally to this work.

[3] Ioana Craiciu, Mi Lei, Jake Rochman, Jonathan M. Kindem, John G. Bartholomew, Evan Miyazono, Tian Zhong, Neil Sinclair, and Andrei Faraon. "Nanophotonic quantum storage at telecommunication wavelength." In: *Physical Review Applied* 12.2 (2019), p. 024062. DOI: 10.1103/PhysRevApplied.12.024062.
M.L. participated in part of the experimental data taking and analyzing, and provided input for the manuscript.

TABLE OF CONTENTS

LIST OF FIGURES

LIST OF TABLES

Chapter 1

INTRODUCTION

Quantum science provides the foundation for modern physics and engineering. From a two-level quantum system to an ensemble of quantum emitters, there are broad implications for exploring emerging exotic fundamental phenomena and developing advanced technologies. Starting with a two-level quantum system, coherent single emitters, such as atoms or atomlike defects, have various applications in quantum networks, including single-photon light sources, quantum logic gates in quantum computing, and spin-photon interfaces for future quantum networks. As we increase the number of atoms, an ensemble of emitters serves as a more efficient light-matter interface for engineering ensemble-based quantum technologies, such as quantum memories and quantum transducers. Moreover, inspired by P.W. Anderson's '*More is Different*'[1], many-body phenomena emerge as we bring multiple atoms together. The study of many-body phenomena not only reveals new physics but also provides insights for developing quantum technologies, along with the potential for quantum simulation and sensing.

In this introductory chapter, we first discuss the motivation for quantum memories, the quantum application we engineered as a part of this thesis. Next, we provide a broad overview of many-body physics, the main focus of this thesis. Then, we introduce a quantum light-matter interface based on cavity quantum electrodynamics (cavity QED) and the specific experimental platform we use—rare-earth ions in solids coupled to a nanophotonic cavity.

1.1 Ensemble-based quantum technology: quantum memories

In the broad context of quantum information science, a quantum network is important for the implementation of quantum computation and quantum communication. A quantum network is comprised of quantum nodes and quantum channels linking them (Fig. 1.1a). Due to optical absorption and other channel noise, it is challenging to generate nearly perfect entangled states between two sites over a distance directly.

One solution is to use quantum repeaters, where the basic idea is to divide the transmission channel into many segments (Fig. 1.1b). Entanglement is generated and purified for each segment. Subsequently, by applying entanglement swapping

between neighboring segments, entanglement can be extended through them. Afterwards, purification is applied to this extended entanglement. By repeating the entanglement swapping and purification processes, the entanglement states can be extended to the entire channel.

One essential requirement in the quantum repeater protocol is to store the created entanglement until it has been established in the neighboring segment as well; otherwise, all the entanglement needs to be created simultaneously. Therefore, the quantum repeater protocol requires quantum memory to synchronize different quantum processes (Fig. 1.1c).

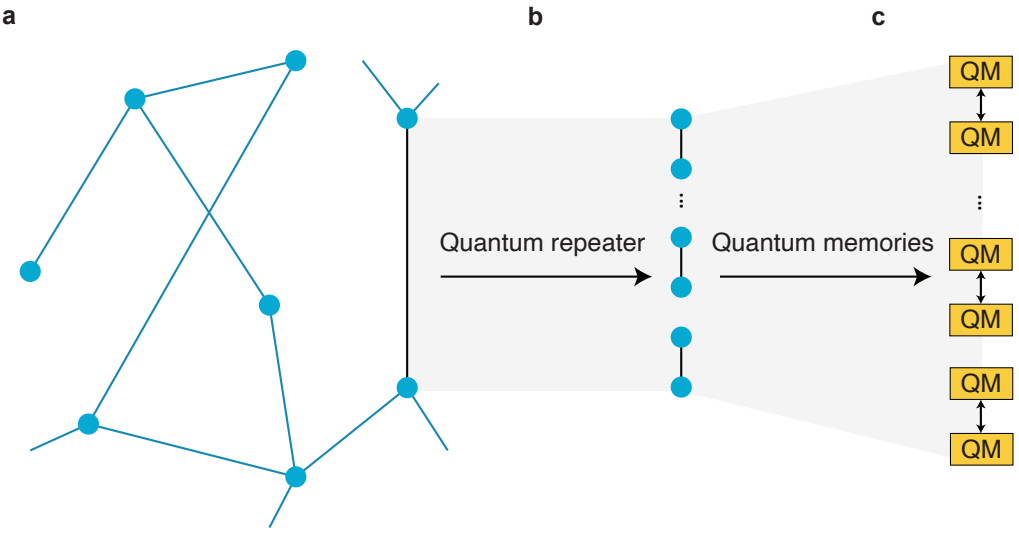

Figure 1.1: **Quantum network, quantum repeater and quantum memories. a.** A quantum network consists of nodes and channels linking them. **b.** The quantum repeater protocol is to divide the transmission line into many segments. c. Quantum memories are needed to store entanglement.

Our work focuses on engineering a quantum memory device with high efficiency and fidelity.

1.2 Quantum many-body physics

In the field of quantum many-body physics, emergent phenomena arise in a group of interacting particles. The properties of quantum many-body systems differ significantly from those of individual components and often lack classical counterparts.

Conventional many-body physics in condensed matter explores exotic equilibrium phases of matter, such as superconducting phases, Bose-Einstein condensates, and spin liquids. This typically involves experimental measurements of material proper-

ties under various conditions and the theoretical development of different models. On the other hand, recent advances in controllable experimental systems provide opportunities to explore new frontiers of many-body physics, including non-equilibrium phenomena [2].

Being out of equilibrium makes the systems much more complicated, increasing the challenge in theoretical modeling. Therefore, understanding and controlling non-equilibrium dynamics from the experimental side are fundamentally important. Moreover, these dynamics could have fruitful applications, such as for quantum information processing and quantum computing [3].

Atomic systems or atom-like systems, such as cold atoms, trapped ions, and solid-state spins, serve as potential candidates for studying many-body dynamics. There are several factors that are needed for them to be suitable for the study, including long coherence time, high-fidelity manipulation, coherent control, and strong interactions. One way to engineer many-body interactions is through their inherent nature, such as magnetic dipole-dipole interaction (Fig. 1.2a), while another way is through a medium, such as cavity photon-mediated interaction (Fig. 1.2b).

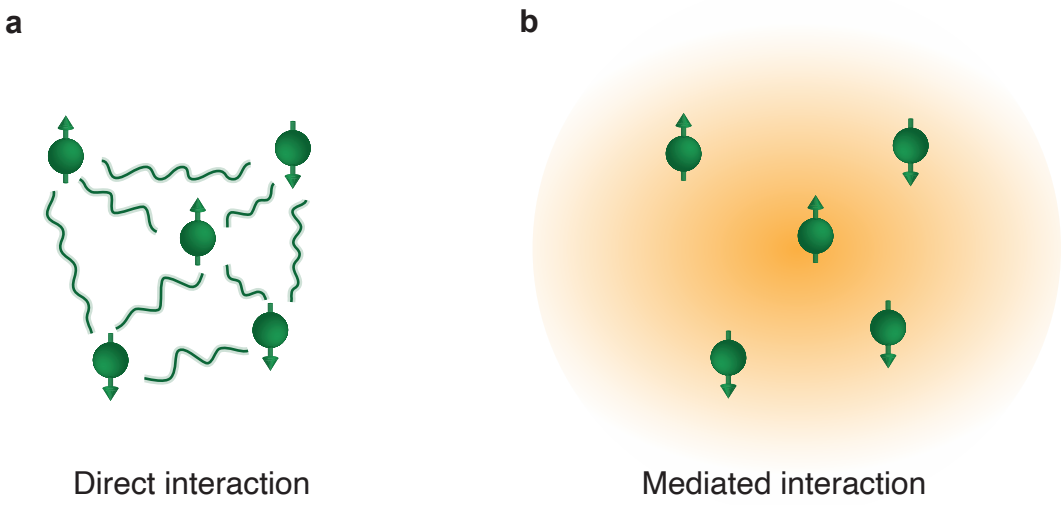

Figure 1.2: **Mechanisms of many-body interactions. a.** Direct interaction between spins. **b.** The interaction between spins is mediated by some medium, such as cavity photons.

Cold atoms and trapped ions systems usually have the advantage of individual control, while solid-state spins have the inherent capability to scale to a large number of emitters and the potential for integration into nano devices. Among the solid-state spins, there have been significant demonstrations in nitrogen-vacancy centers

in diamond for performing quantum simulations, quantum sensing, and realizing exotic phases of matter such as discrete time crystals (DTC) [4–6]. Rare-earth ions (REIs) doped in solids, as an alternative, can inject new vitality into many-body studies, as we will illustrate further in the next section.

1.3 Rare-earth ions in solids

Rare earth elements refer to the 15 lanthanide series elements, as well as yttrium and scandium. Lanthanide elements form trivalent ions when doped into host materials. The 5s and 5p orbitals are filled, while the 4f electron shell is partially filled. Most of the 4f orbitals are much less extended than the 5s and 5p orbitals; thus the 5s and 5p shells form a Faraday shield for 4f from the environment (Fig. 1.3).

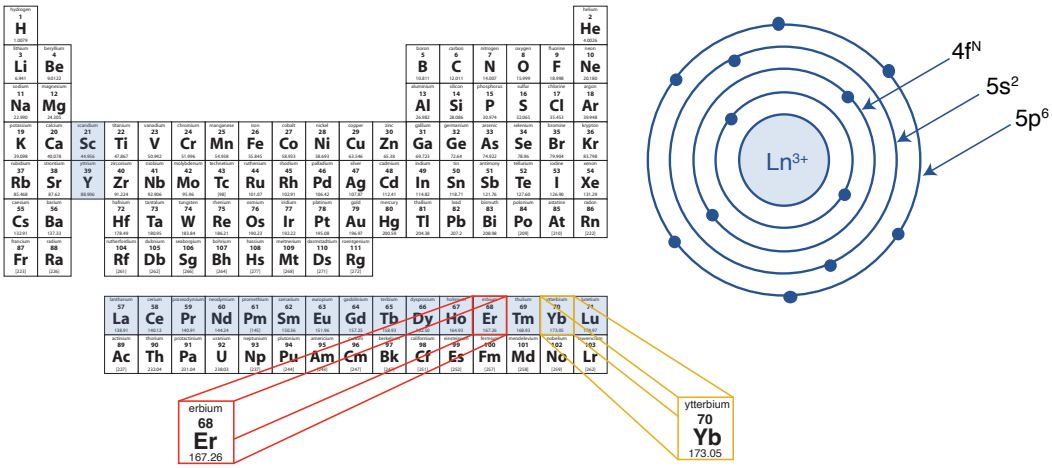

Figure 1.3: **Rare-earth ions.** Rare-earth elements in periodic table and electron structure of lanthanide series elements.

The spectroscopic properties of 4f, including the configuration of energy levels and dynamics of electronic transitions, are important for studying the optical properties of REIs in solids [7]. The 4f ↔ 4f electric dipole optical transitions are forbidden [1] for free ions but partially allowed by the crystal field generated in the host materials. As a result, the optical lifetime is quite long, and optical coherence is mainly determined by the spin properties. The spin lattice relaxlation via phonon couping is the main source for spin decoherence, so cooling down to crygenic temeprature will extend the the optical and spin coherence time. The spin-lattice relaxation via phonon coupling is the main source of spin decoherence, so cooling down to cryogenic temperatures will extend the optical and spin coherence time.

[1] Magnetic dipole transitions are allowed. A substantial fraction of the emission is magnetic dipole for atoms like Erbium.

In this thesis, we are focusing on two species of REIs: Erbium and Ytterbium (Fig. 1.3). Erbium is of particular interest because it has an optical transition in the telecom band, which allows integration with silicon photonics and telecommunication compatibility. Ytterbium has an effective electron spin of 1/2 and a nuclear spin 1/2 isotope (^{171}Yb). The hybridization of electron and nuclear spin forms relatively simple energy levels and can result in zero first-order-Zeeman (ZEFOZ) transitions (clock transitions) at zero magnetic field, which can exhibit high coherence [8, 9].

1.4 Light-matter interface: cavity quantum electrodynamics (cavity QED)

The interaction between light and matter forms the foundation of quantum optics, and an efficient light-matter interface serves as a building block for developing quantum technologies [10]. Cavity quantum electrodynamics (cavity QED) [11] provides a systematic method to achieve such an interface via enhanced light-matter interaction. In cavity QED, emergent phenomena may also arise as light and matter are confined in a small volume, given that the behavior of quantum emitters highly depends on their electromagnetic environment.

The field of cavity QED has enjoyed great experimental advancements in the past decades, as the rapid development of micro- and nano-scopic devices and laser trapping techniques have revealed a diverse and rich set of phenomena [12, 13]. Such progress has also led to cavity QED's use in quantum technology applications, including quantum information processing [14, 15], light field manipulation [16, 17], single photon generation [18], and quantum communication [19–21], as the ability to change the emitters' properties with light (and vice versa) has proven to be an indispensable tool for highly controlled quantum operations.

While many works in cavity QED have focused on one or a few cavity-coupled emitters [15–18, 21–26], there has been growing interest in the study of cavity QED with a macroscopic ensemble of emitters [27–30], as the increased complexity offers deeper fundamental insights as well as expanded technological capabilities. Cavity-coupled ensembles of rare-earth ions doped in solids are an ideal platform for such a study [31, 32], as they offer highly stable transitions in both the optical and microwave domain at cryogenic temperatures [33] and can be readily integrated into nanoscale devices [34]. In contrast to atomic gas systems [27, 29], the solid-state implementation offers the added benefit of on-chip integration for quantum applications such as high bandwidth quantum memories and transducers [35, 36]. In such applications, the high bandwidth is necessary for frequency multiplexing in

memories and high speed conversion in transducers and is achieved as a result of the natural spectral inhomogeneity of the solid-state emitters. In order for such devices to operate efficiently, one must engineer a system with high cooperativity, which is a dimensionless figure of merit that describes the ratio between the collective coupling strength of the cavity-emitter system to dissipation, decoherence, and disorder. As improvements to material and device parameters are made towards increasing this cooperativity, it becomes critical to fully understand any associated cavity QED phenomena that may emerge.

Here, we will introduce some basic concepts from single-emitter cavity QED to multiple emitters [37].

Single-emitter cavity QED

A single two-level system interacting with a quantized mode of an optical cavity (Fig. 1.4a) is described by the Jaynes-Cumming model [38] with the governed Hamiltonian

$$H = \hbar\omega_c a^\dagger a + \frac{1}{2}\hbar\omega\sigma_z + \hbar g(a^\dagger\sigma_- + a\sigma_+). \tag{1.1}$$

Here, a is the bosonic cavity field operator, $\sigma_\pm$ and σ_z are the spin ladder operators and the Pauli-Z operators describing the atomic coherence and inversion of the emitter, respectively. ω_c is the cavity resonant frequency, ω is the atomic transition frequency, g is the atom-cavity coupling rate. g depends on the local electric field such that it is position $\vec{r}$ dependent:

$$g(\vec{r}) = -\sqrt{\frac{\omega_c}{2\hbar\int_{\text{everywhere}}\epsilon(\vec{r})|\vec{E}(\vec{r})|^2 d\vec{r}^3}}\vec{d}\cdot\vec{E}(\vec{r}) \tag{1.2}$$

where $\vec{d}$ is the electric dipole moment of the atom, $\vec{E}(\vec{r})$ is the electric field at location $\vec{r}$ and ϵ is the permittivity. Sometimes $g(\vec{r})$ is also written in terms of mode volume V where

$$V = \frac{\int_{\text{everywhere}}\epsilon(\vec{r})|\vec{E}(\vec{r})|^2 d\vec{r}^3}{\max\{\epsilon(\vec{r})|\vec{E}(\vec{r})|^2\}} \tag{1.3}$$

such that

$$g(\vec{r}) = -\sqrt{\frac{\omega_c}{2\hbar V\max\{\epsilon(\vec{r})|\vec{E}(\vec{r})|^2\}}}\vec{d}\cdot\vec{E}(\vec{r}). \tag{1.4}$$

When the electric field and material inside the cavity is uniform, g will be simplified as

$$g = -\sqrt{\frac{\omega_c}{2\hbar V\epsilon}}\vec{d}\cdot\hat{E} \tag{1.5}$$

where $\hat{E}$ is the unit direction vector of the cavity field. We can further move to the laser frame with a frequency ω_L and focus on the slow-varying part of the operators (rotating-wave approximation in the Heisenberg picture): $a \rightarrow ae^{-i\omega_L t}$ and $\sigma_- \rightarrow \sigma_- e^{-i\omega_L t}$. This gives us:

$$H = \Delta_c a^\dagger a + \frac{1}{2}\Delta\sigma_z + g(a^\dagger\sigma_- + a\sigma_+) \tag{1.6}$$

where $\Delta_c = \omega_c - \omega_L$, $\Delta = \omega - \omega_L$, and $\hbar = 1$ for brevity.

In addition to the Hamiltonian, both the cavity and the atom have dissipative rates (Fig. 1.4a). For the cavity, we define the cavity energy decay rate as $\kappa = \kappa_c + \kappa_i$, including the intrinsic decay rate κ_i and the coupling rate κ_c of the input channel. When we look at the cavity reflection spectrum, both the input and output coupling can be described by κ_c. In the more general case where there are other coupling channels, additional coupling terms should be included in κ. For example, in cavity transmission measurements, one should consider the output coupling rate to the transmitted port, denoted by κ_t, such that the total coupling rate can be written as $\kappa = \kappa_c + \kappa_i + \kappa_\mathrm{t}$. The intrinsic coupling κ_i indicates the incoherent loss rate of the cavity energy, which can be caused by the material absorption or scattering. The ratio $\frac{\kappa_c}{\kappa}$ reflects how well the cavity is coupled to a specific channel, and it is usually referred as under-coupled when $\frac{\kappa_c}{\kappa} < 0.5$, critical-coupled when $\frac{\kappa_c}{\kappa} = 0.5$ and over-coupled when $\frac{\kappa_c}{\kappa} > 0.5$. For the emitter, the decoherence rate is definied as $\gamma = \frac{\gamma_s}{2} + \gamma_d$, including the spontaneous decay rate γ_s and the excess dephasing rate γ_d. This γ indicates the relative energy level fluctuation of the two level system, and it will be reflected in the linewidth of the emitter in the probe spectrum (probe power should be small enough to avoid power broadening).

The performance of the system depends on the competition between g, κ and γ, which is described by cooperativity

$$C = \frac{4g^2}{\kappa\gamma}. \tag{1.7}$$

Many-body cavity QED

A cavity mode interacting with multiple atoms can be described by the Tavis-Cummings Hamiltonian (in the laser frame) [39]:

$$H = \Delta_c a^\dagger a + \frac{1}{2}\sum_{j=1}^{N}\Delta_j\sigma_z^j + \sum_{j=1}^{N} g_j(a^\dagger\sigma_-^j + a\sigma_+^j). \tag{1.8}$$

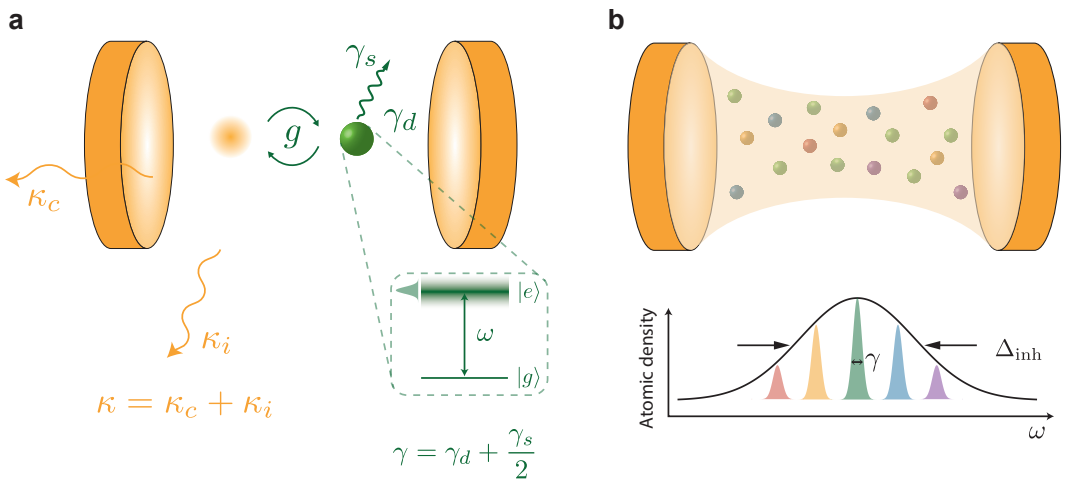

Figure 1.4: **a.** Single-emitter cavity QED. **b.** Many-body cavity QED.

Here, we consider the coupling strength disorder (distribution of g_j) and frequency inhomogeneity (distribution of Δ_j).

The total coupling of the ensemble to the cavity field is determined by the total interaction strength $g_{\text{tot}} = \sqrt{\sum_j g_j^2}$ and their frequency detuning relative to the probe field with frequency, which can be described by collective absorption rate $W(\omega_L)$ [40, 41],

$$W(\omega_L) = g_{\text{tot}}^2 \int \frac{\rho(\omega)}{\omega_L - \omega + i\gamma} d\omega, \tag{1.9}$$

where $\rho(\omega)$ is defined as $\rho(\omega) = \frac{1}{g_{\text{tot}}^2} \sum_j g_j^2 \delta(\omega - \omega_j)$. We can see that when g and frequency are uncorrelated, $\rho(\omega)$ is the spectral density distribution with a center frequency ω_0 and inhomogeneous linewidth Δ_{inh} (Fig. 1.4b). The collective cooperativity is then defined as the ratio between the absorption rate and the cavity decay $C = \frac{|W(\omega_L=\omega_0)|}{\kappa/2}$,

$$C = \frac{2g_{\text{tot}}^2}{\kappa} \int \frac{\rho(\omega)}{\omega_0 - \omega + i\gamma} d\omega = \alpha \frac{2g_{\text{tot}}^2}{\kappa \Delta_{\text{inh}}}, \tag{1.10}$$

where the prefactor α depends on the specific distribution. For example, a Lorentzian distribution gives $\alpha = 2$, a Gaussian distribution gives $\alpha = 2\sqrt{\pi \ln 2}$ and a rectangular distribution gives $\alpha = \pi$ (note that Δ_{inh} is defined as the full width at half maximum of each distribution).

1.5 Outline of the thesis

In this thesis, we are utilizing a rare-earth ions platform to engineer quantum applications, specifically quantum memory, and exploring many-body physics in both

the optical and spin domains. The structure of the thesis is shown in Figure 1.5.

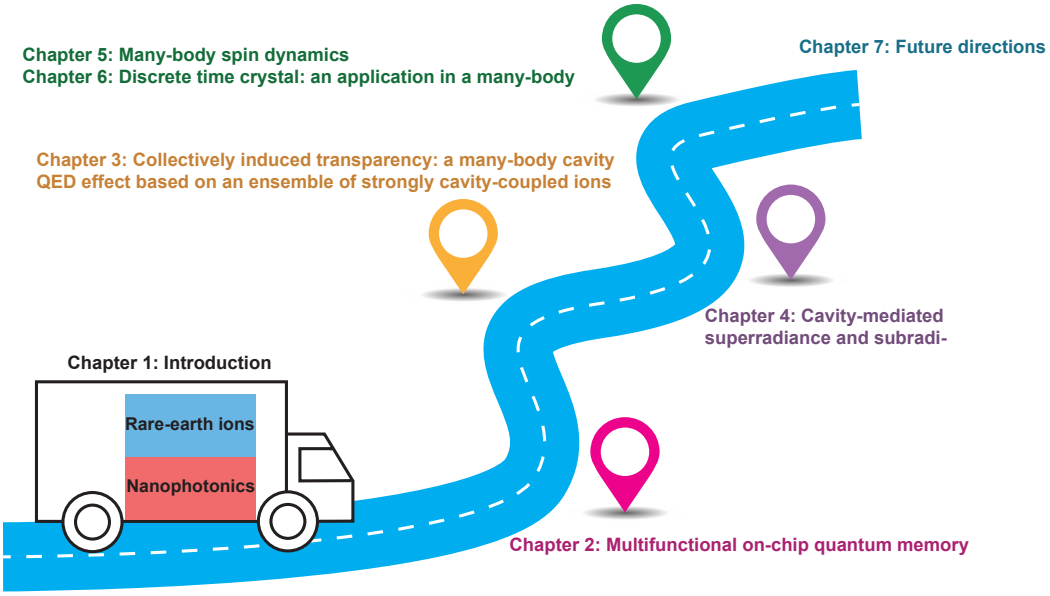

Figure 1.5: **Structure of this thesis.**

Chapter 2

ON-CHIP QUANTUM MEMORIES BASED ON ERBIUM ENSEMBLES

In this chapter, we demonstrate multifunctional on-chip quantum memories at telecommunication wavelengths. The content is adapted from [42].

2.1 Introduction

Optical quantum memories will enable long distance quantum communication using quantum repeater protocols [43–45]. A quantum memory device which can control the bandwidth and frequency of stored light is additionally useful, as it can interface between optical elements which have different optimal operating points. Erbium-doped materials are a promising solid-state platform for ensemble-based optical quantum memories because of their long-lived optical transition in the telecommunication C-band that is highly coherent at cryogenic temperatures [46, 47]. This allows for integration of memory systems with low-loss optical fibers, opening up opportunities for repeaters over continental distances, as well as integration with silicon photonics [41, 48] one of the most advanced platforms for integrated photonics. Spin transitions in $^{167}Er^{3+}$-doped yttrium orthosilicate ($^{167}Er^{3+}$:Y_2SiO_5) have also been shown to have long relaxation and coherence lifetimes at cryogenic temperatures and high magnetic fields [49] which opens the possibility for long term spin wave memories.

There have been several demonstrations of optical storage in erbium-doped materials [50–55], including storage at the quantum level [50, 51, 55], and on-chip storage [51, 55]. These results are part of a larger body of optical quantum memory research [45, 56], using rare-earth-ion-doped crystals [57–60], atomic gases [61, 62], and single atoms or defects [63, 64]. In parallel with efforts to increase the efficiency [61] and storage time [59, 60] of quantum memories, several works have focused on new types of multifunctional devices [65–68] in which control fields are used to modify the state of the light during storage.

In many quantum repeater protocols [69], quantum memories act as interfaces between emitters such as quantum dots [70] or individual atoms [48]. Dynamic control of the optical pulses stored in these memories can correct for differences between

individual emitters, leading to higher indistinguishably for Bell State measurements at the entanglement swapping stage of quantum repeater protocols [43]. In addition, with control over the frequency of stored light, one can map an input mode to a different output mode in a frequency multiplexed quantum memory, which enables quantum networks with fixed-time quantum memories [71].

In this work, we use a silicon resonator evanescently coupled to $^{167}Er^{3+}$:Y_2SiO_5 ions and gold electrodes to realize a multifunctional on-chip device which can not only store light, but also dynamically modify its frequency and bandwidth. Electrodes create a DC electric field that can be rapidly switched, which enables control of the $^{167}Er^{3+}$ ions' optical transition frequency via the DC Stark shift [72]. Using a resonator increases the interaction between light and the ion ensemble, allowing on-chip implementation of the atomic frequency comb (AFC) memory protocol [20]. This protocol allows multiplexing in frequency, which offers a significant advantage in quantum repeater networks [73]. Additionally, the on-chip electrodes are patterned close together to achieve the high electric fields required for Stark shift control with CMOS compatible, applied voltages. We demonstrate dynamic control of memory time in a digital fashion, as well as modification of the frequency and bandwidth of stored light.

2.2 Hybrid αSi-$^{167}Er^{3+}$:Y_2SiO_5 resonator with electrodes

The multifunctional device consists of an optical resonator coupled to $^{167}Er^{3+}$:Y_2SiO_5 ions between gold electrodes. Using the AFC quantum storage protocol [74] and the ions' Stark shift, light can be stored and manipulated in this device. Figure 2.1a shows a schematic of the device and the three functionalities demonstrated in this work: memory time control, frequency control, and bandwidth control. Different electric field configurations are created by applying a positive (blue) or negative (red) bias to each electrode. For the true device dimensions, see the micrograph in Fig. 2.2d.

The optical resonator used in this work is a Fabry-Perot resonator comprised of a 100 μm amorphous silicon (αSi) waveguide on $^{167}Er^{3+}$:Y_2SiO_5 with photonic crystal mirrors on either end. Figures 2.3a-c show simulations and micrographs of this resonator. The waveguide is h = 310 nm tall and w = 605 nm wide. Ten percent of the energy of the transverse-magnetic optical waveguide mode penetrates into the $^{167}Er^{3+}$:Y_2SiO_5 and evanescently couples to the $^{167}Er^{3+}$ ions. Photonic crystal mirrors on either side are formed by a repeating pattern of elliptical air holes in

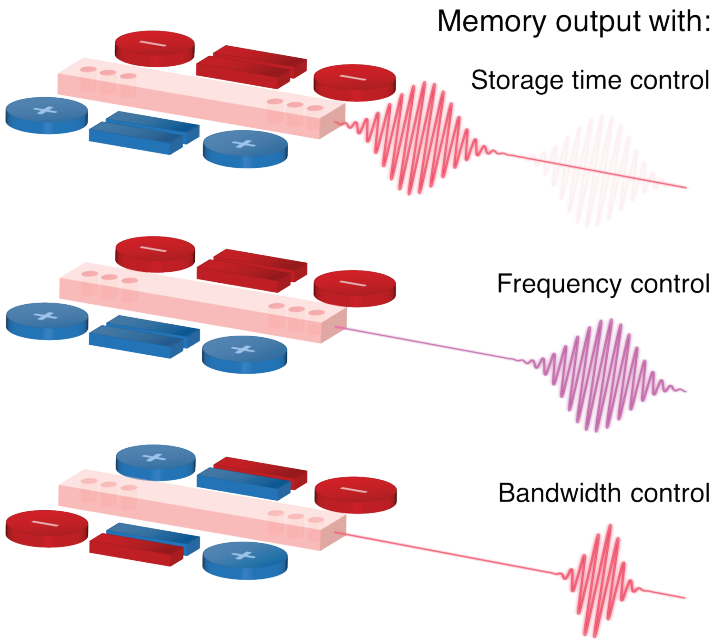

Figure 2.1: **Multifunctional quantum storage device.** Schematic of device functionality showing the optical resonator (pink), electrodes (blue and red), and memory output.

the αSi waveguide with period $a_\circ = 370$ nm. A grating coupler is used to couple light from a free-space mode into and out of the resonator. The amorphous silicon resonator is fabricated on top of an $^{167}Er^{3+}$:Y_2SiO_5 chip using a deposition and etching process similar to Ref. [41]. The $^{167}Er^{3+}$:Y_2SiO_5 substrate is doped with isotopically purified $^{167}Er^{3+}$ ions at 135 ppm, measured by secondary ion mass spectrometry, and cut perpendicular to the D_1 crystal axis, such that the electric field of the transversal magnetic (TM) optical mode is polarized along this axis. The x, y, and z axes in Fig. 2.2 and Fig. 2.3 correspond to the D_2, b and D_1 Y_2SiO_5 crystal axes, respectively.

Quality factors of up to 10^5 were measured for weakly coupled resonators, where the photonic crystal mirrors on both sides were designed to be highly reflective. The device used in this work is made one-sided for more efficient quantum storage [55, 74] by using fewer photonic crystal periods in one mirror to make it less reflective. Light is sent into and measured from the side with the lower reflectivity mirror. The intrinsic quality factor for this device is also lower than the weakly coupled resonators, leading to a quality factor of 3×10^4 and a coupling ratio of $\kappa_{in}/\kappa = 0.2$, where κ_{in} is the coupling rate through the lower reflectivity mirror and

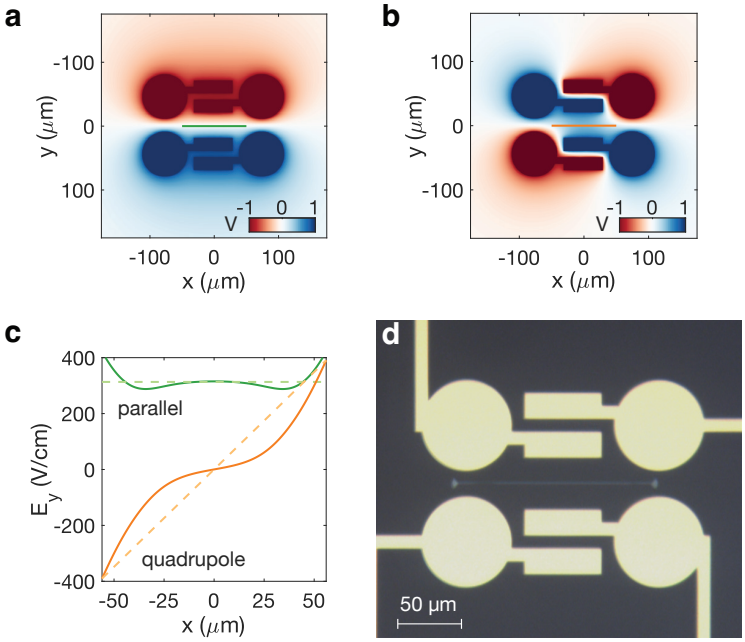

Figure 2.2: **Electrodes on quantum storage device. a-c,** 3D finite element simulation of on-chip electrodes. **a, b,** 2D slice at $z = 0$ showing electric potential (blue-red gradient) in the parallel (**a**) and quadrupole (**b**) biasing configurations. **c,** Electric field $E_y(x)$ along optical resonator in the parallel (green solid line) and quadrupole (orange solid line) configurations; $E_y(x)$ was measured at $z = 0$, $y = 0$, $-56\ \mu\text{m} < x < 56\ \mu\text{m}$ (green lines in **a** and orange lines in **b**); dashed lines indicate ideal parallel (green) and quadrupole (orange) electric field distributions. **d,** Optical micrograph showing an optical resonator, gold electrodes, and gold wires for electrical contact.

κ is the total decay rate [76]. The lower (higher) reflectivity mirror consists of 6 (30) regularly spaced holes, with an additional 15 holes in the tapers on either side. Several one-sided devices with different numbers of regularly spaced holes on the lower reflectivity side were fabricated on the same chip, and the device with the best combination of quality factor and $\kappa_{\text{in}}/\kappa$ was chosen.

Electrodes are used to apply electric fields to those ions coupled to the optical resonator. There are four independently biased gold electrodes, each comprised of a 70 μm diameter circle connected to a 20 μm $\times$ 60 μm rectangle. They are patterned onto the $^{167}\text{Er}^{3+}$:Y_2SiO_5 after the αSi resonators using electron-beam lithography followed by electron-beam gold evaporation and lift-off. Figures 2.2a-d show simulations of the two electrode biasing configurations: parallel, which applies a nearly constant electric field to all ions ($E(x) = a$), and quadrupole, which applies an electric field gradient along the resonator (approximating $\frac{dE(x)}{dx} = b$), where a

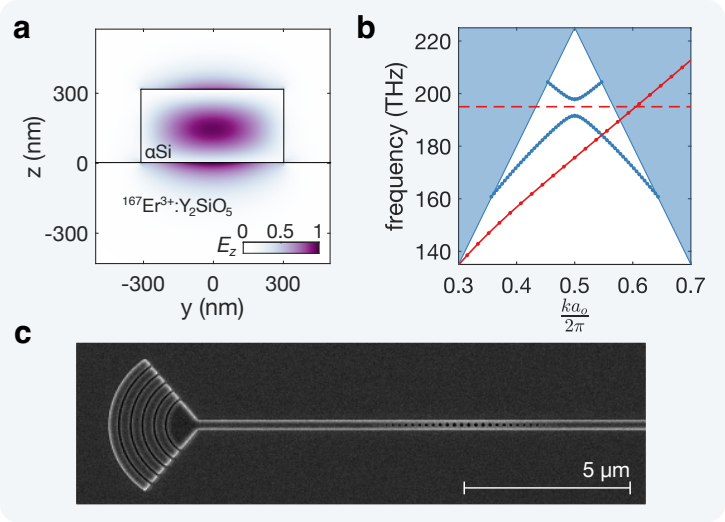

Figure 2.3: α**Si resonator quantum storage device. a,** cross-section of waveguide (black outline) showing 2D finite element simulation of the transverse-magnetic waveguide mode. Purple-white gradient indicates the E_z component of the optical field. **b,** Band diagram showing waveguide mode (solid red line), band gap of a photonic crystal mirror (solid blue lines), and the design frequency of 195 THz (dashed red line). Blue areas indicate the Y_2SiO_5 light cone containing extended modes propagating in bulk Y_2SiO_5 (both sides for photonic crystal, left side only for waveguide). **c,** Scanning electron micrograph showing a grating coupler and photonic crystal mirror including tapered sections on either side to reduce scattering [75].

and b are constants. The electrode geometry was designed to best approximate these two electric field profiles with four independently biased electrodes, while providing a large electric field for a given applied bias (E/V). In the $^{167}Er^{3+}:Y_2SiO_5$ region where ions are coupled to the optical mode, the E_y component of the electric field is dominant ($E_y \gg E_x, E_z$), and it does not vary significantly in the z and y directions. Therefore only $E_y(x)$, which is aligned to the b-axis of the Y_2SiO_5 crystal, is considered.

The device is thermally connected to the coldest plate of a dilution refrigerator, the temperature of which is $\sim$ 100 mK. A static magnetic field of 0.98 T is applied along the Y_2SiO_5 D_1-axis with a superconducting electromagnet. Trim coils are used to cancel any magnetic field component along the b-axis. Two function generators with 120 MHz bandwidth and a total of 4 channels were used to apply pulses with amplitudes up to ±5 V to the electrodes. The remainder of the measurement setup was similar to the one described in Ref. [55].

2.3 DC Stark shift in $^{167}Er^{3+}$:Y_2SiO_5

Er^{3+}:Y_2SiO_5 has been extensively studied for quantum applications [46–48, 52–55, 77, 78], including demonstrations of AFC storage [53, 55]. Erbium ions substitute for yttrium ions in Y_2SiO_5 in 2 crystallographic sites, each of which has four different orientations due to the C_{2h}^6 crystal symmetry [79]. In this work, we use crystallographic site 2, which has an optical transition near 1539 nm [46]. $^{167}Er^{3+}$ has a nuclear spin $I = 7/2$, which together with an effective electron spin, leads to 16 hyperfine levels in both the optical ground and excited states. At high fields and low temperatures, the electron spin is frozen, allowing the lowest 8 ground-state hyperfine levels to be long-lived [49, 55], thereby enabling the spectral holeburning that is required to create atomic frequency combs. Aligning the magnetic field with the D_1 crystal axis enhances this effect because the ground state electron g-tensor of $^{167}Er^{3+}$:Y_2SiO_5 is nearly maximized in that direction for site 2 [79].

Dynamic control is enabled by the DC Stark shift. When a rare earth ion in a crystal interacts with a DC electric field $\vec{E}$, its optical transition frequency is shifted due to the difference between the permanent electric dipole moments in the optical excited and optical ground states $\delta\vec{\mu} = \vec{\mu}_e - \vec{\mu}_g$. For non-centrosymmetric sites such as the yttrium sites in Y_2SiO_5 for which Er^{3+} ions substitute, the linear Stark shift term $\delta f = -\frac{1}{h}\,\delta\vec{\mu}\cdot\overleftrightarrow{L}\cdot\vec{E}$ dominates, where $\overleftrightarrow{L}$ is the local field correction tensor [72].

The Stark shift is dependent on the orientation of the applied field relative to $\delta\vec{\mu}$ [80]. Without knowing $\delta\vec{\mu}$ or $\overleftrightarrow{L}$, the Stark shift can be empirically characterized for an electric field applied in a particular direction $\hat{n}$ ($\hat{n}$ is a unit vector) using the Stark shift parameter $s_{\hat{n}}$ given $\delta f = s_{\hat{n}}E_{\hat{n}}$. We measured $s_{\hat{n}} = 11.8 \pm 0.2$ kHz/(V/cm) for $\hat{n}$ nominally aligned with the Y_2SiO_5 crystal b-axis (Fig. 2.4). Specifically, spectral hole burning was firstly used to create a comb consisting of four narrow teeth, and the frequency shift under a certain applied electric field was then measured with electrodes biased in the parallel configuration (Fig. 2.2a).

In an ensemble of $^{167}Er^{3+}$:Y_2SiO_5 ions, four different Stark shifts will be observed for an arbitrary electric field due to the four orientations of each crystallographic site [79]. For electric fields parallel or perpendicular to the b-axis, the Stark shifts of the four subclasses are pair-wise degenerate, resulting in two Stark shifts $\delta f_\pm = \pm sE$. In this work, all electric fields are applied parallel to the b-axis, so we will simply refer to two $^{167}Er^{3+}$ subclasses.

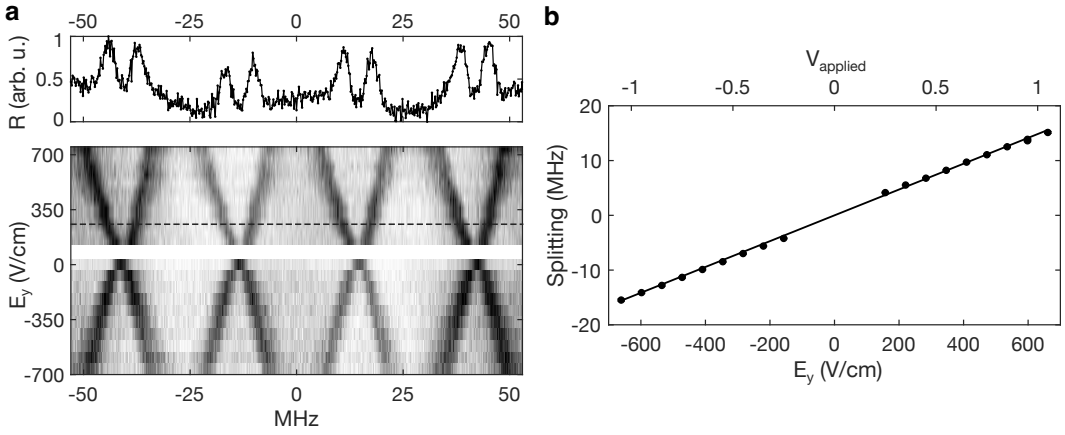

Figure 2.4: **Holeburning spectroscopy measurement of DC Stark shift. a,** Frequency profile of a four-tooth comb as a function of electric field. White-black gradient represents cavity reflectance. Both subclasses of ions are present, leading to a two-fold splitting. Inset shows an example sweep with $E_y = 283$ V/cm, the location of which is indicated with a dashed line on the main plot. **b,** Splitting versus electric field. Black circles are splitting data obtained by fitting the traces in **a** with four sets of two-fold split Gaussians. A negative splitting means the positions of the two subclasses are reversed. Error bars, which are smaller than markers, represent 95% confidence intervals from the fits. Solid line is a linear fit to the data without an offset. The top axis shows V_{applied}, one output of the function generator used to generate electric pulses (the other outputs are either V_{applied} or $-V_{\text{applied}}$). The bottom axis shows E_y, the electric field applied along the Y_2SiO_5 b-axis, calibrated using the average value from simulation $E_y = 314.8$ V/cm when ± 1 V is applied to each electrode (dashed green line in Fig. 1g in main text). There is an additional factor of 2 in the calibration due to the impedance mismatch between the 50 Ω output of the function generator and the open-circuit electrodes.

2.4 Atomic frequency comb storage with dynamic memory time control

After a photon is absorbed by an ensemble of ions, the ensemble of ions is described by a Dicke state [74]:

$$|\Psi\rangle = \sum_{j=1}^{N_{\text{ions}}} c_j \, e^{i2\pi\left(f_j + \delta f_j(t)\right) t} \, e^{-ik\vec{r}_j} \left|0...1_j...0_N\right\rangle . \tag{2.1}$$

Each ion has a different transition frequency f_j and position $\vec{r}_j$. For AFC storage, the transition frequencies $\{f_j\}$ form a frequency comb with period Δ. When a photon is absorbed at $t = 0$, the ensemble of ions first dephase then rephase every $t = \frac{m}{\Delta}$, $m \in \mathbb{N}$, leading to a coherent re-emission of the light [74]. A Stark shift $\delta f_j(t)$ enables dynamic control of light stored in the AFC by changing the optical

transition frequencies of the ions. $\delta f_j(t)$ can be varied over time by changing the amplitude of the applied electric field (slowly relative to optical frequencies). This enables two types of control: electric field pulses applied between the absorption and emission of light modify the phase of the output, while electric field pulses applied during emission of light modify the frequency profile of the output light.

To achieve dynamic control of storage time, the electrodes are biased in a parallel configuration as shown in the top panel of Figure 2.1 (Fig. 2.2a). When an electric pulse is applied, the two $^{167}Er^{3+}$:Y_2SiO_5 subclasses experience opposite frequency shifts, $\pm\delta f(t) = \pm s_b E$. By appropriately choosing the length in time t and amplitude E of the electric pulse, a π phase difference between subclasses can be introduced $\pi = 2\pi \times (+s_b E - (-s_b E)) \times t$, which will prevent any coherent emission from the ensemble. An equal-area electric pulse with opposite sign can then rephase the two subclasses, and allows coherent re-emissions from the AFC. This procedure of dephasing and rephasing the ensemble works even if the electric field distribution is not perfectly homogeneous, as shown in the context of Stark Echo Modulation Memory in Reference [81]. Recently, dynamic control of memory time in AFC was demonstrated using this same procedure in Pr^{3+}:Y_2SiO_5 [82]. Reference [53] proposed a similar protocol but using an electric field gradient.

The pulse sequence used to achieve dynamic control of AFC storage is shown in Figure 2.5a. Not shown is the initialization to move most of the population into one hyperfine state, which is performed before every experiment [42, 49, 55]. First, an AFC with period Δ is created by repeatedly burning away population between the teeth of the comb, $n_{\mathrm{comb}} = 20$ times. Then, an input pulse indicated by the red laser pulse is sent into the resonator at $t = 0$ and is absorbed by the AFC. Shown in light red are possible emissions corresponding to rephasing events of the AFC at times $t = \frac{m}{\Delta}$. Without electric field control, the output of the memory (the first and largest emission), would be centered at $t = \frac{1}{\Delta}$ ($m = 1$). The schematic shows instead an emission in red at $t = \frac{3}{\Delta}$ ($m = 3$), obtained when a first electric pulse is applied before the first emission and a compensating pulse is applied immediately before the third emission.

Figure 2.5b shows the AFC used in this experiment. The period of the comb, extracted from the fit, is 19.7 ± 0.1 MHz, which corresponds to a minimum storage time of $t = \frac{1}{\Delta} = 50$ ns. Figure 2.5c shows dynamically controlled storage for various values of m. The input pulse is a weak coherent pulse corresponding to an average photon number in the resonator of $\langle n_{\mathrm{cav}} \rangle = 1.9$. Two electric pulses were used to

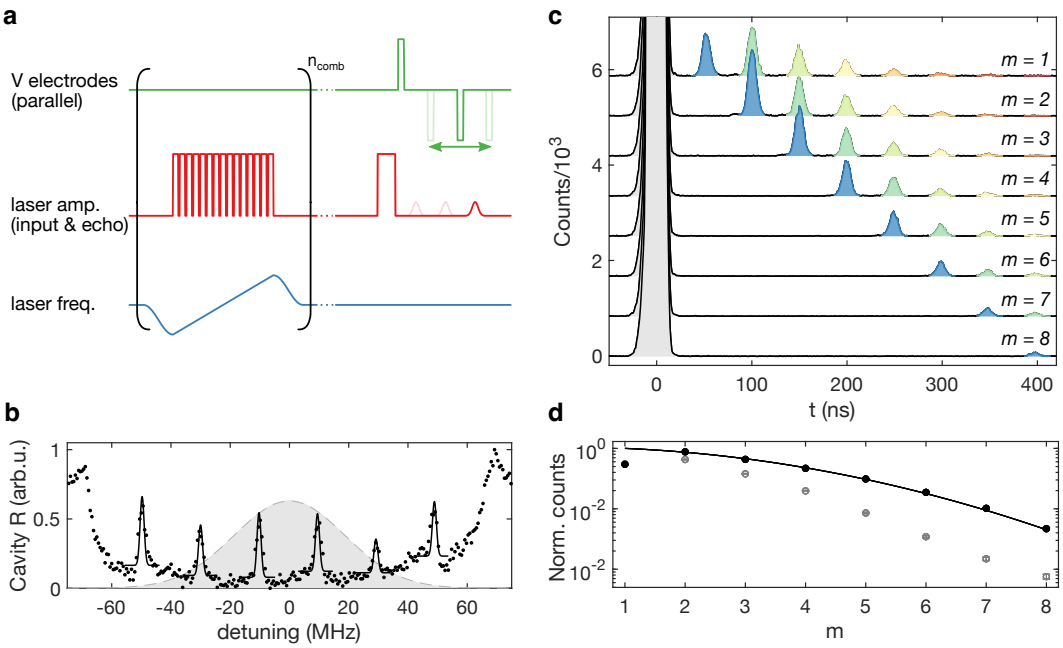

Figure 2.5: **AFC storage with dynamic memory time control.** **a,** Pulse sequence (not to scale, details in main text). **b,** Atomic frequency comb. Cavity reflectance (black points) and fit to six Gaussians (solid black lines). All teeth are fit together, with the finesse fixed to the value from **d**. Detuning is measured from 194822 GHz. Grey Gaussian with dashed outline represents the input pulses in frequency space. **c,** Emission of stored light at different times $t_{\text{memory}} = \frac{m}{\Delta}$. Partly reflected input pulse are shown in grey at $t = 0$. On-demand memory outputs are shown in blue (darkest shade). Subsequent emissions (green to red) are discussed in the main text. Electric pulses are not shown. **d,** Energy emitted in the time bin at $t = \frac{m}{\Delta}$ for each value of m. Black data points represent the normalized counts when all previous emissions are suppressed with electric pulses (blue pulses in **c**). Grey data points represent normalized counts when previous emissions are not suppressed, meaning no electric pulses are used (all pulses on line $m = 1$ in **c**). Error bars, representing $\sqrt{N_{\text{counts}}}$, are smaller than the markers. Solid line is a fit to theory, fitting only for comb finesse.

control memory time. The first was a 10 ns long pulse with amplitude 2 kV/cm centered at $t_{\text{pulse 1}} = 25$ ns. The second was 10 ns long with an opposite amplitude of -2 kV/cm, and its center position was varied as $t_{\text{pulse 2}} = 25 \text{ ns} + (m-1) \times 50$ ns to allow the emission at $t_{\text{memory}} = \frac{m}{\Delta}$. The electric pulses were calibrated to ensure optimal suppression of the emission[42]. Between the two electric pulses, emission was suppressed down to the dark counts level, a factor of 100 lower than peak emission counts. For the $m = 1$ case, no electric pulses were applied. The presence of multiple smaller pulses following the output pulse is a feature of the high finesse and low efficiency of the memory (section 2.9). For higher efficiency, high finesse AFCs, subsequent emissions are significantly suppressed [82].

Figure 2.5d shows the energy emitted in the m^{th} time bin for $t_{\text{memory}} = \frac{m}{\Delta}$. The data is fit to the dephasing term in the theoretical storage efficiency for a comb with Gaussian teeth: $\exp\left(-\frac{\pi^2}{2\ln 2}\frac{m^2}{F^2}\right)$ [53, 74], where $F = \Delta/\gamma$ is the comb finesse, and γ is the full-width at half maximum (FWHM) of each tooth. The $m = 1$ data point is excluded from the fit because the approximately 100 ns dead time of the single photon detector after the input pulse is thought to lead to undercounting in that time bin. A comb finesse of $F = 12.2 \pm 0.2$ ($\gamma = 1.6$ MHz) is extracted from this fit. This corresponds to a $1/e$ point of 240 ns ($m = 4$ for digital storage time). To improve on this scaling requires a smaller tooth width γ. The grey data in Fig. 2.5d show the total counts in the m^{th} time bin when the previous output pulses are not suppressed.

2.5 Dynamic frequency control

The frequency of light stored in an AFC can be dynamically modified during emission. The atomic frequency comb is shifted in frequency during the emission of stored light by biasing the electrodes in the parallel configuration as shown in the middle panel of Figure 2.1 (Fig. 2.2a). The pulse sequence used to achieve AFC storage with frequency control is shown in Figure 2.6a. The first step is to eliminate one of the two $^{167}Er^{3+}$ subclasses from the spectral window, leaving only ions which experience a positive Stark shift, $\delta f_+ = +s_b E$ (the choice of subclass is arbitrary). This is accomplished using a two-part comb burning procedure. With the first burning step, a normal AFC containing both subclasses is created using a sequence of laser pulses. For the second burning step, the two subclasses are split by $\Delta/2$ using a parallel electric field, and a similar sequence of laser pulses is used, but with a frequency shift of $\Delta/4$. This burns away ions with a negative shift $\delta f_- = -s_b E$.

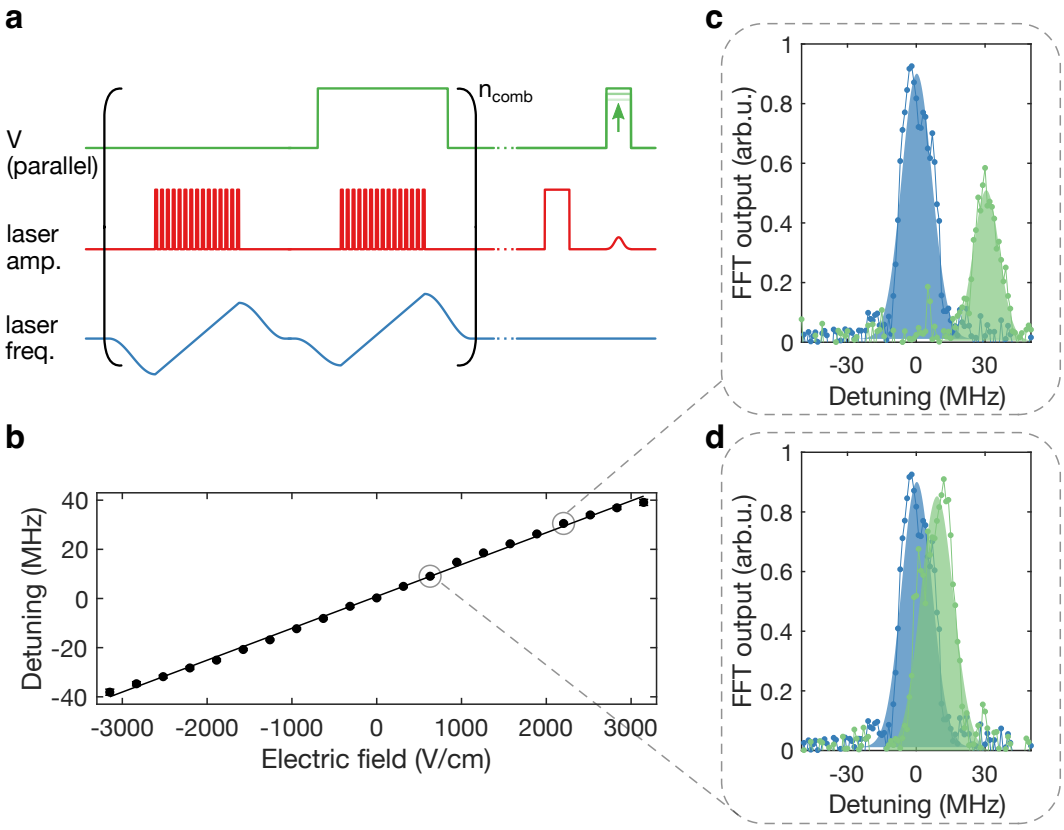

Figure 2.6: **AFC storage with frequency control.** **a,** Pulse sequence (not to scale, details in main text). **b,** The output detuning as a function of electric field applied during emission. Circles are the centers of Gaussian fits (as shown in (b-c)). Error bars, which are smaller than the markers, are 95% confidence intervals for those fits. The solid line is a linear fit to the data, yielding a slope of 13.0 ± 0.3 kHz/(V/cm), similar to the Stark shift value measured by holeburning spectroscopy. **c,d,** Examples of AFC output pulses with (green, lighter) and without (blue, darker) a frequency shift. Filled in area is a Gaussian fit to the data (circles). Detuning is measured from 194822 GHz. Frequency shifts of 9 MHz in **c** and 30 MHz in **d** are shown, with corresponding points in **b** circled.

Repeating the comb burning procedure $n_{\text{comb}} = 5$ times, an AFC with width 145 MHz, and a period $\Delta = 5$ MHz is created. An input pulse is sent in and the rephasing of the AFC causes an emission at $t = \frac{1}{\Delta} = 200$ ns. During this emission, an electric field pulse with amplitude E_{pulse} applied in the parallel configuration will cause the ions to emit with a frequency shift of $f = +s_b E_{\text{pulse}}$. Figures 2.6b-c show the light emitted from the memory, with and without a frequency shift. A heterodyne measurement is used to measure the frequency of the output pulse directly. To detect the output pulse with this lower-sensitivity detection method, bright input pulses were used $\left(\langle n_{\text{cav}} \rangle = 46 \times 10^3\right)$. Figure 2.6d shows the linear frequency shift

as a function of electric field. The decrease in output amplitude with frequency shift evident in Figures 2.6b-c is mainly due to the broadening of the teeth width, which is caused by inhomogeneity of Stark shifts experienced by the ions[42]. This broadening results in a decrease in efficiency via the dephasing term introduced in the previous section.

2.6 Dynamic bandwidth control

The bandwidth of stored light can be dynamically controlled by biasing the electrodes in a quadrupole configuration as shown in the bottom panel of Figure 2.1 (Fig. 2.2b). In the quadrupole configuration, electric pulses create a gradient electric field across the ions so that each ion experiences a different Stark shift. Figure 2.7a shows the pulse sequence used to achieve AFC storage with bandwidth control. First, an AFC with $\Delta = 1.6$ MHz and bandwidth 144 MHz is created by repeatedly burning away population $n_{\mathrm{comb}} = 20$ times. Next, an input pulse ($\langle n_{\mathrm{cav}} \rangle = 1.9$) is sent into the device, leading to an output pulse at $t = \frac{1}{\Delta} = 630$ ns. A gradient field applied during the AFC emission causes the bandwidth of the absorbing ion ensemble to broaden, such that the emitted pulse is also broader in frequency relative to the input pulse. However, the gradient field also alters the phase evolution of each ion by changing its resonant frequency. If not compensated, the different phases accumulated across ions in the ensemble could prevent emission altogether. For this reason, three electric pulses are applied, during the input and output optical pulses, and also during the wait time. These three pulses have the same area but can have different amplitudes. The first and second pulses are used to add phase compensation such that the net electric-field-induced phase shift is zero for each ion, accounting for the fact that AFC storage is first-in-first-out [65, 83].

Figure 2.7b shows AFC storage with no broadening (top) and with the maximum achieved bandwidth broadening (bottom). A broadening in frequency space is seen as a narrowing of the output pulse in time. By fitting the output pulses to Gaussians, the temporal FWHMs (Δt) of input and output pulses are extracted and converted to bandwidth or frequency FWHMs (Δf) using: $\Delta f = \frac{4\ln 2}{2\pi}(\Delta t)^{-1}$. Figure 2.7c shows the trend of output bandwidth as a function of the maximum electric field applied during the third pulse E_{max} (the electric field across the resonator ranges from $-E_{\mathrm{max}}$ to E_{max}). To confirm that the trend observed in the data is expected given the atomic frequency comb profile, the input pulse, and the electric field distribution $E_y(x)$, a simulation of the experiment was performed by numerically integrating the time-evolution equations of the atoms and cavity (section 2.9). The simulation data

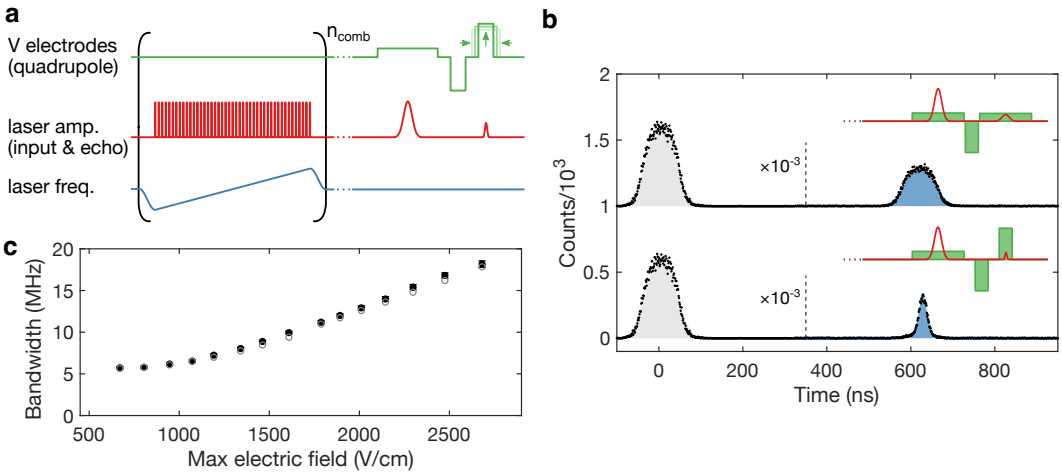

Figure 2.7: **AFC storage with bandwidth control. a,** Pulse sequence (not to scale, details in main text). **b,** AFC storage with (bottom) and without (top) bandwidth broadening. Colored areas are Gaussian fits to photon counts data (circles) from which widths are extracted. The partially reflected input pulse with FWHM 77.4 ns (5.7 MHz FWHM in the frequency domain) is shown in grey (lighter color) in both traces at $t = 0$, demagnified by a factor of 10^3. The top trace shows the case without bandwidth broadening: $E_{\max}(t = 630\ \text{ns}) = E_{\max}(t = 0) = 0.67$ kV/cm, where the width of the output (blue, darker) is 77.1 ± 2.0 ns (5.7 ± 0.1 MHz). The bottom trace shows the maximum bandwidth broadening, $E_{\max}(t = 630\ \text{ns}) = 4 \times E_{\max}(t = 0) = 2.8$ kV/cm, where the width of the output (blue, darker) is 24.3 ± 0.5 ns (18.1 ± 0.4 MHz). Insets show schematics of electrode pulse sequences. **c,** Bandwidth of pulses as a function of the $E^{\max}_{\text{output}}$. In all cases, $E^{\max}_{\text{input}} = 0.67$ kV/cm. Filled black circles are FWHM data. Error bars, which are smaller than the markers, represent 95% confidence intervals from fits. Unfilled grey circles are simulation data (section 2.9).

reproduces the trend in FWHM as a function of field. The only previously unknown parameter used in this simulation was the distance that the optical mode penetrates into the photonic crystal mirrors, which modifies the effective resonator length and changes the value of $E_{\max}$. This parameter was found to be $x_{\text{eff}} = 6\ \mu$m for each mirror by coarsely sweeping x_{eff} in 1 μm increments in the simulation to find the best fit to the data.

2.7 Discussion

In this work, we have demonstrated the capabilities of an on-chip optical storage device with DC Stark shift control. Taking this technology on-chip has two main advantages. First, it allows miniaturization and future integration with other optical components on chip. Second, it enables simple generation of large electric fields. Because the distance between electrodes across the resonator is small (a minimum

of 20 μm), electric fields of 3 kV/cm are generated with just ±5 V of applied bias in the parallel configuration. Such biases were easily supplied by a function generator with no additional amplification. In the quadrupole configuration, electric field gradients of up to 50 V/cm/μm were generated, corresponding to gradient of 0.58 MHz/μm in $^{167}Er^{3+}$:Y_2SiO_5 transition frequencies.

For the dynamically controlled memory times in Fig. 2.5d, an excellent match was found between the amplitude of stored light as a function of time and the theoretical limit due to the dephasing of a comb with finesse $F = 12.2$, indicating that the two electric field control pulses did not introduce any irreversible dephasing. This was also confirmed using a two pulse photon echo measurement, where inserting two electric field pulses with equal area and opposite sign between the first and second optical pulses was found not to decrease the optical coherence time T_2, which was measured in this device to be 108 ± 13 μs.

Frequency control was demonstrated for up to ±39 MHz. In this work, the maximum shift was set by the maximum applied electric field of 3 kV/cm. One technical difficulty is that ions from the other subclass that are outside of the comb will act as an absorbing background when the comb is shifted in frequency and the other subclass experiences an opposite frequency shift. Assuming that the comb can be sufficiently separated in frequency from the other subclass using high electric fields, a more fundamental limit is set by the inhomogeneity of the Stark shifts, which leads to a decrease in storage efficiency with increasing frequency shift. In this device, the Stark shift inhomogeneity was dominated by an electric field distribution that was not perfectly homogeneous (see Fig. 2.2c). Even in a perfectly homogeneous field, however, some inhomogeneity in Stark shifts will exist due to crystal field variations throughout the crystal [72].

The bandwidth of stored light was changed by a factor of three from 6 MHz to 18 MHz. The maximum broadening demonstrated was limited by the maximum electric field gradient of 50 V/cm/μm. With higher gradients, stored pulses could be broadened up to half the bandwidth of the comb and the bandwidth of combs in this material is limited to $\sim$ 150 MHz [55]. Decreasing the bandwidth of a stored pulse is not possible with this procedure, because the AFC cannot be made narrower with a gradient electric field, only wider. Narrowing the AFC could be accomplished with a frequency selective shift such as the AC Stark shift. The storage efficiency was observed to decrease when changing the bandwidth of the stored pulse. This decrease in efficiency, which was also seen in simulation, was stronger when the

bandwidth change was larger, and was not present when the three electric pulses had equal amplitude (corresponding to no change in pulse bandwidth).

An on-chip resonator allows for storage efficiencies approaching unity if the impedance matching condition is met [20]. In this device, the storage efficiency was up to 0.4%, depending on the finesse of the comb created, and was limited by the low coupling between the ensemble of ions and the optical mode of the resonator, characterized by an ensemble cooperativity $C < 1$, and the small coupling ratio of the lower reflectivity mirror, $\kappa_{\text{in}}/\kappa = 0.2$ (see efficiency discussion in Appendix D of Reference [55]). The storage time on an optical transition is ultimately limited by the optical coherence time T_2. However, in $^{167}Er^{3+}$:Y_2SiO_5, superhyperfine coupling to yttrium nuclear spins in the crystal prevents the creation of narrow spectral features, which means a low storage efficiency for storage times longer than $\sim$ 500 ns [55]. Superhyperfine coupling is a major limitation to high-efficiency long lived storage in $^{167}Er^{3+}$:Y_2SiO_5 when using memory protocols based on spectral tailoring such as AFC.

For quantum repeater applications, the efficiency and duration of on-chip storage must be improved. The storage efficiency in hybrid αSi-$^{167}Er^{3+}$:Y_2SiO_5 devices can be increased by using thinner silicon to increase the fraction of the optical mode energy in the $^{167}Er^{3+}$:Y_2SiO_5, which would increase the ensemble cooperativity, and by optimizing the resonator nanofabrication procedure to decrease scattering and absorption loss in order to achieve higher intrinsic quality factors. For example, using crystalline silicon could mitigate absorption loss. Higher intrinsic quality factors would increase both the ensemble cooperativity and the coupling ratio $\kappa_{\text{in}}/\kappa$, both of which affect storage efficiency. To overcome the superhyperfine limit to storage time, creative solutions such as using clock transitions in $^{167}Er^{3+}$:Y_2SiO_5[78, 84, 85], which are less sensitive to superhyperfine coupling, or finding new crystal hosts for erbium ions can be used. Longer storage times can also be realized by combining AFC storage with spin-wave storage, where the optical excitation is reversibly transferred to a hyperfine level [74]. Spin-wave storage could be combined with the bandwidth and frequency control demonstrated here, and it would eliminate the need for memory time control with electric fields. Another requirement of quantum memories is to store quantum states of light with high fidelity. This has already been demonstrated with the AFC protocol [50]. Storage of weak coherent states using the AFC protocol with DC Stark shift control of storage time has also been recently demonstrated [82]. Future work should include demonstrations of on-

chip storage of light at the quantum level with dynamic frequency and bandwidth control. More generally, this type of device could work with different absorbers that experience linear Stark shifts, or with other quantum storage protocols that do not require spectral tailoring such as Stark echo modulation memory [81].

The functionality of the device is not limited to the demonstrations in this work. For example, a gradient field could be used instead of a homogeneous field to dynamically control the storage time. The bandwidth or frequency of emissions at any time $t = \frac{m}{\Delta}$ could be modified, frequency and bandwidth control could be combined, and the order of two pulses could be reversed. A device which enables Stark shift control of an ion's transition frequency is useful for other technologies as well. For example, a gradient electric field could be used to tune two $^{167}Er^{3+}$ ions coupled to the same resonator into resonance with one another. This would enable entangling gates between the two ions, a key step in quantum repeater protocols using single ions [86].

2.8 Conclusion

In this work we demonstrated a multifunctional on-chip device that can store light while dynamically modifying its storage time, frequency and bandwidth. Dynamic control of the memory time and the frequency profile of the output light was achieved via the linear DC stark shift of $^{167}Er^{3+}$ ions in Y_2SiO_5 . We demonstrated dynamic control of memory time in a digital fashion with storage times that were multiples of 50 ns, for up to 400 ns. The frequency of stored light was changed by up to ±39 MHz, and the bandwidth of stored light was increased by up to a factor of three, from 6 MHz to 18 MHz. This on-chip platform, comprising a resonator evanescently coupled to an ensemble of atoms that experience a DC Stark shift and on-chip electrodes, can be adapted to other materials and other quantum memory protocols.

2.9 Theory of higher-order memory efficiency and simulation of time evolution

In this section, we provide more detail on deriving the m^{th} quantum memory efficiency in the AFC protocol and developing the simulation method for time evolution.

Amplitude of the m^{th} light emission

The following section expands upon the analysis by Afzelius et al. in References [20, 74] to consider multiple emissions. An ensemble of ions is coupled to a cavity

with field decay rate κ. An AFC is created in this ensemble of ions, which leads ion distribution to be $n(\omega)$, where $\int n(\omega)d\omega = N$, and N is the number of ions. Each ion has a detuning ω relative to cavity center frequency, coherent decay rate γ_h, and ion-cavity coupling rate g. After sending a photon into the cavity that is resonant with it, the dynamic equations [20, 87] of cavity field $\mathcal{E}$ and atomic polarization σ_ω in the rotating frame of photon frequency are

$$\dot{\mathcal{E}} = -\kappa\mathcal{E} + \sqrt{2\kappa_{\text{in}}}\mathcal{E}_{\text{in}} + ig\int n(\omega)\sigma_\omega d\omega, \tag{2.2}$$

$$\dot{\sigma}_\omega = -(i\omega + \gamma_h)\sigma_\omega + ig\mathcal{E}. \tag{2.3}$$

The input output formalism gives

$$\mathcal{E}_{\text{out}} = -\mathcal{E}_{\text{in}} + \sqrt{2\kappa_{\text{in}}}\mathcal{E} \tag{2.4}$$

where κ_{in} is the cavity decay rate to the input channel. We can solve Eq. 2.3 and get

$$\sigma_\omega(t) = ig\int_{-\infty}^{t} e^{-(i\omega+\gamma_h)(t-t')}\mathcal{E}(t')dt'. \tag{2.5}$$

Then, inserting Eq. 2.5 into Eq. 2.2, we find

$$\begin{aligned}\dot{\mathcal{E}}(t) &= -\kappa\mathcal{E}(t) + \sqrt{2\kappa_{\text{in}}}\mathcal{E}_{\text{in}}(t)\\ &\quad - g^2\int_{-\infty}^{t} e^{-\gamma_h(t-t')}\int n(\delta)e^{-i\omega(t-t')}d\omega\mathcal{E}(t')dt'\\ &= -\kappa\mathcal{E}(t) + \sqrt{2\kappa_{\text{in}}}\mathcal{E}_{\text{in}}(t)\\ &\quad - g^2\int_{-\infty}^{t} e^{-\gamma_h(t-t')}\widetilde{n}(t-t')\mathcal{E}(t')dt'\end{aligned} \tag{2.6}$$

where $\widetilde{n}(t)$ is the Fourier transform of $n(\omega)$ [74].

We have an atomic frequency comb with period Δ, and each tooth has a shape described by $f(\omega)$, so $n(\omega)$ can be written as

$$\begin{aligned}n(\omega) &\propto \sum_{k=-\infty}^{+\infty} f(\omega - k\Delta)\\ &\propto \sum_{k=-\infty}^{+\infty} f(\omega) * \delta(\omega - k\Delta).\end{aligned} \tag{2.7}$$

The Fourier transform of $n(\omega)$ is $\widetilde{n}(t)$:

$$\begin{aligned}\widetilde{n}(t) &\propto \sum_{k=-\infty}^{+\infty} \widetilde{f}(t)\delta\left(t - \frac{k}{\Delta}\right)\\ &\propto \sum_{k=-\infty}^{+\infty} \widetilde{f}(\frac{k}{\Delta})\delta\left(t - \frac{k}{\Delta}\right).\end{aligned} \tag{2.8}$$

Inserting Eq. 2.8 into Eq. 2.6, we find

$$\begin{aligned}\dot{\mathcal{E}}(t) = &-\kappa\mathcal{E}(t) + \sqrt{2\kappa_{\text{in}}}\mathcal{E}_{\text{in}}(t) - \Gamma_{\text{comb}}\mathcal{E}(t) \\ &- 2\Gamma_{\text{comb}} \sum_{k=1}^{+\infty} e^{-\gamma_h \frac{k}{\Delta}} \widetilde{f}\left(\frac{k}{\Delta}\right) \mathcal{E}\left(t - \frac{k}{\Delta}\right)\end{aligned} \tag{2.9}$$

where Γ_{comb} is the absorption rate of atomic frequency comb [55], and $\Gamma_{\text{comb}} \propto g^2$.

Consider the time after the ensemble of ions absorb the light ($t > 0$). There are no input pulses after $t = 0$, so $\mathcal{E}_{\text{in}}(t > 0) = 0$. Applying adiabatic elimination of the cavity mode ($\dot{\mathcal{E}}(t) = 0$) leads to

$$\mathcal{E}(t) = -\frac{2\Gamma_{\text{comb}}}{\kappa + \Gamma_{\text{comb}}} \sum_{k=1}^{+\infty} e^{-\gamma_h \frac{k}{\Delta}} \widetilde{f}\left(\frac{k}{\Delta}\right) \mathcal{E}\left(t - \frac{k}{\Delta}\right). \tag{2.10}$$

The cavity field at time $t = \frac{m}{\Delta}$ goes as

$$\mathcal{E}\left(t = \frac{m}{\Delta}\right) = -\frac{2\Gamma_{\text{comb}}}{\kappa + \Gamma_{\text{comb}}} \sum_{k=1}^{m} e^{-\gamma_h \frac{k}{\Delta}} \widetilde{f}\left(\frac{k}{\Delta}\right) \mathcal{E}\left(\frac{m-k}{\Delta}\right). \tag{2.11}$$

From this, we can see that the amplitude of the cavity field at time $t = \frac{m}{\Delta}$ is determined by the cavity field at all earlier times $t = \frac{k}{\Delta}$, where $k = 0, 1, ..., m-1$. We can theoretically find the amplitude of the cavity field at any time, which depends on how we modulate the cavity field at previous times. In our case, γ_h is much smaller than the teeth width [55], so we can ignore the term $e^{-\gamma_h \frac{k}{\Delta}}$. We assume each tooth has Gaussian shape, which gives

$$\begin{aligned}\widetilde{f}\left(\frac{k}{\Delta}\right) &= \exp\left(-\frac{1}{2}\left(\frac{k}{\Delta}\right)^2 \left(\frac{\pi\gamma}{\sqrt{2\ln 2}}\right)^2\right) \\ &= \exp\left(-\frac{\pi^2}{4\ln 2}\frac{k^2}{F^2}\right)\end{aligned} \tag{2.12}$$

where γ is the FWHM of the Gaussian peak, and $F = \Delta/\gamma$ as we defined in the main text, Eq. 2.11 becomes

$$\mathcal{E}\left(t = \frac{m}{\Delta}\right) = -\frac{2\Gamma_{\text{comb}}}{\kappa + \Gamma_{\text{comb}}} \sum_{k=1}^{m} \exp\left(-\frac{\pi^2}{4\ln 2}\frac{k^2}{F^2}\right) \mathcal{E}\left(\frac{m-k}{\Delta}\right). \tag{2.13}$$

We also know from Eq. 2.4 that the amplitude of the k^{th} emission (for $k > 0$) is

$$\mathcal{E}_{\text{out}}\left(t = \frac{k}{\Delta}\right) = \sqrt{2\kappa_{\text{in}}}\mathcal{E}\left(t = \frac{k}{\Delta}\right). \tag{2.14}$$

At time $t = 0$ we have

$$\mathcal{E}(t=0) = \frac{\sqrt{2\kappa_{\text{in}}}}{\kappa + \Gamma_{\text{comb}}}\mathcal{E}_{\text{in}}(t=0). \tag{2.15}$$

From the above three equations, the emission at time $t = \frac{m}{\Delta}$ has the following amplitude

$$\begin{aligned}\mathcal{E}_{\text{out}}\left(t=\frac{m}{\Delta}\right) = &-\frac{2\Gamma_{\text{comb}}}{\kappa+\Gamma_{\text{comb}}}\times \\ &\left(\sum_{k=1}^{m-1}\exp\left(-\frac{\pi^2}{4\ln 2}\frac{k^2}{F^2}\right)\mathcal{E}_{\text{out}}\left(\frac{m-k}{\Delta}\right)\right. \\ &\left.+\exp\left(-\frac{\pi^2}{4\ln 2}\frac{m^2}{F^2}\right)\frac{2\kappa_{\text{in}}}{\kappa+\Gamma_{\text{comb}}}\mathcal{E}_{\text{in}}(t=0)\right).\end{aligned} \tag{2.16}$$

The m^{th} emission is the sum of 1^{st} to $(m-1)^{\text{th}}$ emission and the input. In the case where we do not apply electric fields to prevent any emissions, the first and second emitted field amplitudes are

$$\mathcal{E}_{\text{out}}\left(t=\frac{1}{\Delta}\right) = -\frac{4\kappa_{\text{in}}\Gamma_{\text{comb}}}{(\kappa+\Gamma_{\text{comb}})^2}\exp\left(-\frac{\pi^2}{4\ln 2}\frac{1}{F^2}\right)\mathcal{E}_{\text{in}}(t=0) \tag{2.17}$$

$$\mathcal{E}_{\text{out}}\left(t=\frac{2}{\Delta}\right) = -\frac{4\kappa_{\text{in}}\Gamma_{\text{comb}}}{(\kappa+\Gamma_{\text{comb}})^2}\exp\left(-\frac{\pi^2}{2\ln 2}\frac{1}{F^2}\right)\mathcal{E}_{\text{in}}(t=0)\left(\exp\left(-\frac{\pi^2}{2\ln 2}\frac{1}{F^2}\right)-\frac{2\Gamma_{\text{comb}}}{\kappa+\Gamma_{\text{comb}}}\right). \tag{2.18}$$

As Eq. 2.18 shows, the amplitude of the second emission is composed of two parts. The first part is from the light absorbed at $t = 0$, and the second part is from the light reabsorbed at the first emission time $t = 1/\Delta$. The competition between these two terms determines the amplitude and the phase of the output at $t = \frac{2}{\Delta}$. When we operate in the high finesse regime (since we always want the dephasing term $\exp\left(-\frac{\pi^2}{2\ln 2}\frac{1}{F^2}\right)$ to be close to 1), if the amplitude of the first output is small, the amplitude of the second output will be dominated by the first term in Eq. 2.18, so it will still have an observable amplitude. If the amplitude of the first output is high, the amplitude of the second output will be small due to the minus sign between the two terms in Eq. 2.18. In particular, when the impedance matching condition[20] holds where $\frac{2\Gamma_{\text{comb}}}{\kappa+\Gamma_{\text{comb}}} \to 1$, the second emission will be zero. This trend also holds for higher order emissions, as can be seen by extending the analysis of Eq. 2.16.

In the case where we apply an electric field to suppress all the lower order emissions (from 1 to $m-1$), we find the m^{th} output amplitude to be

$$\mathcal{E}_{\text{out}}\left(t=\frac{m}{\Delta}\right) = -\frac{4\kappa_{\text{in}}\Gamma_{\text{comb}}}{(\kappa+\Gamma_{\text{comb}})^2}\exp\left(-\frac{\pi^2}{4\ln 2}\frac{m^2}{F^2}\right)\mathcal{E}_{\text{in}}(t=0). \tag{2.19}$$

Then, we can find the efficiency of the m^{th} output pulse to be

$$\begin{aligned}\eta &= \left|\frac{\mathcal{E}_{\text{out}}(t=\frac{m}{\Delta})}{\mathcal{E}_{\text{in}}(t=0)}\right|^2 \\ &= \left(\frac{\kappa_{\text{in}}}{\kappa}\frac{4\Gamma_{\text{comb}}/\kappa}{(1+\Gamma_{\text{comb}}/\kappa)^2}\right)^2 \exp\left(-\frac{\pi^2}{2\ln 2}\frac{m^2}{F^2}\right).\end{aligned} \tag{2.20}$$

Time evolution simulations

Simulations of the cavity-ion system were performed to confirm the trends observed in the bandwidth control experiment. These simulations involved numerically solving the discrete form of Eq. 2.2 and Eq. 2.3 for the cavity field $\mathcal{E}$ and the atomic polarization σ_i of a number n of ions in the rotating frame, following Reference [40]:

$$\dot{\mathcal{E}}(t) = -\left(\kappa + i\Delta\omega_a\right)\mathcal{E}(t) + \sqrt{2\kappa_{\text{in}}}\mathcal{E}_{\text{in}}(t) + i\sum_{i=1}^{n} g\sigma_i(t), \tag{2.21}$$

$$\dot{\sigma}_i(t) = -\left(\gamma_h + i\Delta\omega_i(t)\right)\sigma_i(t) + ig\mathcal{E}(t), \tag{2.22}$$

where $\Delta\omega_a$ is the cavity detuning and $\Delta\omega_i(t)$ is the detuning of each ion, which can vary in time as a function of applied electric field at the location of the ion $\Delta\omega_i(t) = \Delta\omega_{i,0} \pm sE_y(x_i, t)$. $\Delta\omega_{i,0}$ is the detuning of each ion in the absence of an applied electric field and the $\pm$ sign depends on which subclass the ion is in. The cavity field is coupled to external fields as described by input-output formalism (see Equation 2.4). The initial conditions are $\mathcal{E}(0) = 0$, $\sigma_i(0) = 0$.

For the simulation, a system of $n + 1$ differential equations (Equations 2.22 and 2.21) are numerically solved. To keep the number of equations to a reasonable size, the number of ions simulated $n \sim 10^4$ is significantly smaller than the true number of ions coupled to the cavity $\sim 10^7$. To accurately represent the strength of the interaction between the ion ensemble and the cavity, g in the simulation is chosen such that $g_{\text{total}}^2 = ng^2$, where $g_{\text{total}} = 2\pi \times 0.6$ GHz is measured from the cavity reflectance curve [55]. The time-independent frequency distribution of the ions (frequency comb) is described as a continuous distribution, and n values of $\Delta\omega_{i,0}$ are sampled from it. A time dependent scalar $\pm sE_y(x_i, t)$ representing the Stark shift is added to all ion detunings. $E_y(x_i, t)$ for each ion is given by randomly sampling the x-position along the resonator, and obtaining the corresponding electric field from Figure 1g in the main text, then varying it in amplitude and time to represent each electric pulse.

Using this simulation, the output pulse profile $\mathcal{E}_{\text{out}}(t)$ can be computed given $\mathcal{E}_{\text{in}}(t)$, the input pulse profile centered around $t = 0$, and certain set of electric field control pulses.

Chapter 3

COLLECTIVELY INDUCED TRANSPARENCY (CIT)

In this chapter, we will discuss the experimental discovery and theoretical proof of a novel phenomenon in many-body cavity QED, which we name collectively induced transparency (CIT) [88]. This chapter is adapted from the [88].

3.1 Overview

We study an ensemble of approximately 10^6 $^{171}Yb^{3+}$ ions embedded in YVO_4 coupled to a nanophotonic cavity (Fig. 3.1a, Fig. 3.3c), subjected to a strong driving field such that the resonant ions are excited. The relatively low spectral inhomogeneity, the strong transition dipole moment [8], and the cavity coupling lead to a high optical cooperativity of up to 24 (Table 3.1). This allows for strongly enhanced light-matter interactions, enabling the probing of complex collective and many-body phenomena [89]. In particular, we discover a sharp transparency window in the cavity reflection spectrum which we call CIT (Fig. 3.1b, d). We find that the quantum interference of many inhomogeneously broadened emitters plays a critical role in producing the CIT window, mechanistically distinguishing itself from other types of transparencies [90].

3.2 Experimental observation

To explore cQED phenomena for a driven, inhomogenous many-body system, we first characterize the cavity-ion coupling by measuring the cavity reflection spectrum. Scanning with low laser power, the spectrum reveals broad peaks centered around the atomic resonances reaching unit reflection with about 3 GHz width, larger than the ensemble inhomogeneous linewidth of 150 MHz (Fig. 3.1b, middle, Fig. 3.3d). These peaks are known as dipole induced reflectivity (DIR), resulting from strong ion-cavity coupling [91]. Specifically, in steady state under continuous driving, the cavity field $\langle a \rangle$ depends on the sum of the atomic coherences $\langle \sigma_j^- \rangle$ of individual emitters as $\langle a \rangle \propto \sum_{j=1}^{N} \langle \sigma_j^- \rangle$, where $\sigma_j^- = |g\rangle_j \langle e|$ for the j^{th} ion. As such, even if most ions remain in the ground state at weak excitation, the Yb ions still modify the internal cavity field due to the nonzero atomic coherence. This in turn influences the cavity reflectivity, leading to DIR. However, when the laser power is increased, we observe the formation of a sharp dip around the center of the DIR, which both

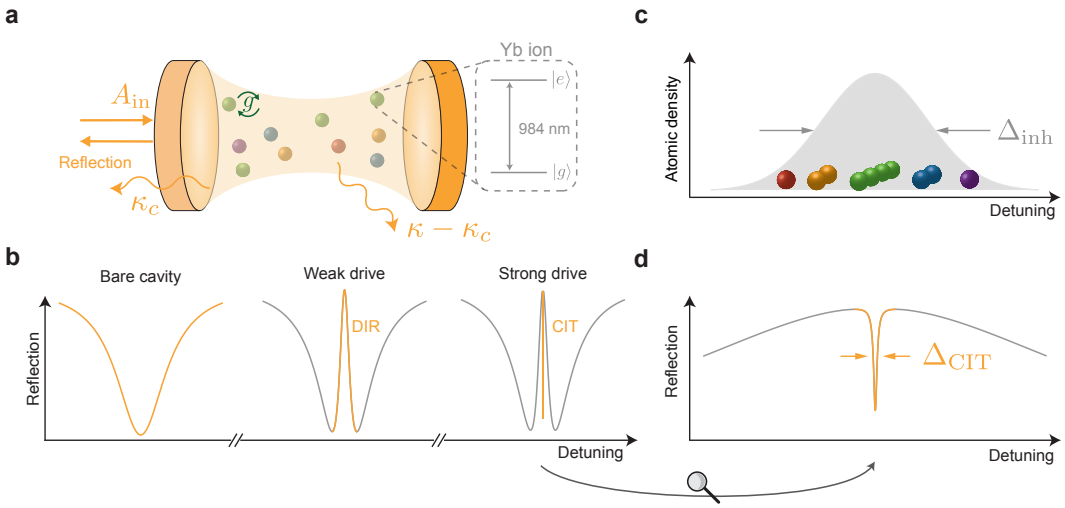

Figure 3.1: **Cavity QED with driven inhomogeneous emitters. a,** Schematic description of the cavity-ion interaction. An inhomogeneous ensemble of ions is coupled to a one-sided cavity with total decay rate κ. The input field A_{in} is coupled into the cavity with rate κ_c. The interaction strength between the cavity field and a single ion is g. Each Yb ion can be regarded as an effective two-level system consisting of a ground ($|g\rangle$) and excited ($|e\rangle$) state, whose transition wavelength is around 984 nm (grey dotted box). **b,** Reflection spectrum of a cavity without ions showing the bare cavity resonance (left), with ions under weak drive showing DIR (middle), and with ions under strong drive showing DIR and CIT (right). **c,** The atomic distribution of ions with inhomogeneous linewidth Δ_{inh}. **d,** Zoom in of the right panel of b, showing CIT. CIT opens a transmissive window narrower than the inhomogeneous linewidth, and allows for the excitation of ions in the center of the ion distribution.

deepens and narrows with increasing power (Fig. 3.2b). A Lorentzian fit to the dip gives a minimum width of 50 MHz, and a maximum normalized depth approaching 1 (Fig. 3.2d).

We find that the origin of such a transparency window can be understood as the collective contribution of the inhomogeneous ensemble to the cavity field (Fig. 3.2a). For clarity the individual contributions of on- and off-resonance ions (with respect to the laser) should be considered separately. For resonant ions, strong driving saturates their steady-state populations to the completely mixed state, where both atomic inversion and coherence vanish, thus having no influence on the cavity field. In contrast, the off-resonant ions are only weakly excited, such that their atomic coherence is inversely proportional to the ion detuning Δ_j, that is, $\langle \sigma_j^- \rangle \propto \Delta_j^{-1}$ (section 3.5). This means that ions at equal and opposite detunings are out of phase with equal amplitude, such that their pairwise contributions to the cavity field will

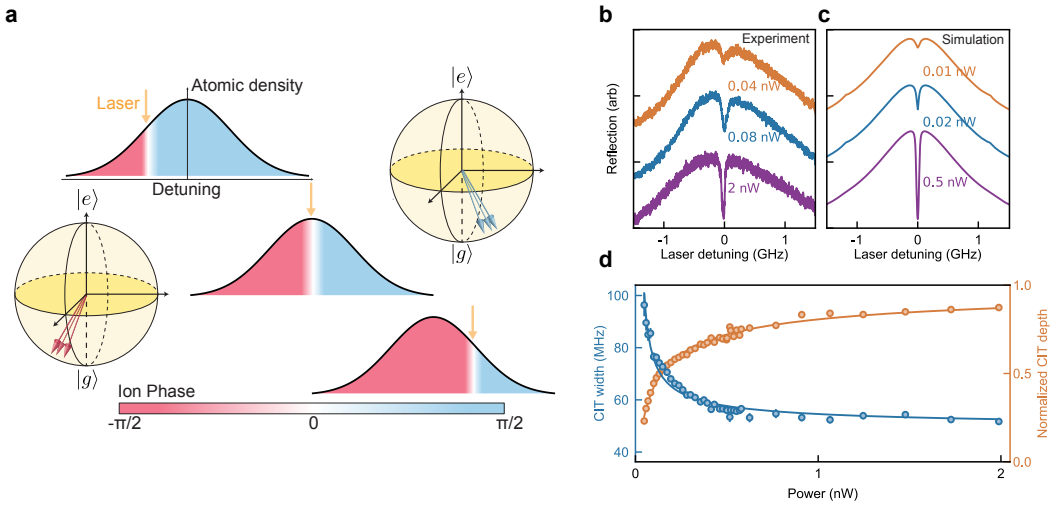

Figure 3.2: **Experimental observation of CIT. a,** Physical origin of CIT, showing the phase distribution of atomic coherence of the inhomogeneous ensemble. The ions far-detuned from the laser frequency are out of phase on the two sides, denoted in red and blue. The resonant ions are denoted in white. The left and right Bloch spheres contain the Bloch vectors of the red- and blue-detuned ions, respectively. Three scenarios with different laser frequencies are shown. If the laser is detuned from the ensemble center (top, bottom), there is imbalance in the ion phases, while if the laser is centered (middle), the ion phases cancel and lead to CIT. **b,** Measured cavity reflection spectra at three different powers, vertically shifted for clarity. Sharp dips due to CIT appear at the center of the DIR peaks, which get deeper and narrower with increased power. **c,** Corresponding simulated cavity reflection spectra. **d,** Extracted Lorentzian fit width (blue) and depth (orange) with power, error bars represent the standard errors of the fit. The CIT depth is normalized with respect to the cavity depth. Solid lines are the fits from our theoretical prediction.

destructively interfere. In particular, when the laser frequency is in the center of the inhomogeneous line, all of the contributions from the detuned ions cancel with each other (Fig. 3.2a, center). Thus, the combination of these two effects, (1) the saturation of the on-resonance ions and (2) the pairwise destructive interference of the off-resonant ions, leads to a transparency (the CIT) that emerges at the center of the inhomogeneous line. It is worth noting that CIT is unique to systems consisting of a large ensemble of emitters with fixed frequency and an appreciable inhomogeneous broadening [92], and does not occur for just a few emitters (section 3.5).

Going beyond the qualitative description, we derive an analytical expression for the width of CIT (Δ_{CIT}) using the N-atom Tavis-Cummings Hamiltonian [39] under

appropriate approximations (section 3.5):

$$\Delta_{\mathrm{CIT}} \approx \frac{\Delta_{\mathrm{inh}}}{C} \frac{1}{\left(1 - C\sqrt{\frac{\gamma_s \gamma}{4g^2 \mu}}\right)} \tag{3.1}$$

where $\gamma = \frac{\gamma_s}{2} + \gamma_d$ is the total decoherence rate, comprised of the spontaneous decay rate γ_s and the excess dephasing rate γ_d, g is the single ion-cavity coupling rate, $C = 4Ng^2/(\kappa\Delta_{\mathrm{inh}})$ is the ensemble cooperativity, and μ is the cavity mean photon number in the absence of ions, representing the rescaled driving laser power. The measured CIT widths and depths show excellent agreement with the predicted power dependence (Fig. 3.2d). Crucially, at high powers we expect the dip width to be narrowed by the ensemble cooperativity, reaching $\Delta_{\mathrm{CIT}} \approx \Delta_{\mathrm{inh}}/C$. Intuitively, this is because higher cooperativity leads to a larger contribution towards DIR for even a small number of imbalanced ions, effectively increasing the sensitivity to the imbalance near the ensemble center, which narrows the CIT. This indicates that if $C \gg 1$, the CIT width can be significantly narrower than the inhomogeneous broadening of an ensemble, ultimately limited by the homogeneous linewidth (section 3.6). Given our C and Δ_{inh}, the expected minimum linewidth is 13 MHz, narrower than the measured value of 50 MHz. This discrepancy can be partially attributed to spectral diffusion, which effectively increases γ and causes a breakdown of some of the assumptions made in order to derive the approximate analytical expression Eq. 3.1. To account for this, numerical simulations of the cavity reflection (without the above approximations) provides a better match to the experimental width (Fig. 3.2c, more detail in section 3.6).

3.3 Device and system parameters

Device

The substrate is a 3×3×0.5 mm piece of $^{171}Yb^{3+}$:YVO_4 (a × a × c), measured to have a Yb doping concentration of 86 parts-per-million using glow discharge mass spectrometry [93]. The device is fabricated directly in the substrate using focused ion-beam milling. The optical cavity is formed by periodic grooves milled into a triangular nanobeam waveguide, with a slight aperiodicity in the center which forms a defect creating the cavity mode. A 45-degree angled coupler couples the light from free-space to the waveguide with an efficiency of ≈ 25%. Further details on the device fabrication can be found in [34].

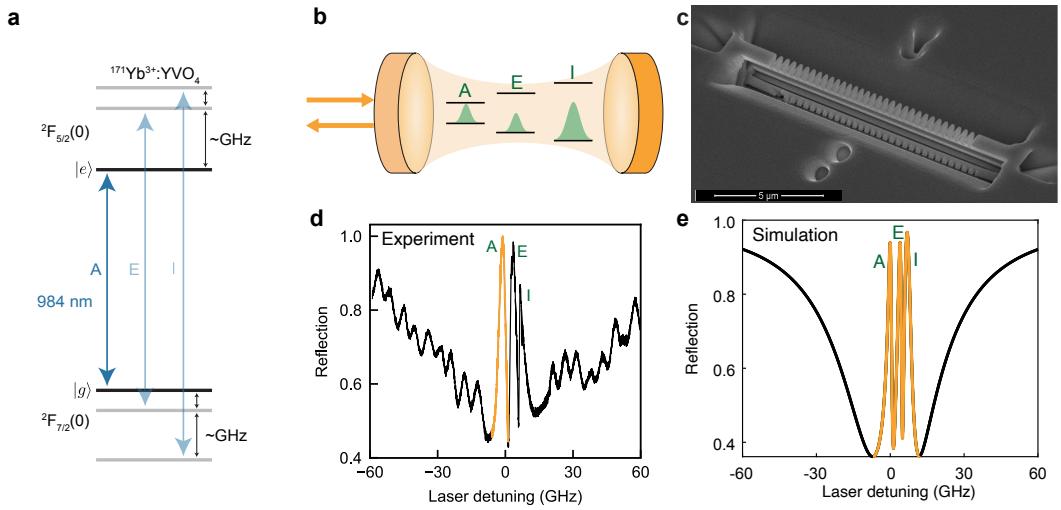

Figure 3.3: **Cavity-ion coupling.** **a,** Energy level spectrum of $^{171}Yb^{3+}:YVO_4$ at zero external magnetic field. The optical transitions whose polarizations are along the cavity mode are shown in blue (A, E, I). Since the three transitions are separated by $\sim$ GHz, larger than the inhomogeneous broadening, each transition is spectrally well-resolved and can be regarded as an isolated, effective two-level system; for example the levels labelled $|e\rangle$ and $|g\rangle$ form a two-level system for the A transition. **b,** Schematic showing the relative population of ions in each transition, where the I transition has double the population due to a doubly-degenerate ground state. **c,** Scanning electron microscope image of the device. **d,** Cavity reflection spectrum at weak laser power reveals three DIR peaks corresponding to the A, E, and I transitions. The peak corresponding to A is marked with orange, as we focus on this transition. **e,** Theoretical cavity reflection as a function of laser detuning in the low excitation regime (DIR), showing ion-cavity coupling. Three DIR peaks (orange) corresponding to the A, E, and I transitions of a Yb ion are identified using Eq. 3.9, showing high cavity reflectivity.

System parameters

Based on the concentration of Yb ions and the cavity volume, we estimate that about $N \approx 7 \times 10^5$ ions are coupled to the cavity with varying coupling strengths. The cavity is tuned into resonance with the $^2F_{7/2}$ to $^2F_{5/2}$ transition of Yb around $\lambda = 984$ nm using nitrogen gas condensation. The large cavity linewidth ($\kappa = 2\pi \times 44$ GHz) covers all three transitions aligned along the cavity polarization (labelled as A, E, I, Fig. 3.3b). The narrow optical inhomogeneous linewidths ($\Delta_{\text{inh}} = 2\pi \times 150$ MHz) compared to the separation between those transitions (a few GHz) enables each transition to be addressed as independent two-level systems. The nanoscale cavity allows for tight confinement of the electromagnetic field, resulting in a small mode volume of about a cubic wavelength ($\approx 1(\lambda/n)^3$, where n is the refractive index). In

conjunction with the relatively strong dipole moment of Yb in YVO_4 [8, 33], these factors enable high vacuum Yb ion-cavity coupling g up to $\approx 2\pi \times 35$ MHz, leading to a large collective ensemble cooperativity $C = 4Ng^2/(\kappa\Delta_{\text{inh}}) > 1$ in the optical regime.

The ion-cavity coupling rate g has a particular distribution, arising from inhomogeneity of the cavity field across the device. Simulating the cavity structure in COMSOL, the total YVO_4 volume is 3.058 um^3, with total coupling rate $\Omega = 2\pi \times 9$ GHz, calculated assuming uniformly distributed Yb ions across the YVO_4. In order to obtain the distribution of g, we generate the histogram of varying g across the entire nanobeam volume of 3.058 um^3. Since there are many ions with very small g, we ignore ions with $g < 1.39$ MHz which retains 98.4% of Ω, resulting in a total coupling rate of $\Omega = 2\pi \times 8.86$ GHz and the distribution shown in Fig. S1. The considered ions occupy a physical volume of 0.636 um^3 and their total number is $\approx 7 \times 10^5$. From this, the root mean square of g is estimated to be $\sqrt{\langle g^2 \rangle} = \frac{\Omega}{\sqrt{N}} \approx 2\pi \times 10.6$ MHz. Additionally, we calculate the optical mode volume to be $V_{\text{mode}} = 0.0918\,\text{um}^3$, based on the maximum field strength.

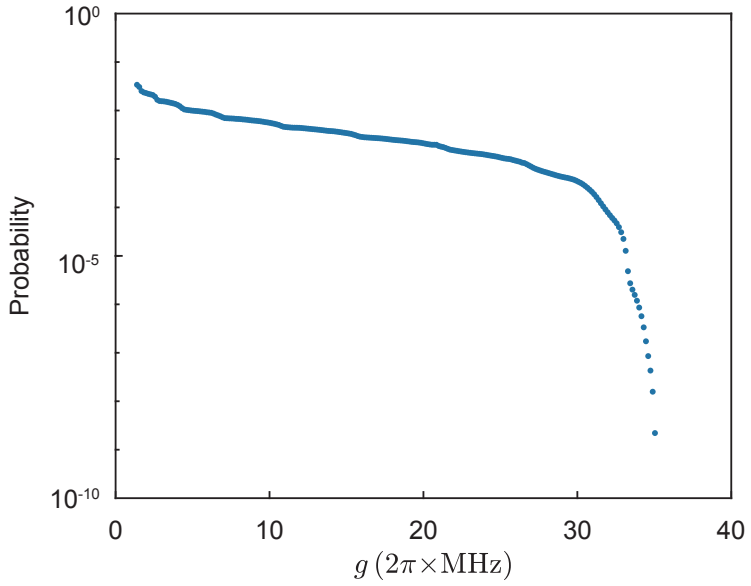

Figure 3.4: **The simulated probability distribution of cavity-ion coupling strength g in the device.**

3.4 Theoretical analysis: from DIR to a few driven emitters

In this and the next section, we will give a more detailed theoretical analysis of CIT. Due to the fact that the CIT dip is observed within the broad DIR peak, we will

Parameter Description	Symbol	Value
Optical Frequency	ω	$2\pi \times 304500$ GHz
Spontaneous decay rate	γ_s	$2\pi \times 0.6$ kHz
Excess dephasing rate	γ_d	$2\pi \times 6$ kHz
Optical inhomogeneous linewidth (FWHM)	Δ_{inh}	$2\pi \times 150$ MHz
Cavity energy decay rate	κ	$2\pi \times 44$ GHz
Cavity external coupling rate	κ_c	$2\pi \times 8.8$ GHz
Maximum Yb ion-cavity coupling rate	g	$2\pi \times 35$ MHz
Number of Yb ions in cavity	N	700000
Cavity mode volume	V_{mode}	$0.0918\mu\text{m}^3$
Ensemble cooperativity	$C_{\text{A}}(C_{\text{I}})$	12(24)

Table 3.1: **Relevant system parameters.**

start by introducing the DIR at the weak-excitation limit and then proceed to analyze some simple cases with only a few driven ions.

General formalism

We start with the Tavis-Cummings Hamiltonian for N two-level systems coupled to a single cavity field under the rotating-wave approximation in the laser frame (setting $\hbar = 1$):

$$H = \Delta_c a^\dagger a + \frac{1}{2}\sum_{j=1}^{N} \Delta_j \sigma_j^z + \sum_{j=1}^{N} g_j (a^\dagger \sigma_j^- + \sigma_j^+ a) - i\sqrt{\kappa_c} A_{\text{in}} (a^\dagger - a). \tag{3.2}$$

In our case, the two-level system consists of the ground ($|g\rangle$) and excited state of the A (E, I) transition. Here g_j is the j^{th} ion-cavity coupling strength, a is the bosonic cavity field operator, $\sigma_j^{\pm}, \sigma_j^z$ are the j^{th} spin ladder operators and the Pauli-Z operators, respectively. Note that here we consider the general case where each ion has a different coupling strength g_j. Δ_c is the cavity-laser detuning and Δ_j is the j^{th} ion-laser detuning, accounting for inhomogeneous broadening. Compared to Eq. 1.8, $\sqrt{\kappa_c} A_{\text{in}}$ is added to include the coupling from the input power P_{in}, which is associated with the cavity mean photon number in the absence of ions μ, as:

$$\sqrt{\kappa_c} A_{\text{in}} = \frac{\kappa}{2}\sqrt{\mu} \tag{3.3}$$

where μ is defined as

$$\mu = \frac{\kappa_c}{(\kappa/2)^2 + \Delta_c^2} \frac{P_{\text{in}}}{\hbar\omega} \approx \frac{\kappa_c}{(\kappa/2)^2} \frac{P_{\text{in}}}{\hbar\omega}. \tag{3.4}$$

Here, three variables A_{in}, P_{in}, and μ all represent the excitation power, and they are related to each other by system parameters. We will use μ to represent power in the following theoretical analysis for brevity.

Starting with Eq. 3.2, we obtain the equations of motion for a, σ_j^- and σ_j^z in the Heisenberg picture, with dissipation terms, given as (we need to be careful here, especially 3.7, see more detailed analysis in Appendix A):

$$\dot{a} = -(i\Delta_c + \frac{\kappa}{2})a - i\sum_{j=1}^{N} g_j\sigma_j^- - \frac{\kappa}{2}\sqrt{\mu} \tag{3.5}$$

$$\dot{\sigma}_j^- = -(i\Delta_j + \gamma)\sigma_j^- + ig_j\sigma_j^z a \tag{3.6}$$

$$\dot{\sigma}_j^z = 2ig_j(a^\dagger\sigma_j^- - \sigma_j^+ a) - \gamma_s(1+\sigma_j^z) \tag{3.7}$$

where $\gamma = \frac{\gamma_s}{2} + \gamma_d$. Using Eq. 3.3 and input-output formalism, $A_{\text{out}} = \sqrt{\kappa_c}a + A_{\text{in}}$, we obtain the cavity reflection:

$$R = \left|\frac{\langle A_{\text{out}}\rangle}{\langle A_{\text{in}}\rangle}\right|^2 = \left|\frac{2\kappa_c}{\kappa\sqrt{\mu}}\langle a\rangle + 1\right|^2 \tag{3.8}$$

where cavity field a is determined by solving Eqs. 3.5-3.7 and thus depends on the state of ions.

Weak-excitation case (DIR)

Under the weak-excitation condition ($\langle\sigma_z\rangle \approx -1$), an analytical expression for the cavity reflection $R(\omega)$ as a function of laser frequency ω is derived in [40] as:

$$R(\omega) = \left|1 - \frac{i\kappa_c}{\omega - \omega_c + i\kappa/2 - W_{\text{A}}(\omega) - W_{\text{E}}(\omega) - W_{\text{I}}(\omega)}\right|^2 \tag{3.9}$$

where W_{X} accounts for the coupling of an X (X = A, E, I) transition to each of the inhomogeneously broadened ensembles:

$$W_{\text{X}}(\omega) = \frac{\Omega_{\text{X}}^2}{\omega - \omega_{\text{X}} + i\gamma_X + i\Delta_{\text{X}}/2}. \tag{3.10}$$

Here, Δ_X is the full-width half-maximum (FWHM) of a Lorentzian distribution, $\Omega_{\text{X}} = \sqrt{\sum g_{\text{X}}^2}$ is the total ion-cavity coupling rate, γ_{X} is the dephasing rate, and ω_{X} is the center frequency of an X transition. From COMSOL simulations, we estimate that $\Omega_{\text{A}} = \Omega_{\text{E}} = \Omega_{\text{I}}/\sqrt{2} = 2\pi \times 4.4$ GHz, where the $1/\sqrt{2}$ factor in Ω_{I} comes from the double degeneracy in that ground state of the I transition. We plot the cavity reflection using Eq. 3.9 in Fig. 3.3e, which qualitatively matches the experimental data in Extended Data Fig. 2c. From this, the cooperativity $C_{\text{X}} = \frac{|W_{\text{X}}(\omega=\omega_0)|}{\kappa/2}$ [41] of the three transitions is computed as $C_{\text{A,E}} \approx 12, C_{\text{I}} \approx 24$.

Driven single-ion case

We would now like to see if CIT appears for just a few ions, starting by considering a single ion coupled to the cavity. Since there is only one ion, the subscript j is dropped. In the fast-cavity limit, we adiabatically eliminate the cavity mode by setting $\dot{a} = 0$, and using the fact that $\Delta_c \ll \kappa$ we get

$$a = \frac{-ig\sigma^- - \frac{\kappa}{2}\sqrt{\mu}}{i\Delta_c + \frac{\kappa}{2}} \approx \frac{-ig\sigma^-}{\frac{\kappa}{2}} - \sqrt{\mu}. \tag{3.11}$$

Substituting Eq. 3.11 into Eq. 3.6 and Eq. 3.7, we obtain linear differential equations for σ^z and σ^-:

$$\dot{\sigma}^- = -(i\Delta + \gamma + \frac{2g^2}{\kappa})\sigma^- - ig\sigma^z\sqrt{\mu} \tag{3.12}$$

$$\dot{\sigma}^z = -(\gamma_s + \frac{4g^2}{\kappa})(1 + \sigma^z) + 2ig\sqrt{\mu}(\sigma^+ - \sigma^-). \tag{3.13}$$

Then we solve the expectation value of the operators in the steady-state $\langle\dot{\sigma}^z\rangle = \langle\dot{\sigma}^-\rangle = 0$ as:

$$\langle\sigma^z\rangle = -\frac{1}{1 + \frac{4g^2\mu}{\left(\gamma_s + \frac{4g^2}{\kappa}\right)} \frac{\left(\gamma + \frac{2g^2}{\kappa}\right)}{\left(\Delta^2 + \left(\gamma + \frac{2g^2}{\kappa}\right)^2\right)}} \tag{3.14}$$

$$\langle\sigma^-\rangle = \frac{ig\sqrt{\mu}}{\left(i\Delta + \gamma + \frac{2g^2}{\kappa}\right)} \frac{1}{\left(1 + \frac{4g^2\mu}{\left(\gamma_s + \frac{4g^2}{\kappa}\right)} \frac{\left(\gamma + \frac{2g^2}{\kappa}\right)}{\left(\Delta^2 + \left(\gamma + \frac{2g^2}{\kappa}\right)^2\right)}\right)}. \tag{3.15}$$

The cavity reflection is

$$R = \left|\frac{-4i\kappa_c}{\kappa^2\sqrt{\mu}} g\langle\sigma^-\rangle - \frac{\kappa_c}{i\Delta_c + \frac{\kappa}{2}} + 1\right|^2 \tag{3.16}$$

where $\frac{-4i\kappa_c}{\kappa^2\sqrt{\mu}} g\langle\sigma^-\rangle$ is the contribution from the ion, which is related to the power, and $-\frac{\kappa_c}{i\Delta_c + \frac{\kappa}{2}} + 1$ is the contribution from the bare cavity. We plot the cavity reflection for varying $\sqrt{\mu}$ using Eq. 3.16 in Fig. 3.5a. We see that in the weak-excitation regime ($\sqrt{\mu} \to 0$, black), there is a DIR centered at the ion frequency, reaching unit cavity reflection. Upon increasing the power, the entire DIR profile decreases, and finally disappears, as the cavity reflection reaches the bare cavity value of $R = \left|-\frac{2\kappa_c}{\kappa} + 1\right|^2$ ($R \approx 0.36$ for our case). This occurs when we fully saturate the ion.

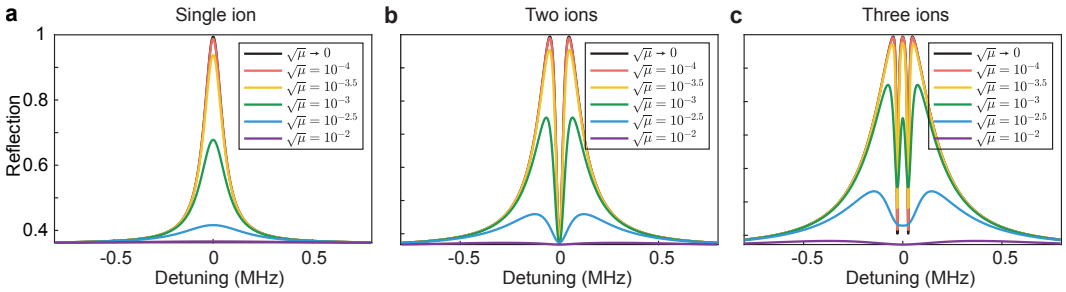

Figure 3.5: **Cavity reflection spectrum of one, two, and three atoms. a,** Cavity reflection spectrum of a single ion coupled to the cavity with rate $g = 2\pi \times 35$ MHz, using Eq. 3.16. DIR is observed for small powers, and decreases with increasing powers. **b,** Simulation of the cavity reflection spectrum of two symmetrically detuned ions at $\pm 2\pi \times 0.048$ MHz. There are two DIR peaks at each of the ion frequencies, and destructive interference between two ions form a dip at 0 MHz. **c,** Three ion simulation, adding an ion at 0 MHz. The dip from the two-ion case disappears at low powers due to DIR from the added third ion.

Driven two- and three-ion cases

Since there is no dip for the single ion case, we add another ion, where the ions are now symmetrically detuned around 0 MHz, with detunings $\pm 2\pi \times 0.048$ MHz. The cavity reflection for $\sqrt{\mu} \to 0$ is plotted using an analytical expression under the weak-excitation condition, similar to Eq. 3.9. Additionally, we sweep the power from $\sqrt{\mu} = 10^{-4}$ to $\sqrt{\mu} = 10^{-2}$ and simulate using the master equation (Section 4.5). First, we note that $\sqrt{\mu} = 10^{-4}$ is very close to the weak-excitation limit. In this case, we observe two DIRs centered around each ion frequency. The two DIRs overlap at zero detuning where the ions destructively interfere, producing a narrow window even with low excitation, indicating that this is not exactly CIT (Fig. 3.5b). When $\sqrt{\mu}$ is increased, both DIRs decrease, similar to the single ion case.

We now add a third ion between the two ions at zero detuning, where a third DIR peak appears (Fig. 3.5c). At the same time, two sharp dips appear between the first/second ion and second/third ion. When $\sqrt{\mu}$ is increased, all three DIR peaks decrease where the center peak decreases the fastest. This eventually leads to a single, wide dip at $\sqrt{\mu} = 10^{-2.5}$. From the results of the two- and three-ion cases, we see hints of the origins of CIT, from the destructive interference between different ions.

3.5 Theoretical analysis: driven multi-ion coupling leading to CIT

In this section, we will extend our discussion to the multi-ion case, where we can see that CIT results from a large ensemble of ions with an inhomogeneous distribution.

Analytical derivation

From the simple cases analyzed in the last section, we get the intuition that an inhomogeneously broadened ensemble of ions is required for a narrow dip to form. To see this more rigorously, we derive the analytical expression for CIT under certain conditions. We first set the steady state of Eqs. 3.5 – 3.7 ($\dot{a} = \dot{\sigma}^z = \dot{\sigma}^- = 0$), which gives $2N + 1$ equations for $2N + 1$ variables:

$$-(i\Delta_c + \frac{\kappa}{2})\langle a\rangle - i\sum_{j=1}^{N} g_j\langle\sigma_j^-\rangle - \frac{\kappa}{2}\sqrt{\mu} = 0 \tag{3.17}$$

$$-(i\Delta_j + \gamma)\langle\sigma_j^-\rangle + ig_j\langle\sigma_j^z\rangle\langle a\rangle = 0 \tag{3.18}$$

$$2ig_j(\langle a^\dagger\rangle\langle\sigma_j^-\rangle - \langle\sigma_j^+\rangle\langle a\rangle) - \gamma_s(1 + \langle\sigma_j^z\rangle) = 0. \tag{3.19}$$

Note that here we adopt the hypothesis that quantum correlation between atomic and cavity field operators can be neglected ($\langle\sigma_j^z a\rangle = \langle\sigma_j^z\rangle\langle a\rangle$ and $\langle a^\dagger\sigma_j^-\rangle = \langle a^\dagger\rangle\langle\sigma_j^-\rangle$) [94]. Eliminating $\langle\sigma_j^-\rangle$, we get the equation relating $\langle\sigma_j^z\rangle$ and $\langle a\rangle$ as:

$$\langle a\rangle = \frac{-\sqrt{\mu}}{1 - \sum_{j=1}^{N}\frac{2g_j^2\langle\sigma_j^z\rangle}{\kappa(\gamma+i\Delta_j)}} \tag{3.20}$$

$$\langle\sigma_j^z\rangle = -\frac{1}{1 + \frac{4g_j^2\langle a^\dagger\rangle\langle a\rangle}{\gamma_s}\left(\frac{\gamma}{\gamma^2+\Delta_j^2}\right)}. \tag{3.21}$$

We define $\langle a\rangle = -\frac{\sqrt{\mu}}{1+x}$, where

$$x = -\sum_{j=1}^{N}\frac{2g_j^2\langle\sigma_j^z\rangle}{\kappa(\gamma + i\Delta_j)} = \frac{\sum_{j=1}^{N} 2ig_j\langle\sigma_j^-\rangle}{\kappa\langle a\rangle} \tag{3.22}$$

which represents the ions' response to the cavity field. Here, we also ignore Δ_c for simplicity based on the fact that $\Delta_c \ll \kappa$. We can get an implicit equation for x as:

$$x = \sum_{j=1}^{N}\frac{2g_j^2}{\kappa(\gamma + i\Delta_j)}\frac{1}{\left(1 + \frac{4g_j^2\mu}{|1+x|^2\gamma_s}\left(\frac{\gamma}{\gamma^2+\Delta_j^2}\right)\right)} \tag{3.23}$$

where the distribution of coupling strength g_j is not correlated with the distribution of ion frequency detuning Δ_j, as the physical position of the ion in the cavity is unrelated

to its resonance frequency. We first consider $g_j = g$ and define $y(x) = \frac{4g^2\mu\gamma}{|1+x|^2\gamma_s}$ for simplicity, and convert the summation to integral in the limit of large N:

$$x = \frac{2Ng^2}{\kappa} \int \frac{\rho(\omega)d\omega}{(\gamma + i(\omega - \omega_L)) \left(1 + \frac{y(x)}{\gamma^2 + (\omega-\omega_L)^2}\right)} \tag{3.24}$$

where ω_L is laser frequency and $\rho(\omega)$ is the probability distribution of a given ion frequency ω. Given x, the cavity reflection is now simply

$$R = \left| -\frac{2\kappa_c}{\kappa} \frac{1}{(1+x)} + 1 \right|^2. \tag{3.25}$$

We consider a Lorentzian distribution of ions with $\rho(\omega) = \frac{\Delta_{\text{inh}}/2}{\pi} \frac{1}{(\Delta_{\text{inh}}/2)^2 + (\omega-\omega_0)^2}$ where Δ_{inh} is the FWHM and ω_0 is the center frequency of the ion distribution, which gives us:

$$x = \frac{N\Delta_{\text{inh}}g^2}{\pi\kappa} \int_{-\infty}^{+\infty} \frac{(\gamma - i(\omega - \omega_L))\, d\omega}{\left(\gamma^2 + (\omega - \omega_L)^2 + y(x)\right) \left((\Delta_{\text{inh}}/2)^2 + (\omega - \omega_0)^2\right)}. \tag{3.26}$$

Making the approximations $\Delta_{\text{inh}} \gg |\omega_L - \omega_0|, \gamma, \sqrt{y(x)}$ and $y(x) \gg \gamma^2$ as well as $\sqrt{\mu} > \frac{2Ng\sqrt{\gamma_s\gamma}}{\kappa\Delta_{\text{inh}}}$ (summarized and justified below), allows us to solve for x explicitly:

$$x = \frac{1}{\frac{\Delta_{\text{inh}}\kappa}{2Ng}\sqrt{\frac{\mu}{\gamma_s\gamma}} - 1} + \frac{8i(\omega_L - \omega_0)}{\frac{\Delta_{\text{inh}}^2\kappa}{Ng^2}}. \tag{3.27}$$

Plugging Eq. 3.27 into Eq. 3.25, we get the explicit expression of the reflectivity relative to the laser frequency ω_L as:

$$R = 1 + \frac{\frac{\kappa_c}{\kappa}\left(\frac{\Delta_{\text{inh}}}{C}\right)^2 \left(\frac{\kappa_c}{\kappa} - \frac{C\Delta_{\text{CIT}}}{\Delta_{\text{inh}}}\right)}{\left(\frac{\Delta_{\text{CIT}}}{2}\right)^2 + (\omega_L - \omega_0)^2} \tag{3.28}$$

where $C = \frac{|W(\omega=\omega_0)|}{\kappa/2} (= \frac{4Ng^2}{\kappa\Delta_{\text{inh}}}$ when $\Delta_{\text{inh}} \gg \gamma)$ and

$$\Delta_{\text{CIT}} = \frac{\Delta_{\text{inh}}}{C} \frac{1}{\left(1 - C\sqrt{\frac{\gamma_s\gamma}{4g^2\mu}}\right)}. \tag{3.29}$$

According to Eq. 3.28, it is apparent that the profile of the CIT dip is a Lorentzian function with width Δ_{CIT} and depth η_{CIT}, which is determined by the reflectivity at $\omega_L = \omega_0$ as

$$\begin{aligned} \eta_{\text{CIT}} &= \frac{A}{\left(\frac{\Delta_{\text{CIT}}}{2}\right)^2 \eta_{\text{bare}}} \\ &= \frac{1}{(1 - \frac{\kappa_c}{\kappa})} \left(1 - C\sqrt{\frac{\gamma_s\gamma}{4g^2\mu}} - \frac{\kappa_c}{\kappa}\left(1 - C\sqrt{\frac{\gamma_s\gamma}{4g^2\mu}}\right)^2\right) \end{aligned} \tag{3.30}$$

where the depth has been normalized against the bare cavity depth $\eta_{\text{bare}} = 1 - \left(1 - \frac{2\kappa_c}{\kappa}\right)^2$. The lower bound of Δ_{CIT} is $\Delta_{\text{CIT, min}} = \frac{\Delta_{\text{inh}}}{C}$, as the laser power μ becomes large. Additionally in the same limit, the depth reaches 1. Here we summarize the assumptions made to derive the analytical expressions of the CIT width and depth.

High cooperativity:

$$C \gg 1. \tag{3.31a}$$

Intermediate power:

$$\left(\frac{\Delta_{\text{inh}}}{4g}\right)^2 \frac{\gamma_s}{\gamma} \gg \mu \gg \frac{\gamma\gamma_s}{4g^2}. \tag{3.31b}$$

Appreciable inhomogeneity and good coherence:

$$\frac{\Delta_{\text{inh}}}{\gamma} \gg C. \tag{3.31c}$$

We note that for a uniform (rectangular) ensemble distribution, the CIT depth and width have the same power and cooperativity dependence up to a factor of $\frac{\pi}{2}$. From this we anticipate CIT to be a ubiquitous phenomenon for any distribution satisfying Eq. 3.31.

Inhomogeneity of g distribution

For simplicity, we have so far assumed that all ions are coupled equally to the cavity ($g_j = g$). Now we consider inhomogeneously distributed g, with a probability distribution given by $p(g)$. Using the fact that $p(g)$ is uncorrelated with $\rho(\omega)$, Eq. 3.24 can be written as:

$$x = \frac{2}{\kappa} \int N g^2 p(g) dg \int \frac{\rho(\omega) d\omega}{(\gamma + i(\omega - \omega_L)) \left(1 + \frac{y(x,g)}{\gamma^2 + (\omega - \omega_L)^2}\right)}. \tag{3.32}$$

Note that $y(x, g)$ is now also a function of g. We can first calculate the integral over frequency ω, then over g to get the solution of x similar to Eq. 3.27:

$$x = \frac{1}{\frac{\Delta_{\text{inh}}\kappa}{2N g_{\text{avg}}} \sqrt{\frac{\mu}{\gamma_s \gamma}} - 1} + \frac{8i\omega_L}{\frac{\Delta_{\text{inh}}^2 \kappa}{\Omega^2}} \tag{3.33}$$

where $\Omega^2 = \int N g^2 p(g) dg$, and we define $g_{\text{avg}} = \int g p(g) dg$. Now, we obtain the width

$$\Delta_{\text{CIT}} = \Delta_{\text{inh}} \frac{\frac{\Delta_{\text{inh}}\kappa}{4\Omega^2}}{1 - \frac{2N g_{\text{avg}}}{\Delta_{\text{inh}}\kappa} \sqrt{\frac{\gamma_s \gamma}{\mu}}}. \tag{3.34}$$

From this, we can see that the CIT profile and the minimum width do not depend on the specific distribution of cavity-ion coupling strength, but only the total coupling strength. Ensemble cooperativity $C \propto \frac{\Omega^2}{\kappa\Delta_{\text{inh}}}$ also only depends on the total coupling strength Ω^2, so the expression of the minimum FWHM relative to the cooperativity will still be $\Delta_{\text{CIT, min}} \sim \frac{\Delta_{\text{inh}}}{C}$, regardless of the specific distribution of g.

Intuitive understanding

From the above derivations, we see that for high cooperativity ($C > 1$), we will get a CIT dip with width approximately equal to the inhomogeneous linewidth divided by C. Looking back at Eq. 3.22, the contribution of each ion to x can be extracted using Eq. 3.18 (still assuming $g_j = g$ since g_j and Δ_j are uncorrelated):

$$\frac{\langle\sigma^-_{\Delta_j}\rangle}{\langle a\rangle} = \frac{ig\sigma^z_{\Delta_j}(\gamma - i\Delta_j)}{\gamma^2 + \Delta_j^2}. \tag{3.35}$$

Here, we use notation $\langle\sigma^-_j\rangle = \langle\sigma^-_{\Delta_j}\rangle$ and $\langle\sigma^z_j\rangle = \langle\sigma^z_{\Delta_j}\rangle$, where the subscript now denotes the ion-laser detuning. For ions with detuning much larger than a homogeneous linewidth $|\Delta_j| \gg \gamma$, if a ion is blue-detuned ($\Delta_j > 0$), its atomic coherence phase $\arg\left(\frac{\langle\sigma^-_{\Delta_j}\rangle}{\langle a\rangle}\right) \to -\pi$ while its red-detuned pair has $\arg\left(\frac{\langle\sigma^-_{-\Delta_j}\rangle}{\langle a\rangle}\right) \to 0$. Their amplitudes are $\left|\frac{\langle\sigma^-_{\Delta_j}\rangle}{\langle a\rangle}\right| = \left|\frac{\langle\sigma^-_{-\Delta_j}\rangle}{\langle a\rangle}\right| \sim \frac{g}{|\Delta_j|}|\langle\sigma^z_{|\Delta_j|}\rangle|$. We can see that for the above pair of ions with $\pm\Delta_j$, the phase difference will be π, such that their phases will cancel and their contribution to the cavity field will be

$$\frac{\langle\sigma^-_{\Delta_j}\rangle}{\langle a\rangle} + \frac{\langle\sigma^-_{-\Delta_j}\rangle}{\langle a\rangle} = \frac{ig\langle\sigma^z_{|\Delta_j|}\rangle(2\gamma)}{\gamma^2 + \Delta_j^2} \sim \frac{2g\gamma}{\Delta_j^2}|\langle\sigma^z_{|\Delta_j|}\rangle|. \tag{3.36}$$

Note that the phase we talk about here is the phase of $\langle\sigma^-_j\rangle$ relative to $\langle a\rangle$. For the Fig. 3.2a, we add a global phase of $\frac{\pi}{2}$ to the ion phases for visual clarity.

To summarize:

1. The contribution from any ion to cavity reflection will decrease as the ion gets excited ($\langle\sigma^z_j\rangle > -1$), and finally disappear when the ion is saturated to the completely mixed state where $\langle\sigma^z_j\rangle = \langle\sigma^-_j\rangle = 0$.

2. The phase of each ion relative to the cavity field is determined by the detuning of an ion relative to the laser frequency. For blue-detuned ions ($\Delta_j > 0$), the phases are between $-\frac{\pi}{2}$ to $-\pi$, while for the red-detuned ions ($\Delta_j < 0$), the phases are between $-\frac{\pi}{2}$ to 0.

3. A pair of symmetrically detuned ions relative to the laser frequency will have a reduced contribution to the cavity field compared to a single ion due to the phase cancellation, by a factor of $\sim \frac{\gamma}{\Delta_j}$. This is obtained by comparing Eq. 3.36 to Eq. 3.35 in the case of $|\Delta_j| \gg \gamma$.

Validity of Mean-Field Approximation

In the above derivation of CIT, we have used the mean-field approximation [95, 96] where the mean values of the products of the operators a and σ_j^z are factorized: $\langle \sigma_j^z a \rangle = \langle \sigma_j^z \rangle \langle a \rangle$. In the following, we will justify why such an approximation can be made for this system when considering CIT. To start, we introduce the term $\langle \sigma_j^z a \rangle - \langle \sigma_j^z \rangle \langle a \rangle$ which considers the correlations between a and σ_j^z, and we would like to show that this term is negligible. Using adiabatic elimination $a \approx \frac{-2i}{\kappa} \sum_{k=1}^{N} g_k \sigma_k^- - \sqrt{\mu}$, we expand this as:

$$\begin{aligned}\langle \sigma_j^z a \rangle - \langle \sigma_j^z \rangle \langle a \rangle &= -\frac{2i}{\kappa} \sum_{k=1}^{N} g_k \left(\langle \sigma_j^z \sigma_k^- \rangle - \langle \sigma_j^z \rangle \langle \sigma_k^- \rangle \right) \\ &= -\frac{2i}{\kappa} \left(g_j \left(\langle \sigma_j^z \sigma_j^- \rangle - \langle \sigma_j^z \rangle \langle \sigma_j^- \rangle \right) + \sum_{k \neq j}^{N} g_k \left(\langle \sigma_j^z \sigma_k^- \rangle - \langle \sigma_j^z \rangle \langle \sigma_k^- \rangle \right) \right).\end{aligned} \tag{3.37}$$

The first term is the self-correlation between σ_j^z and σ_j^- of ion j, and the second term is the cross-correlation between different ions. Setting the second term $\langle \sigma_j^z \sigma_k^- \rangle - \langle \sigma_j^z \rangle \langle \sigma_k^- \rangle = 0 \, (k \neq j)$ indicates that the final states of different ions are not entangled. For the first term (self-correlation), we use the commutation rule between σ_j^z and σ_j^- ($\sigma_j^z \sigma_j^- = -\sigma_j^-$) to rewrite it as

$$-\frac{2ig_j}{\kappa} \left(\langle \sigma_j^z \sigma_j^- \rangle - \langle \sigma_j^z \rangle \langle \sigma_j^- \rangle \right) = \frac{2ig_j}{\kappa} \left(1 + \langle \sigma_j^z \rangle \right) \langle \sigma_j^- \rangle. \tag{3.38}$$

It is true that this term can be nonzero based on the solution in CIT. However, we now want to show that the influence of this term of the final cavity field $\langle a \rangle$ is very small. To do this, we introduce $\delta(\langle \sigma_j^- \rangle)$, which is the modification to $\langle \sigma_j^- \rangle$ if we were to consider this self-correlation term. Using Eq. 3.18,

$$\delta(\langle \sigma_j^- \rangle) = -\frac{2g_j^2}{(i\Delta_j + \gamma)\kappa} \left(1 + \langle \sigma_j^z \rangle \right) \langle \sigma_j^- \rangle. \tag{3.39}$$

We can then plug this back into our expression for the cavity field a using Eq. 3.17, and get the modification to the cavity field introduced by this self-correlation:

$$\begin{aligned}\delta(\langle a\rangle) &= -\frac{2i}{\kappa}\sum_{k=1}^{N} g_k \delta(\langle\sigma_k^-\rangle \\ &= \frac{4i}{\kappa^2}\sum_{k=1}^{N}\frac{g_k^3}{i\Delta_k+\gamma}\left(1+\langle\sigma_k^z\rangle\right)\langle\sigma_k^-\rangle \\ &= -\frac{4}{\kappa^2}\sum_{k=1}^{N}\frac{g_k^4}{(i\Delta_k+\gamma)^2}\left(1+\langle\sigma_k^z\rangle\right)\langle\sigma_k^z\rangle\langle a\rangle. \end{aligned} \tag{3.40}$$

If we plug solution Eq. 3.21 into Eq. 3.40, we get

$$\delta(\langle a\rangle) = \frac{4}{\kappa^2}\sum_{k=1}^{N}\frac{g_k^4}{(i\Delta_k+\gamma)^2}\frac{\frac{4g_k^2|\langle a\rangle|^2\gamma}{\gamma_s(\gamma^2+\Delta_k^2)}}{\left(1+\frac{4g_k^2|\langle a\rangle|^2\gamma}{\gamma_s(\gamma^2+\Delta_k^2)}\right)^2}\langle a\rangle. \tag{3.41}$$

Assuming $g_k = g$ for all the ions, we can obtain the relative change of $\langle a\rangle$ is

$$\left|\frac{\delta(\langle a\rangle)}{\langle a\rangle}\right| < \frac{16g^6\gamma}{\kappa^2\gamma_s}\sum_{k=1}^{N}\frac{|\langle a\rangle|^2}{(i\Delta_k+\gamma)^2(\gamma^2+\Delta_k^2)} \sim \frac{16Ng^6\gamma}{\kappa^2\gamma_s\Delta_{\text{inh}}^4}|\langle a\rangle|^2 \sim \frac{16Ng^6\gamma}{\kappa^2\gamma_s\Delta_{\text{inh}}^4}\mu. \tag{3.42}$$

Using Eq. 3.31b where $\mu \ll \left(\frac{\Delta_{\text{inh}}}{4g}\right)^2\frac{\gamma_s}{\gamma}$ we can then get $\left|\frac{\delta(\langle a\rangle)}{\langle a\rangle}\right| \ll \frac{Cg^2}{4\kappa\Delta_{\text{inh}}} \ll 1$, which is validated both in experiment and simulation for our system. The conclusion is that $\left|\frac{\delta(\langle a\rangle)}{\langle a\rangle}\right| \ll 1$, or that the fractional change in the cavity field due to the self-correlation term will be very small.

Validity of the Tavis-Cummings model

It has been shown in [30] that large collective coupling rates can lead to a breakdown of the standard Tavis-Cummings model. The relevant condition for the validity of the Tavis-Cummings model is FSR $\gg W$, where FSR is the free-spectral range of the cavity, and W is the ensemble absorption derived in Eq. 3.10. Plugging in the parameters of our system, we find FSR $= 2\pi \times 25$ THz, and $W = 2\pi \times 0.5$ THz, thus satisfying the above inequality, and validating our use of the Tavis-Cummings model.

3.6 Analysis of CIT widths and depths

In this section, we will provide a more detailed analysis of fitting the experimental data, comparing CIT widths and depths for different transitions. We will also discuss the numerical simulation of CIT when some approximations in Eq. 3.31 break down, and thus the analytical expression of CIT in Eq. 3.1 does not hold.

The fits for CIT widths and depths

As the distribution of ions in our experimental system is approximately Lorentzian, based on Eq. 3.29 and Eq. 3.30, we use the following functions to fit the power dependent CIT width and the depth

$$\Delta_{\text{CIT,fit}} = \frac{p_1}{1 - \frac{p_2}{\sqrt{P}}} \tag{3.43}$$

$$\eta_{\text{CIT,fit}} = p_4 \left(1 - \frac{p_2}{\sqrt{P}} - p_3 \left(1 - \frac{p_2}{\sqrt{P}}\right)^2\right) \tag{3.44}$$

where $p_{1,2,3,4}$ are free fitting parameters and P is the excitation power. The fit parameters are left floating as the purpose of these fits are to validate the analytically derived power scaling, which contains some approximations that may make it inexact in certain regimes. This is already apparent in the discrepancy of the minimum CIT width, where the analytical value is a few times smaller than the experimental and numerically simulated values.

Comparison between A and I transition

We find that the extracted fit parameters from Fig. 3.2d and Fig. 3.6 are physically reasonable based on our system parameters, for both the A and I transitions. First p_1, representing the minimum CIT width, is fit to 42(36) MHz for the A(I) transitions. p_2, the prefactor to the excitation power, is fit to 0.08(0.25), where the larger value for the I transition reflects both the larger cooperativity and dephasing. The analytical expression of p_2 is $C\sqrt{\frac{\hbar\omega\gamma_s\gamma\kappa^2}{g^2\kappa_c}}$, and plugging in system parameters we obtain about 0.07(1.4), accounting for optical losses and the factor of 4 discrepancy found in the numerical simulations. We attribute the discrepancy of p_2 for the I transition to an overestimation of the dephasing rate, which we assumed to be a hundred times worse than the A transition. p_3 is the extracted fit for the cavity in-coupling ratio κ_c/κ, fit to 0.3(0.1), a good match to the estimated value of $\kappa_c/\kappa \sim 0.2$ measured in similar devices. Correspondingly, p_4 is fit to 1.2(1.1), consistent with its analytical expression $\frac{1}{(1-\kappa_c/\kappa)}$.

We note that the measured CIT depths in Fig. 3.2d and Fig. 3.6 are normalized against the bare cavity depth, determined by κ_c. For the experiment data, we set the cavity resonance minimum to be 0 (which we take to be the minimum of the edge of the DIR, since the cavity is broad), and the DIR maximum to be 1. This is done to eliminate the background counts of reflected light that do not enter the cavity.

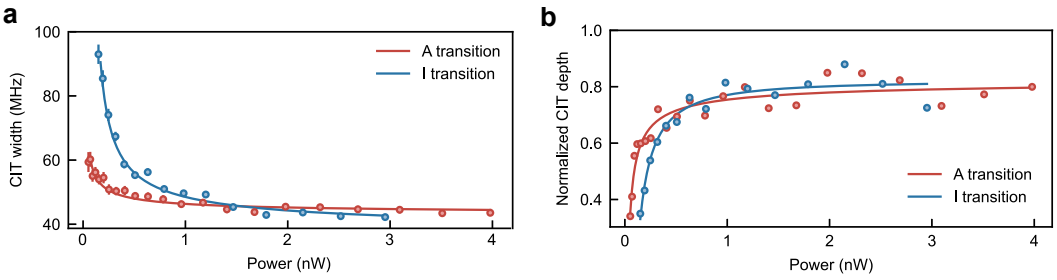

Figure 3.6: **CIT width and depth comparison between the A and I transitions. a,** Measured CIT width and **b,** depth with power and corresponding fits for the A (red) and I (blue) transitions. We expect the I transition to have different width and depth values, as the cooperativity is twice as high, but the dephasing rate is expected to be more than 100 times larger than A. While we find similar depth values, the width differs between the two. In particular, the I transition starts out much broader than A, as expected from the worse coherence properties. Despite this, the minimum width is slightly narrower for the I transition, indicating that indeed the cooperativity is larger for the I transition.

Numerical simulation

While the analytical expressions above give the intuition behind CIT , an arbitrary distribution can be numerically solved without making the assumptions listed in Eq. 3.31. The simulation model still follows the mean-field approximation, thus solving the $2N + 1$ equations of $2N + 1$ variables in Eq. 3.17-3.19. The simulation method is very similar to the steady-state solution in [97].

This is how the results in Fig. 3.2c are obtained. This gives CIT widths closer to the experimental values. Note that the power used in simulation in Fig. 3.2c is four times smaller than the experiment in Fig. 2b, which is attributed to discrepancy of the realistic distribution of ions and power calibration errors in experiment. Specifically, we found that making the simulated ion distribution imperfect or asymmetric resulted in requiring more power to effectively reach the high power regime, where the CIT width reaches its minimum.

From the derivation in section 3.5, we note that the lower limit of CIT width does not depend on homogeneous linewidth γ as long as $\frac{\Delta_{\text{inh}}}{C} \gg \gamma$. When the cooperativity is high enough such that $\frac{\Delta_{\text{inh}}}{C} \sim \gamma$, Eq. 3.29 and Eq. 3.30 do not hold anymore; In such a high cooperativity regime, numerical simulation is neede and shows that the CIT will finally be limited by homogeneous linewidth (Fig. 3.7a,b).

From the simulation, we can also look at the phase of the cavity field, and we found that the phase has a sudden shift (Fig. 3.8c).

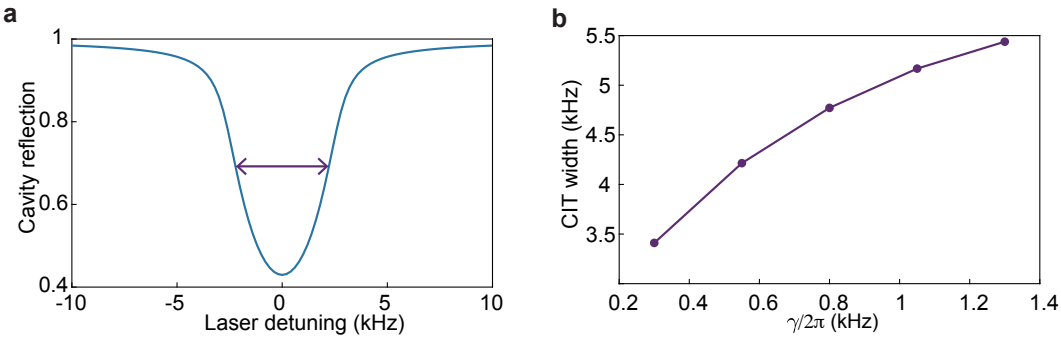

Figure 3.7: **Numerical simulation for a higher cooperativity in CIT a,** Simulated cavity reflection showing narrow CIT for $\Delta_{\text{inh}}/(2\pi C) = 1$ kHz and $\gamma/2\pi = 0.3$ kHz. **b,** CIT width with varying γ in this high cooperativity system, showing a strong dependence on γ.

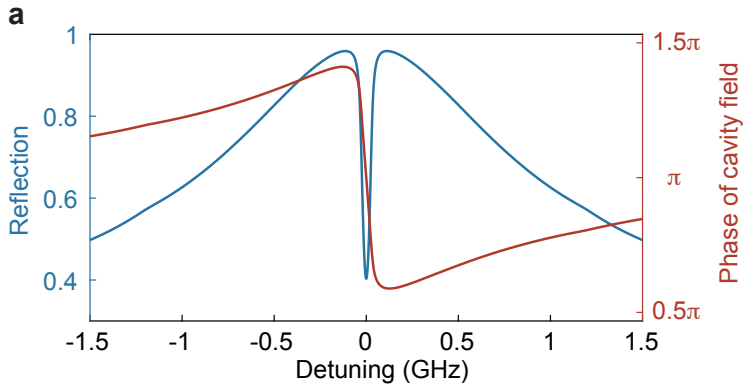

Figure 3.8: **Phase shift in CIT a.** The simulated cavity phase Arg(a) (red) across the CIT for a laser power of 0.5 nW, exhibiting a relative π phase shift. The corresponding cavity reflection spectrum (blue) as a function of laser frequency for reference, identical to Fig. 2c purple. Note that this phase shift can be reproduced either by numerical simulation or by the analytical expression in Eq. 3.27. Here, we are presenting the numerical simulation results to better match experimental data.

3.7 Potential applications for CIT

In this section, we will discuss two potential applications for CIT.

Description of CIT in the good-cavity regime

We have so far focused on the resonant bad-cavity regime, such that $\Delta_c = \omega_c - \omega_L$, the cavity detuning from the laser, was ignored. Here we generalize the CIT derivation to the case where Δ_c is considered, and 3.24 becomes:

$$x = \frac{2Ng^2}{\kappa + 2i\Delta_c} \int \frac{\rho(\omega)d\omega}{(\gamma + i(\omega - \omega_L))\left(1 + \frac{y(x)}{\gamma^2 + (\omega - \omega_L)^2}\right)} \tag{3.45}$$

where now $y(x) = \frac{4g^2\mu\gamma}{|1+x|^2\gamma_s(1+4\Delta_c^2/\kappa^2)} \approx \frac{4g^2\mu\gamma}{|1+x|^2\gamma_s}$, keeping the first order of Δ_c/κ. Solving for x:

$$x = \frac{1}{\frac{2g}{C}\sqrt{\frac{\mu}{\gamma_s\gamma}} - 1}\left(1 - \frac{2i(\omega_c - \omega_L)}{\kappa}\right) + \frac{2i(\omega_L - \omega_0)}{\frac{\Delta_{\text{inh}}}{C}}. \tag{3.46}$$

Using this, we can write our cavity reflection coefficient as

$$\begin{aligned} r &= 1 - \frac{2\kappa_c}{(\kappa + 2i(\omega_c - \omega_L))(1+x)} \\ &= 1 - \frac{\Delta_{\text{CIT,min}}\kappa_c/\kappa}{\Delta_{\text{CIT}}/2 + i(\omega_L - \omega_{\text{center}})}. \end{aligned} \tag{3.47}$$

From this the center of CIT and width of CIT are:

$$\omega_{\text{center}} = \left(\frac{\omega_0 C}{\Delta_{\text{inh}}} - \frac{\omega_c}{\kappa}\right)\frac{\frac{\Delta_{\text{inh}}}{C}}{\left(1 - \frac{\Delta_{\text{inh}}}{C\kappa}\right)} = \frac{1}{\left(1 - \frac{\Delta_{\text{inh}}}{C\kappa}\right)}\omega_0 - \frac{\frac{\Delta_{\text{inh}}}{C\kappa}}{\left(1 - \frac{\Delta_{\text{inh}}}{C\kappa}\right)}\omega_c, \tag{3.48}$$

$$\Delta_{\text{CIT}} = \frac{\frac{\Delta_{\text{inh}}}{C}}{\left(1 - \frac{C}{2g}\sqrt{\frac{\gamma_s\gamma}{\mu}}\right)\left(1 - \frac{\Delta_{\text{inh}}}{C\kappa}\right)} \rightarrow \Delta_{\text{CIT,min}} = \frac{\frac{\Delta_{\text{inh}}}{C}}{\left(1 - \frac{\Delta_{\text{inh}}}{C\kappa}\right)}. \tag{3.49}$$

In the experiment, we measure the CIT for different cavity resonance frequencies, as shown in Fig. 3.9, where we can observe the linear dependence as expected.

The above derivations show the following:

1. The CIT spectrum is similar to a cavity resonance, with Δ_{CIT} linewidth and input relative coupling ratio $\frac{\Delta_{\text{CIT,min}}\kappa_c}{\Delta_{\text{CIT}}\kappa} \rightarrow \frac{\kappa_c}{\kappa}$. This means that CIT is a mechanism in which a new resonance can be produced from a cavity, where this new resonance will be much narrower than the original cavity, whilst maintaining the input relative coupling ratio.

2. This narrow feature can be used for precision sensing. The effective cavity (CIT) fluctuation is reduced by a factor of $\frac{\frac{\Delta_{\text{inh}}}{C\kappa}}{\left(1-\frac{\Delta_{\text{inh}}}{C\kappa}\right)} \rightarrow \frac{\Delta_{\text{inh}}}{C\kappa}$ compared to the original cavity fluctuation.

3. The above derivation requires $\frac{\Delta_{\text{inh}}}{C\kappa} \ll 1$ (besides the conditions in Eq. 3.31), which gives $\Delta_{\text{inh}} \ll 2\sqrt{N}g$. However, we can see that there is no individual requirement for κ, so the CIT phenomenon is not necessarily restricted to the bad cavity regime, and can work for cavities with higher quality factors. We

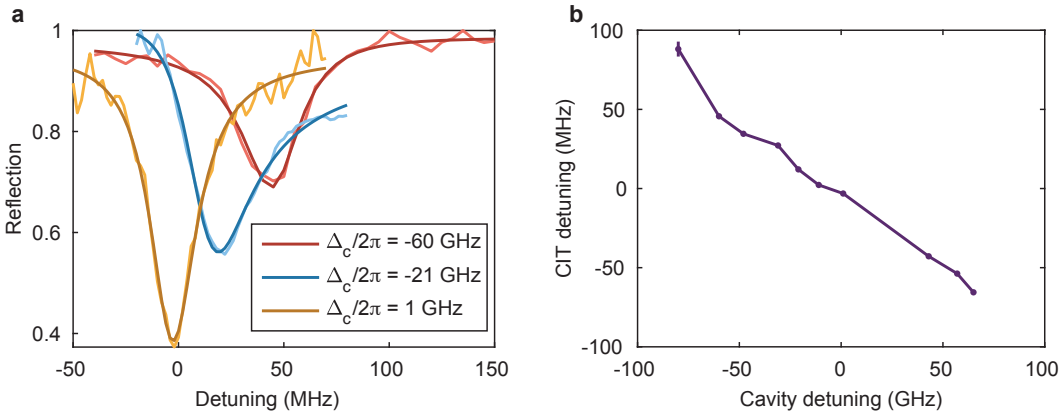

Figure 3.9: **CIT dependence on cavity resonance frequency. a,** CIT spectrum for different cavity detunings, fit to a Fano resonance. **b,** Relation between CIT detunings and cavity detunings, showing the expected linear dependence. The error bar is from the fit.

note that if the cavity becomes extremely narrow, the mean-field approximation may not hold and a more exact model may be required. It is unclear, however, if we must be in the mean-field regime for CIT to occur.

Response time of CIT and application for optical switch

In the previous sections, CIT has been investigated in the steady state regime. However, CIT has a finite response time, which is important to explore for certain applications such as an optical switch. To this end, we park the laser at the center of the CIT, and measure the reflection as a function of time (Extended Data Fig. 10).

We find a fast response time of 600 ns, and posit that a two-port optical switch with an integrated filter can be realized using CIT. This current device has not been optimized for this particular application, hence we are unable to measure the other port (transmission) nor apply a transverse pump. Additionally, the contrast suffers from reflection due to an imperfect beam overlap with our optical coupler and our cavity being under-coupled. However, this problem can be solved by critically coupling and coupling the laser better into the cavity. This will result in increased contrast, important for improving the extinction ratio of the switch. For the best extinction ratio, the cavity should be designed as critical-coupled where $\kappa_1/\kappa = \kappa_2/\kappa = 0.5$ where κ_1 and κ_2 are the coupling rate from ports 1 and 2. We note that the pump light is to create the CIT, which is an absorptive process where the ions absorb light and get excited. In contrast, as long as the signal is weak enough, the optical switch can be non-absorptive. Furthermore, we believe the

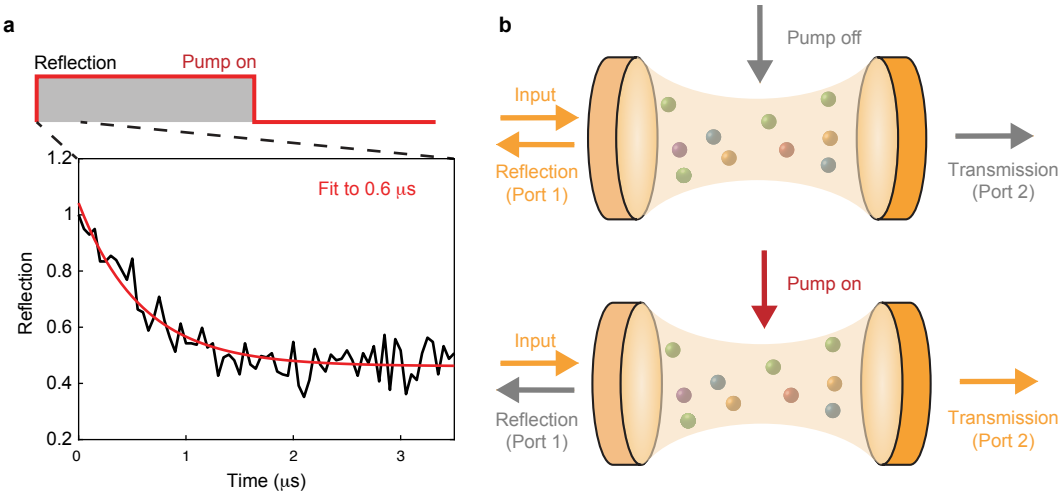

Figure 3.10: **Optical switch based on CIT. a,** CIT response time. We park the laser at the center of the CIT, and measure the reflection as a function of time after turning the pump on. The reflection signal decreases as the CIT is created in sub-μs timescales. **b,** Schematic of an ideal two-port optical switch with an integrated filter with CIT. A transmission port and a transverse pump port are added to realize this application. For the best extinction ratio, the cavity should be two-sided and critically coupled such that $\kappa_1/\kappa = \kappa_2/\kappa = 0.5$ where κ_1 and κ_2 are the coupling rates from ports 1 and 2. The top schematic shows that when the pump is off and DIR is formed, the signal is entirely reflected (port 1). The bottom schematic shows that when the pump is on and CIT is created, the signal is transmitted (port 2) within the CIT window (spectral filter).

current switching time is limited by how fast the ions can reach saturation, which can be faster by engineering a larger g.

3.8 Discussion and outlook

In this work we have investigated the spectral response and open quantum dynamics of a large cavity QED system, revealing a sharp CIT appearing in the reflection spectrum. Notably, the CIT width is found to be narrowed by cooperativity, indicating that improvements in fabrication and material properties towards increasing cooperativity can lead to much narrower transparencies, potentially useful as frequency references. The sudden cavity phase shift across the CIT (Extended Data Fig. 3.8) can provide a novel mechanism to achieve optical nonlinearities and the storage of light [98]. In particular, we demonstrate a proof-of-principle optical switch using CIT, and posit that with further optimization a fast, high contrast two-port optical switch can be realized (Fig. 3.10).

Chapter 4

DISSIPATIVE MANY-BODY DYNAMICS: CAVITY-MEDIATED SUPERRADIANCE AND SUBRADIANCE

In chapter 3, we demonstrate the newly discovered CIT appearing in a many-body cavity QED system with high ensemble cooperativity. This phenomenon can be well explained under the mean-field approximation (section 3.5), which holds in the relatively small power[1], and quantum correlation can be ignored. Furthermore, as we increase the optical driving, such highly cooperative systems can exhibit many-body phenomena [89]. One example is Dicke superradiance and subradiance [99], the collective enhancement and suppression of radiation due to quantum interference between identical emitters, respectively. Indeed, thanks to the transparency window opened by CIT, we are able to send enough power into the cavity and study the dissipative many-body dynamics–cavity-mediated superradiance and subradiance–which will be the topic in this chapter. This chapter is adapted from [88], and all simulation results in this chapter are provided by Riku Fukumori.

4.1 Introduction

Previously, superradiance has mostly been explored with cold atoms [27, 100–102], microwave resonators coupled to spins [28] and superconducting qubits [24, 103]. In particular, *optical* superradiance in the solid state has only been studied for few emitters [104–106] and signatures have been observed only with very few examples for larger ensembles [32]. This is because superradiance is a coherent process that requires cooperative decay to overcome disorder, which is typically challenging to achieve in solid state systems due to large optical inhomogeneities [31]. Phenomenologically similar to superradiance, the so-called superfluorescence (SF) has been observed in several solid-state platforms, including quantum dots [107] and rare-earths doped in crystals [108, 109]. However, SF is distinct from superradiance as an initially incoherent system that self-evolves to build up a coherent polarization. Superradiance, on the other hand, happens when the coherent polarization is deterministically generated by external coherent excitation.

Furthermore, in the presence of dissipation, subradiance can also emerge as a

[1] We call it intermediate power in Eq. 3.31 since it has an upper and a lower bound. The overall experimental power regime discussed in chapter 3 is smaller than in this chapter.

result of the interplay between interatomic interaction and decoherence. Due to its intrinsically weak coupling to the environment, however, subradiance has been demonstrated only a few times, mostly in cold atom systems [102, 110, 111]. Unique experimental systems that exhibit both superradiance and subradiance can provide fundamental insights into the dynamics of complex open quantum systems, leading to multiple emerging applications including narrow linewidth superradiant lasers [112] and long-lived subradiant memories [113, 114].

4.2 System overview

We study an inhomogeneously broadened ensemble of Yb ions embedded in a crystal coupled to a nanophotonic cavity with high cooperativity. The cavity-mediated dissipation allow us to control the population distribution within the Dicke space [99] and observe many-body dynamics in the form of superradiance and subradiance (Fig. 4.1). The features of the observed dynamics are well explained by numerical simulations based on a many-body master equation. In the single-ion case, the Purcell effect enhances the ion's emission by increasing the decay rate by $4g^2/\kappa$ when coupled to a cavity. When an ensemble of ions is coupled to the same cavity, we will see that $4g^2/\kappa$ acts as a collective decay channel, ultimately leading to many-body dissipative dynamics.

Our system consists of an ensemble of Yb ions embedded in YVO_4, with approximately 10^6 ions coupled to a nanophotonic cavity (Fig. 4.1a). The cavity is tuned into resonance with $\lambda = 984$ nm optical transition of Yb, where the large cavity linewidth ($\kappa = 2\pi \times 44$ GHz) covers all three transitions aligned along the cavity polarization (A, E, I in Fig. 4.1). The narrow optical inhomogeneous linewidths ($\Delta_{\text{inh}} = 2\pi \times 150$ MHz) compared to the separation between those transitions (a few GHz) enables each transition to be addressed as independent two-level systems. The high ensemble cooperativity ($C_A = C_E = C_I/2 = 12$) opens a CIT window around the center of the inhomogeneous line and enables the investigation of the rich dynamics of a driven subensemble near the transparency window. This is because the effect of the off-resonant ions on the cavity field is cancelled, allowing more light to enter the cavity, and we will able to isolate the resonant ions. More details about the system parameters can be found in section 3.3.

4.3 Experimental observation and analysis

To probe the dynamics, we tune the laser to the center of the CIT, and detect the cavity emission after pulsed excitation (Fig. 4.2a). For state initialization, the system

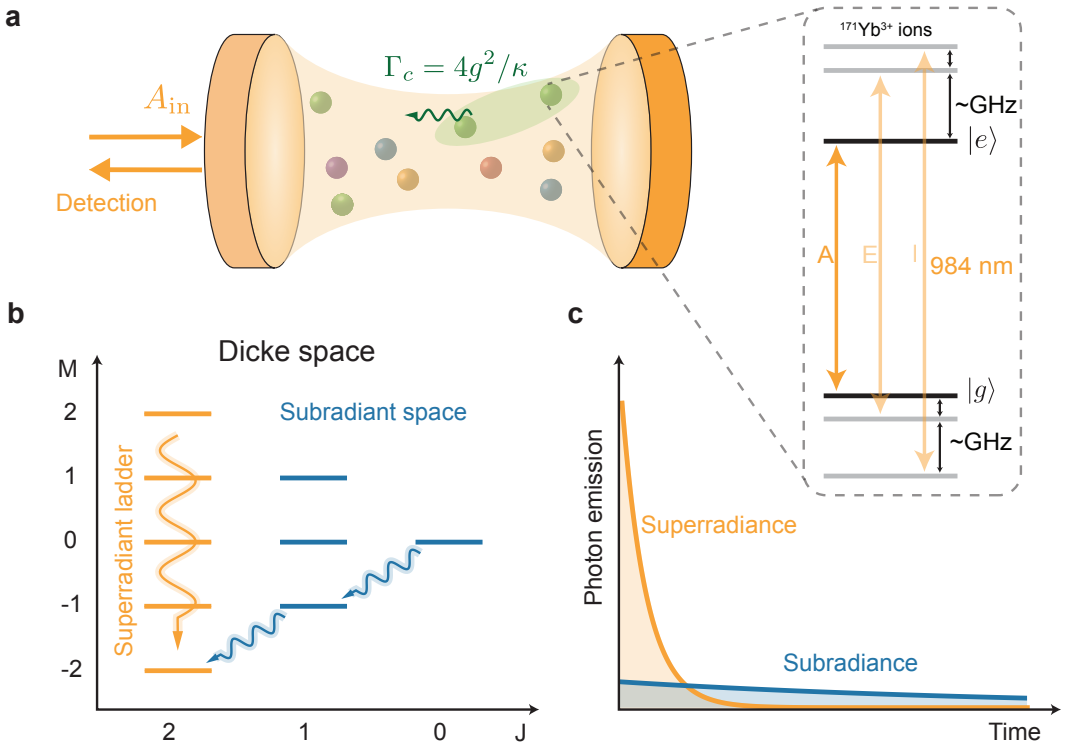

Figure 4.1: **Cavity-mediated suprradiance and subradiance. a,** Schematic description of the cavity-ion interaction. An inhomogeneous ensemble of ions is coupled to a one-sided cavity with total decay rate κ. The input field A_{in} is sent into the cavity, and the dynamics is detected through the same channel. The interaction strength between the cavity field and a single ion is g. Two spectrally indistinguishable ions have an effective cavity-mediated dissipation rate $\Gamma_c = 4g^2/\kappa$. Each Yb ion has an energy structure, as shown in the zoomed-in dashed frame. The A, E, and I transitions are around 984 nm and coupled to the cavity mode. Each transition, such as A, forms an effective two-level system, consisting of a ground state ($|g\rangle$) and an excited ($|e\rangle$) state. **b,** The Dicke space for 4 two-level systems in the $|J, M\rangle$ basis [115], where the $J = 2$ manifold forms the superradiant ladder and the rest form the subradiant subspace. **c,** Schematic of superradiance (orange) and subradiance (blue) which are enhanced (suppressed) decays where emissions from ions constructively (destructively) interfere.

is driven to a non-equilibrium steady state using a long pulse. Varying the excitation power prepares the system into different initial states, followed by distinct emission dynamics (Fig. 4.2b). Analyzing the peak counts of the emission, we find that the trend of peak counts with power is strongly non-monotonic, forming an S-shaped curve (Fig. 4.2c).

To systematically characterize the observed nonlinear dynamics, we classify three power regimes (I, II, III) based on the slope of the S-curve. In regime I with low powers, the decay is predominantly fast. A characteristic $1/e$ decay time is measured to be ≈ 150 ns, faster than the fastest expected Purcell decay of a single ion coupled to the cavity (≈ 1.4 μs, Fig. 4.2b inset). In regime II, with intermediate powers, both a fast and a slow decay compared to the Purcell-enhanced rate are observed. In regime III, with higher power, a continuum of different decay lifetimes are observed, leading to a stretched exponential decay.

To gain a microscopic understanding of this nonlinear power dependence, we use a master equation to describe driven dynamics in the presence of decoherence and dissipation. The numerical simulation of the entire inhomogeneous ensemble of $N \sim 10^6$ ions is not tractable. However, the phase cancellation in CIT negates the influence of the off-resonance ions on cavity field, which allows us to initially only consider the dynamics of the resonant ions. Additionally, we note that the cavity mediates photon exchange between ions, which triggers collective dissipation with rate proportional to $\Gamma_c = 4g^2/\kappa$ (section 4.5). As the system dissipation is dominated by Γ_c, a smaller number of ions that sit within a spectral window whose width is about Γ_c can be treated as indistinguishable ions. To this end, we first simulate a small-scale homogeneous ensemble. Specifically, we study a toy model of 6 identical ions whose dynamics can be described using the Dicke states, the coupled basis defined for indistinguishable two-level systems [99]. As shown in Fig. 4.1b and Fig. 4.3, vertical decays between the Dicke states are enhanced and superradiant, and diagonal decays are suppressed and can only decay through individual dissipation channels, which we call subradiance (section 4.6). To effectively capture the existence of multiple decay rates among the various Dicke states, as well as a clear separation between fast (superradiant) and slow (subradiant) decays, we employ a phenomenological stretched bi-exponential fit and extract the relevant fit parameters, which also clearly reveals the presence of the distinct three regimes discussed earlier (Fig. 4.2d).

By simulating this system's dynamics using the master equation, we find that the peak emission is a good indicator for the population distribution of the Dicke states

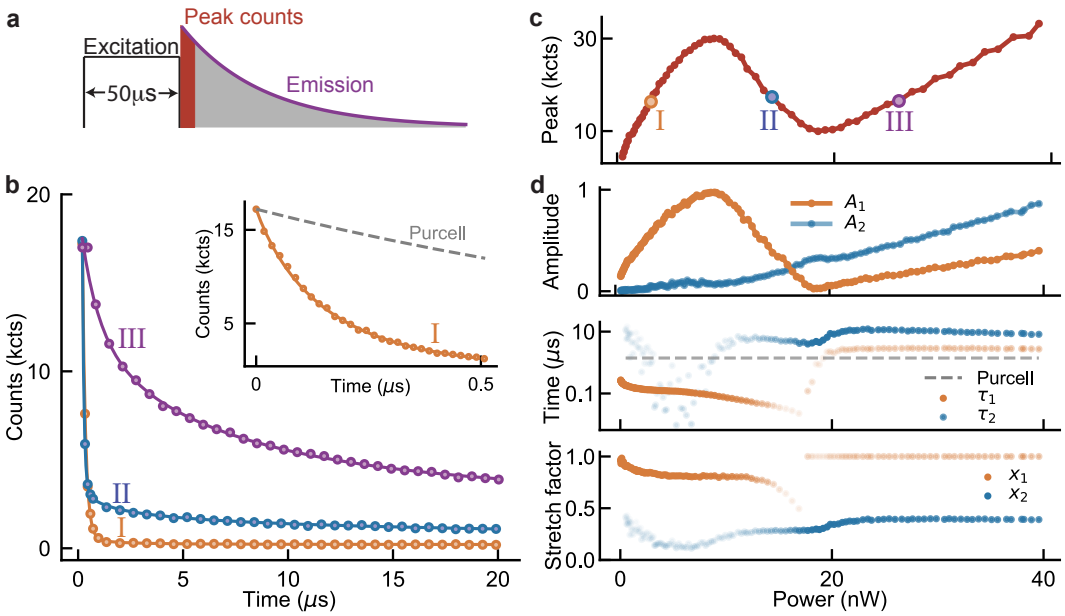

Figure 4.2: **Observation of dissipative many-body cavity emission. a,** Measurement schematic. After a 50 μs long excitation pulse, peak counts are obtained by integrating the counts within the first 128 ns. **b,** Three representative cavity emission time traces from each of the three power regimes with equal peak counts (3, 14, 26 nW). All traces are fit to a phenomenological stretched bi-exponential fit, $A_1 \exp[-(t/\tau_1)^{x_1}] + A_2 \exp[-(t/\tau_2)^{x_2}] + b$ (section 4.6). Inset: single exponential fit for the first 500 ns of the emission excited with 3 nW, with higher time resolution. The fitted decay lifetime of $\approx$ 150 ns (solid line) shows an enhancement beyond the fastest expected Purcell decay of $\approx$ 1.4 μs (gray dashed). **c,** Peak counts with varying excitation power. The three labelled points correspond to the data shown in b. **d,** Fit parameters, $A_{1,2}$, $\tau_{1,2}$, and $x_{1,2}$, of the time traces. The transparency of the data points in the decay times $\tau_{1,2}$ and stretch factors $x_{1,2}$ are weighted by their relative amplitudes $\frac{A_{1,2}}{A_1+A_2}$ to emphasize the significance of the parameters. In regime III (for powers greater than 20 nW), x_1 is set to 1, as there is no longer a distinct fast decay (section 4.6).

prepared by the drive (Methods). The simulated peak emission matches the trend measured in regimes I and II, where distinct temporal dynamics are attributed to decays from different parts of the Dicke space (Fig. 4.4). In regime I we attribute the fast decay to superradiance, dominantly from the collective dissipation within the superradiant ladder, as we expect to have populated only the low-excitation superradiant states within a narrow bandwidth of the ensemble (Fig. 4.5). From the measured fast decay rate, we estimate the number of ions participating in superradi-

[2]Note that the x-axis is different from what we presented in [88]. For this paper, we rescaled the x-axis to match the experiment for simplicity.

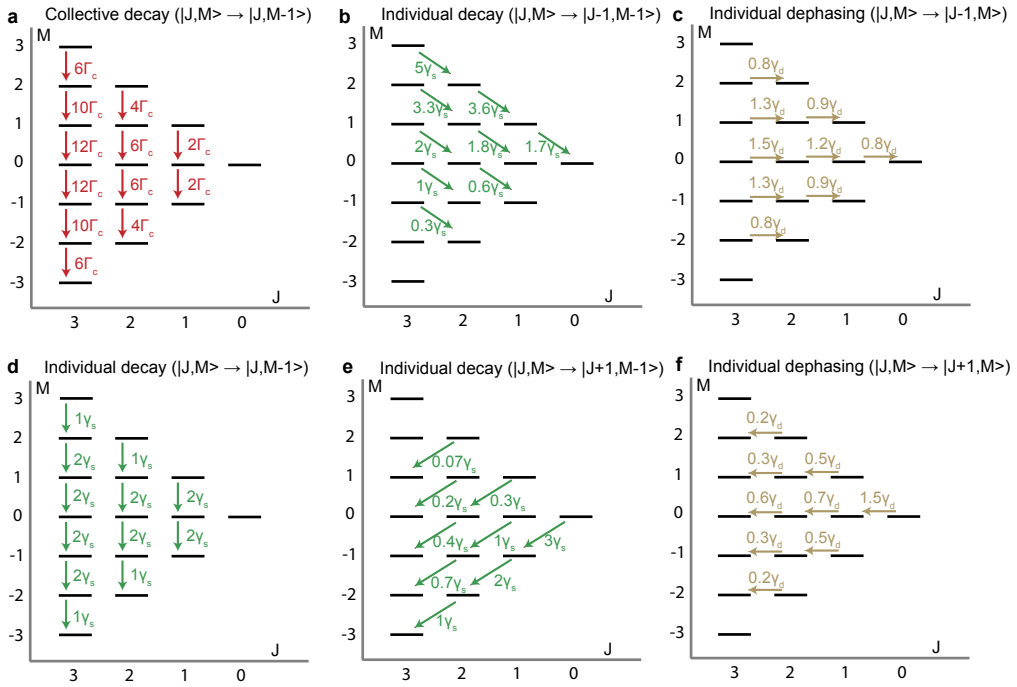

Figure 4.3: **Decay rates between Dicke states in a bad cavity regime [116].** Here, Dicke states are formed by 6 identical two-level systems. **a,** Collective decay (red) governed by $\Gamma_c = 4g^2/\kappa$ decays vertically, preserving total spin J. **b, d, e,** Individual decay (green) governed by spontaneous emission γ_s decays diagonally, and **c, f,** individual dephasing (beige) γ_d couples neighboring J states with the same M. With higher M, the diagonal decay rates are faster towards larger J, and slower towards smaller J.

ance to be on the order of ~ 50 (section 4.6). With increased power, we expect that the system climbs up the superradiant ladder and reaches Dicke states with larger decay rates, leading to even faster emission. This is consistent with the observed trend of decreasing τ_1 in regime I as shown in Fig. 4.2d. At even higher powers, strong driving of the superradiant ladder allows for significant population to diffuse into the subradiant space via decoherence processes, resulting in the slow decay observed in regime II (Fig. 4.5) [101, 102]. Populating multiple dark subradiant states exhibiting different decay rates manifests as a stretched exponential decay in the emission dynamics.

In regime III a completely mixed state of equal population in each Dicke state can be reached (Fig. 4.5). Further increasing the power excites more of the off-resonance ions, while the subensemble of the on-resonance ions addressed in regimes I and II remains in the completely mixed state. This leads to the emergence of interme-

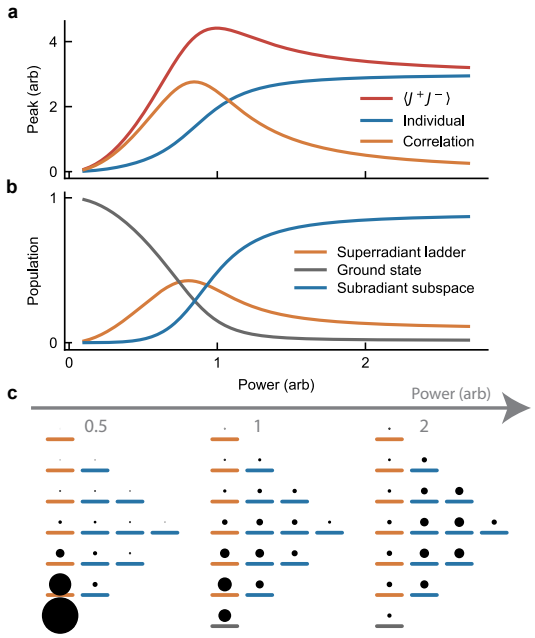

Figure 4.4: **Master equation simulation of dissipative many-body dynamics. a,** Simulation of 6 identical ions excited with a long (50 μs) pulse. The peak of total squared atomic polarization $\langle J^+J^-\rangle$ (red) is plotted as a function of excitation power along with individual (blue) and correlation (orange) terms from Eq. 4.11, where the peak amplitudes are calculated from the values right after the excitation pulse, to emulate the peak counts measurements. **b,** Simulated population dynamics of different subspaces in the Dicke basis as a function of excitation power. Note that the superradiant ladder here refers to all of the states in the $J = 3$ manifold except the ground state. We find that the evolution of the superradiant population with power aligns with the correlation term in **a**. **c,** Simulated Dicke state population distribution for different powers. The size of the black circles represents the relative population weights at the end of the excitation pulse. With low power (Power = 0.5 a.u., left), primarily the lower excitation superradiant ladder (orange bars) is populated. With increased power (Power = 1 a.u., middle), the subradiant subspace (blue bars) begins to populate, including the long-lived dark subradiant states. At high power (Power = 2 a.u., right) the system approaches a completely mixed state. Here, the population distribution appears to be unequal among the Dicke states due to the varying degeneracies of the states in the subradiant subspace.

diate decays, departing from the homogeneous Dicke subensemble picture, which suggests that a wider excitation bandwidth at high powers should be considered in numerical simulations. To this end, we simulate a larger number of emitters by including a Lorentzian distributed ensemble of ions with experimental inhomogeneous linewidth (Methods). Specifically, the dynamics of each subensemble is computed separately and incoherently added, by assuming that the subensembles

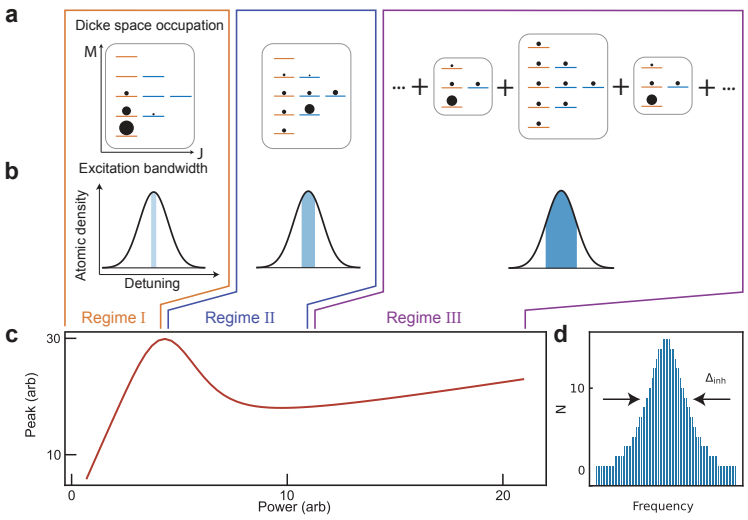

Figure 4.5: **Simulation of dissipative many-body cavity emission with $N = 569$ ions. a, b,** Schematics of excitation bandwidth and Dicke space occupation in the three power regimes. In regime I, only a narrow bandwidth is excited, and primarily the low-excitation superradiant states are occupied. In regime II, the bandwidth increases, and the subradiant subspace becomes populated. In regime III, the bandwidth further increases, and the off-resonant subensembles get excited while leaving the on-resonance subensemble in a completely mixed state. **c,** Master equation simulation of 91 subensembles of identical ions, for a total of $N = 569$ ions. Incoherently adding the peak emission of detuned subensembles qualitatively reproduces the S-curve observed in experiment (section 4.5)[2]. d. Subsensemble distribution, where each subensemble is separated by 5 MHz (inset).

are effectively non-interacting (more detail section 4.5 Fig. 4.9). The emergence of the upturn of the peaks counts at high powers is reproduced by the simulation (Fig. 4.5c), consistent with the experimental observation in regime III.

4.4 Control over coherent emission

To demonstrate control over the dissipative many-body dynamics, and to show further evidence of the beyond-single atom nature of the cavity emission, we first modify the decay dynamics by changing the number of ions. Specifically, we tune the number of ions resonant with our excitation laser N_{res} via optical hole burning, and then observe the changes in the S-curve (Fig. 4.6a,b). Upon increasing N_{res}, the S-curve shifts towards higher power in regimes I and II, along with an increase in the maximum of peak counts (Fig. 4.6c). The shift implies the formation of a larger superradiant ladder when the number of local homogeneous ions increases, which requires more excitation power to optically pump into the subradiant subspace

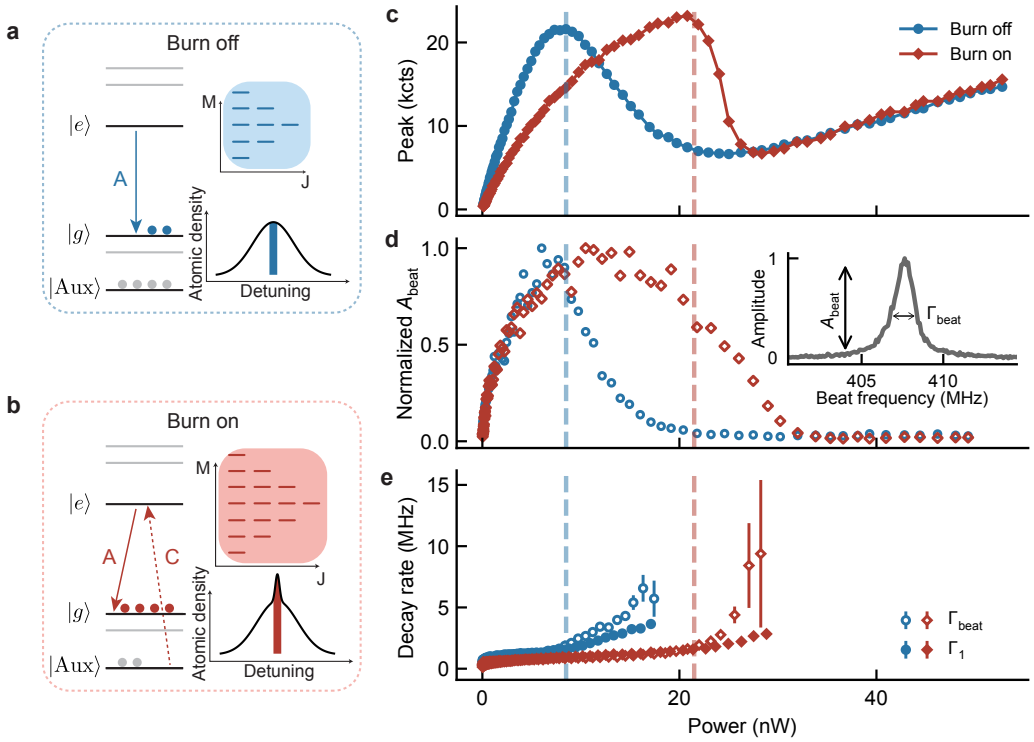

Figure 4.6: **Control and characterization of dissipative many-body dynamics via hole-burning. a,b,** Schematic representations of hole-burning (**a**: no hole burning, **b**: with hole burning). The C transition connects another state $|\text{Aux}\rangle$ in the ground-state manifold to the excited state $|e\rangle$. Optical pumping on the C transition transfers population from $|\text{Aux}\rangle$ to $|g\rangle$, introducing an anti-hole in the original distribution of the A transition. This increases the local ion density of the A transition at the probe frequency (colored thin bars), and expands the Dicke space (shaded areas). See Methods for the detailed description of the A, C transitions and the $|\text{Aux}\rangle$ state. **c,** Peak emission counts measured as a function of excitation laser power with (red) and without (blue) hole burning. S-curve shifts towards higher power when the burning is on. **d,** Normalized beat note amplitude A_{beat} for burning off (blue) and on (red). The two data sets are separately normalized, as the amplitude strongly depends on the local oscillator polarization, which can vary between experiments. Inset shows the experimental characterization of width Γ_{beat} and amplitude A_{beat} of a beat signal from a heterodyne measurement (Methods). **e,** Single exponential fit Γ_1 (filled markers) from the time-dynamics measurement and extracted width Γ_{beat} from a Lorentzian fit (open markers) from coherence measurements for burning off (blue) and on (red). Error bars represent standard errors of the fits. In b-d, vertical dotted lines indicate the turning points between regimes I and II.

(section 4.6). However, regime III is observed to be largely insensitive to a change in N_{res}, as indicated by the overlap of the S-curves, since spectral hole-burning only changes the population locally in frequency without affecting the number of detuned ions as illustrated in Fig. 4.6b.

We provide additional evidence of the traversal of the Dicke space by measuring the coherence of the emission via heterodyne detection (Methods). The beat-note between the emission and the excitation laser provides the rate and amount of coherent decay through its width Γ_{beat} and amplitude A_{beat}, respectively (Fig. 4.6d, inset). We first note the rise of A_{beat} in regime I, indicating the increase in population of the superradiant ladder. Later, A_{beat} decreases in regime II, corresponding to the incoherent coupling to the subradiant subspace. Finally in regime III, A_{beat} vanishes because of the absence of coherent decay, as the population has undergone incoherent processes to reach the completely mixed state.

Since only decays within the superradiant ladder are coherent with respect to the excitation, Γ_{beat} represents the rate of superradiance within the superradiant ladder. For comparison, we extract the fast decay part of the time dynamics of photon emission as a single exponential with the rate Γ_1, which captures all of the enhanced decays from both superradiant and subradiant subspaces (Fig. 4.6e, filled markers). The comparison between Γ_{beat} and Γ_1 can then be used to evaluate the relative decay contributions from the two subspaces. We find that Γ_1 overlaps with Γ_{beat} for low powers, confirming that all of the fast decays in regime I are within the superradiant ladder. However, entering regime II, Γ_1 deviates from Γ_{beat} (for powers beyond dashed lines in Fig. 4.6e). This observation of $\Gamma_1 < \Gamma_{\mathrm{beat}}$ in regime II indicates that Γ_1 also includes some incoherent decays slower than Γ_{beat}, which point to the enhanced decays within the subradiant subspace (Fig. 4.3a).

Lastly, we vary the frequency of the probe laser near the A transition to control the number of driven ions and observe that the nonlinear S-curve shifts in the expected direction (Fig. 4.7). We can also extend this variation of frequency to cover all the transitions (Fig. 4.8). The laser frequency is swept from the lower frequency side of the A transition to the higher frequency side of I. In Fig. 4.8a we plot the reflected pulse amplitude and in Fig. 4.8b we show the integrated total emission counts. There are two aspects of the plot in Fig. 4.8b. Firstly, we find three tall peaks corresponding to A, E, and I. Zooming into one of these transitions, we can see that the spectral width of the emission is narrower than the inhomogeneous linewidth of the ensemble, and resembles more a flat top rather than a Gaussian/Lorentzian

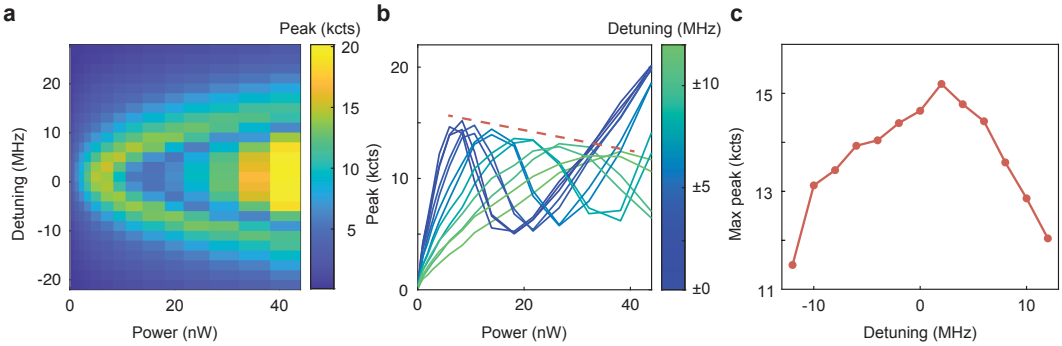

Figure 4.7: **Frequency and power dependence of peak counts. a,** Peak counts with excitation power and laser detuning. We repeat the pulsed excitation measurement at different frequencies along the inhomogeneous line in the A transition, and observe that the S-curve shifts to higher power. **b,** Horizontal cuts of **a** at different detunings. Red dashed line indicates the maximum peak counts for different detunings. **c,** Extracted local maximum of peak counts as a function of laser detuning. The maximum of peak counts decreases with increased detuning from the center. We note that this behavior differs from Fig. 4.6c, where while the S-curve also shifted towards higher powers, the maximum of peaks counts *increased* with laser detuning. Here, the S-curve shifts towards higher powers because of the CIT profile; as the laser is detuned from the center, less power enters the cavity, resulting in effectively more power being required to excite the ions. At the same time, the *decrease* of the maximum of peak counts indicates there are less ions resonant with the laser when detuned from the center.

(see zoom in of Fig. 4.8b). This is because CIT creates a transparency window in the center of the inhomogeneous line, allowing more light to enter through that window. Thus, the CIT shapes the incoming light with width approximately equal to the CIT width (zoom in for Fig. 4.8a). Secondly, between the A and E, and E and I transitions, at detuning around 1.5 and 5.5 GHz, there are elevated counts where there are no resonant ions. This is related to the phase cancellation effect observed in CIT. Specifically, when there are balanced ions on either side of the laser frequency, more light can enter the cavity, resulting in enhanced off-resonant excitation for the same input power.

Similar to CIT, we have also confirmed that the experimental findings for sub- and superradiance are reproducible and consistent with our theoretical predictions, independent of the choice of the optical emission lines between the A, E, and I transitions. All of these complementary experiments lend strong support to our microscopic understanding and control of an inhomogeneous ensemble.

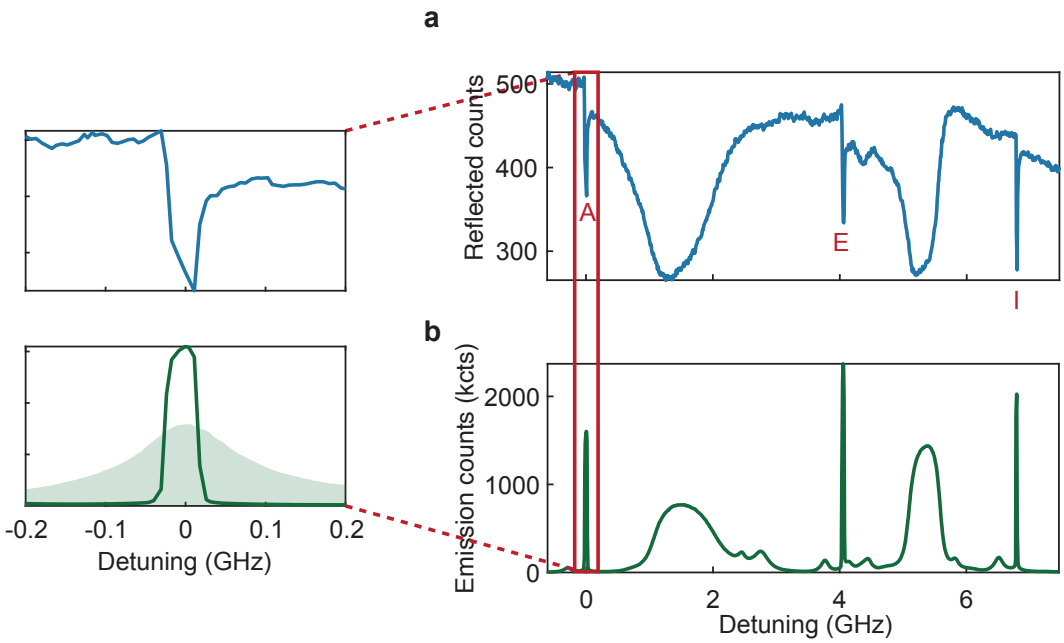

Figure 4.8: **Cavity emission and reflection of the entire spectrum.** Pulsed excitation with 47 nW as a function of laser detuning, where the **a,** reflected pulse amplitude and **b,** integrated emission counts after the pulse are extracted. The x-axis denotes the laser detuning relative to A transition. The other sharp peaks at ~ 4 and ~ 7 GHz correspond to E and I transitions, respectively. The green shaded area indicated the inhomogeneous ion distribution, clearly showing that the emission is nonlinear and narrower than the ion distribution due to phase cancellation.

4.5 Theoretical modelling for dynamics

Master equation formalism

For simulating the dynamics of a driven inhomogeneous ensemble, we use the same Hamiltonian in Eq. 3.2, and introduce various dissipative mechanisms through the Lindblad operators:

$$\mathcal{L}_{\text{cav}} = \kappa(a\rho_t a^\dagger - \frac{1}{2}a^\dagger a\rho_t - \frac{1}{2}\rho_t a^\dagger a) \tag{4.1}$$

$$\mathcal{L}_{\text{em}} = \gamma_s \sum_{j=1}^{N}(\sigma_j^- \rho_t \sigma_j^+ - \frac{1}{2}\sigma_j^+\sigma_j^-\rho_t - \frac{1}{2}\rho_t\sigma_j^+\sigma_j^-) \tag{4.2}$$

$$\mathcal{L}_{\text{deph}} = \gamma_d \sum_{j=1}^{N}(\sigma_j^z \rho_t \sigma_j^z - \frac{1}{2}\sigma_j^z\sigma_j^z\rho_t - \frac{1}{2}\rho_t\sigma_j^z\sigma_j^z) = \gamma_d \sum_{j=1}^{N}(\sigma_j^z \rho \sigma_j^z - \rho_t) \tag{4.3}$$

where $\mathcal{L}_{\text{cav}}$ is the cavity dissipation, $\mathcal{L}_{\text{em}}$ is the free-space spontaneous emission, $\mathcal{L}_{\text{deph}}$ is the local dephasing, and ρ_t is the total density operator consisting of cavity field and the atoms.

We operate in the fast cavity limit, where $\kappa \gg g, \gamma_s, \gamma_d$, and adiabatically eliminate the cavity mode by setting $\dot{a} = 0$ (Appendix A). This allows us to replace the cavity field operator a with atomic operators as:

$$a = \frac{-i \sum_{j=1}^{N} g_j \sigma_j^- - \frac{\kappa}{2}\sqrt{\mu}}{i\Delta_c + \frac{\kappa}{2}}. \tag{4.4}$$

We then rewrite H and $\mathcal{L}_{cav}$ to H_{at} and $\mathcal{L}_{\text{col}}$ (collective dissipation) in terms of atomic operators[3]:

$$\begin{aligned} H_{\text{at}} = -\frac{\Delta_c}{(\kappa/2)^2 + \Delta_c^2} \sum_{j=1}^{N} g_j \sigma_j^+ \sum_{k=1}^{N} g_k \sigma_k^- + \frac{1}{2} \sum_{j=1}^{N} \Delta_j \sigma_j^z \\ - \sum_{j=1}^{N} \frac{g_j \kappa \sqrt{\mu}}{2} \left(\frac{\sigma_j^+}{\kappa/2 + i\Delta_c} + \frac{\sigma_j^-}{\kappa/2 - i\Delta_c} \right) - \frac{\mu \Delta_c \kappa^2}{4\Delta_c^2 + \kappa^2} \end{aligned} \tag{4.5}$$

$$\mathcal{L}_{\text{col}} = \frac{\kappa}{(\kappa/2)^2 + \Delta_c^2} \sum_{j,k}^{N} g_j g_k (\sigma_j^- \rho \sigma_k^+ - \frac{1}{2}\sigma_j^+ \sigma_k^- \rho - \frac{1}{2}\rho \sigma_j^+ \sigma_k^-). \tag{4.6}$$

We can further simplify H_{at} and $\mathcal{L}_{\text{col}}$ by noting that κ is large and the cavity is tuned to be on resonance with our atomic transition ($\Delta_c \to 0$) as[4]:

$$H_{\text{at}} \approx \frac{1}{2} \sum_{j=1}^{N} \Delta_j \sigma_j^z - \sum_{j=1}^{N} g_j \sqrt{\mu} (\sigma_j^+ + \sigma_j^-) \tag{4.7}$$

$$\mathcal{L}_{\text{col}} \approx \frac{4}{\kappa} \sum_{j,k}^{N} g_j g_k (\sigma_j^- \rho \sigma_k^+ - \frac{1}{2}\sigma_j^+ \sigma_k^- \rho - \frac{1}{2}\rho \sigma_j^+ \sigma_k^-). \tag{4.8}$$

The system master equation now reads:

$$\dot{\rho} = -i[H_{\text{at}}, \rho] + \mathcal{L}_{\text{col}} + \mathcal{L}_{\text{em}} + \mathcal{L}_{\text{deph}}. \tag{4.9}$$

Here $\mathcal{L}_{\text{em}}$ and $\mathcal{L}_{\text{deph}}$ can be reduced to the many-body atomic density operator ρ, obtained by taking the trace over the cavity field subspace.

However, since this requires atoms to be identical, we stick to the full simulation in cases where we add inhomogeneities or want to look at correlations between ions.

[3] We note that Eq. 4.5 represents the correct form of the atomic Hamiltonian, while the same expression shown in Eq. S51 in [88] contains some typos.

[4] We note that Eq. 4.7 represents the correct form of the atomic Hamiltonian under $\Delta \to 0$, while the expressions shown in Eq. 10 and Eq. S53 in [88] both contain a typo, specifically a missing square root.

Master equation simulations of dynamics

For modelling the dynamics, we solve the master equation in Eq. 4.9 using QuTIP [117]. Assuming ions with identical coupling strengths g, we have:

$$\mathcal{L}_{\text{col}} = \Gamma_c (J^- \rho J^+ - \frac{1}{2} J^+ J^- \rho - \frac{1}{2} \rho J^+ J^-) \tag{4.10}$$

where $J^{\pm} = \sum_{j=1}^{N} \sigma_j^{\pm}$ is the collective atomic coherence and $\Gamma_c = 4g^2/\kappa$ is the Purcell-enhanced decay rate of a single ion. Here, Γ_c describes the cavity-mediated collective dissipation rate among ions, defining an effective spectral bandwidth within which the ions are considered to be indistinguishable. Hence, we simulate a mesoscopic, homogeneous ensemble to aid in the qualitative understanding of our system dynamics.

In simulating our system, we must first establish a connection between experimental measurements and simulatable quantities. We note that the peak counts reflects the cavity population at the end of the excitation pulse (section 4.5). In the fast-cavity regime, and in the absence of an input field, the cavity population depends on the atomic states as $\langle a^\dagger a \rangle = \Gamma_c \langle J^+ J^- \rangle$, where $\langle J^+ J^- \rangle$ can be written as:

$$\langle J^+ J^- \rangle = \underbrace{\sum_{i=1}^{N} \langle \sigma_i^+ \sigma_i^- \rangle}_{\text{Individual}} + \underbrace{\sum_{i \neq j}^{N} \langle \sigma_i^+ \sigma_j^- \rangle}_{\text{Correlation}} . \tag{4.11}$$

Here the first term is the sum of the emission of individual ions, and the second term represents the correlation between different ions. We simulate different parts in Eq. 4.11 with a toy model of 6 identical ions with experimental coupling and dissipation rates (Fig. 4.4a). The trend of $\langle J^+ J^- \rangle$ indeed qualitatively matches the experimental observations for regimes I and II. The initial increase of $\langle J^+ J^- \rangle$ is due to the build-up of positive correlations, or superradiance. With higher power, the correlations decrease, due to an increase of population in the subradiant subspace. This is substantiated by the evolution of the population in the superradiant and subradiant subspaces with power (Fig. 4.4b, c).

While the modelling of a small, homogeneous ensemble qualitatively captures the experimental behavior in regimes I and II (Fig. 4.4a), regime III cannot be modelled in this way. To this end, we include some frequency inhomogeneity to our model to capture the fact that as we increase power, we increase our excitation bandwidth, and thus excite more ions detuned from the laser. In order to incorporate more ions in our

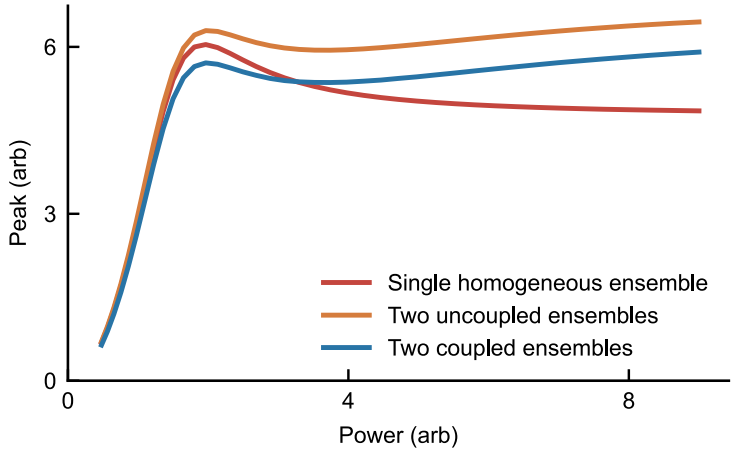

Figure 4.9: **Comparison of simulated uncoupled and coupled ensembles.** Master equation simulation of the peak counts with power for a single homogeneous ensemble of 5 ions (red), two *coupled* subensembles of 5 ions at 0 MHz and 2 ions detuned by 5 MHz (blue), and two *uncoupled* subensembles of 5 ions at 0 MHz and 2 ions detuned by 5 MHz (orange). Here uncoupled refers to the fact that the peak emission is simulated separately for the subensembles of 5 and 2 ions, and later added together. Note that the peak emission reflects the cavity population $\langle a^\dagger a \rangle$ (Methods). The qualitatively similar behavior of the uncoupled and coupled subensemble cases motivates the simulation of an inhomogeneous ensemble via incoherent addition of many uncoupled smaller subensembles in Fig. 4.5c.

simulation, we first exploit the permutational symmetry of identical particles using Permutational Invariant Quantum Solver (PIQS, [118]) to decrease our computation time, allowing upwards of 30 identical ions to be readily simulated.

Additionally to incorporate inhomogeneity, we would ideally like to approximate sufficiently detuned ions as separate ensembles whose contribution to the cavity population $\langle a^\dagger a \rangle$ can be incoherently summed. To this end we compare two cases with 7 ions in Fig. 4.9. One case is simulating the full system of 7 ions, with 2 ions detuned by 5 MHz. Another case is the incoherent addition of 5 ions on resonance and 2 ions detuned by 5 MHz, where each system is solved separately and the peak emission summed after. While there is an offset in the values of the peak emission at certain powers, the qualitative behavior remains the same.

Combining the above two assumptions, we simulate an inhomogeneous ensemble of ions following a Lorentzian distribution. We indeed qualitatively reproduce the experimentally observed behavior in regime III, where the excitation of off-resonant ions leads to the increase of peak emission at high powers, giving rise to the nonlinear S-shaped profile.

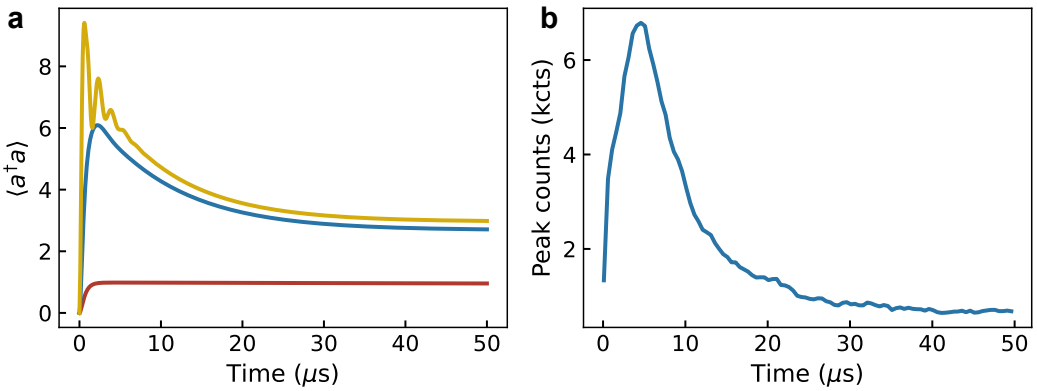

Figure 4.10: **Excitation pulse length dependence. a,** Simulation of the cavity field population $\langle a^\dagger a \rangle$ during a 50 μs pulse applied to a system of $N = 6$ identical ions, for different powers. The power increases from red (0.6 a.u.) to blue (1 a.u.) to yellow (1.5 a.u.) curves. Regardless of the power, here 50 μs is long enough for the cavity to enter steady state. **b,** Experimental data for pulse length dependence of peak counts, with 10 nW of power, showing steady-state behavior at 50 μs.

Excitation pulse length dependence

Here we study the non-steady state regime where the driving pulse length is short. We first theoretically investigate the atomic states during the driving period. In the case of 6 identical atoms, we plot the normalized cavity mean photon number $\langle a^\dagger a \rangle \propto \langle J^+ J^- \rangle$ during the drive for three different powers (Fig. 4.10a).

For a low drive (Fig 4.10a, red), we see that $\langle a^\dagger a \rangle$ quickly and monotonically increases to reach steady state. The steady-state population at this power consists primarily of lower excitation states, as the system is unable to be excited into the higher Dicke state manifolds. As we increase our drive, we see the appearance of Rabi-like oscillations among the Dicke states (Fig. 4.10a, yellow) and then a decay into steady state. The origin of this decay is two-fold: one is the dampening of the oscillations. This is due to collective decays (which go as g^2/κ) that drive the system towards equal population within a single vertical Dicke ladder. In other words, even in the absence of individual decay and dephasing, collective emission will spread the population out evenly among the superradiant states, leading to damped oscillations. Another decay type is the overall decay of the magnitude of $\langle a^\dagger a \rangle$. This is due to the coupling to the subradiant subspace through individual decay and dephasing, similar to the experimentally observed decrease in peak counts with power in regime II.

We explore this experimentally by measuring the excitation pulse length dependence

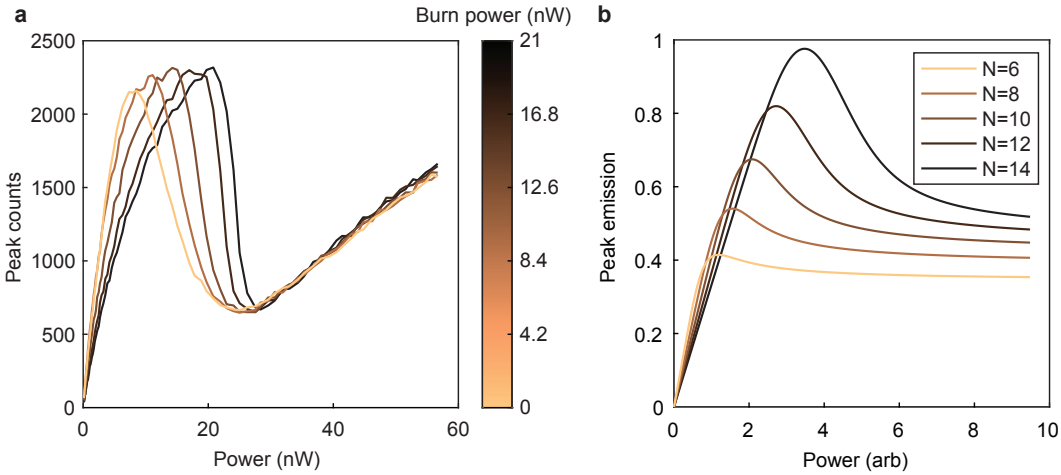

Figure 4.11: ***N*-dependence of S-curve. a,** Extended data of Fig. 4.6c, showing more burning powers. For higher burning power, N_{res} is larger and S-curve shifts towards the higher probe power. **b,** Simulation of varying ion number for the S-curve, showing a shift of the S-curve to higher powers. We find that, as expected, the turning point between regimes I and II shifts towards larger power, as our Dicke space expands and it requires more power to populate the subradiant subspace. As a result, at smaller powers, larger number of ions will have smaller peak emission, while the global maximum of peak emission increases for more ions.

of peak counts, shown in Fig. 4.10b. We find a qualitative match to the simulation of the initial build up of photons as we populate the superradiant states, and then a decay towards a steady state as we pump into the subradiant subspace. However, despite increasing the pump power, we do not observe the oscillations seen in Fig. 4.10a for high power (yellow). We attribute this to an averaging effect over our ensemble, as the oscillation frequency depends on g and ion detuning, both inhomogeneous in our system.

N-dependence of S-curve

Using PIQS, we simulate the dependence of the S-curve with varying system size N (Fig. 4.11b). We find that as expected, the turning point between regimes I and II shifts towards larger power, as our Dicke space expands and it requires more power to populate the subradiant subspace. As a result, at smaller powers, larger number of ions will have smaller peak emission, while the global maximum of peak emission increases for more ions. This qualitatively matches what we see in the experiment (Fig. 4.11a). We note that regime III is not reproduced in this simulation as we do not consider the detuned ions.

4.6 Methods

Considering the complexity of the experiment and simulation results, we will provide more details on the experimental setup, decay data fitting method, and additional analysis.

Experimental setup

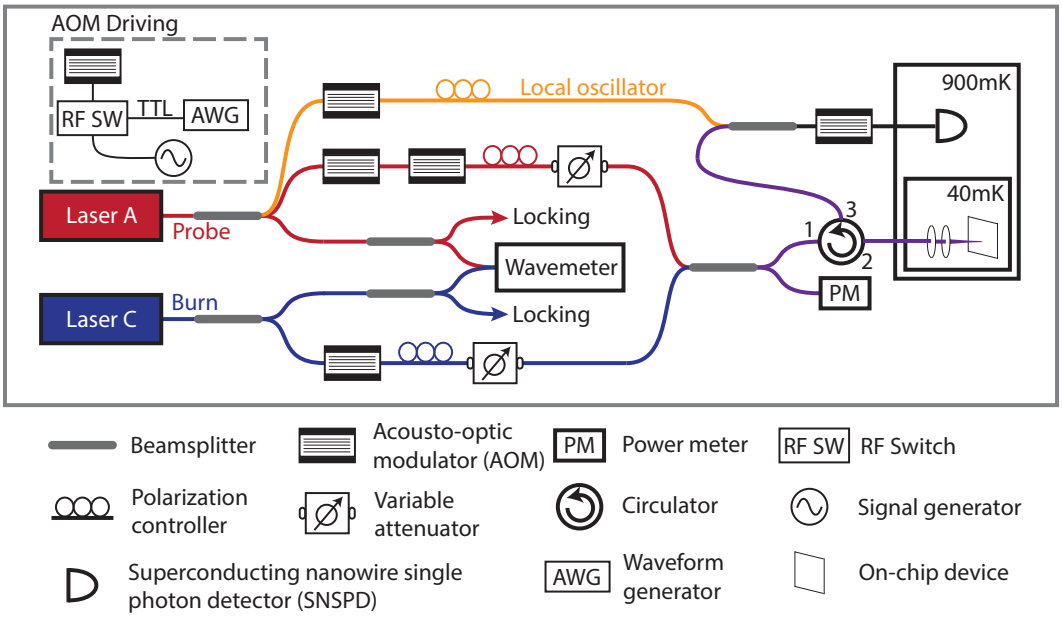

Figure 4.12: **Experimental Setup.** Laser A addresses the A transition. Optical pulses are generated using AOMs, which are driven with gated RF sources. Part of it can be split off for use as a local oscillator for heterodyne measurements. A second laser, Laser C can be used to perform optical hole burning on the C transition. The combined light is sent through a circulator, to the device, and the reflected light is sent to a superconducting nanowire single photon detector for time-resolved photon counting.

The optical setup for the experiments is shown in Fig. 4.12. Not all parts of the setup are used in all of the measurements. The lasers addressing transitions A and C are both Toptica DL Pro, tunable around 980 nm. Both lasers can be frequency locked (not shown in Fig. 4.12) to a stable reference optical cavity using the Pound-Drever-Hall method, and we measure a laser linewidth of approximately 600 Hz over 10 μs using the delayed homodyne method. The lasers can also be frequency-swept by modulating the internal piezo-electric actuator. In this mode the laser is free-running, where the linewidth is measured to be 50 kHz, with a slower drift in the center frequency on the order of a few MHz over tens of seconds. A Thorlabs S130 photodiode power sensor is used to measure excitation powers. The actual

powers that reach the cavity are calibrated by measuring round-trip losses from the cavity. We measure approximately 10% of the light reaches the device, including the angled coupler efficiency of $\approx 25\%$. However, we note that due to slight differences between measurements of the laser polarization and device coupling, there is likely slight discrepancies in all calibrated powers.

Acousto-optic modulators (AOMs) are used to gate optical pulses for pulsed measurements. Two AOMs are used in series for the probe laser giving an extinction of ≈ 100 dB. The light is sent to the device via an optical circulator (Precision Micro-Optics), and focused onto the angled coupler with an aspheric lens doublet, which is mounted on a 3-axis piezo nano-positioner stack (Attocube) for fine alignment. The device itself is mounted on the mixing chamber plate of a Bluefors dilution refrigerator with a base temperature of around 40 mK with no external magnetic field applied. The reflected signal from the circulator is sent to a superconducting nanowire single photon detector (SNSPD) held at 900 mK, and photon counts are time-tagged with a Swabian Time Tagger 20. A gating AOM is used before the SNSPD to selectively attenuate the intense reflected input pulses.

The coherence measurements of the cavity emission were taken by splitting off part of the input laser as a local oscillator to beat with the emission [119]. The beat signal was subsequently detected by the SNSPD and Fourier transformed to obtain the power spectra. All of the RF drives used to drive the AOMs were phase synchronized. To maximize the signal-to-noise ratio, it is desirable to integrate for a long time. However, long integration time requires phase stability of all of the parts of the experiment, particularly the fibers. Due to this, we found that an integration time of 1 second provides sufficient signal-to-noise ratio while maintaining the phase stability. To further improve the signal-to-noise ratio, we repeatedly integrated the signal for 1 second and averaged the power spectra. An example of the power spectra is shown in Fig. 4.6d inset, where the beating frequency is around 408 MHz, given our chosen frequency difference between our probe and local oscillator.

Decay data fits method

To characterize the power-dependent, non-single exponential decay profiles in Fig. 4.2, we employ the following phenomenological stretched bi-exponential fit

$$y(t) = A_1 \exp[-(t/\tau_1)^{x_1}] + A_2 \exp[-(t/\tau_2)^{x_2}] + b \tag{4.12}$$

with a fast stretched exponential decay with time constant τ_1, amplitude A_1, and stretch factor x_1 and a slower stretched exponential decay with time constant τ_2,

amplitude A_2, stretch factor x_2, and background b. The fit parameters (Fig. 4.2d) reflect the distinct decay behaviors in each of the three regimes consistent with the observations in Figs. 4.2b and 4.2c. In particular, we see a clear transition in the fitted decay time from superradiance to subradiance at around 20 nW of power, as there is an emergence of slow decay (τ_2) and increase of τ_1.

Here we provide justification for the above fitting function (Eq. 4.12). To find the best fit, one could start with a naive guess of a bi-exponential, to capture the superradiant and subradiant decays. A representative curve with a bi-exponential fit is shown in Fig. 4.13a. We see that the fit fails due to the strong multi-exponential nature of the subradiant decay. We then try a single stretched exponential fit in Fig. 4.13b. However, we still see that the fit fails at the crux between the slow and fast decay, shown in the inset.

To capture both the multi-exponential fast and slow decay, we now attempt a fast stretched exponential + slow stretched exponential (Fig. 4.13c). In particular, the fit function is $A_1 \exp[-(t/\tau_1)^{x_1}] + A_2 \exp[-(t/\tau_2)^{x_2}] + b$, where there is a fast decay with subscript 1 and slower decay with subscript 2. We find that this fits the data well in all power regimes, and most importantly does so with fit parameters that match our qualitative expectations from the picture provided in Fig. 3f in the main text. Additionally, while there are 7 fit parameters, we take several steps to minimize any overfitting of the data. First, the background b is set to be the count level at a time much longer than the longest observed lifetime, essentially the dark counts and any leakage through our setup. Second, the existence of two decays is only relevant in regime II where there is a clear distinction between a fast and slow decay. In both regime I (III), the fast (slow) decay component is dominant over the other, effectively resulting in just a single stretched exponential.

We note that we employ two different data taking methodologies to capture both the fast decay (which requires fine timing resolution at the nanosecond level) and the slow decay (which requires data out to 100s of microseconds after the excitation). To first capture the fast decay, we zoom into the first few microseconds of the decay with 1 ns resolution. This allows us to fit the decay to a stretched exponential in regimes I and II. At the same time, a separate data set with a timing resolution of 128 ns is taken such that we can probe out to longer timescales. We use this data set to fit the slow decay in blue. However in regime III, as shown in Fig. 3b, the decay is smoother without a clear distinction between fast and slow decay. Because of this we only use the 128 ns timing resolution dataset, and force $x_1 = 1$ as here the fast

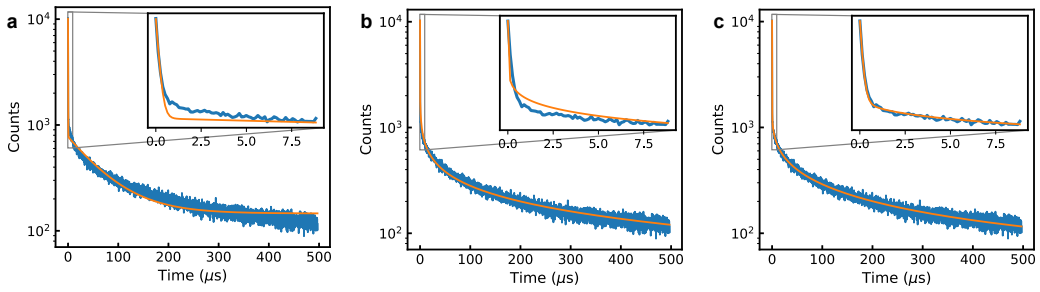

Figure 4.13: **Fit function justification.** Fit of an emission curve to a **a,** Bi-exponential, **b,** Stretched exponential, and **c,** Addition of two stretched exponentials. The blue and orange lines are from experiments and fits, respectively. Insets show early-time comparisons between the data and the fits.

decay simply samples the fastest decay in the smooth, multi-exponential profile.

Dicke states

The Dicke states can be described in the $|J, M\rangle$ basis, with $J = [N/2,\ N/2 - 1,\ ...]$ $(J \geq 0)$ and $M = [-J,\ -J + 1,\ ...,\ J]$, where M is is the projection quantum number associated with the number of atomic excitations (Fig. 4.1b). The states with maximum J are symmetric under permutation of atoms, forming the so-called superradiant ladder. Decays between states with the same J (Fig. 4.3a) are all collectively enhanced beyond Γ_c, and in particular, we call such decays within the superradiant ladder superradiance. Meanwhile, any process that does not conserve J is forbidden by symmetry to occur collectively, and must occur via individual dissipation such as spontaneous emission (Fig. 4.3b, d, e) or dephasing (Fig. 4.3c, f) [116]. Since the system starts in the ground state and the coherent laser drives the system up the superradiant ladder, the states with $J < N/2$, which form the subradiant subspace, can only be populated through decoherence. In particular, the states $|J, -J\rangle$ in the subradiant subspace cannot collectively decay, and thus are the long-lived dark subradiant states.

Here we also clarify our reasoning for the nomenclature used for the Dicke states. The superradiant ladder is comprised of the states with $J = N/2$, and decays between them are all superradiant. Technically, Dicke defined the $J = N/2, M = 0$ state to be the superradiant state [99], however for our purposes we consider all of the enhanced, coherent decays within the ladder to be superradiant as they are enhanced beyond the single-atom decay. Meanwhile, the subradiant subspace is defined as the space formed by the rest of the states, as such states cannot be driven collectively

with a coherent drive. We note that decays within the subradiant subspace are not always slower than Γ_c. In fact, all of the decays within the same J are faster than Γ_c even in the subradiant subspace, as shown in Fig. 4.3a for $J \leq 2$.

Strictly speaking, subradiance is defined as inhibition of emission due to the destructive interference among indistinguishable emitters. By this definition, subradiant decay is forbidden and cannot be observed. However, there are some processes that can break subradiance in order for us to observe that there was suppression of decay. Hence, the experimentally observed slow decay is due to dephasing and individual spontaneous emission processes from the dark subradiant states ($J < N/2, M = -J$). For simplicity, in the main text we refer to this decay as subradiant decay or subradiance, as they provide evidence of subradiance.

Comparison to the saturation effect

An increase and subsequent decrease in emission can also occur due to the saturation of the atomic coherence (below, saturation effect), which occurs even for a single atom and is unrelated to the Dicke model. Here, we will show that we do not see the saturation effect, and explain the difference and the connection to the saturation effect. First, let us consider the single ion case, where we have already derived the analytical solution in Eq. 3.12 and Eq. 3.13.

We can see that the intensity of the coherence ($|\sigma^-|^2$) first increases and then decreases with power where power $P \propto g^2\mu$. However, what is measured from cavity emission is

$$\langle a^+ a^- \rangle = \frac{4g^2 \langle \sigma^+ \sigma^- \rangle}{\kappa^2} = \frac{4g^2}{\kappa^2} \frac{(\langle \sigma^z \rangle + 1)}{2}. \tag{4.13}$$

Here we have applied Eq. 3.11 and the commutation rule. Then, by plotting both $|\sigma^-|^2$ and $|\frac{\sigma_z+1}{2}|$, we can see that while $|\sigma^-|^2$ has the non-monotonic trend, our measure $|\frac{\sigma_z+1}{2}|$ does not (Fig. 4.14). In other words, since we are not directly measuring the coherence by detecting the cavity emission, our S-curve cannot be explained by saturation of coherence.

Once we move to the multiple ions case, the measure becomes $\langle a^+ a^- \rangle = \frac{4g^2 J^+ J^-}{\kappa^2}$,

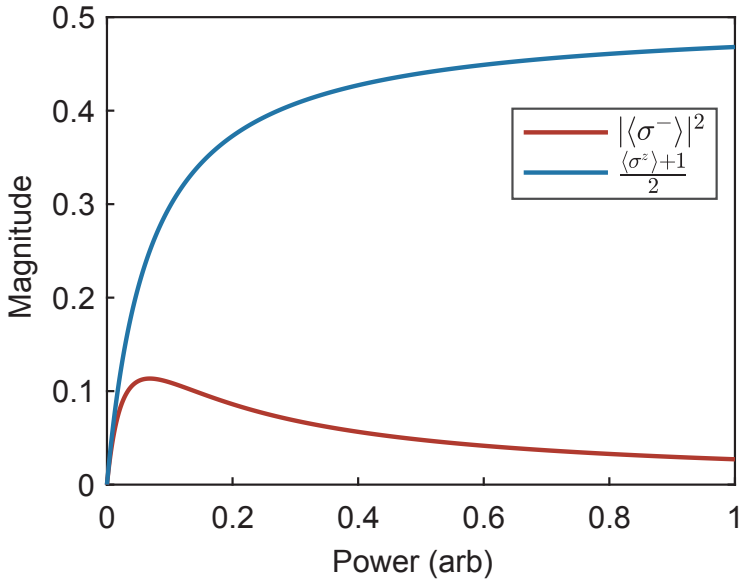

Figure 4.14: **Comparison to the saturation effect.** Comparison between excited state population, $|\frac{\langle\sigma_z\rangle+1}{2}|$, and the intensity of coherence, $|\langle\sigma^-\rangle|^2$, of a single atom as a function of excitation power.

thus

$$\langle a^+a^-\rangle = \frac{4g^2}{\kappa^2}\left(\underbrace{\sum_{i=1}^{N}\langle\sigma_i^+\sigma_i^-\rangle}_{\text{Individual}} + \underbrace{\sum_{i\neq j}^{N}\langle\sigma_i^+\sigma_j^-\rangle}_{\text{Correlation}}\right) = \frac{4g^2}{\kappa^2}\left(\underbrace{\sum_{i=1}^{N}\left(\frac{\langle\sigma_i^z\rangle+1}{2}\right)}_{\text{Individual}} + \underbrace{\sum_{i\neq j}^{N}\langle\sigma_i^+\sigma_j^-\rangle}_{\text{Correlation}}\right) \tag{4.14}$$

as we analyzed in Eq. 4.11 in section 4.5. The first term is monotonically increasing relative to driving power, so the existence of the second term is necessary to observe S-curve shape. This second term is correlation between distinct ions, and will be absent for the single ion case, hence distinct from the saturation effects.

Estimation of the number of ions participating in superradiance

From Fig. 4.2d, we see that x approaches 1 as the decay becomes single exponential for very low powers. In this case, we expect to be primarily exciting the single-excitation manifold, leading to a decay rate of $N\Gamma_c$, where N is the number of atoms in our Dicke space, and Γ_c is the Purcell enhanced decay rate of a single atom. While N (and thus τ) changes continuously in this regime due to power broadening, we still can estimate an effective Dicke space.

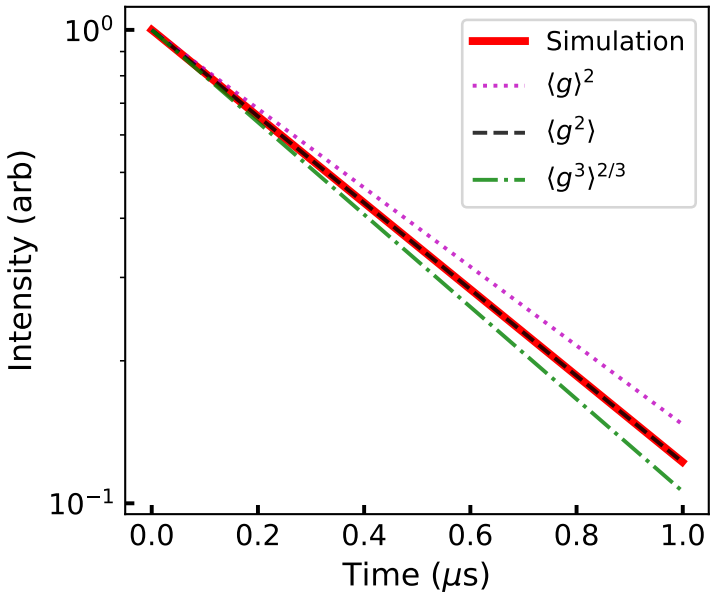

Figure 4.15: **Different methods of calculating the average of g.** Master equation simulation of the decay of $N = 6$ ions with inhomogeneous g (red) with low excitation. The three dashed lines (pink, black, green) are single exponential decays with decay rate $\frac{4N\langle g\rangle^2}{\kappa}$, $\frac{4N\langle g^2\rangle}{\kappa}$, $\frac{4N\langle g^3\rangle^{2/3}}{\kappa}$, respectively. The results show that, as expected, the superradiant decay from the single excitation manifold is governed by the average of g^2 for the case of inhomogeneous g.

In order to estimate N, we first show that the superradiant decay rate is N times the average Purcell decay rate, given that our system has inhomogeneous g. To this end, we simulate the time dynamics of 6 ions with varying g, excited with low power (Fig. 4.15). We find that as expected, the superradiant decay time from the lowest manifold is given by $\frac{4N\langle g^2\rangle}{\kappa}$, indicated by the overlap of the simulation and analytical time decay curves. From Section 1, we estimate the average Purcell enhancement by using $\sqrt{\langle g^2\rangle} = 2\pi \times 10.6$ MHz, giving an average Purcell decay time of 15.6 μs. Meanwhile, we measured a decay time of 270 ns in the low power regime with $x \approx 1$ (Fig. 3d), from which we can estimate the effective number of ions participating in superradiance at this particular power to be ~ 50.

Cooperativity required to observe superradiance

For a general symmetric distribution of ions, $\frac{iW(\omega=\omega_0)}{N\rho(\omega=\omega_0)} = \pi g^2$ [40] where $\rho(\omega = \omega_0)$ is the ion probability distribution at $\omega = \omega_0$, from which we obtain $C = \frac{|W(\omega=\omega_0)|}{\kappa/2} = \frac{2\pi g^2 N\rho(\omega=\omega_0)}{\kappa}$. This ensemble cooperativity represents the ratio of the absorption rate to the cavity decay rate, which indicates the number of ions a photon can interact

with before it leaks out of the cavity. The condition to observe superradiance in an inhomogeneous ensemble is roughly given by $\tau_R < T_2^*$ [31], where τ_R is the slowest superradiant decay time in the absence of inhomogeneity, and T_2^* is the inhomogeneous dephasing time. Assuming there are N_{eff} ions participating in superradiance, spanning a frequency Δ_{eff}, this leads to the requirement that the superradiance decay rate $N_{\text{eff}}\frac{4g^2}{\kappa}$ must be larger than the effective bandwidth Δ_{eff} of the participating ions. For the ions around ω_0, we know $N_{\text{eff}} = \Delta_{\text{eff}} N\rho(\omega = \omega_0)$. Using $N_{\text{eff}}\frac{4g^2}{\kappa} > \Delta_{\text{eff}}$, we obtain $\frac{4g^2 N\rho(\omega=\omega_0)}{\kappa} > 1$, giving an estimate of the cooperativity required to observe superradiance as $C > \frac{\pi}{2}$.

4.7 Outlook

The observed optical superradiance and subradiance represent a key step towards enabling narrow linewidth superradiant lasers [112] and long-lived subradiant memories [113, 114] in solid-state, while the control over the population of the Dicke space opens the door for dissipation-based engineering of state preparation [120, 121]. In addition, operating with a detuned cavity may allow the probing of coherent photon-mediated interaction between the ions (Eq. 4.5 in section 4.5), opening new possibilities for studying coherent spin exchange effects and quantum simulations [27, 122] in a solid-state platform. Finally, the improved understanding in this regime of collective and many-body cQED phenomena informs the development of high-cooperativity solid-state quantum memories and transducers [20, 123].

Chapter 5

MANY-BODY SPIN DYNAMICS

In this chapter, we will transition from the optical regime to the spin regime, focusing on direct spin-spin interaction.

5.1 Introduction

A strongly interacting ensemble of spins serves as a potential platform for exploring many-body physics. The addition of coherent manipulation and control enables the investigation of fundamental scientific concepts, such as the mechanisms of quantum thermalization [124] and the emergence of out-of-equilibrium phases of matter [3]. This capability further allows quantum engineering for the development of a system robust against decoherence and noise.

Among the plethora of systems exhibiting many-body physics, solid-state spin ensembles have emerged as a rich system to study. This is due to their inherent capability to scale to a large number of emitters, and motivated by their potential usefulness as quantum devices. In particular, researches in vacancy centers in diamond have demonstrated significant advancements in performing quantum simulations, quantum sensing, and realizing exotic phases of matter such as discrete time crystals (DTC) [4, 125].

Rare-earth ions (REIs) doped in solids can inject new vitality into studies of many-body physics due to their highly coherent optical and spin transitions at cryogenic temperatures, as well as their potential for long-range interactions [126]. Because of their remarkable properties in coherence, REIs have been investigated to develop quantum technologies such as quantum transducers, memories and sensors [42, 93, 127]. Although there have been numerous fundamental studies on REIs, they typically characterize the decoherence process via macroscopic angles and semiclassical methods with the sole intention of extending coherence times for engineering quantum applications [128–130]. However, a more microscopic and quantum approach is necessary for a deeper understanding of decoherence mechanisms, not only to provide insight for improving the performance of quantum technologies but also to open the door for the study of many-body physics.

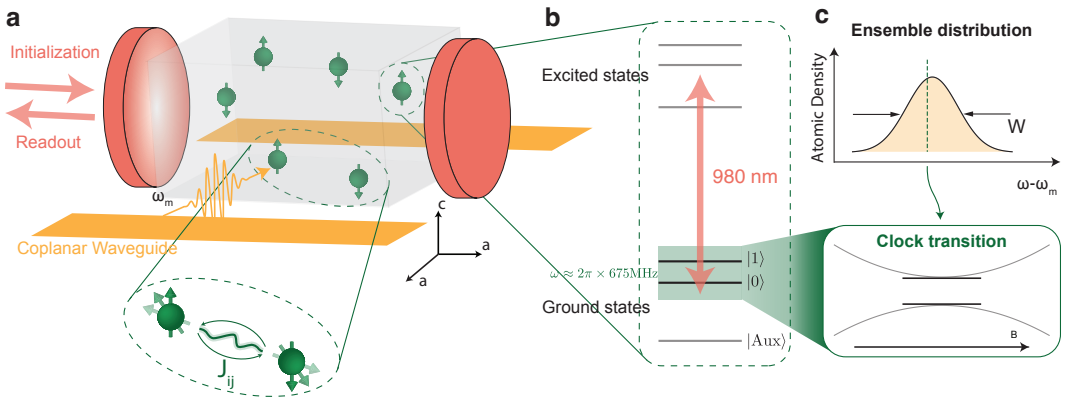

Figure 5.1: **Many-body spin systems.** **a,** An ensemble of 3D spins is coupled to an optical cavity for initialization and fast readout and to a coplanar waveguide for microwave drive ω_m. Zoom in: two spins (i and j) interact with a strength of J_{ij}. **b,** The full energy levels of each spin include optical ground states and excited states, where the ground states consist of qubit manifolds ($|1\rangle$, $|0\rangle$) and the double degenerate state $|\text{Aux}\rangle$. **c,** Upper: The ensemble distribution of spin detuning relative to the microwave drive $\omega - \omega_m$ exhibits inhomogeneity (disorder) with a linewidth of W. Lower: For each spin, the qubit manifolds feature a clock transition that is insensitive to the magnetic field.

5.2 System overview

We focus on an ensemble of $^{171}Yb^{3+}$ ions doped in yttrium orthovanadate (YVO_4), where $^{171}Yb^{3+}$ replaces yttrium sites in a 3D lattice at a concentration of 86 ppm (Fig. 5.1a). The 980 nm optical transitions of Yb ions couple to the optical cavity, enabling emergent phenomena as discussed in chapter 3 and chapter 4, and also facilitating initialization and fast readout for the spin systems. The microwave drive is transmitted through coplanar waveguides for both initialization within excited states manifolds at around 3.37 GHz and spin control over qubit manifolds ($|1\rangle \leftrightarrow |0\rangle$) at around 675 MHz (Fig. 5.1b).

Focusing on the qubit manifolds $|1\rangle$, $|0\rangle$ among the optical ground states, each spin exhibits a clock transition that is insensitive to the magnetic field to the first order (or ZEFOZ transition, zero first-order Zeeman), resulting in a narrow spin inhomogeneity (on-site disorder) W within the ensemble (see fig. 5.1c). Among the spins, the long-range magnetic dipole-dipole interaction leads to a certain distribution of interaction strengths J_{ij}. The ratio between interaction strength and disorder is essential, as their interplay results in rich spin dynamics.

5.3 Spin exchange interaction and on-site disorder

Firstly, let us start with the magnetic dipole-dipole interaction and derive an effective spin-spin interaction within the qubit manifolds.

The qubit states ($|1\rangle$,$|0\rangle$) can be written as [19]:

$$|0\rangle = \frac{1}{\sqrt{2}}(|\uparrow\Downarrow\rangle - |\downarrow\Uparrow\rangle) \tag{5.1}$$

$$|1\rangle = \frac{1}{\sqrt{2}}(|\uparrow\Downarrow\rangle + |\downarrow\Uparrow\rangle) \tag{5.2}$$

where $\{|\uparrow\rangle, |\downarrow\rangle\}$ are effective electron spins and $\{|\Uparrow\rangle, |\Downarrow\rangle\}$ are nuclear spins.

The magnetic dipole-dipole interaction Hamiltonian between spins i and j is as follows:

$$H_{dd} = -\frac{\mu_0}{4\pi r_{ij}^3}(3(\vec{\mu}_i \cdot \hat{r}_{ij})(\vec{\mu}_j \cdot \hat{r}_{ij}) - \vec{\mu}_i \cdot \vec{\mu}_j) \tag{5.3}$$

where $\vec{r}_{ij} = r_{ij}\hat{r}_{ij}$ is the vector from ion i to ion j. The magnetic dipole moment operator for our system is

$$\vec{\mu}_j = \mu_B \mathbf{g} \cdot \tilde{\mathbf{S}} = \mu_B \begin{pmatrix} g_\perp & & \\ & g_\perp & \\ & & g_\parallel \end{pmatrix} \begin{pmatrix} \tilde{S}_x^j \\ \tilde{S}_y^j \\ \tilde{S}_z^j \end{pmatrix} = \mu_B \begin{pmatrix} g_\perp \tilde{S}_x^j \\ g_\perp \tilde{S}_y^j \\ g_\parallel \tilde{S}_z^j \end{pmatrix}. \tag{5.4}$$

Here, the $\tilde{\mathbf{S}} = \{\tilde{S}_x, \tilde{S}_y, \tilde{S}_z\}$ are defined in the effective electron spin basis $\{|\uparrow\rangle, |\downarrow\rangle\}$, which is different than the $\{|1\rangle, |0\rangle\}$ basis. We can see the zero sensitivity to the magnetic field along the z-direction from the fact that $\langle 0|\, \tilde{S}_z\, |0\rangle = \langle 1|\, \tilde{S}_z\, |1\rangle = \langle 0|\, \tilde{S}_{zn}\, |0\rangle = \langle 1|\, \tilde{S}_{zn}\, |1\rangle = 0$ where $\tilde{S}_{zn}$ is the nuclear spin operator.

Then we can calculate the magnetic dipole moment within the qubit manifolds $\{|1\rangle, |0\rangle\}$.

$$\langle 0|_j\, \vec{\mu}_j\, |1\rangle_j = \mu_B \begin{pmatrix} g_\perp \langle 0|_j\, \tilde{S}_x^j\, |1\rangle_j \\ g_\perp \langle 0|_j\, \tilde{S}_y^j\, |1\rangle_j \\ g_\parallel \langle 0|_j\, \tilde{S}_z^j\, |1\rangle_j \end{pmatrix} = \frac{1}{2}\mu_B \begin{pmatrix} 0 \\ 0 \\ g_\parallel \end{pmatrix}$$

$$\langle 0|_j\, (\vec{\mu}_j \cdot \hat{r}_{ij})\, |1\rangle_j = \frac{1}{2}\mu_B g_\parallel \hat{r}_{ij,z}$$

$$\langle 0|_j\, \vec{\mu}_j\, |0\rangle_j = 0.$$

H_{dd} is a 4x4 matrix, so there are 16 elements. Among these, only 4 terms are non-zero, allowing H_{dd} to be expressed as:

$$H_{dd} = -\frac{\mu_0 \mu_B^2 g_{/\!/}^2}{16\pi r_{ij}^3}(3\hat{r}_{ij,z}^2 - 1)(S_+^i S_-^j + S_-^i S_+^j + S_+^i S_+^j + S_-^i S_-^j). \tag{5.5}$$

Here, $S_\pm = S_x \pm iS_y$, and we use $S_{x,y,z}$ to denote spin operators in the $\{|0\rangle, |1\rangle\}$ basis. We can see that we get flip-flop, flop-flip, flip-flip, and flop-flop terms. Using secular approximation, the last two terms should be neglected. Considering the fact that $S_+^i S_-^j + S_-^i S_+^j = 2(S_x^i S_x^j + S_y^i S_y^j)$, we have:

$$H_{dd} = -\frac{\mu_0 \mu_B^2 g_{/\!/}^2}{8\pi r_{ij}^3}(3\hat{r}_{ij,z}^2 - 1)(S_x^i S_x^j + S_y^i S_y^j). \tag{5.6}$$

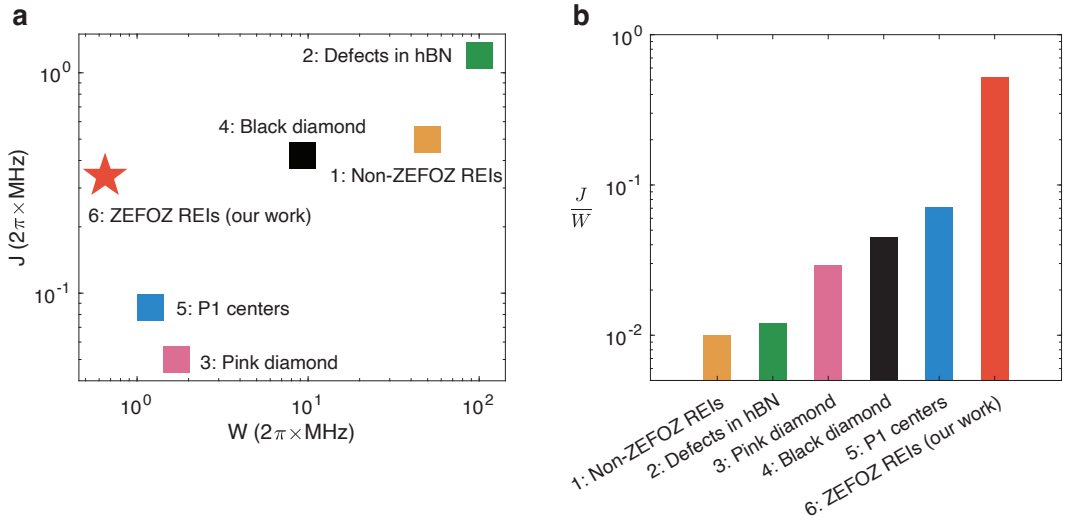

Figure 5.2: **Average interaction strength J and disorder W for various solid-state electronic spin systems. a,** The positions of our work and other electronic spin systems on the J-W map. 1: Non-ZEFOZ REIs [131, 132]; 2: Defects in hBN [133]; 3: Pink diamond [133]; 4: Black diamond [134]; 5: P1 centers [135]. **b,** The bar chart shows the ratio between average interaction strength J and disorder W for different systems in **a**.

As a result, the systems can be described by a full Hamiltonian

$$H = \sum_i^N \Delta_i S_z^i + \sum_{i,j}^N J_{ij}(S_x^i S_x^j + S_y^i S_y^j) \tag{5.7}$$

where $\Delta_i = \omega_i - \omega_m$ is the ion spin detuning relative to the microwave drive frequency, $J_{ij} = -\frac{\mu_0 \mu_B^2 g_{/\!/}^2}{8\pi r_{ij}^3}(3\hat{r}_{ij,z}^2 - 1)$ is the interaction strength between a pair of

spins, and generates a distribution based on the position of the spins in the lattice. The combination of clock transitions and long-range spin exchange interaction thus provides us with a comparable magnitude of on-site disorder and interaction strength, resulting in a high J/W ratio among different electronic spin systems (Fig. 5.2).

5.4 Controllable many-body system: tunability of J

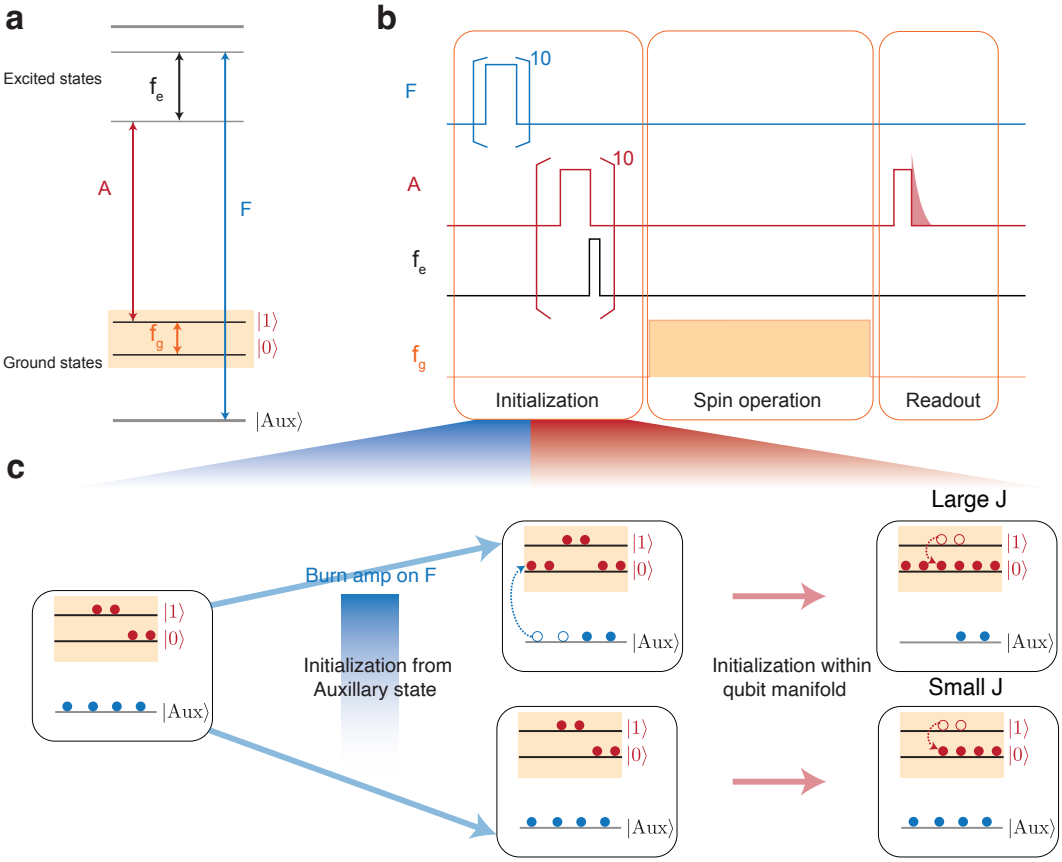

Figure 5.3: **Initialization for spin systems. a,** The energy levels of Yb ions. The optical A and E transitions, f_g and f_e, are labeled for use in the pulse sequences. **b,** Pulse sequences for the experiment include three parts: initialization, spin operation, and readout. Initialization involves optical driving on the F transition to move population from $|\text{Aux}\rangle$ to $|1\rangle$, followed by a combination of driving on the A transition and a π pulse on f_e to transfer population from $|0\rangle$ to $|1\rangle$. Spin operation represents different spin control on f_g. Readout is a short optical pulse on A and we collect fast superradiance afterwards. **c,** Population changes within ground states during initialization part of the pulse sequences. By controlling the amplitude of burning on the F transition, the amount of population transferred from $|\text{Aux}\rangle$ to $|1\rangle$ varies. A larger amplitude results in more population within $|1\rangle$ after the initialization within the qubit manifolds, leading to a larger interaction strength J.

In order to explore system behaviors, having tunability over certain parameters (such as J, W) broadens the study of spin dynamics by providing more data points. This deepens understanding and increases the versatility of a many-body platform for potential applications. Thanks to the multiple energy levels provided by rare-earth ion systems, we have designed some initialization sequences to shift population among different ground states (Fig. 5.3b).

Specifically, $|1\rangle$, $|0\rangle$, and $|\text{Aux}\rangle$ are initially populated with a certain number of ions following Boltzmann distribution. Firstly, we pump the optical F transition with a chirping frequency across the entire inhomogeneous line to transfer population from $|\text{Aux}\rangle$ to $|0\rangle$. After repeating this process 10 times, we then apply a similar chirped pump on the A transition, followed by a microwave π pulse on the excited spin transition f_e. This combination is also repeated 10 times, and thus, we obtain polarized spins within the qubit manifolds (Fig. 5.3c). The amplitude of burning on the F transition controls the amount of population we transfer from the $|\text{Aux}\rangle$ state, thus determining the final population in the $|1\rangle$ state. As we recall the expression for the interaction strength between a pair of spins $J_{ij} \propto \frac{1}{r_{ij^3}}$, more population within the qubit manifolds indicates a smaller distance r_{ij}, consequently resulting in a larger interaction strength J_{ij}. Since J_{ij} has a distribution, we define the average interaction strength J using the average nearest neighbor distance r and $\hat{r}_z^2 = 1$. We find that

$$J = \frac{\mu_0 \mu_B^2 g_{/\!/}^2}{4\pi r^3} = \frac{2\pi \times 467.4}{r^3} \text{ MHz} \tag{5.8}$$

where r is in the unit of nm and can be calculated using the lattice structure and doping concentration. Here, $g_{/\!/} = 6$ for our system, while $g = 2$ for NV systems, which leads to $J \cdot r^3 = 2\pi \times 52 \text{ MHz} \cdot \text{nm}^3$ as a comparison [135].

The combination of a strongly interacting spin system along with robust controls, including coherent microwave drive, fast readout, and system parameter control (interaction strength J), showcases our system as a platform for studying many-body spin dynamics under Hamiltonian engineering, leading to various applications, including exotic phases of matter such as discrete time crystals (DTC), quantum sensing, and quantum simulation (Fig. 5.4).

5.5 Experimental characterization of many-body spin interaction using spin echo and Ramsey sequences

We characterize the spin interaction in our system using spin echo and Ramsey measurements. To begin, we apply the spin echo sequence during the spin operation

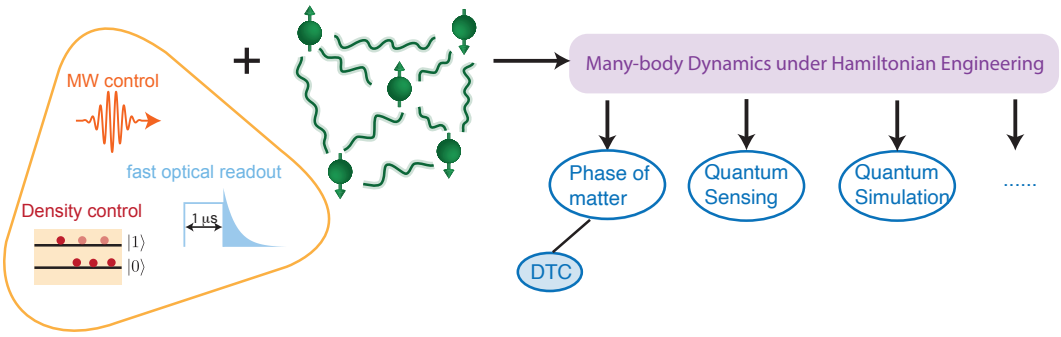

Figure 5.4: **Many-body platform.** Our platform consists of a strongly interacting ensemble (green spins) and robust controls (triangular frame), which include coherent microwave drive, fast optical readout, and the ability to change the effective density. This enables us to study many-body dynamics under Hamiltonian engineering and has applications such as DTC (chapter 6), quantum sensing, quantum simulation, and so on.

(Fig. 5.3b) to decouple the disorder to the zeroth order and focus solely on the interaction (Fig. 5.5a). For a given free evolution time τ, the phase θ of the last $\pi/2$ pulse is swept from 0 to 2π. We collect the fast photoluminescence (superradiance) after a readout pulse on the A transition to measure the population projected onto the $|1\rangle$ state as a function of θ. A cosine dependence of population counts on θ is then obtained as $P = P_{\text{amp}} \cos\theta + P_{\text{offset}}$, and the coherence is extracted using $C = P_{\text{amp}}/P_{\text{offset}}$. The coherence at $\tau = 0$ is related to the polarization rate η_{pol} as $C(\tau = 0) = 2\eta_{\text{pol}} - 1$. From this, we extract our polarization rate within qubit manifolds to be around 75%. Afterward, we divide the coherence by $C(\tau = 0)$ to obtain the normalized coherence for different τ as a decoherence profile (Fig. 5.5a).

Focusing on the first 1us, we observe that the decay rate significantly exceeds the rate observed in the single-ion case, due to the interaction-dominated dynamics. As we increase J, the decay becomes even faster. By matching the simulation to the experiment, we extract the effective concentration of ions within qubit manifolds as 46 ppm for the large J case and 25 ppm for the small J case, with corresponding average interaction strengths of $2\pi \times 0.34$ MHz and $2\pi \times 0.19$ MHz, respectively (section 5.6).

Next, we perform the Ramsey measurement to account for the influence of disorder at an early time scale (Fig. 5.5b). The decoherence profile is obtained using the same method as in the echo measurement. Within the same time window of $1\mu s$, the coherence decays faster under the Ramsey sequence compared to the echo sequence for both small and large J cases (Fig. 5.5). By aligning the simulation

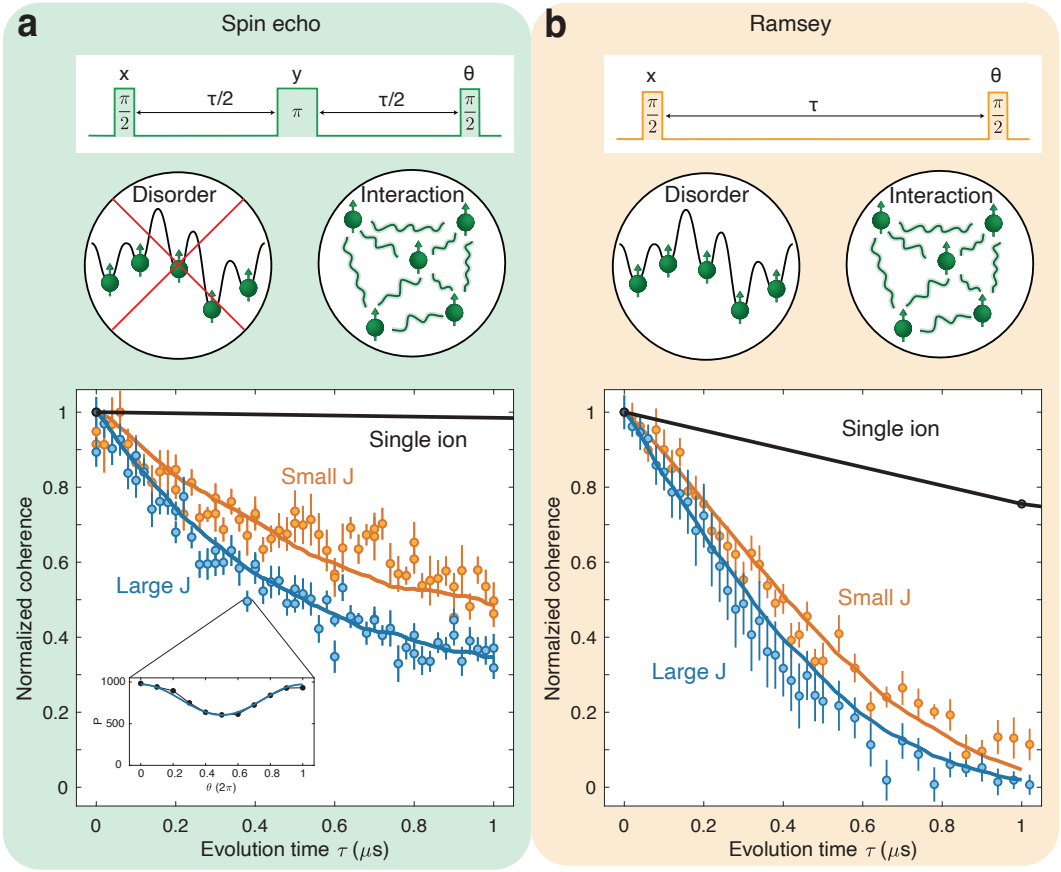

Figure 5.5: **Spin echo and Ramsey measurement.** **a,** Spin echo measurement decouples disorder to the zeroth order and isolates the interaction. The coherence after the free evolution time τ under the spin echo sequence is measured for the large J (blue) and small J (orange) cases and then normalized relative to the maximum coherence for each trace. The data are represented by filled circles with error bars, and the solid line represents the simulation (section 5.6). The single ion case is plotted in gray as a reference. Inset: An example of the collected readout counts for the swept phase θ of the last $\pi/2$ pulse. **b,** Ramsey measurements include the influence of disorder and the interaction. The data is taken and normalized using a similar method to that used in **a**.

with experimental data, we extract a common disorder for both the small and large J cases as $W = 2\pi \times 0.65$ MHz (section 5.6). We do not expect tuning J to change W; thus, the common W supports our use of this method for extracting parameters.

In our coherence measurements (for both spin echo and Ramsey sequences), the first $\pi/2$ pulse along the $\hat{x}$ axis prepares all the spins to align along the $\hat{y}$ direction[1], such that the decoherence profile essentially describes the depolarization process along

[1]We use the convention of the rotation operator $U = e^{-i\frac{\theta}{2}\hat{n}\cdot\vec{\sigma}}$ here, which indicates counter-clockwise rotation relative to the laser unit vector $\hat{n}$ by an angle θ.

the $\hat{y}$ axis. In the Ramsey measurement, the system evolves under both interaction and disorder (Eq. (5.7)), $\Delta_i S_z^i$ acts as a pinning field along the $\hat{z}$ axis with strength Δ_i, and $J_{ij} S_x^i S_x^j$ acts as a pinning field along the $\hat{x}$ axis with a strength of J_{ij}. Due to the finite width of the distribution of Δ_i and J_{ij}, the total polarization along the $\hat{y}$ axis starts to decay over time. In contrast, a spin echo sequence adds an additional π pulse in the middle of the system evolution, where the pinning field introduced by $\Delta_i S_z^i$ cancels out both before and after the π pulse, while the influence of $J_{ij} S_x^i S_x^j$ remains.

Having established the dominant role of dipolar interactions in the short time scales ($< 1\mu s$) of the spin echo sequence, we include the longer time scales ($> 1\mu s$) in our discussion, where the coherence profile now exhibits two distinct decay rates (Fig. 5.6). In the next two sections, we will provide a detailed analysis of how the second, slower decay is attributed to the system's disorder. Put simply, while the detuning $\Delta_i S_z^i$ is canceled by the middle π pulse in the echo sequence, the relative detuning between a pair of spins, $\Delta_i - \Delta_j$, determines how resonant they are, thereby affecting the way that interaction $J_{ij} S_x^i S_x^j$ depolarizes the spins.

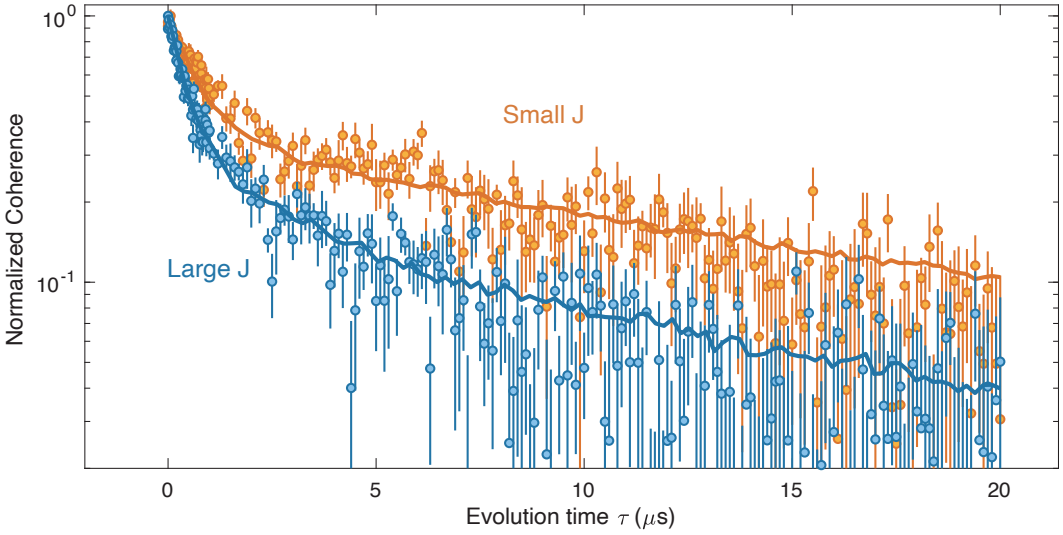

Figure 5.6: **Spin echo measurement extending to longer time scales.** The data are represented by filled circles with error bars, and the solid line represents the simulation (section 5.6). A log scale is used to show two distinct rates.

5.6 Microscopic numerical simulation

In this section, we present the method of microscopic numerical simulations for many-body dynamics. This simulation was conducted by Riku Fukumori.

We start with the realistic lattice structure of YVO_4 and position a number, N, of Yb ions in the Y sites based on the doping concentration. We then randomly assign each ion a frequency detuning Δ_i based on the Lorentzian distribution with a certain linewidth, W, and calculate the interaction strength J_{ij} between each pair according to their relative positions using Eq. 5.6. For a given free evolution time, τ, a complete solution of spin states is obtained for a system under Hamiltonian Eq. (5.7) and a certain pulse sequence (such as spin echo or Ramsey). Note that we only read out the final state of the center spin to avoid finite size effects. The above process is then repeated with many Monte-Carlo runs to obtain the ensemble dynamics. A convergence test has been conducted to investigate the dependence of the decay profile on the simulated Yb number N in order to determine a reasonable value for N. We find that 8 ions are sufficient when only reading out the central spin, as adding more ions only includes those far away, which do not significantly contribute to the dynamics (Fig. 5.7a).

From the simulation, we deduce that the decay for a short time scale depends solely on the interaction strength by comparing the cases with and without disorder (Fig. 5.7b). Although the doping concentration of Yb in this sample has been measured to be approximately 86 ppm [93], the ion concentration within the qubit manifolds remains unknown. This concentration largely depends on the temperature of the system and can be tuned via initialization sequences. By matching the decay rate at small time $\tau < 1\mu s$ of simulation to that of the experiment, we can extract the ion concentration within the qubit manifolds for different cases, ranging from 25 ppm for the small J case to 46 ppm for the large J case (Fig. 5.5a). Subsequently, introducing the common disorder variable $W = 2\pi \times 0.65$ MHz into the simulation enables us to align the simulation results with the experimental data in the Ramsey sequence across all cases (Fig. 5.5b). Moreover, this same disorder value W successfully matches the decay rates at large time τ in the spin echo measurement as well (Fig. 5.6), which indicates that decay at a longer time scale can be predicted by a closed Hamiltonian without excess dephasing.

We also find that the initial polarization rate η_{pol} only scales the overall decoherence profile by a factor of $2\eta_{\text{pol}} - 1$ without influencing the decay rate (Fig. 5.7b,c). Therefore, for brevity in state representations, we set $\eta_{\text{pol}} = 1$ in the following analysis.

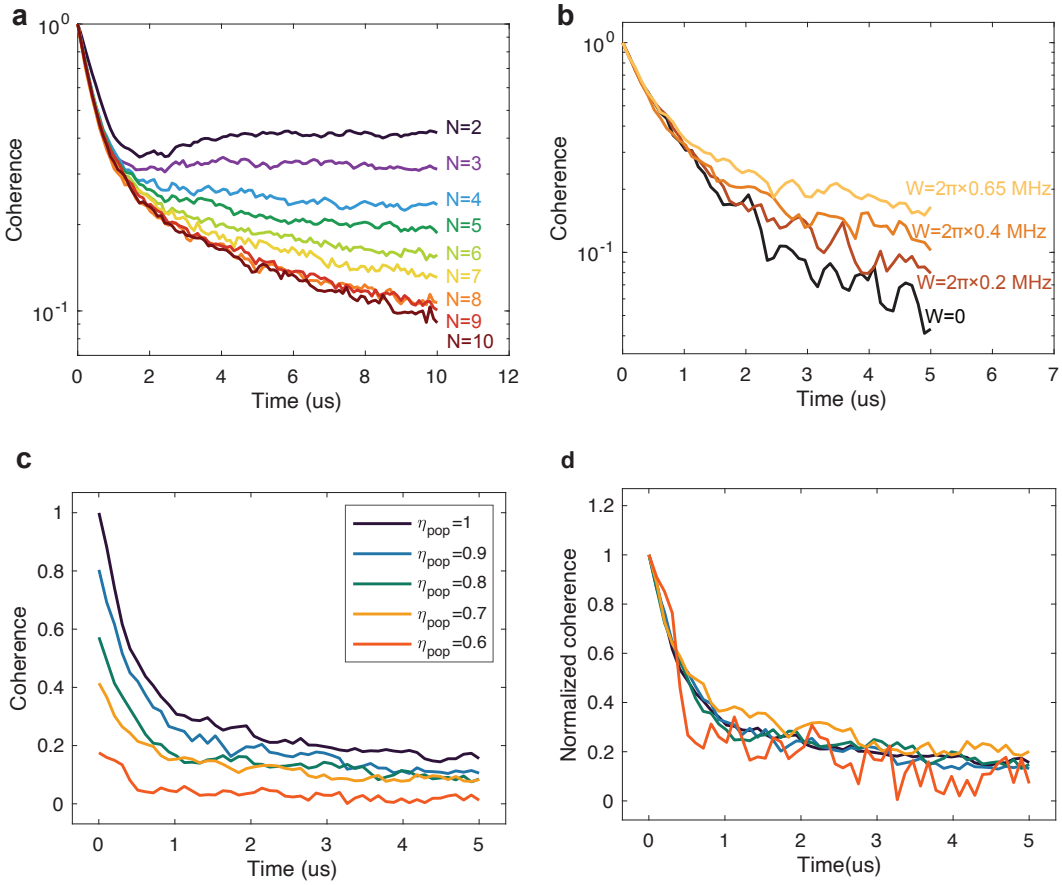

Figure 5.7: **Many-body simulation.** Simulation of decoherence profile for **a,** different numbers of simulated spins N; **b,** different disorder W; **c,** different polarization rate η_{pop}. **d,** Normalized coherence for **c**.

5.7 Theoretical analysis: from a pair of spins to many spins with frequency disorder

In this section, we will use some toy models to deepen the understanding of how interactions and disorder influence the dynamics in the echo measurement.

A pair of spins with interaction strength J and detuning Δ

For a pair of spins with interaction strength J and detuning Δ, we can derive the total polarization along $\hat{y}$ at time τ under the echo sequence as follows (section B.1).

$$P(\tau) = \frac{\Delta^2}{\Delta^2 + J^2} + \frac{J^2}{\Delta^2 + J^2} \cos\left(\frac{\sqrt{\Delta^2 + J^2}}{2}\tau\right) \tag{5.9}$$

For the resonant spins with $\Delta = 0$, $P(\tau) = \cos(\frac{J}{2}\tau)$. This implies that the two spins oscillate between pointing $\hat{y}$ and $-\hat{y}$ with a frequency of $J/2$. The corresponding

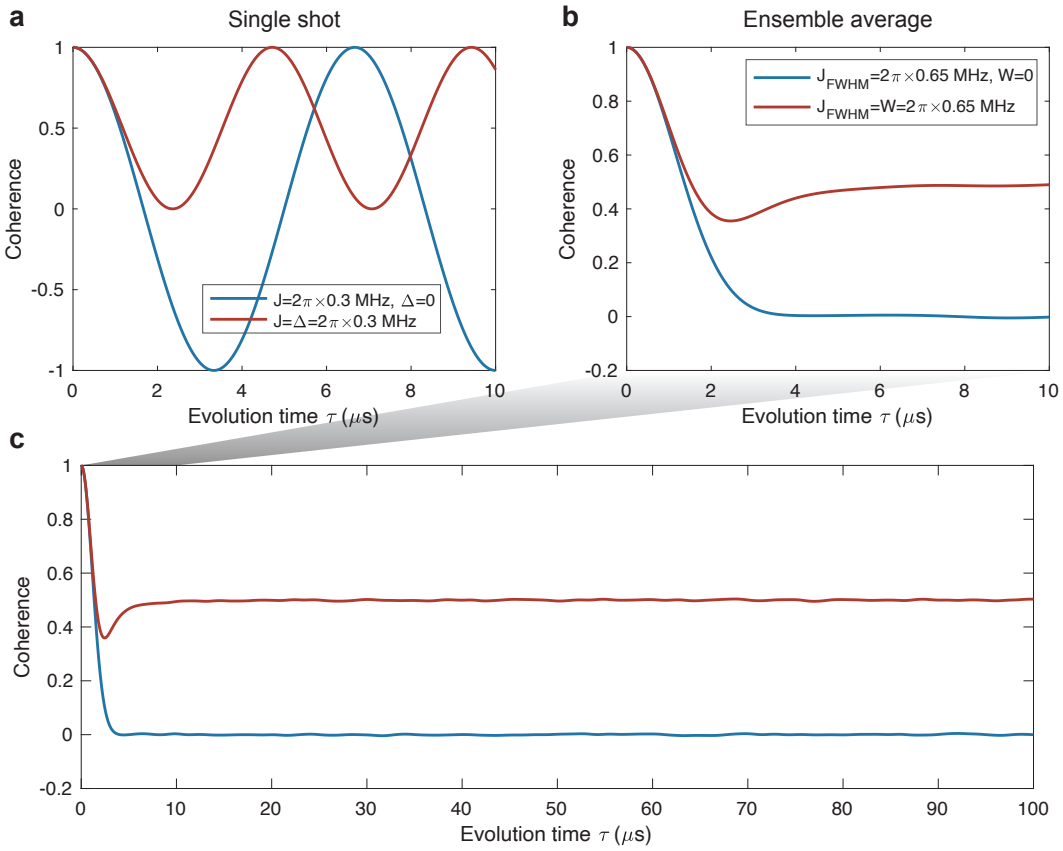

Figure 5.8: **Evolution of a pair of spins with interaction strength J and detuning Δ. a,** For a fixed $J = 2\pi \times 0.3$ MHz, we compare $\Delta = 0$ (blue) and $\Delta = J$ (red). **b,** We average different J and Δ values, where J follows a Gaussian distribution with a FWHM of $2\pi \times 0.65$ MHz for both without disorder ($W = 0$, blue) and with disorder ($W = 2\pi \times 0.65$ MHz, red). **c,** Longer time scale for **b**.

measured $P(\tau)$ ranges from 1 to -1 where 1 is defined relative to the initial state. Averaging a distribution of J will lead to a spin polarization decay to 0.

However, when the detuning is introduced with $\Delta \neq 0$, the total spin ranges from 1 to $\frac{\Delta^2-J^2}{\Delta^2+J^2}$ with an offset of $\frac{\Delta^2}{\Delta^2+J^2}$ (Fig. 5.8a). Although the oscillation frequency increases from $J/2$ to $\sqrt{\Delta^2+J^2}/2$, the decay rate at small τ remains the same:

$$\left.\frac{dP(\tau)}{d\tau}\right|_{\tau\to 0} = -\frac{J^2}{2\sqrt{\Delta^2+J^2}}\sin\left(\frac{\sqrt{\Delta^2+J^2}}{2}\tau\right)\Bigg|_{\tau\to 0} = -\frac{J^2}{4}\tau. \tag{5.10}$$

From this, we can see that the decay rate at small τ depends only on J. Consequently, after averaging different J values, the decoherence profiles at small τ overlap, regardless of the presence of disorder (Fig. 5.8b).

What changes is that with disorder, the spins have a preferred direction of $\hat{y}$, and averaging a distribution of J will result in a residual polarization (Fig. 5.8b, c). In this two-atom model, the residual polarization does not decay at a longer time scale (Fig. 5.8c). This implies more atoms need to be involved to explain our experimental observation of a second decay in the decoherence profile.

From two spins to three spins

Next, let us introduce a third spin to see what happens. Given that the interaction strength scales as $J_{ij} \propto \frac{1}{r_{ij}^3}$, the third spin is likely to have a much smaller interaction compared to the first pair. Let us consider the case without disorder for simplicity. The three-atom Hamiltonian is given by

$$H = H_0 + V = J_0(S_x^1 S_x^2 + S_y^1 S_y^2) + J_1(S_x^1 S_x^3 + S_y^1 S_y^3) + J_2(S_x^2 S_x^3 + S_y^2 S_y^3), \quad (5.11)$$

where $H_0 = J_0(S_x^1 S_x^2 + S_y^1 S_y^2)$ and $|J_0| \gg |J_1|, |J_2|$, so V is a perturbation relative to H_0. By solving the problem using second-order perturbation theory, we obtain the final population under the echo sequence. Let us only measure spin 1 at the end to avoid finite size effects (section 5.6): $P_1 = \langle \phi(\tau)| \, 2S_x^1 \, |\phi(\tau)\rangle$. The value should range from -1 to 1. We can list terms with different frequencies separately (section B.2).

$$P_1^{DC} = \frac{J_2}{2J_0} + \frac{3J_1^2 + J_2^2 + 4J_1J_2}{2J_0^2} \quad (5.12)$$

$$P_1^{\frac{J_1J_2}{J_0}} = -\frac{1}{2}\left(\frac{J_2}{J_0} - \frac{J_2(J_1+J_2)}{J_0^2}\right)\cos\frac{J_1J_2}{J_0}\tau \quad (5.13)$$

$$P_1^{J_0} = \frac{J_1(J_1-J_2)}{2J_0^2}\cos\,(J_0 + \frac{J_1^2+J_2^2}{2J_0})\tau \quad (5.14)$$

$$P_1^{J_0/2,1} = \frac{1}{2}\left(1 - \frac{J_1+J_2}{2J_0} - \frac{13J_1^2+7J_2^2+12J_1J_2}{4J_0^2}\right)\cos\,(\frac{J_0}{2} + \frac{J_1^2+J_2^2+6J_1J_2}{4J_0})\tau \quad (5.15)$$

$$P_1^{J_0/2,2} = \frac{1}{2}\left(1 + \frac{J_1+J_2}{2J_0} - \frac{J_1^2+3J_2^2+4J_1J_2}{4J_0^2}\right)\cos\,(\frac{J_0}{2} + \frac{(J_1+J_2)^2}{4J_0})\tau \quad (5.16)$$

$$P_1^{J_0/2,3} = \frac{1}{2}\left(\frac{J_1-J_2}{2J_0} + \frac{3(J_2^2-J_1^2)}{4J_0^2}\right)\cos\,(\frac{J_0}{2} + \frac{J_1^2+J_2^2-6J_1J_2}{4J_0})\tau \quad (5.17)$$

$$P_1^{J_0/2,3} = \frac{1}{2}\left(\frac{J_2-J_1}{2J_0} + \frac{J_1^2-J_2^2}{4J_0^2}\right)\cos\,(\frac{J_0}{2} + \frac{(J_1-J_2)^2}{4J_0})\tau \quad (5.18)$$

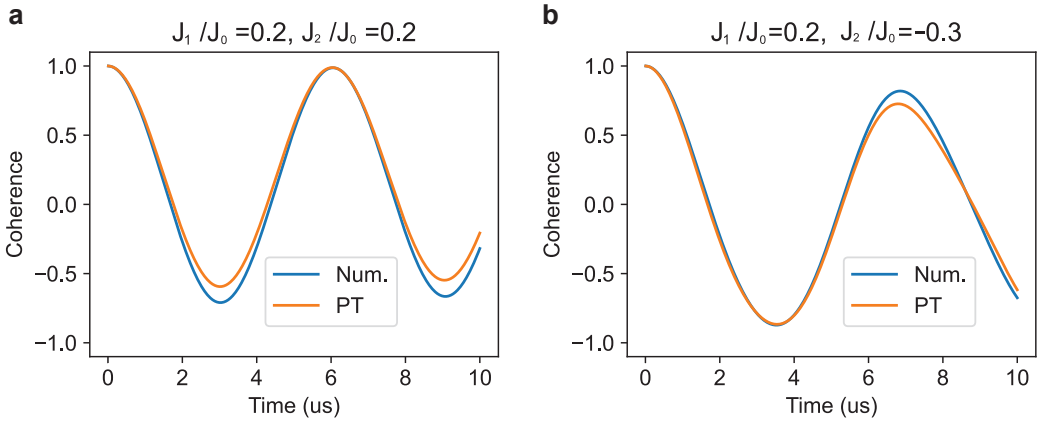

Figure 5.9: **Comparison between numerical simulation and perturbation theory for three resonant spins.** For J_0 fixed at $2\pi \times 0.3$ MHz, we compare numerical simulations (Num., blue), obtained using the same method as in section 5.6, with predictions by perturbation theory (PT, orange) at different values of J_1/J_0 and J_2/J_0.

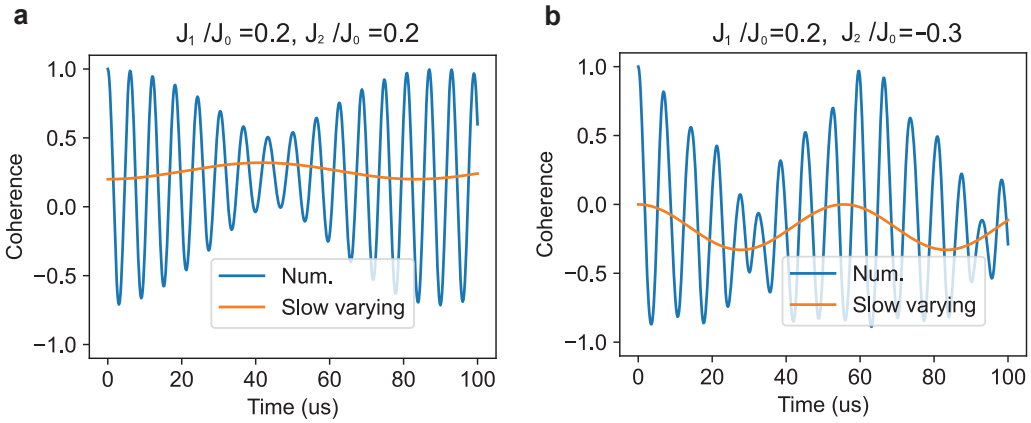

Figure 5.10: **Slowly varying component in three resonant interaction spins.** For J_0 fixed at $2\pi \times 0.3$ MHz, we compare numerical simulations (Num., blue) with P_1^{slow} (slow varying, orange) at different values of J_1/J_0 and J_2/J_0.

where $P_1 = P_1^{DC} + P_1^{\frac{J_1 J_2}{J_0}} + P_1^{J_0} + P_1^{J_0/2,1} + P_1^{J_0/2,2} + P_1^{J_0/2,3}$. The validity of Eqs. 5.12 - 5.18 can be verified by comparing them to numerical simulations, and we can see that they match to a good extent (Fig. 5.9). Similar to the case when we add detuning to a pair of spins, adding a third spin makes the polarization prefer the initial direction and never reach -1. Moreover, by looking at a larger time scale, a

new slowly varying term appears, as predicted by Eqs. 5.12-5.13.

$$P_1^{\text{slow}} = P_1^{DC} + P_1^{\frac{J_1 J_2}{J_0}} = \frac{J_2}{2J_0} + \frac{3J_1^2 + J_2^2 + 4J_1J_2}{2J_0^2} + \frac{J_1(J_1 - J_2)}{2J_0^2} \cos\left(J_0 + \frac{J_1^2 + J_2^2}{2J_0}\right)\tau \tag{5.19}$$

This slowly varying term indicates that adding a third spin will introduce a slow time scale into the system dynamics (Fig. 5.10). Finally, when comparing the three-atom

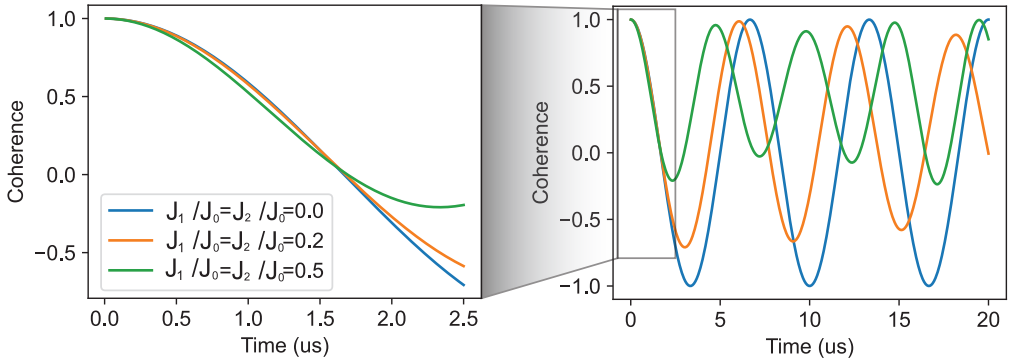

Figure 5.11: **Comparison of different interaction strengths for three resonant spins.** J_0 is fixed at $2\pi \times 0.3$ MHz. $J_1/J_0 = J_2/J_0 = 0$ represents the two-atom case. Curves are generated by numerical simulation.

case with the two-atom case, we observe in the numerical simulation that the decay rate at small τ changes only minimally (Fig. 5.11), as predicted by:

$$\left.\frac{dP(\tau)}{d\tau}\right|_{\tau \to 0} = -\frac{J_0^2 + J_1^2}{4}\tau. \tag{5.20}$$

Decoherence profile explanation by dividing into three time regimes

After understanding the above toy model well, we can now return to our experimental data and gain a deeper insight into the dynamics. Here, we plot the experimental data together with three different simulation cases (Fig. 5.12). Case I and Case II are without disorder. In Case I, only the nearby spin with the largest $|J|$ is included for a given readout spin (two-atom case), while in Case II, all surrounding spins are considered (8 atoms are sufficient, as proven by the convergence test; further details are provided in section 5.6). Case III is the same simulation as Case II but with the addition of disorder to the system.

As mentioned earlier, Case III closely matches the experimental results. For the three simulations, they all overlap at a very early timescale with $\tau < 0.6\ \mu s$. This means the early-time dynamics of a spin can be described by a pairwise process,

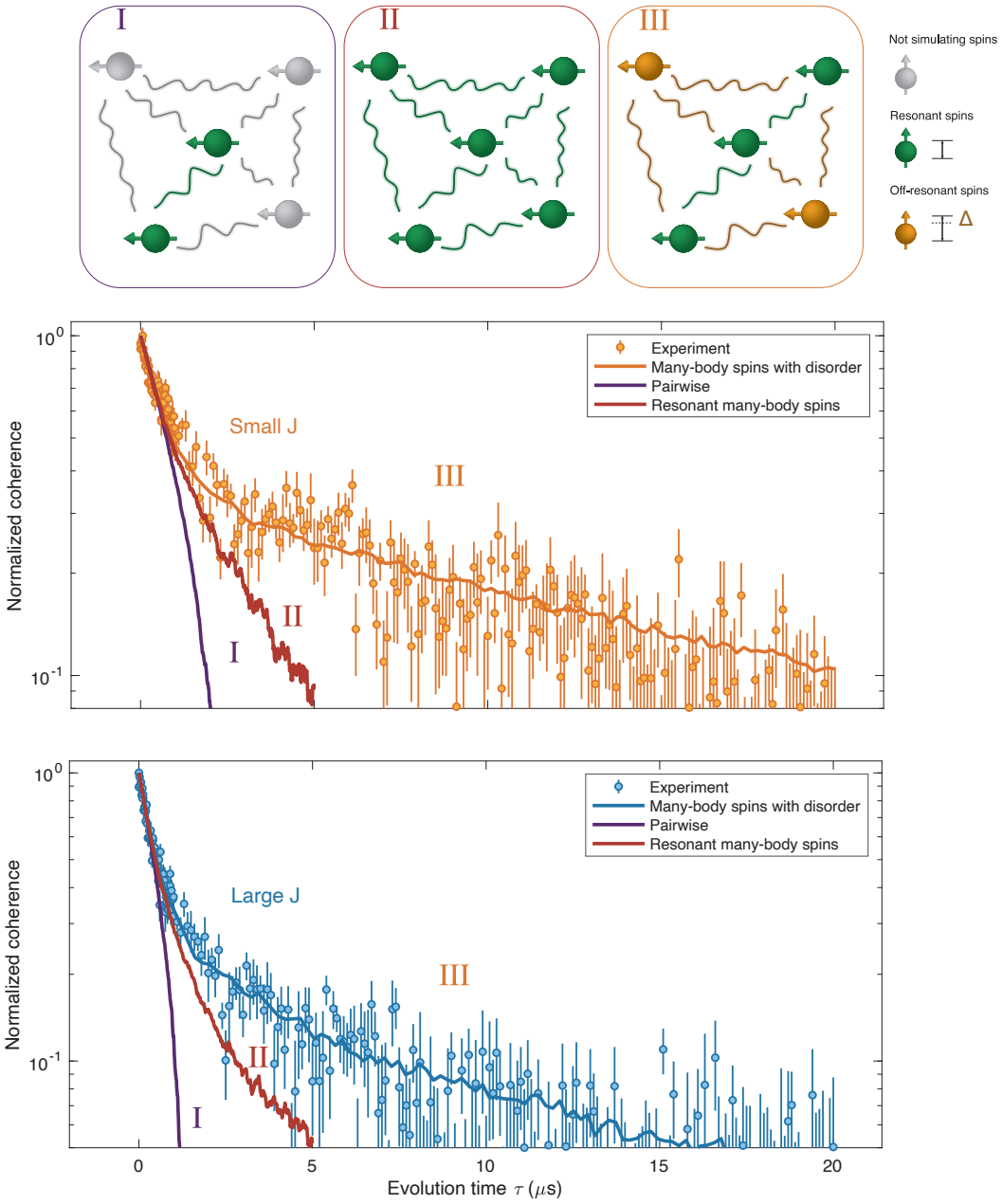

Figure 5.12: **Three time regimes in decoherence profile of echo measurements.** All of the solid lines are generated by numerical simulation using the real lattice (section 5.6). Case I (purple): Without disorder, for a given readout spin, choosing the nearby spin with the largest $|J|$. Case II (red): Many-body simulation without disorder. Case III (orange): Many-body simulation with disorder. Filled circles with error bars are experimental data.

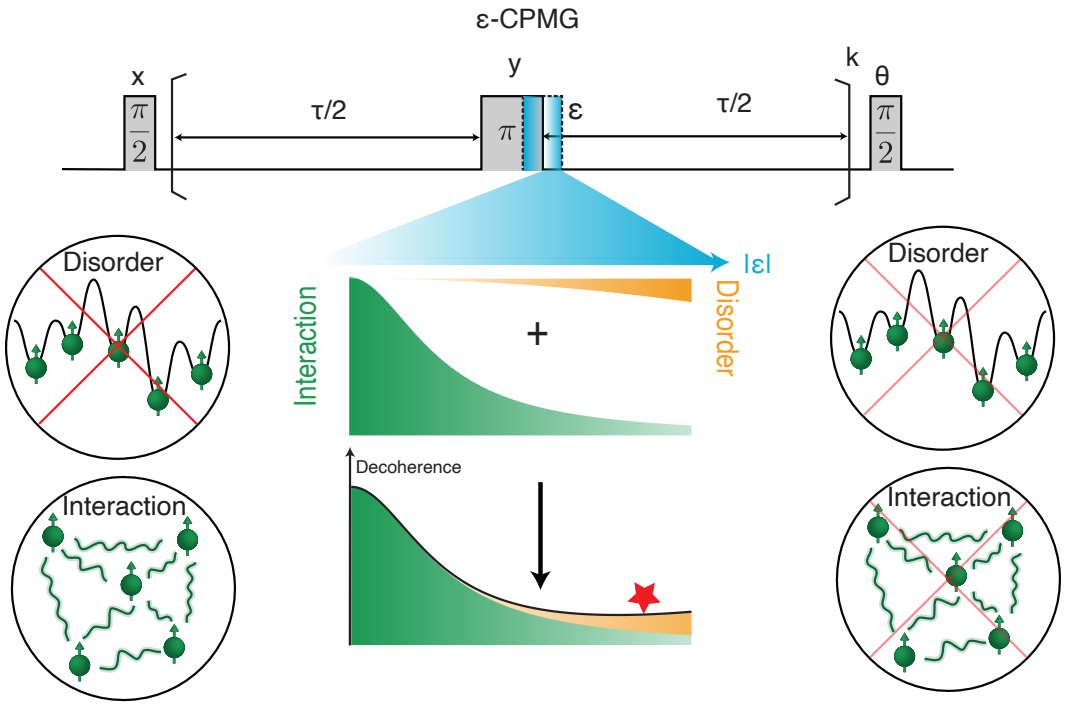

Figure 5.13: **Illustration for the ϵ-CPMG sequence[2].** Pulse sequence: middle π pulse with a rotation offset ϵ. As $|\epsilon|$ increases from 0 to $\pi/2$, the decoherence from interaction is decoupled more, while the disorder decouples the best at $|\epsilon| = 0$ but worse at $|\epsilon| = \pi/2$.

where decoherence is dominated by interacting with the nearby spin with the largest interaction strength. We can call this time regime I. At $\tau \approx 0.6\ \mu s$, Case I and Case II start to diverge. Now, we enter time regime II, where the spin can interact with more than one spin. As we have seen in the three-atom case, this would slow down the decoherence (depolarization). Later, at $\tau \approx 1\ \mu s$, Case II and Case III start to diverge. This is the time regime III when disorder begins to play a role, and detuning between spins makes depolarization difficult to occur, as we have seen in the detuned two-atom case. This gives rise to an overall double-exponential-like behavior, with interaction-dominated dynamics in the early time period and disorder slowing the dynamics later.

5.8 Experimental characterization of many-body spin interaction using ϵ-CPMG sequence

[2]We note that the decoupling of influence from interaction and disorder is not independent. Therefore, it is not strictly correct to simply 'add' the influence from disorder and interaction, as there exist higher-order coupling terms between them. We provide an illustration like this to start with, for intuitive understanding.

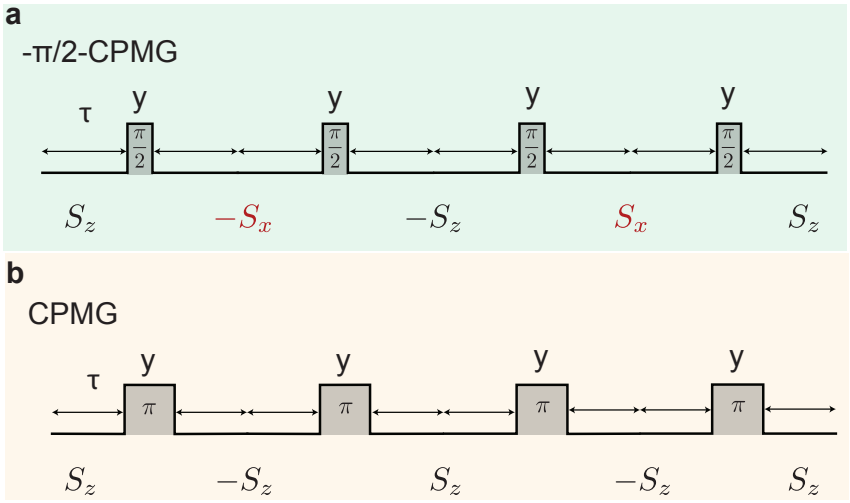

Figure 5.14: **Time-domain transformations of the single-body S_z operator in the toggling frame.** The pulse sequence and the corresponding S_x transformation in the toggling frame for **a,** $-\frac{\pi}{2}$-CPMG sequence and **b,** CPMG sequence.

As we gain a comprehensive understanding of echo measurement, we now turn to more complicated pulse sequences to study many-body interactions. Here, we firstly introduce a recently demonstrated sequence called ϵ-CPMG sequence [136]. On the basis of the normal CPMG sequence [137], a rotation offset ϵ is added to the middle π pulse (Fig. 5.13). This effectively adds a pinning field proportional to ϵ along the $\hat{y}$ direction, which can alter the interplay between interaction and disorder.

Introduction to ϵ-CPMG sequence

Let us analyze the effective Hamiltonian for two extreme cases with $\epsilon = 0$ and $\epsilon = -\frac{\pi}{2}$ in the toggling frame [138]. It is well-known that under the CPMG sequence, the single-body operator alternates between $S^i_{x,y,z}$ and $-S^i_{x,y,z}$, while the two-body operators such as $S^i_x S^j_x$ remain the same (Fig. 5.14). As a result, the disorder is decoupled while the interaction is not. In contrast, for the $-\frac{\pi}{2}$-CPMG sequence, the $\pi/2$ pulse transforms the S_z operator to $-S_x$.The effective zeroth-order approximation of the parent Hamiltonian (Eq. 5.7) then becomes:

$$H_0 = \sum_{i,j}^{N} \frac{J_{ij}}{2} (S^i_y S^j_y + \vec{S}^i \cdot \vec{S}^j) \tag{5.21}$$

where $\vec{S}^i \cdot \vec{S}^j = S^i_x S^j_x + S^i_y S^j_y + S^i_z S^j_z$ is the Heisenberg interaction. We can see that the state after the initial $\pi/2$ pulse is the eigenstate of H_0. Thus, both the interaction and

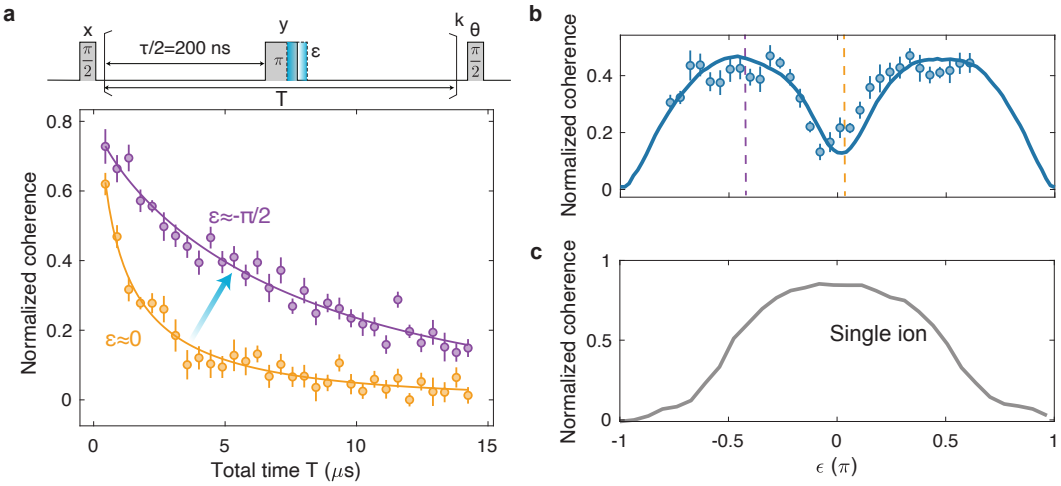

Figure 5.15: **ϵ-CPMG measurement.** For this set of experiments, $\tau/2 = 200$ ns, and a large J is chosen (46 ppm). **a,** For a fixed $\epsilon \approx 0$ (yellow) and $\epsilon \approx -\pi/2$ (purple), we change the loop number k to obtain the normalized coherence relative to the total time T, including the middle pulse length. Here, the coherence is normalized to a constant value, which is the maximum coherence in the spin echo measurement (Fig. 5.5a). Filled dots with error bars represent experimental data, and solid lines are phenomenological stretched exponential fits. **b,** For $k = 5$, the normalized coherence is measured at different ϵ values. Filled dots with error bars represent experimental data, and solid lines are simulated results scaled with a prefactor < 1, independent of ϵ. Dashed vertical lines indicate the location of ϵ for the time traces in **a**. **c,** The ϵ-CPMG measurement in the single-ion case for reference.

disorder are decoupled to zeroth order under the $-\frac{\pi}{2}$-CPMG sequence[3]. However, higher-order terms related to J_{ij} and Δ_i, under Magnus expansion [138, 139], could still depolarize the spins and lead to a decay of the coherence profile. This is indicated by the cross sign with certain transparency in Figure 5.13.

Experimental observation

We then apply an ϵ-CPMG sequence to our platform. Firstly, we study the case with a large J, with $\tau/2 = 200$ ns in the pulse sequence (Fig. 5.15). The coherence is extracted by sweeping the rotation axis θ of the last $\pi/2$ pulse to obtain the contrast and normalizing it to the contribution from the polarization rate $2\eta_{\text{pol}} - 1$, similar to the echo measurement. With a fixed ϵ, we sweep the loop number k to obtain the time traces of normalized coherence, where the total time T includes the varying middle pulse lengths for different ϵ. Comparing $\epsilon \approx 0$ and $\epsilon \approx -\pi/2$, we observe

[3]This analysis holds when k is an integer multiple of 4.

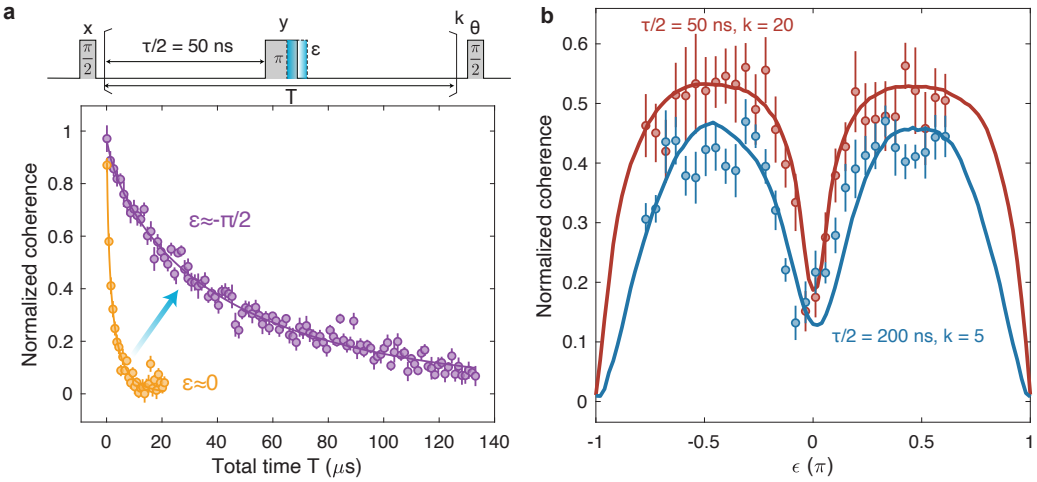

Figure 5.16: **ϵ-CPMG measurement for different τ and k. a,** $\tau/2 = 50$ ns, and a large J is chosen (46 ppm). Normalized coherence relative to total time T is plotted for $\epsilon \approx 0$ (yellow) and $\epsilon \approx -\pi/2$ (purple). **b,** For $\tau/2 = 50$ ns and $k = 20$, the normalized coherence is measured at different ϵ values. The corresponding curve or $\tau/2 = 200$ ns and $k = 5$ are plotted for reference.

that the decay time extends as we change ϵ from 0 to $-\pi/2$, which is attributed to better decoupling for the interaction (Fig 5.15a). Then, with a fixed $k = 5$, we sweep ϵ to observe the double-humped feature [136], as the coherence is maximized at non-zero ϵ (Fig 5.15b). We note that the experimental data matches simulated results well up to a rescale factor, which we attribute to decay due to finite pulse error and excess dephasing. Furthermore, in comparison with the normalized coherence dependence on ϵ for a single ion case (Fig. 5.15c), we can observe that our system exhibits strong interaction characteristics.

The choice of τ and k will affect how effectively the interaction and disorder are decoupled (in other words, how many terms in the Magnus expansion we should retain), thereby influencing the sensitivity to ϵ. As an extreme case, when $\tau \to 0$, the ϵ-CPMG sequence becomes a spin locking sequence (more details in section 5.9), and coherence becomes independent of ϵ. Conversely, when τ or k are too large, the coherence has already vanished, such that almost no features could be observed. Intermediate values of τ and k should be selected to achieve the double-humped feature in the coherence-ϵ dependence. For comparison, a similar measurement to that in Figure 5.15 but with a shorter $\tau/2$ of 50 ns has been conducted (Fig. 5.16a). Compared to the case with $\tau/2 = 200$ ns, the extension of coherence time is even more prominent from $\epsilon \approx 0$ to $\epsilon \approx \pi/2$ for $\tau/2 = 50$ ns, as the interaction has been decoupled more rapidly once $|\epsilon|$ is leveraged. Especially, the decoherence

profile measured at $\tau/2 = 50$ ns and $\epsilon = -\pi/2$ shows a decay time of around 43 μs (Fig. 5.16a), reaching $T_{1,\rho}$, as measured by the spin locking experiment (see section 5.9). In terms of the coherence-ϵ curve, we choose $k = 20$ for the $\tau/2 = 50$ ns condition to ensure that the total free evolution time (excluding pulse length) is the same as in Figure 5.15b. A sharper dip in the center of the double-humped feature has been observed for smaller τ, indicating a greater sensitivity of coherence to ϵ (Fig. 5.16b).

Next, let us examine the difference between large J and small J in the ϵ-CPMG measurement. We pick $\tau/2 = 150$ ns and choose $k = 8$ to satisfy the integer multiple of 4 condition (Fig. 5.17). Firstly, the overall normalized coherence is lower for the large J case. This occurs because, theoretically, even at optimized ϵ, interaction and disorder cannot be perfectly decoupled; hence, it leads to smaller coherence, qualitatively illustrated by simulations (Fig. 5.17b). Experimentally, this difference is even more pronounced, as reflected by the fact that the prefactor required to match the simulation to the experiment is far smaller than 1. We attribute this discrepancy to the larger excess dephasing associated with large J (section 5.9). Secondly, the optimal ϵ for the largest coherence should be slightly further away from 0 for the large J case (Fig. 5.17b), but this difference is too small to be observed in experiment.

5.9 Hamiltonian engineering for exploring rich dynamics

To explore the many-body dynamics in our systems under different Hamiltonians, we further apply various pulse sequences, such as the Waugh-Huber-Haberlen (WAHUHA) echo [138, 140] and spin locking sequences, to probe the decoherence profile.

Engineering Hamiltonian via different pulse sequences

For all of the pulse sequences, the system is initially prepared in the $|\psi(0)\rangle$ state using a rotation around $\hat{x}$ by $\pi/2$, where $|\psi(0)\rangle$ is the fully polarized state along $\hat{y}$: $|\psi(0)\rangle = |y_1...y_i...y_j..\rangle$. After an evolution time T, the system transforms into $|\psi(T)\rangle = U(T,0)\,|\psi(0)\rangle$. The final state is then read out by sweeping the rotation axis θ of the last $\pi/2$ pulse to obtain the remaining polarization along $\hat{y}$ (Fig. 5.18a).

The time evolution operator $U(T,0) = e^{-iH_{\text{av}}T}$ is determined by the applied pulse sequences using average Hamiltonian theory [138, 141]. Here, we only consider the leading-order contribution (zeroth-order Magnus expansion) and assume that the pulses are perfect and infinitely short. Let us then calculate the effective Hamiltonian

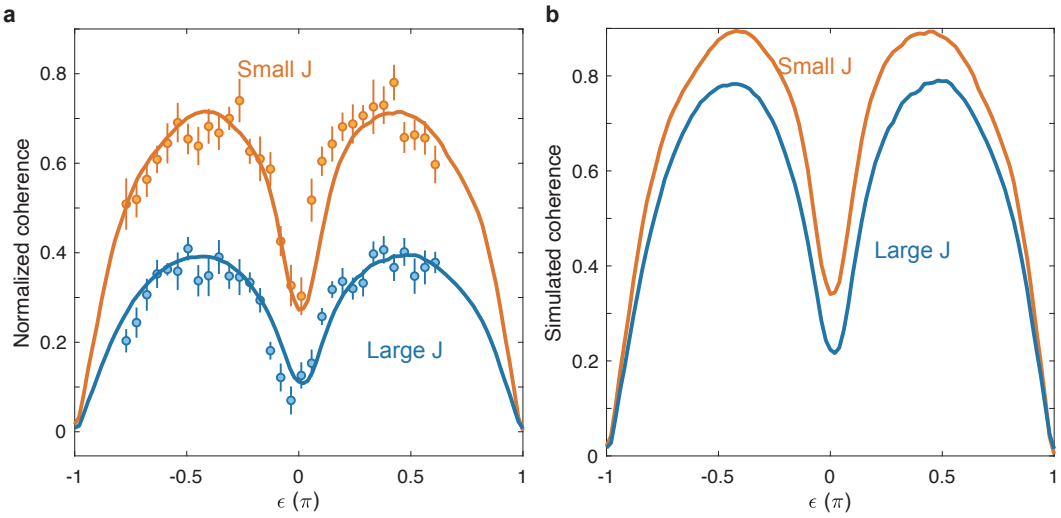

Figure 5.17: **Comparison between large J and small J case for ϵ-CPMG measurement.** For $\tau/2 = 150$ ns and $k = 8$, normalized coherence is measured at different ϵ values for large J (blue) and small J (orange). **a,** Filled dots with error bars represent experimental data, and solid lines are simulated results scaled with a prefactor. **b,** Simulated coherence without rescaling. ϵ steps increment by 0.02 and are smoothed every 7 values.

for each pulse sequence (Fig. 5.18b).

For the Ramsey sequence, the effective Hamiltonian remains the same as the parent Hamiltonian shown in Eq. 5.7, but we can rewrite it as

$$H_{\text{av}}^{\text{Ramsey}} = H_{\text{disorder}}^{\hat{z}} + H_{\text{Heis}} - H_{\text{Ising}}^{\hat{z}} \tag{5.22}$$

where $H_{\text{disorder}}^{\hat{z}} = \sum_i^N \Delta_i S_z^i$ represents the disorder, $H_{\text{Heis}} = \sum_{i,j}^N J_{ij} \vec{S}^i \cdot \vec{S}^j$ represents the Heisenberg interaction, and $H_{\text{Ising}}^{\hat{z}} = \sum_{i,j}^N J_{ij} S_z^i S_z^j$ represents the Ising interaction along $\hat{z}$. Since $|\psi(0)\rangle$ is the eigenstate of H_{Heis} (shown in gray in Fig. 5.18b), in the Ramsey sequence, depolarization is caused by disorder and the Ising interaction along $\hat{z}$.

For the spin echo sequence, the disorder is decoupled to the zeroth order, while the interaction remains the same, which gives us:

$$H_{\text{av}}^{\text{spin echo}} = H_{\text{Heis}} - H_{\text{Ising}}^{\hat{z}}. \tag{5.23}$$

In the WAHUHA echo sequence, not only is the disorder decoupled to the zeroth order by the middle π pulse, but the interaction has also been symmetrized through four $\pi/2$ rotations along $\hat{x}$ and $\hat{y}$. We have that:

$$H_{\text{av}}^{\text{WAHUHA echo}} = \frac{2}{3} H_{\text{Heis}}. \tag{5.24}$$

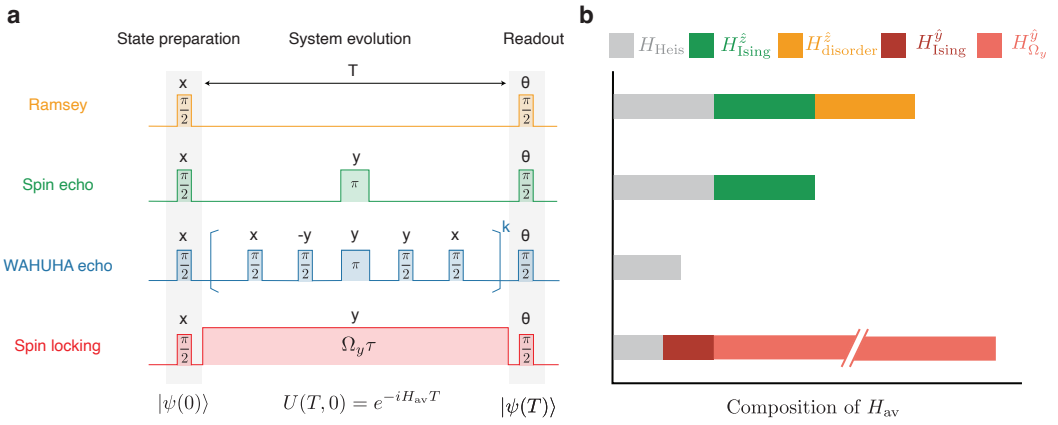

Figure 5.18: **Pulse sequence design for Hamiltonian engineering.** **a,** Pulse sequence for Ramsey, spin echo, WAHUHA echo and spin-locking sequences. **b,** The composition of different components in the leading-order average Hamiltonian $H_{\rm av}$. The lengths of the bars represent the corresponding strengths.

The initial state should be an eigenstate of the above Hamiltonian so that it remains unchanged during the evolution over time.

In the spin locking sequence, a strong Rabi drive Ω_y is applied along $\hat{y}$, resulting in the original Hamiltonian:

$$H = \Omega_y \sum_i^N S_y^i + \sum_i^N \Delta_i S_z^i + \sum_{i,j}^N J_{ij}(S_x^i S_x^j + S_y^i S_y^j). \tag{5.25}$$

We provide two methods here to obtain the effective Hamiltonian while remaining in the same rotating frame. One way is to first apply a unitary transformation with $U_1 = \exp(-i\Omega_y \sum_i^N S_y^i)$, such that we obtain $H_1 = \sum_{i,j}^N \frac{J_{ij}}{2}(\vec{S}^i \cdot \vec{S}^j + S_y^i S_y^j)$ using the rotating-wave approximation. We then transform back by applying $U_1^\dagger$, which gives us $H_0 = \Omega_y \sum_i^N S_y^i + \sum_{i,j}^N \frac{J_{ij}}{2}(\vec{S}^i \cdot \vec{S}^j + S_y^i S_y^j)$. Another way is to follow the procedure as in [142], where we define a new quantization axis along $\hat{y}$ with $S_\pm = S_z \pm iS_x$. $S_x^i S_x^j$ thus can be expressed as $\frac{1}{4}(S_+^i S_-^j + S_-^i S_+^j - S_+^i S_+^j - S_-^i S_-^j)$. Using the secular approximation, we discard energy non-conserving terms $S_+^i S_+^j$, $S_-^i S_-^j$ and S_z^i. We also get the same H_0 as:

$$H_{\rm av}^{\text{spin locking}} = H_0 = H_{\Omega_y}^{\hat{y}} + \frac{1}{2}(H_{\rm Heis} + H_{\rm Ising}^{\hat{y}}) \tag{5.26}$$

where we define $H_{\Omega_y}^{\hat{y}} = \Omega_y \sum_i^N S_y^i$ and $H_{\rm Ising}^{\hat{y}} = \sum_{i,j}^N J_{ij} S_y^i S_y^j$. The initial state is also an eigenstate of the this effective Hamiltonian. The coherence time measured by spin locking sequence is called $T_{1,\rho}$ relaxation time [143]. Using the above

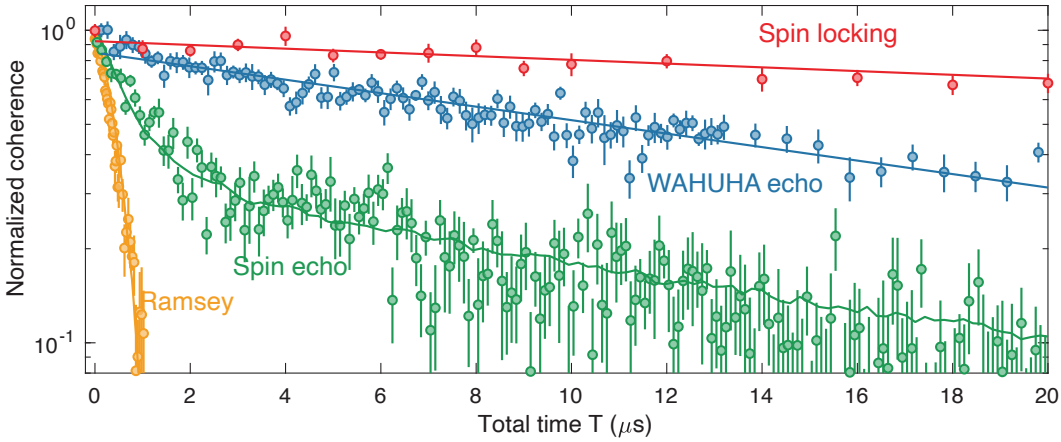

Figure 5.19: **Decoherence profiles for different Hamiltonian engineering.** Filled circles with error bars represent experimental data for the small J case. The solid lines are simulations for Ramsey (yellow) and spin echo (green) measurements, and are single exponential fits for WAHUHA echo (blue) and spin locking (red, $\Omega_y \approx 2\pi \times 10$ MHz) measurements.

expressions, we can clearly see that only the Hamiltonian related to z, indicating a pinning field along $\hat{z}$, could introduce depolarization.

Experimental results

We now examine the decoherence profile to study the system dynamics under different Hamiltonians. We have previously analyzed the Ramsey and echo measurements (refer to section 5.5), where the depolarization sources are $H^{\hat{z}}_{\text{disorder}}$ and $H^{\hat{z}}_{\text{Ising}}$ in Ramsey, and $H^{\hat{z}}_{\text{Ising}}$ in spin echo. For WAHUHA echo and spin locking measurements, theoretically, depolarization should not occur, as the initial state $|\psi(0)\rangle$ is the eigenstate of the Hamiltonian shown in Eq. 5.24 and Eq. 5.26. This is further supported by the fact that numerical simulation shows no decay in the decoherence profile using the method outlined in section 5.6. However, experimentally, decays of 20 μs and 73 μs are extracted by fitting the data to a single exponential decay for the WAHUHA echo and spin locking measurements, respectively (Fig. 5.19). We attribute the decay in the spin locking measurement to excess dephasing, such as nuclear spin noise, while additional factors should be considered for the WAHUHA echo measurement.

Firstly, the higher-order terms in the Magnus expansion are non-zero for the current WAHUHA echo sequence and need to be added to the effective Hamiltonian. Indeed, a symmetrized WAHUHA echo sequence can be designed to cancel higher-order

effects [138]. Secondly, finite pulse duration and spin-manipulation error could lead to imperfect control [138]. Additionally, there is a sweep parameter in the WAHUHA echo sequence, which is the pulse separation τ. The current decoherence profile under the WAHUHA echo sequence is obtained by fixing τ and increasing k to extend T. Different values of τ will lead to decay times in the decoherence profile, and theoretically, a smaller τ is preferred. From the perspective of Hamiltonian engineering, as τ is decreased, Eq. 5.24 becomes more valid since the mth order in the Magnus expansion scales as τ^m, resulting in reduced contributions. From the viewpoint of dynamical decoupling, the interaction has been decoupled more rapidly for smaller τ. However, in the experimental implementation, for a fixed T, the imperfections from finite pulse duration and spin-manipulation errors accumulate more for smaller τ since more pulses are needed. Experimentally sweeping τ to find a decay time dependence is usually necessary to determine the optimized τ (Fig. 5.20a). In our experimental results, with a $\pi/2$ pulse duration of 22 ns, the value of τ that provides the longest coherence time is 22 ns for small J and 33 ns for large J. In the case of small J, the coherence time could be extended if we could implement shorter $\pi/2$ pulse lengths.

Lastly, we compare the decoherence profiles in the spin-locking measurement for large J and small J.We observe a 50 μs decay time for large J and a 73 μs decay time for small J. This difference might be due to an increased dephasing rate in the case of large J, caused by extra heating introduced during the optical initialization when transitioning population from $|\text{Aux}\rangle$ to qubit manifolds.

In summary, this platform provides us with a testbed for various Hamiltonian engineering, enabling us to observe the dynamics under the interplay between different types of interactions and disorder.

5.10 Conclusion and outlook

Our results introduce an ensemble of rare-earth ions as a many-body platform with plenty of future possibilities and applications. Firstly, we probe the interaction-dominated dynamics and observe two distinct decoherence processes, for which we provide a comprehensive analysis using microscopic many-body modeling and toy models. This methodology can be transplanted to other disordered and interacting spin ensembles. Additionally, controlling the interaction strength through optical pumping and modifying the interaction format via Hamiltonian engineering enables us to study the system's response under various conditions, laying the foundation

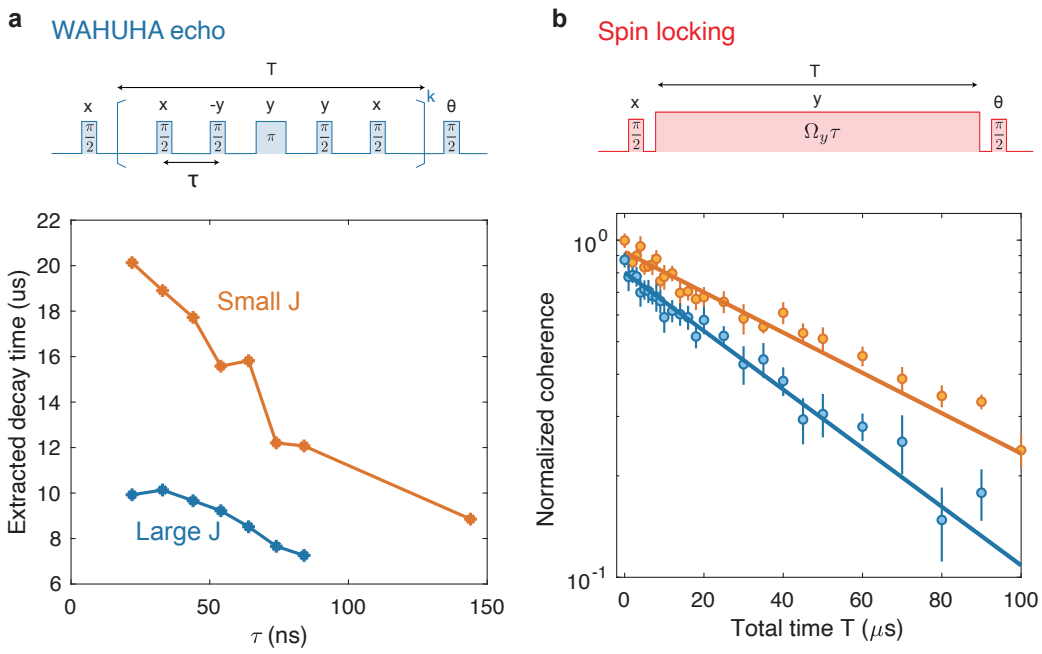

Figure 5.20: **WAHUHA echo and spin locking measurements for large J and small J. a,** The single exponential fit times for the decay in WAHUHA echo measurements as a function of τ are extracted for large J (blue) and small J (orange). **b,** Decoherence profiles for large J (blue) and small J (orange) in the spin locking measurement. Filled circles with error bars represent experimental data, and the solid lines are phenomenological single exponential fits.

for more advanced quantum engineering and quantum simulation.

Rare-earth ion systems have their own specialties for serving as many-body platforms to study fundamental physics and develop quantum simulation. Firstly, operating with rare-earth ion ensembles provides great flexibility, offering a variety of choices for species, host crystal, as well as various doping concentrations, ranging from very dilute samples of tens of ppb to stoichiometric samples. These flexibilities allow us to integrate the ensemble with nanotechnology and scale the system to a large size. Secondly, co-doping different rare-earth ions makes it possible to engineer two species of many-body systems simultaneously and study their interplay [144–146]. Thirdly, we can also form another many-body platform by making use of the nearby nuclei. For example, each Yb ion in our system is surrounded by four protected vanadium registers with longer coherence time and lifetime [147]. Although the vanadium nuclei do not interact with each other directly, the Yb ions interact with each other and with the vanadium. The interaction between the vanadium is then mediated through the Yb ions. Manipulating the interaction and changing the states

of Yb ions are equivalent to controlling the interaction between vanadiums. The vanadium ensemble then forms a highly coherent many-body system with a decent level of interaction.

Reciprocally, many-body studies of rare-earth ions help to understand the mechanism of decoherence and engineer techniques to decouple the interaction, adding significant knowledge to rare-earth ion-based quantum technologies.

Chapter 6

DISCRETE TIME CRYSTAL

In this chapter, we will discuss one of the applications we implemented on the many-body platform that we characterized and discussed in chapter 5. Specifically, we observe the signature of discrete time crystals (DTC), a robust phase of matter in driven systems, resulting from many-body interactions and playing an important role in understanding complex many-body systems. There are a few comprehensive or concise reviews on this topic, such as [4–6]. Here, we will provide a relatively simple introduction and focus more on our experimental observations.

6.1 Introduction

Starting with the well-known space crystal, the Hamiltonian exhibits continuous spatial translation symmetry, remaining invariant under continuous translations in space, while periodic crystals only have discrete translation symmetry. This is an example that the existence of crystals manifests spontaneous symmetry breaking. In the time domain, for a periodically driven system, the Hamiltonian exhibits discrete time-translation symmetry. If this system evolves with a different periodicity, such as subharmonics, then the broken discrete time-translation symmetry indicates the formation of a DTC. We notice that subharmonic behaviors are ubiquitous, such as in spin echo measurements and parametric down conversion. However, the existence of a DTC requires the subharmonic behavior to be robust in the parameter space without requiring fine-tuning [148–151].

There are different mechanisms for achieving DTCs. The canonical ones are realized by many-body localization (MBL), which has been experimentally demonstrated in one-dimensional systems such as trapped ions [152], ^{13}C nuclear spins in diamond [153], and superconducting qubits [154]. Other types include prethermal DTC [155, 156], dissipative DTC [157, 158], and slow-decaying DTC [125, 159].

In our study, we focus on rare-earth ions doped in solids, specifically $^{171}Yb^{3+}$:YVO_4, to probe the signatures of discrete time crystals. Our system, comprised of three-dimensional spins interacting via long-range dipolar interaction, exhibits certain similarities to the NV centers in diamond [125], enabling us to realize the same type of DTC [160]. Meanwhile, the inherent existence of spin-exchange interaction in

our system provides some special features to the field.

6.2 Experimental demonstration

As shown in section 5.9, we can engineer different Hamiltonians through pulse sequence design. Especially, the spin locking sequence gives us $T_{1,\rho}$ of 50 μs for large J and 73 μs for small J. This long relaxation time provides us with a good starting point to observe system behavior at longer time scales after periodically inserting $\pi(1+\epsilon)$ rotations into the spin-locking sequence to perform Floquet driving. Starting with a $\pi/2$ rotation around $\hat{x}$ to prepare the spins along $\hat{y}$, we then apply a Floquet pulse sequence as illustrated in Figure 6.1 and observe the spin dynamics along $\hat{y}$. The Floquet operation includes continuous microwave driving along $\hat{y}$ and a rotation of $\pi(1+\epsilon)$ around $\hat{x}$. During continuous microwave driving (spin locking) with a Rabi frequency of $\Omega_y = 2\pi \times 11.7$ MHz for a period of time τ (interaction time), the system is governed by the effective system Hamiltonian:

$$H_{\text{eff}} = H^{\hat{y}}_{\Omega_y} + \frac{1}{2}(H_{\text{Heis}} + H^{\hat{y}}_{\text{Ising}}), \tag{6.1}$$

as derived in Eq. 5.26. The following rotation around the $\hat{x}$ axis flips the spin polarization between $\hat{y}$ and $-\hat{y}$ for every period, with an additional angle of $\pi\epsilon$. After repeating this Floquet operation k times, the remaining polarization along $\hat{y}$ is finally read out.

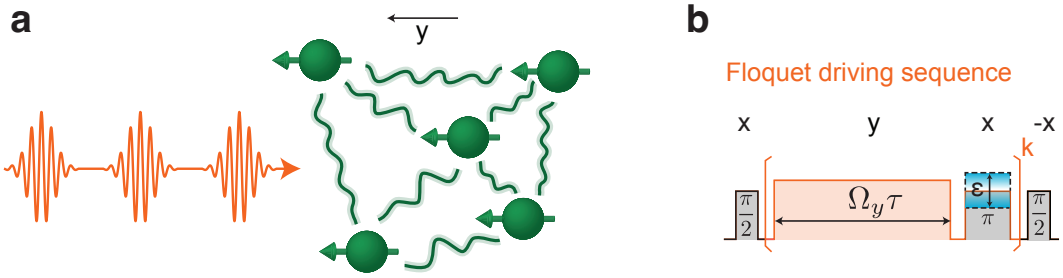

Figure 6.1: **Schematics for DTC. a,** Illustration of spin interactions along $\hat{y}$ under periodic driving. **b,** All spins are initialized into states along the $\hat{y}$ axis by a rotation of $\pi/2$ around $\hat{x}$, followed by the Floquet operation repeated k times. This operation involves spin locking along the $\hat{y}$ axis for a time τ and a $\pi(1+\epsilon)$ rotation around $\hat{x}$. The system is then read out by rotating back to the $\hat{z}$ direction using a $\pi/2$ rotation around $-\hat{x}$.

We analyze the final polarization for different values of τ and ϵ in both the time and frequency domains (Fig. 6.2). Here, frequency spectra are obtained by taking the Fourier transform of the time traces and normalized to the entire area of each

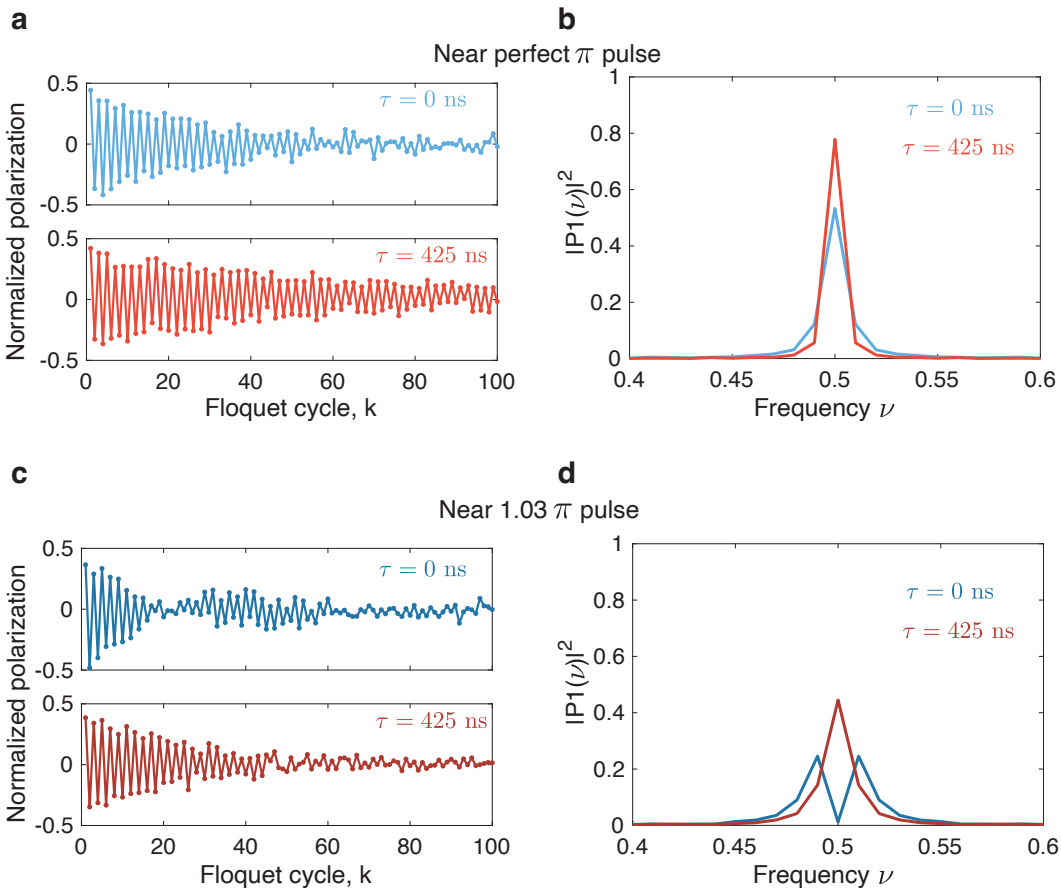

Figure 6.2: **Representative time traces and Fourier transform spectra. a,** Time traces using nearly π pulse with $\tau = 0$ ns (light blue) and $\tau = 425$ ns (light red). **b,** Corresponding Fourier transform spectra for **c**, which have been normalized to the area of the spectra. **a,** Time traces using nearly 1.03π pulse with $\tau = 0$ ns (dark blue) and $\tau = 425$ ns (dark red). **d,** Corresponding Fourier transform spectra for **c**.

spectrum. We choose τ to satisfy $\Omega_y \tau = 2\pi n$, where n is an integer number, to avoid accidental dynamical decoupling [125, 160]. Figure 6.2 shows the representative time traces and Fourier transform spectra in experiments. The straightforward case is that when nearly perfect π pulses are applied, different values of τ exhibit similar behavior. We observe the total polarization alternating between positive and negative values in time traces, with a corresponding subharmonic peak at $\nu = 1/2$ in the frequency domain. In contrast, when a certain amount of perturbation ϵ (e.g., $\epsilon \approx 0.03$) is added to the π pulse, the spin dynamics becomes highly dependent on τ. For $\tau = 0$ ns, there appears the beating on the basis of 2T-periodic response, resulting in a splitting of peaks at $\nu = 1/2 \pm \epsilon/2$. As τ increases, the subharmonic behavior is recovered, corresponding to a stabilized $\nu = 1/2$ peak in the frequency

domain (Fig. 6.2c, d).

The stabilization of this subharmonic behavior is then systematically studied by sweeping τ and ϵ. In the Fourier spectrum, the normalized intensity at $\nu = 1/2$ ($|P(\nu = 1/2)|^2$), which indicates the crystalline fraction, is extracted for a given τ and ϵ. A phase diagram is thus obtained to show the degree of the periodic order in the parameter space (Fig. 6.3). We roughly draw the red dashed line in Figure 6.3 to denote the phase boundary, where the system becomes more robust to the perturbation ϵ as the interaction time τ increases.

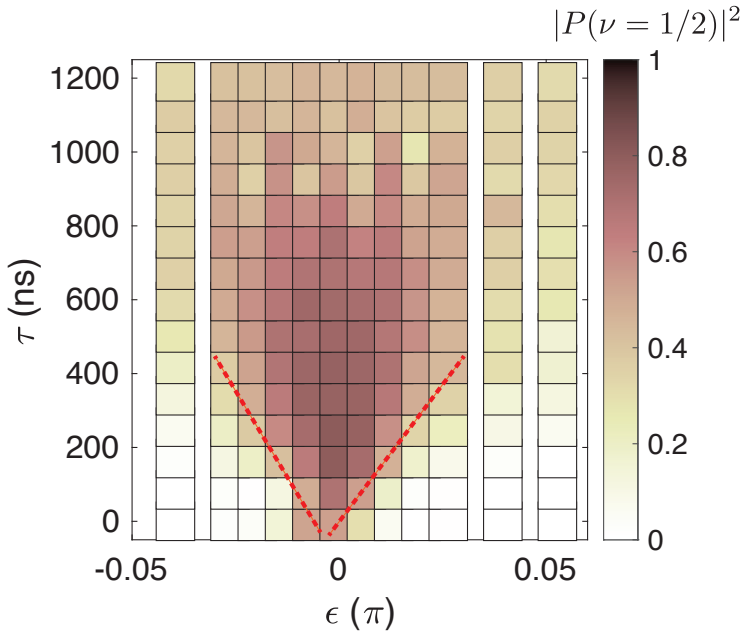

Figure 6.3: **DTC phase diagram.**

To understand the role of the interaction in stabilizing the subharmonic behavior, we notice that the Ising interaction $H_{\text{Ising}}^{\hat{y}}$ appears in the effective Hamiltonian during the time period τ (Eq. 6.1). Based on previous studies on 3D dipolar interaction spins [125, 160], we know that the Ising interaction stabilizes the DTC phase. The addition in our system is the Heisenberg interaction H_{Heis}, and it turns out that the existence of both Ising and Heisenberg interactions can also stabilize the DTC phase.

6.3 Comparing phase boundaries for different interaction strengths J

Next, let us take a closer look at the phase boundary by quantitatively defining it at $|P(\nu = 1/2)|^2 = 0.4$ point and comparing it for the different interaction strengths

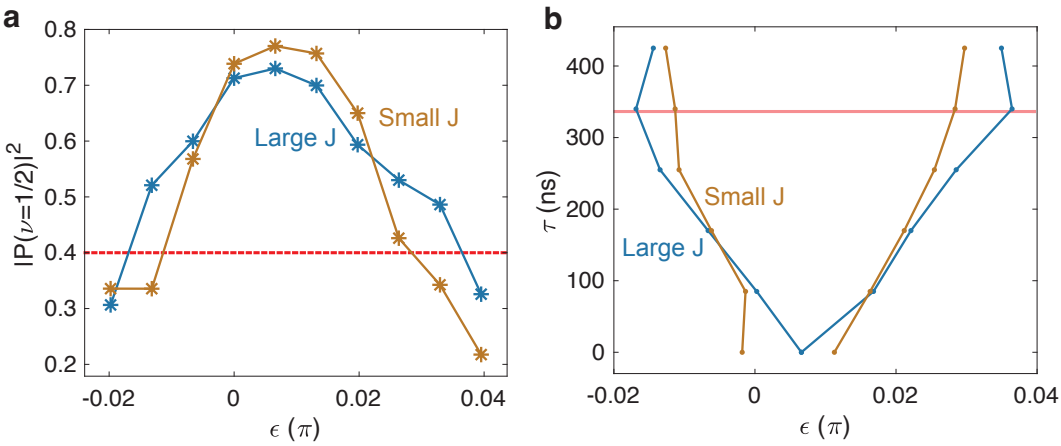

Figure 6.4: **Phase boundaries for large and small J. a,** $|P(\nu = 1/2)|^2$ in Fourier transform spectra at different ϵ for $\tau = 340$ ns in large J (blue) and small J (orange) cases. The dashed red line indicates $|P(\nu = 1/2)|^2 = 0.4$. **b,** Extracted phase boundary in large J (blue) and small J (orange) cases. The transparent red line indicates the condition where **a** is shown.

J. Specifically, the normalized intensity at $\nu = 1/2$, $|P(\nu = 1/2)|^2$, in the Fourier transform spectrum is plotted as a function of ϵ for a given τ. By intersecting it with $|P(\nu = 1/2)|^2 = 0.4$, we find the ϵ_c value at the phase boundary for this τ, where linear interpolation is applied to the $|P(\nu = 1/2)|^2$-ϵ dependence curve (Fig. 6.4a). In the comparison of the phase boundaries for large and small J, we can observe that the large J case has a wider DTC phase area (Fig. 6.4b). This is because larger interactions have a better ability to prevent the system from thermalization, thus making it more robust to perturbations. The above observation supports the argument that interaction is the cause of stabilizing the subharmonic behavior, and reciprocally provides further examination of our strongly interacting system.

6.4 Robustness to the initial states

Finally, we investigate the robustness of our DTC phase relative to the initial states. Different initial states are prepared by rotating a varying angle ϕ of the first pulse in the spin control sequence (Fig. 6.5a). For each initial state, we then sweep ϵ and τ to generate a phase diagram (Fig. 6.5b-f). In the experimental results, a robust DTC phase appears for those initial states with $|\phi - \pi/2| \leq \pi/4$ (Fig. 6.5d-f). For $\phi = 0$ and $\phi = \pi/8$, the subharmonic pattern only exists in a small area of the parameter space (Fig. 6.5b,c). In these cases, it is likely that the temperature determined by the initial state is too high for the interaction to stabilize the subharmonic behavior. Furthermore, for the cases of $\phi = \pi/4$, $3\pi/8$, and $\pi/2$, the corresponding phase

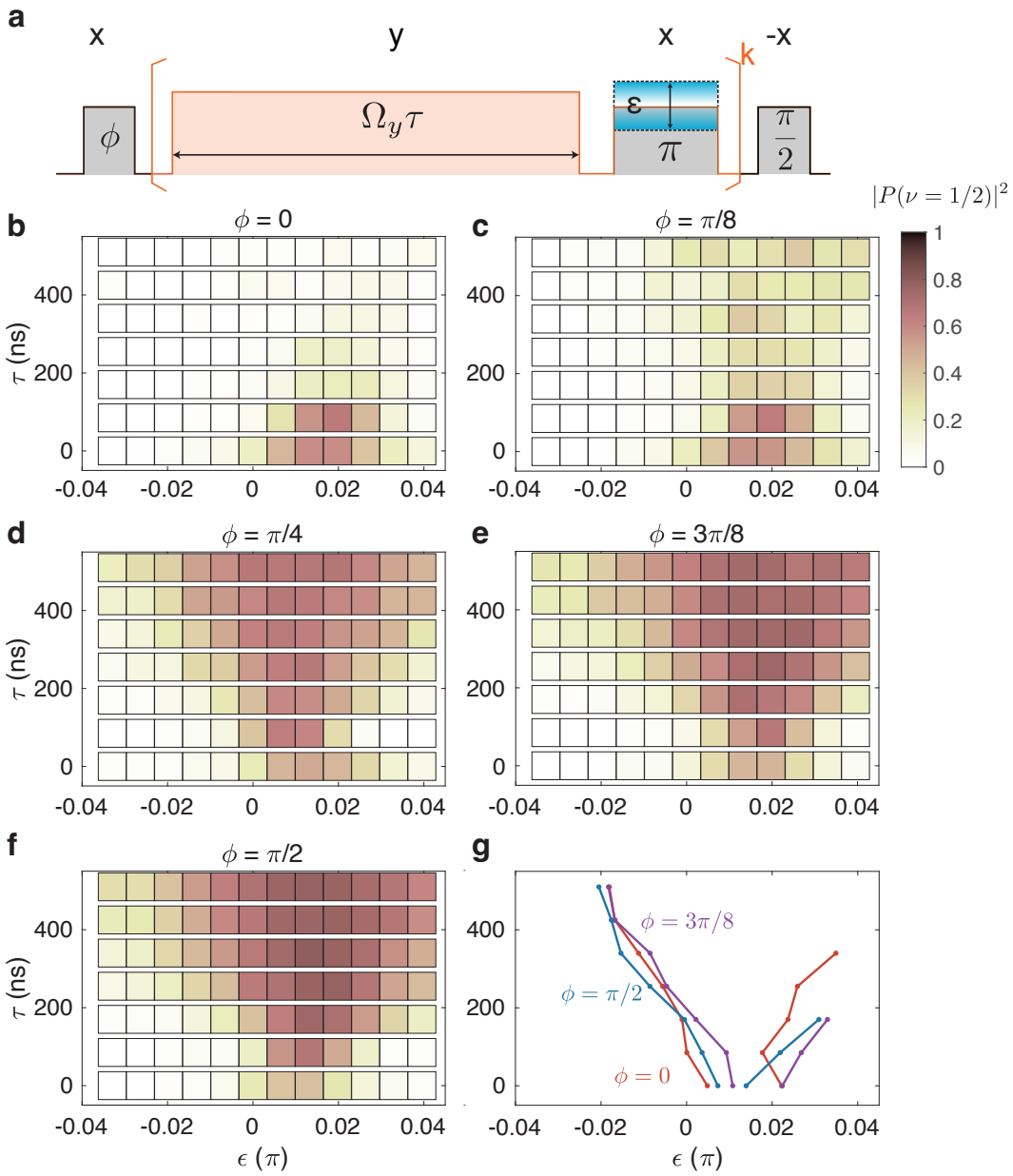

Figure 6.5: **Robustness of DTC phase to the initial states.** **a,** Spin control sequence with different initial rotations of ϕ to prepare various initial states. **b-f,** Phase diagram for different initial rotations of ϕ. **g,** Phase boundaries for **d-f**. We note that **b-g** share the same x-axis and y-axis ranges.

boundaries are extracted using the condition $|P(\nu = 1/2)|^2 = 0.4$ (Fig. 6.5g). We can see that the slope of the phase boundaries is similar for different ϕ, indicating a robustness relative to the initial states.

6.5 Conclusion and outlook

To conclude, we observe a signature of DTC in the rare-earth ions system, which serves as an example of the applications in our system as a many-body platform. The inherent spin-exchange interaction, the large ratio between interaction strength and disorder, and the tunability of interaction strength distinguish our system from other solid-state spins, and provide new possibilities in the field of DTC. Here, we focus on spin locking driving in the Floquet operation, while other pulse designs have been implemented for Hamiltonian engineering (section 5.9), enabling us to integrate them for studying subharmonic behavior under periodic driving. For example, we can also study the system's phase diagram under the spin exchange interaction or the Heisenberg interaction, with or without disorder. Those studies can broaden the mechanism for realizing DTC.

Chapter 7

FUTURE DIRECTIONS

From chapter 3 to chapter 6, we investigate many-body physics in an ensemble of rare-earth ions, specifically $^{171}Yb^{3+}$:YVO, ranging from novel optical cavity QED phenomena to dynamics of strongly interacting spins. Different from conventional methods for studying rare-earth ions, such as engineering highly quantum memories or characterizing the spectroscopy of materials, we provide insights for studying these systems from a more fundamental perspective, thus opening the door to several future directions. In this chapter, we will briefly enumerate some possible directions to explore.

7.1 Narrower structure using CIT

The sharp feature (CIT) we discovered in chapter 3 occurs under the most basic conditions, where continuous wave driving is applied and the ions start with a natural distribution with inhomogeneous broadening. To extend this work, we can prepare the ions with some spectral structure, such as using hole-burning technique to create a narrow feature. When we probe this hole via cavity reflection, an even narrower structure is expected, referring to the fact that the inhomogeneous linewidth has been narrowed by a factor of C, the ensemble cooperativity, in CIT. Indeed, we have utilized optical pumping in chapter 4 and chapter 5 to modify the ion population, providing grounds for further spectral tailoring.

7.2 Cavity-mediated interaction in the detuned cavity regime

The superradiance and subradiance studied in chapter 4 arise through dissipative interactions mediated by the cavity field. This occurs when the cavity is in resonance with the frequencies of the ions. When the cavity is tuned off resonance, coherent interactions between ions can be engineered (Eq. 4.5). Indeed, we have demonstrated a tens of GHz increment in our cavity tunability (Fig. 3.9), such that controlling this coherent interaction is possible.

7.3 Discrete time crystal for spins in optical excited states

The f_e transition in Figure 5.3 is also a clock transition and could be controlled using microwaves at 3.37 GHz. We currently only use this transition for initialization

using a π pulse, but more complicated spin control can be implemented. The dipolar interaction strength between these spins is $J \cdot r^3 = 2\pi \times 81.8$ MHz (Eq. 5.8 for spins in ground states). Although the spin lifetime will be limited by the optical lifetime, thanks to the subradiance regime, the spins can remain in the optical excited state for up to the bulk lifetime (267 μs). To this end, it will be interesting to look at the interaction-induced dynamics for those spins and the possibility of realizing a discrete time crystal.

BIBLIOGRAPHY

[1] Philip W Anderson. "More Is Different: Broken symmetry and the nature of the hierarchical structure of science." In: *Science* 177.4047 (1972), pp. 393–396.

[2] Anatoli Polkovnikov, Krishnendu Sengupta, Alessandro Silva, and Mukund Vengalattore. "Colloquium: Nonequilibrium dynamics of closed interacting quantum systems". In: *Rev. Mod. Phys.* 83 (3 Aug. 2011), pp. 863–883. DOI: 10.1103/RevModPhys.83.863.

[3] Anatoli Polkovnikov, Krishnendu Sengupta, Alessandro Silva, and Mukund Vengalattore. "Colloquium: Nonequilibrium dynamics of closed interacting quantum systems". In: *Reviews of Modern Physics* 83.3 (2011), p. 863.

[4] Michael P Zaletel, Mikhail Lukin, Christopher Monroe, Chetan Nayak, Frank Wilczek, and Norman Y Yao. "Colloquium: Quantum and classical discrete time crystals". In: *Reviews of Modern Physics* 95.3 (2023), p. 031001.

[5] Dominic V Else, Christopher Monroe, Chetan Nayak, and Norman Y Yao. "Discrete time crystals". In: *Annual Review of Condensed Matter Physics* 11 (2020), pp. 467–499.

[6] Norman Y Yao and Chetan Nayak. "Time crystals in periodically driven systems". In: *Physics Today* 71.9 (2018), pp. 40–47.

[7] Guokui Liu and Bernard Jacquier. *Spectroscopic properties of rare earths in optical materials*. Vol. 83. Springer Science & Business Media, 2006.

[8] Jonathan M. Kindem, John G. Bartholomew, Philip J. T. Woodburn, Tian Zhong, Ioana Craiciu, Rufus L. Cone, Charles W. Thiel, and Andrei Faraon. "Characterization of $^{171}Yb^{3+}$: YVO_4 for photonic quantum technologies". In: *Phys. Rev. B* 98 (2 July 2018), p. 024404.

[9] Antonio Ortu, Alexey Tiranov, Sacha Welinski, Florian Fröwis, Nicolas Gisin, Alban Ferrier, Philippe Goldner, and Mikael Afzelius. "Simultaneous coherence enhancement of optical and microwave transitions in solid-state electronic spins". In: *Nature materials* 17.8 (2018), pp. 671–675.

[10] David D. Awschalom, Ronald Hanson, Jörg Wrachtrup, and Brian B. Zhou. "Quantum technologies with optically interfaced solid-state spins". In: *Nature Photonics* 12.9 (Sept. 2018), pp. 516–527. ISSN: 1749-4893. DOI: 10.1038/s41566-018-0232-2.

[11] Serge Haroche and Daniel Kleppner. "Cavity Quantum Electrodynamics". In: *Physics Today* 42.1 (1989), pp. 24–30. DOI: 10.1063/1.881201.

[12] Herbert Walther, Benjamin TH Varcoe, Berthold-Georg Englert, and Thomas Becker. "Cavity quantum electrodynamics". In: *Reports on Progress in Physics* 69.5 (2006), p. 1325.

[13] Alexandre Blais, Arne L. Grimsmo, S. M. Girvin, and Andreas Wallraff. "Circuit quantum electrodynamics". In: *Rev. Mod. Phys.* 93 (2 May 2021), p. 025005. DOI: 10.1103/RevModPhys.93.025005.

[14] L.-M. Duan and H. J. Kimble. "Scalable Photonic Quantum Computation through Cavity-Assisted Interactions". In: *Phys. Rev. Lett.* 92 (12 Mar. 2004), p. 127902. DOI: 10.1103/PhysRevLett.92.127902.

[15] Tamara Dordević, Polnop Samutpraphoot, Paloma L. Ocola, Hannes Bernien, Brandon Grinkemeyer, Ivana Dimitrova, Vladan Vuletić, and Mikhail D. Lukin. "Entanglement transport and a nanophotonic interface for atoms in optical tweezers". In: *Science* 373.6562 (2021), pp. 1511–1514.

[16] Martin Mücke, Eden Figueroa, Joerg Bochmann, Carolin Hahn, Karim Murr, Stephan Ritter, Celso J. Villas-Boas, and Gerhard Rempe. "Electromagnetically induced transparency with single atoms in a cavity". In: *Nature* 465.7299 (June 2010), pp. 755–758. ISSN: 1476-4687. DOI: 10.1038/nature09093.

[17] Dirk Englund, Andrei Faraon, Ilya Fushman, Nick Stoltz, Pierre Petroff, and Jelena Vučković. "Controlling cavity reflectivity with a single quantum dot". In: *Nature* 450.7171 (Dec. 2007), pp. 857–861.

[18] Matthias Keller, Birgit Lange, Kazuhiro Hayasaka, Wolfgang Lange, and Herbert Walther. "Continuous generation of single photons with controlled waveform in an ion-trap cavity system". In: *Nature* 431.7012 (Oct. 2004), pp. 1075–1078. ISSN: 1476-4687. DOI: 10.1038/nature02961.

[19] H Jeff Kimble. "The quantum internet". In: *Nature* 453.7198 (2008), pp. 1023–1030.

[20] Mikael Afzelius and Christoph Simon. "Impedance-matched cavity quantum memory". In: *Phys. Rev. A* 82 (2 Aug. 2010), p. 022310. DOI: 10.1103/PhysRevA.82.022310.

[21] Andreas Reiserer and Gerhard Rempe. "Cavity-based quantum networks with single atoms and optical photons". In: *Rev. Mod. Phys.* 87 (4 Dec. 2015), pp. 1379–1418.

[22] RJ Thompson, Gerhard Rempe, and HJ Kimble. "Observation of normal-mode splitting for an atom in an optical cavity". In: *Physical review letters* 68.8 (1992), p. 1132.

[23] T. Yoshie, A. Scherer, J. Hendrickson, G. Khitrova, H. M. Gibbs, G. Rupper, C. Ell, O. B. Shchekin, and D. G. Deppe. "Vacuum Rabi splitting with a single quantum dot in a photonic crystal nanocavity". In: *Nature* 432.7014 (Nov. 2004), pp. 200–203.

[24] J. A. Mlynek, A. A. Abdumalikov, C. Eichler, and A. Wallraff. "Observation of Dicke superradiance for two artificial atoms in a cavity with high decay rate". In: *Nature Communications* 5.1 (Nov. 2014), p. 5186.

[25] Mohammad Mirhosseini, Eunjong Kim, Xueyue Zhang, Alp Sipahigil, Paul B. Dieterle, Andrew J. Keller, Ana Asenjo-Garcia, Darrick E. Chang, and Oskar Painter. "Cavity quantum electrodynamics with atom-like mirrors". In: *Nature* 569.7758 (May 2019), pp. 692–697. ISSN: 1476-4687. DOI: 10.1038/s41586-019-1196-1.

[26] R. E. Evans, M. K. Bhaskar, D. D. Sukachev, C. T. Nguyen, A. Sipahigil, M. J. Burek, B. Machielse, G. H. Zhang, A. S. Zibrov, E. Bielejec, H. Park, M. Lončar, and M. D. Lukin. "Photon-mediated interactions between quantum emitters in a diamond nanocavity". In: *Science* 362.6415 (2018), pp. 662–665. DOI: 10.1126/science.aau4691.

[27] Matthew A. Norcia, Robert J. Lewis-Swan, Julia R. K. Cline, Bihui Zhu, Ana M. Rey, and James K. Thompson. "Cavity-mediated collective spin-exchange interactions in a strontium superradiant laser". In: *Science* 361.6399 (2018), pp. 259–262.

[28] Andreas Angerer, Kirill Streltsov, Thomas Astner, Stefan Putz, Hitoshi Sumiya, Shinobu Onoda, Junichi Isoya, William J Munro, Kae Nemoto, Jörg Schmiedmayer, et al. "Superradiant emission from colour centres in diamond". In: *Nature Physics* 14.12 (2018), pp. 1168–1172.

[29] Avikar Periwal, Eric S Cooper, Philipp Kunkel, Julian F Wienand, Emily J Davis, and Monika Schleier-Smith. "Programmable interactions and emergent geometry in an array of atom clouds". In: *Nature* 600.7890 (2021), pp. 630–635.

[30] Martin Blaha, Aisling Johnson, Arno Rauschenbeutel, and Jürgen Volz. "Beyond the Tavis-Cummings model: Revisiting cavity QED with ensembles of quantum emitters". In: *Phys. Rev. A* 105 (1 Jan. 2022), p. 013719.

[31] Vasily V. Temnov and Ulrike Woggon. "Superradiance and Subradiance in an Inhomogeneously Broadened Ensemble of Two-Level Systems Coupled to a Low-Q Cavity". In: *Phys. Rev. Lett.* 95 (24 Dec. 2005), p. 243602.

[32] C. Greiner, B. Boggs, and T. W. Mossberg. "Superradiant Emission Dynamics of an Optically Thin Material Sample in a Short-Decay-Time Optical Cavity". In: *Phys. Rev. Lett.* 85 (18 Oct. 2000), pp. 3793–3796.

[33] C.W. Thiel, Thomas Böttger, and R.L. Cone. "Rare-earth-doped materials for applications in quantum information storage and signal processing". In: *Journal of Luminescence* 131.3 (2011). Selected papers from DPC'10, pp. 353–361.

[34] Tian Zhong, Jake Rochman, Jonathan M. Kindem, Evan Miyazono, and Andrei Faraon. "High quality factor nanophotonic resonators in bulk rare-earth doped crystals". In: *Opt. Express* 24.1 (Jan. 2016), pp. 536–544.

[35] M. Businger, L. Nicolas, T. Sanchez Mejia, A. Ferrier, P. Goldner, and Mikael Afzelius. “Non-classical correlations over 1250 modes between telecom photons and 979-nm photons stored in 171Yb3+:Y2SiO5”. In: *Nature Communications* 13.1 (Oct. 2022), p. 6438.

[36] Nikolai Lauk, Neil Sinclair, Shabir Barzanjeh, Jacob P Covey, Mark Saffman, Maria Spiropulu, and Christoph Simon. “Perspectives on quantum transduction”. In: *Quantum Science and Technology* 5.2 (Mar. 2020), p. 020501.

[37] Daniel A Steck. “Quantum and atom optics”. In: (2007).

[38] E.T. Jaynes and F.W. Cummings. “Comparison of quantum and semiclassical radiation theories with application to the beam maser”. In: *Proceedings of the IEEE* 51.1 (1963), pp. 89–109.

[39] Michael Tavis and Frederick W. Cummings. “Exact Solution for an N-Molecule—Radiation-Field Hamiltonian”. In: *Phys. Rev.* 170 (2 June 1968), pp. 379–384.

[40] I. Diniz, S. Portolan, R. Ferreira, J. M. Gérard, P. Bertet, and A. Auffèves. “Strongly coupling a cavity to inhomogeneous ensembles of emitters: Potential for long-lived solid-state quantum memories”. In: *Phys. Rev. A* 84 (6 Dec. 2011), p. 063810.

[41] Evan Miyazono, Ioana Craiciu, Amir Arbabi, Tian Zhong, and Andrei Faraon. “Coupling erbium dopants in yttrium orthosilicate to silicon photonic resonators and waveguides”. In: *Optics express* 25.3 (2017), pp. 2863–2871.

[42] Ioana Craiciu, Mi Lei, Jake Rochman, John G Bartholomew, and Andrei Faraon. “Multifunctional on-chip storage at telecommunication wavelength for quantum networks”. In: *Optica* 8.1 (2021), pp. 114–121.

[43] H.-J. Briegel, W. Dür, J. I. Cirac, and P. Zoller. “Quantum Repeaters: The Role of Imperfect Local Operations in Quantum Communication”. In: *Phys. Rev. Lett.* 81 (26 Dec. 1998), pp. 5932–5935. DOI: 10.1103/PhysRevLett.81.5932. URL: https://link.aps.org/doi/10.1103/PhysRevLett.81.5932.

[44] H J Kimble. “The quantum internet”. In: *Nature* 453 (2008), pp. 1023–1030. DOI: 10.1038/nature07127.

[45] K. Heshami, D. G. England, P. C. Humphreys, P. J. Bustard, V. M. Acosta, J. Nunn, and B. J. Sussman. “Quantum memories: Emerging applications and recent advances”. In: *J. Mod. Opt.* 63.20 (2016), pp. 2005–2028. DOI: 10.1080/09500340.2016.1148212. URL: https://doi.org/10.1080/09500340.2016.1148212.

[46] Thomas Böttger, Y. Sun, C. W. Thiel, and R. L. Cone. "Spectroscopy and dynamics of Er^{3+}:Y_2SiO_5 at 1.5μm". In: *Phys. Rev. B* 74 (7 Aug. 2006), p. 075107. DOI: 10.1103/PhysRevB.74.075107. URL: https://link.aps.org/doi/10.1103/PhysRevB.74.075107.

[47] Thomas Böttger, C. W. Thiel, R. L. Cone, and Y. Sun. "Effects of magnetic field orientation on optical decoherence in Er^{3+}:Y_2SiO_5". In: *Phys. Rev. B* 79 (11 Mar. 2009), p. 115104. DOI: 10.1103/PhysRevB.79.115104. URL: https://link.aps.org/doi/10.1103/PhysRevB.79.115104.

[48] A. M. Dibos, M. Raha, C. M. Phenicie, and J. D. Thompson. "Atomic Source of Single Photons in the Telecom Band". In: *Phys. Rev. Lett.* 120 (24 June 2018), p. 243601. DOI: 10.1103/PhysRevLett.120.243601. URL: https://link.aps.org/doi/10.1103/PhysRevLett.120.243601.

[49] Miloš Rančić, Morgan P. Hedges, Rose L. Ahlefeldt, and Matthew J. Sellars. "Coherence time of over a second in a telecom-compatible quantum memory storage material". In: *Nat. Phys.* 14 (2018), pp. 50–54. DOI: 10.1038/nphys4254.

[50] Erhan Saglamyurek, Jeongwan Jin, Varun B. Verma, Matthew D. Shaw, Francesco Marsili, Sae Woo Nam, Daniel Oblak, and Wolfgang Tittel. "Quantum storage of entangled telecom-wavelength photons in an erbium-doped optical fibre". In: *Nat. Photonics* 9 (2015), pp. 83–87. DOI: 10.1038/nphoton.2014.311.

[51] Mohsen Falamarzi Askarani, Marcel.li Grimau Puigibert, Thomas Lutz, Varun B. Verma, Matthew D. Shaw, Sae Woo Nam, Neil Sinclair, Daniel Oblak, and Wolfgang Tittel. "Storage and Reemission of Heralded Telecommunication-Wavelength Photons Using a Crystal Waveguide". In: *Phys. Rev. Appl.* 11 (5 May 2019), p. 054056. DOI: 10.1103/PhysRevApplied.11.054056. URL: https://link.aps.org/doi/10.1103/PhysRevApplied.11.054056.

[52] Björn Lauritzen, J. Miná ř, Hugues de Riedmatten, Mikael Afzelius, Nicolas Sangouard, Christoph Simon, and Nicolas Gisin. "Telecommunication-Wavelength Solid-State Memory at the Single Photon Level". In: *Phys. Rev. Lett.* 104 (8 Feb. 2010), p. 080502. DOI: 10.1103/PhysRevLett.104.080502. URL: https://link.aps.org/doi/10.1103/PhysRevLett.104.080502.

[53] Björn Lauritzen, J. Miná ř, Hugues de Riedmatten, Mikael Afzelius, and Nicolas Gisin. "Approaches for a quantum memory at telecommunication wavelengths". In: *Phys. Rev. A* 83 (1 Jan. 2011), p. 012318. DOI: 10.1103/PhysRevA.83.012318. URL: https://link.aps.org/doi/10.1103/PhysRevA.83.012318.

[54] Julián Dajczgewand, Jean-Louis Le Gouët, Anne Louchet-Chauvet, and Thierry Chanelière. "Large efficiency at telecom wavelength for optical quantum memories". In: *Opt. Lett.* 39.9 (May 2014), pp. 2711–2714. DOI: 10.1364/OL.39.002711. URL: http://ol.osa.org/abstract.cfm?URI=ol-39-9-2711.

[55] Ioana Craiciu, Mi Lei, Jake Rochman, Jonathan M. Kindem, John G. Bartholomew, Evan Miyazono, Tian Zhong, Neil Sinclair, and Andrei Faraon. "Nanophotonic Quantum Storage at Telecommunication Wavelength". In: *Phys. Rev. Appl.* 12 (2 Aug. 2019), p. 024062. DOI: 10.1103/PhysRevApplied.12.024062. URL: https://link.aps.org/doi/10.1103/PhysRevApplied.12.024062.

[56] Gavin Brennen, Elisabeth Giacobino, and Christoph Simon. "Focus on Quantum Memory". In: *New J. Phys.* 17.5 (May 2015), p. 050201. DOI: 10.1088/1367-2630/17/5/050201. URL: https://doi.org/10.1088/1367-2630/17/5/050201.

[57] Morgan P Hedges, Jevon J Longdell, Yongmin Li, and Matthew J Sellars. "Efficient quantum memory for light". In: *Nature* 465.7301 (2010), pp. 1052–1056. ISSN: 1476-4687. DOI: 10.1038/nature09081. URL: https://doi.org/10.1038/nature09081.

[58] Daniel Schraft, Marcel Hain, Nikolaus Lorenz, and Thomas Halfmann. "Stopped Light at High Storage Efficiency in a Pr^{3+}:Y_2SiO_5 Crystal". In: *Phys. Rev. Lett.* 116 (7 Feb. 2016), p. 073602. DOI: 10.1103/PhysRevLett.116.073602. URL: https://link.aps.org/doi/10.1103/PhysRevLett.116.073602.

[59] Adrian Holzäpfel, Jean Etesse, Krzysztof T Kaczmarek, Alexey Tiranov, Nicolas Gisin, and Mikael Afzelius. "Optical storage for 0.53 s in a solid-state atomic frequency comb memory using dynamical decoupling". In: *New J. Phys.* 22.6 (June 2020), p. 063009. DOI: 10.1088/1367-2630/ab8aac. URL: https://doi.org/10.1088/1367-2630/ab8aac.

[60] Georg Heinze, Christian Hubrich, and Thomas Halfmann. "Stopped Light and Image Storage by Electromagnetically Induced Transparency up to the Regime of One Minute". In: *Phys. Rev. Lett.* 111 (3 July 2013), p. 033601. DOI: 10.1103/PhysRevLett.111.033601. URL: https://link.aps.org/doi/10.1103/PhysRevLett.111.033601.

[61] Ya-Fen Hsiao, Pin-Ju Tsai, Hung-Shiue Chen, Sheng-Xiang Lin, Chih-Chiao Hung, Chih-Hsi Lee, Yi-Hsin Chen, Yong-Fan Chen, Ite A. Yu, and Ying-Cheng Chen. "Highly Efficient Coherent Optical Memory Based on Electromagnetically Induced Transparency". In: *Phys. Rev. Lett.* 120 (18 May 2018), p. 183602. DOI: 10.1103/PhysRevLett.120.183602. URL: https://link.aps.org/doi/10.1103/PhysRevLett.120.183602.

[62] Yunfei Wang, Jianfeng Li, Shanchao Zhang, Keyu Su, Yiru Zhou, Kaiyu Liao, Shengwang Du, Hui Yan, and Shi-Liang Zhu. "Efficient quantum memory for single-photon polarization qubits". In: *Nat. Photonics* 13.5 (2019), pp. 346–351. ISSN: 1749-4893. DOI: 10.1038/s41566-019-0368-8. URL: https://doi.org/10.1038/s41566-019-0368-8.

[63] Holger P Specht, Christian Nölleke, Andreas Reiserer, Manuel Uphoff, Eden Figueroa, Stephan Ritter, and Gerhard Rempe. "A single-atom quantum memory". In: *Nature* 473.7346 (2011), pp. 190–193. ISSN: 1476-4687. DOI: 10.1038/nature09997. URL: https://doi.org/10.1038/nature09997.

[64] M K Bhaskar, R Riedinger, B Machielse, D S Levonian, C T Nguyen, E N Knall, H Park, D Englund, M Lončar, D D Sukachev, and M D Lukin. "Experimental demonstration of memory-enhanced quantum communication". In: *Nature* 580.7801 (2020), pp. 60–64. ISSN: 1476-4687. DOI: 10.1038/s41586-020-2103-5. URL: https://doi.org/10.1038/s41586-020-2103-5.

[65] Mahdi Hosseini, Ben M. Sparkes, Gabriel Hétet, Jevon J. Longdell, Ping Koy Lam, and Ben C. Buchler. "Coherent optical pulse sequencer for quantum applications". In: *Nature* 461.7261 (2009), pp. 241–245. DOI: 10.1038/nature08325. URL: https://doi.org/10.1038/nature08325.

[66] Kent A G Fisher, Duncan G England, Jean-Philippe W MacLean, Philip J Bustard, Kevin J Resch, and Benjamin J Sussman. "Frequency and bandwidth conversion of single photons in a room-temperature diamond quantum memory". In: *Nat. Commun.* 7.1 (2016), p. 11200. ISSN: 2041-1723. DOI: 10.1038/ncomms11200. URL: https://doi.org/10.1038/ncomms11200.

[67] Mateusz Mazelanik, Michał Parniak, Adam Leszczyński, Michał Lipka, and Wojciech Wasilewski. "Coherent spin-wave processor of stored optical pulses". In: *NPJ Quantum Inf.* 5.1 (2019), p. 22. ISSN: 2056-6387. DOI: 10.1038/s41534-019-0136-0. URL: https://doi.org/10.1038/s41534-019-0136-0.

[68] O. Morin, M. Körber, S. Langenfeld, and G. Rempe. "Deterministic Shaping and Reshaping of Single-Photon Temporal Wave Functions". In: *Phys. Rev. Lett.* 123 (13 Sept. 2019), p. 133602. DOI: 10.1103/PhysRevLett.123.133602. URL: https://link.aps.org/doi/10.1103/PhysRevLett.123.133602.

[69] Yufeng Wu, Jianlong Liu, and Christoph Simon. "Near-term performance of quantum repeaters with imperfect ensemble-based quantum memories". In: *Phys. Rev. A* 101 (4 Apr. 2020), p. 042301. DOI: 10.1103/PhysRevA.101.042301. URL: https://link.aps.org/doi/10.1103/PhysRevA.101.042301.

[70] Hui Wang, Hai Hu, T.-H. Chung, Jian Qin, Xiaoxia Yang, J.-P. Li, R.-Z. Liu, H.-S. Zhong, Y.-M. He, Xing Ding, Y.-H. Deng, Qing Dai, Y.-H. Huo, Sven Höfling, Chao-Yang Lu, and Jian-Wei Pan. "On-Demand Semiconductor Source of Entangled Photons Which Simultaneously Has High Fidelity, Efficiency, and Indistinguishability". In: *Phys. Rev. Lett.* 122 (11 Mar. 2019), p. 113602. DOI: 10.1103/PhysRevLett.122.113602. URL: https://link.aps.org/doi/10.1103/PhysRevLett.122.113602.

[71] Neil Sinclair, Erhan Saglamyurek, Hassan Mallahzadeh, Joshua A. Slater, Mathew George, Raimund Ricken, Morgan P. Hedges, Daniel Oblak, Christoph Simon, Wolfgang Sohler, and Wolfgang Tittel. "Spectral Multiplexing for Scalable Quantum Photonics using an Atomic Frequency Comb Quantum Memory and Feed-Forward Control". In: *Phys. Rev. Lett.* 113 (5 July 2014), p. 053603. DOI: 10.1103/PhysRevLett.113.053603. URL: https://link.aps.org/doi/10.1103/PhysRevLett.113.053603.

[72] Roger M. Macfarlane. "Optical Stark spectroscopy of solids". In: *J. Lumin.* 125.1 (2007). Festschrift in Honor of Academician Alexander A. Kaplyanskii, pp. 156–174. ISSN: 0022-2313. DOI: https://doi.org/10.1016/j.jlumin.2006.08.012. URL: http://www.sciencedirect.com/science/article/pii/S0022231306005837.

[73] Christoph Simon, Hugues de Riedmatten, Mikael Afzelius, Nicolas Sangouard, Hugo Zbinden, and Nicolas Gisin. "Quantum Repeaters with Photon Pair Sources and Multimode Memories". In: *Phys. Rev. Lett.* 98 (19 May 2007), p. 190503. DOI: 10.1103/PhysRevLett.98.190503. URL: https://link.aps.org/doi/10.1103/PhysRevLett.98.190503.

[74] Mikael Afzelius, Christoph Simon, Hugues de Riedmatten, and Nicolas Gisin. "Multimode quantum memory based on atomic frequency combs". In: *Phys. Rev. A* 79 (5 May 2009), p. 052329. DOI: 10.1103/PhysRevA.79.052329. URL: https://link.aps.org/doi/10.1103/PhysRevA.79.052329.

[75] Parag B. Deotare, Murray W. McCutcheon, Ian W. Frank, Mughees Khan, and Marko Loncar. "High quality factor photonic crystal nanobeam cavities". In: *Appl. Phys. Lett.* 94.12 (2009), p. 121106. DOI: 10.1063/1.3107263. URL: https://doi.org/10.1063/1.3107263.

[76] Simon Gröblacher, Jeff T. Hill, Amir H. Safavi-Naeini, Jasper Chan, and Oskar Painter. "Highly efficient coupling from an optical fiber to a nanoscale silicon optomechanical cavity". In: *Appl. Phys. Lett.* 103.18 (2013), p. 181104. DOI: 10.1063/1.4826924. URL: https://doi.org/10.1063/1.4826924.

[77] S. R. Hastings-Simon, B. Lauritzen, M. U. Staudt, J. L. M. van Mechelen, C. Simon, H. de Riedmatten, M. Afzelius, and N. Gisin. "Zeeman-level lifetimes in Er^{3+}:Y_2SiO_5". In: *Phys. Rev. B* 78 (8 Aug. 2008), p. 085410.

DOI: 10.1103/PhysRevB.78.085410. URL: https://link.aps.org/doi/10.1103/PhysRevB.78.085410.

[78] Jelena V. Rakonjac, Yu-Hui Chen, Sebastian P. Horvath, and Jevon J. Longdell. "Long spin coherence times in the ground state and in an optically excited state of $^{167}Er^{3+}$: Y_2SiO_5 at zero magnetic field". In: *Phys. Rev. B* 101 (18 May 2020), p. 184430. DOI: 10.1103/PhysRevB.101.184430. URL: https://link.aps.org/doi/10.1103/PhysRevB.101.184430.

[79] Yongchen Sun, Thomas Böttger, C. W. Thiel, and R. L. Cone. "Magnetic g tensors for the $^4I_{15/2}$ and $^4I_{13/2}$ states of Er^{3+}:Y_2SiO_5". In: *Phys. Rev. B* 77 (8 Feb. 2008), p. 085124. DOI: 10.1103/PhysRevB.77.085124. URL: https://link.aps.org/doi/10.1103/PhysRevB.77.085124.

[80] Felix R. Graf, Alois Renn, Urs P. Wild, and Masaharu Mitsunaga. "Site interference in Stark-modulated photon echoes". In: *Phys. Rev. B* 55 (17 May 1997), pp. 11225–11229. DOI: 10.1103/PhysRevB.55.11225. URL: https://link.aps.org/doi/10.1103/PhysRevB.55.11225.

[81] A. Arcangeli, A. Ferrier, and Ph. Goldner. "Stark echo modulation for quantum memories". In: *Phys. Rev. A* 93 (6 June 2016), p. 062303. DOI: 10.1103/PhysRevA.93.062303. URL: https://link.aps.org/doi/10.1103/PhysRevA.93.062303.

[82] Sebastian P. Horvath, Mohammed K. Alqedra, Adam Kinos, Andreas Walther, Stefan Kröll, and Lars Rippe. *Noise Free On-Demand Atomic-Frequency Comb Quantum Memory*. 2020. arXiv: 2006.00943.

[83] Imam Usmani, Mikael Afzelius, Hugues de Riedmatten, and Nicolas Gisin. "Mapping multiple photonic qubits into and out of one solid-state atomic ensemble". In: *Nat. Commun.* 1.1 (2010), p. 12. DOI: 10.1038/ncomms1010. URL: https://doi.org/10.1038/ncomms1010.

[84] M. Businger, A. Tiranov, K. T. Kaczmarek, S. Welinski, Z. Zhang, A. Ferrier, P. Goldner, and M. Afzelius. "Optical Spin-Wave Storage in a Solid-State Hybridized Electron-Nuclear Spin Ensemble". In: *Phys. Rev. Lett.* 124 (5 Feb. 2020), p. 053606. DOI: 10.1103/PhysRevLett.124.053606. URL: https://link.aps.org/doi/10.1103/PhysRevLett.124.053606.

[85] D. L. McAuslan, J. G. Bartholomew, M. J. Sellars, and J. J. Longdell. "Reducing decoherence in optical and spin transitions in rare-earth-metal-ion–doped materials". In: *Phys. Rev. A* 85 (3 Mar. 2012), p. 032339. DOI: 10.1103/PhysRevA.85.032339. URL: https://link.aps.org/doi/10.1103/PhysRevA.85.032339.

[86] F Kimiaee Asadi, S C Wein, and C Simon. "Protocols for long-distance quantum communication with single ^{167}Er ions". In: *Quantum Sci. Technol.* 5.4 (Sept. 2020), p. 045015. DOI: 10.1088/2058-9565/abae7c. URL: https://doi.org/10.1088/2058-9565/abae7c.

[87] John G. Bartholomew, Tian Zhong, Jonathan M. Kindem, Raymond Lopez-Rios, Jake Rochman, Ioana Craiciu, Evan Miyazono, and Andrei Faraon. "Controlling rare-earth ions in a nanophotonic resonator using the ac Stark shift". In: *Phys. Rev. A* 97 (6 June 2018), p. 063854. DOI: 10.1103/PhysRevA.97.063854. URL: https://link.aps.org/doi/10.1103/PhysRevA.97.063854.

[88] Mi Lei, Rikuto Fukumori, Jake Rochman, Bihui Zhu, Manuel Endres, Joonhee Choi, and Andrei Faraon. "Many-body cavity quantum electrodynamics with driven inhomogeneous emitters". In: *Nature* (2023), pp. 1–6.

[89] Michael Reitz, Christian Sommer, and Claudiu Genes. "Cooperative Quantum Phenomena in Light-Matter Platforms". In: *PRX Quantum* 3 (1 Jan. 2022), p. 010201.

[90] Haoye Qin, Ming Ding, and Yiheng Yin. "Induced Transparency with Optical Cavities". In: *Advanced Photonics Research* 1.1 (2020), p. 2000009.

[91] Edo Waks and Jelena Vuckovic. "Dipole Induced Transparency in Drop-Filter Cavity-Waveguide Systems". In: *Phys. Rev. Lett.* 96 (15 Apr. 2006), p. 153601.

[92] Gavin G. G. King, Peter S. Barnett, John G. Bartholomew, Andrei Faraon, and Jevon J. Longdell. "Probing strong coupling between a microwave cavity and a spin ensemble with Raman heterodyne spectroscopy". In: *Phys. Rev. B* 103 (21 June 2021), p. 214305.

[93] John G. Bartholomew, Jake Rochman, Tian Xie, Jonathan M. Kindem, Andrei Ruskuc, Ioana Craiciu, Mi Lei, and Andrei Faraon. "On-chip coherent microwave-to-optical transduction mediated by ytterbium in YVO4". In: *Nature Communications* 11.1 (June 2020), p. 3266.

[94] Leslie Allen and Joseph H Eberly. *Optical resonance and two-level atoms*. Vol. 28. Courier Corporation, 1987.

[95] Antoine Glicenstein, Giovanni Ferioli, Nikola Šibali ć, Ludovic Brossard, Igor Ferrier-Barbut, and Antoine Browaeys. "Collective Shift in Resonant Light Scattering by a One-Dimensional Atomic Chain". In: *Phys. Rev. Lett.* 124 (25 June 2020), p. 253602.

[96] T. S. do Espirito Santo, P. Weiss, A. Cipris, R. Kaiser, W. Guerin, R. Bachelard, and J. Schachenmayer. "Collective excitation dynamics of a cold atom cloud". In: *Phys. Rev. A* 101 (1 Jan. 2020), p. 013617.

[97] Xavier Fernandez-Gonzalvo, Sebastian P Horvath, Yu-Hui Chen, and Jevon J Longdell. "Cavity-enhanced Raman heterodyne spectroscopy in Er 3+: Y 2 SiO 5 for microwave to optical signal conversion". In: *Physical Review A* 100.3 (2019), p. 033807.

[98] Irina Novikova, Ronald L Walsworth, and Yanhong Xiao. "Electromagnetically induced transparency-based slow and stored light in warm atoms". In: *Laser & Photonics Reviews* 6.3 (2012), pp. 333–353.

[99] R. H. Dicke. "Coherence in Spontaneous Radiation Processes". In: *Phys. Rev.* 93 (1 Jan. 1954), pp. 99–110.

[100] Michelle O Araújo, Ivor Krešić, Robin Kaiser, and William Guerin. "Superradiance in a large and dilute cloud of cold atoms in the linear-optics regime". In: *Physical review letters* 117.7 (2016), p. 073002.

[101] Antoine Glicenstein, Giovanni Ferioli, Antoine Browaeys, and Igor Ferrier-Barbut. "From superradiance to subradiance: exploring the many-body Dicke ladder". In: *Opt. Lett.* 47.6 (Mar. 2022), pp. 1541–1544.

[102] A. Cipris, N. A. Moreira, T. S. do Espirito Santo, P. Weiss, C. J. Villas-Boas, R. Kaiser, W. Guerin, and R. Bachelard. "Subradiance with Saturated Atoms: Population Enhancement of the Long-Lived States". In: *Phys. Rev. Lett.* 126 (10 Mar. 2021), p. 103604.

[103] Zhen Wang, Hekang Li, Wei Feng, Xiaohui Song, Chao Song, Wuxin Liu, Qiujiang Guo, Xu Zhang, Hang Dong, Dongning Zheng, H. Wang, and Da-Wei Wang. "Controllable Switching between Superradiant and Subradiant States in a 10-qubit Superconducting Circuit". In: *Phys. Rev. Lett.* 124 (1 Jan. 2020), p. 013601.

[104] A. Goban, C.-L. Hung, J. D. Hood, S.-P. Yu, J. A. Muniz, O. Painter, and H. J. Kimble. "Superradiance for Atoms Trapped along a Photonic Crystal Waveguide". In: *Phys. Rev. Lett.* 115 (6 Aug. 2015), p. 063601.

[105] Je-Hyung Kim, Shahriar Aghaeimeibodi, Christopher J. K. Richardson, Richard P. Leavitt, and Edo Waks. "Super-Radiant Emission from Quantum Dots in a Nanophotonic Waveguide". In: *Nano Letters* 18.8 (Aug. 2018), pp. 4734–4740.

[106] Alp Sipahigil, Ruffin E Evans, Denis D Sukachev, Michael J Burek, Johannes Borregaard, Mihir K Bhaskar, Christian T Nguyen, Jose L Pacheco, Haig A Atikian, Charles Meuwly, et al. "An integrated diamond nanophotonics platform for quantum-optical networks". In: *Science* 354.6314 (2016), pp. 847–850.

[107] Gabriele Rainò, Michael A. Becker, Maryna I. Bodnarchuk, Rainer F. Mahrt, Maksym V. Kovalenko, and Thilo Stöferle. "Superfluorescence from lead halide perovskite quantum dot superlattices". In: *Nature* 563.7733 (Nov. 2018), pp. 671–675.

[108] F. Chiossi, C. Braggio, A. Khanbekyan, G. Carugno, A. Ortolan, G. Ruoso, R. Calabrese, A. Di Lieto, L. Tomassetti, and M. Tonelli. "Cascade superfluorescence in Er:YLF". In: *Phys. Rev. Research* 3 (1 Feb. 2021), p. 013138.

[109] C. Braggio, F. Chiossi, G. Carugno, A. Ortolan, and G. Ruoso. "Spontaneous formation of a macroscopically extended coherent state". In: *Phys. Rev. Research* 2 (3 July 2020), p. 033059. DOI: 10.1103/PhysRevResearch.2.033059. URL: https://link.aps.org/doi/10.1103/PhysRevResearch.2.033059.

[110] William Guerin, Michelle O. Araújo, and Robin Kaiser. "Subradiance in a Large Cloud of Cold Atoms". In: *Phys. Rev. Lett.* 116 (8 Feb. 2016), p. 083601.

[111] Nina Stiesdal, Hannes Busche, Jan Kumlin, Kevin Kleinbeck, Hans Peter Büchler, and Sebastian Hofferberth. "Observation of collective decay dynamics of a single Rydberg superatom". In: *Phys. Rev. Research* 2 (4 Dec. 2020), p. 043339.

[112] Justin G. Bohnet, Zilong Chen, Joshua M. Weiner, Dominic Meiser, Murray J. Holland, and James K. Thompson. "A steady-state superradiant laser with less than one intracavity photon". In: *Nature* 484.7392 (Apr. 2012), pp. 78–81.

[113] Z. Shen and A. Dogariu. "Subradiant directional memory in cooperative scattering". In: *Nature Photonics* 16.2 (Feb. 2022), pp. 148–153.

[114] Giovanni Ferioli, Antoine Glicenstein, Loic Henriet, Igor Ferrier-Barbut, and Antoine Browaeys. "Storage and Release of Subradiant Excitations in a Dense Atomic Cloud". In: *Phys. Rev. X* 11 (2 May 2021), p. 021031.

[115] Michel Gross and Serge Haroche. "Superradiance: An essay on the theory of collective spontaneous emission". In: *Physics reports* 93.5 (1982), pp. 301–396.

[116] Yuan Zhang, Yu-Xiang Zhang, and Klaus Mølmer. "Monte-Carlo simulations of superradiant lasing". In: *New Journal of Physics* 20.11 (Nov. 2018), p. 112001. DOI: 10.1088/1367-2630/aaec36.

[117] J.R. Johansson, P.D. Nation, and Franco Nori. "QuTiP 2: A Python framework for the dynamics of open quantum systems". In: *Computer Physics Communications* 184.4 (2013), pp. 1234–1240.

[118] Nathan Shammah, Shahnawaz Ahmed, Neill Lambert, Simone De Liberato, and Franco Nori. "Open quantum systems with local and collective incoherent processes: Efficient numerical simulations using permutational invariance". In: *Phys. Rev. A* 98 (6 Dec. 2018), p. 063815.

[119] M. Shcherbatenko, Y. Lobanov, A. Semenov, V. Kovalyuk, A. Korneev, R. Ozhegov, A. Kazakov, B. M. Voronov, and G. N. Goltsman. "Potential of a superconducting photon counter for heterodyne detection at the telecommunication wavelength". In: *Opt. Express* 24.26 (Dec. 2016), pp. 30474–30484.

[120] Frank Verstraete, Michael M Wolf, and J Ignacio Cirac. "Quantum computation and quantum-state engineering driven by dissipation". In: *Nature physics* 5.9 (2009), pp. 633–636.

[121] M. J. Kastoryano, F. Reiter, and A. S. Sørensen. "Dissipative Preparation of Entanglement in Optical Cavities". In: *Phys. Rev. Lett.* 106 (9 Feb. 2011), p. 090502.

[122] Robert J. Lewis-Swan, Diego Barberena, Julia R. K. Cline, Dylan J. Young, James K. Thompson, and Ana Maria Rey. "Cavity-QED Quantum Simulator of Dynamical Phases of a Bardeen-Cooper-Schrieffer Superconductor". In: *Phys. Rev. Lett.* 126 (17 Apr. 2021), p. 173601. DOI: 10.1103/PhysRevLett.126.173601.

[123] Lewis A. Williamson, Yu-Hui Chen, and Jevon J. Longdell. "Magneto-Optic Modulator with Unit Quantum Efficiency". In: *Phys. Rev. Lett.* 113 (20 Nov. 2014), p. 203601. DOI: 10.1103/PhysRevLett.113.203601.

[124] Marcos Rigol, Vanja Dunjko, and Maxim Olshanii. "Thermalization and its mechanism for generic isolated quantum systems". In: *Nature* 452.7189 (2008), pp. 854–858.

[125] Soonwon Choi, Joonhee Choi, Renate Landig, Georg Kucsko, Hengyun Zhou, Junichi Isoya, Fedor Jelezko, Shinobu Onoda, Hitoshi Sumiya, Vedika Khemani, et al. "Observation of discrete time-crystalline order in a disordered dipolar many-body system". In: *Nature* 543.7644 (2017), pp. 221–225.

[126] Manjin Zhong, Morgan P Hedges, Rose L Ahlefeldt, John G Bartholomew, Sarah E Beavan, Sven M Wittig, Jevon J Longdell, and Matthew J Sellars. "Optically addressable nuclear spins in a solid with a six-hour coherence time". In: *Nature* 517.7533 (2015), pp. 177–180.

[127] Tian Zhong, Jonathan M Kindem, John G Bartholomew, Jake Rochman, Ioana Craiciu, Evan Miyazono, Marco Bettinelli, Enrico Cavalli, Varun Verma, Sae Woo Nam, et al. "Nanophotonic rare-earth quantum memory with optically controlled retrieval". In: *Science* 357.6358 (2017), pp. 1392–1395.

[128] Thomas Böttger, CW Thiel, Y Sun, and RL Cone. "Optical decoherence and spectral diffusion at 1.5 μ m in Er 3+: Y 2 SiO 5 versus magnetic field, temperature, and Er 3+ concentration". In: *Physical Review B* 73.7 (2006), p. 075101.

[129] B Car, L Veissier, A Louchet-Chauvet, J-L Le Gouët, and Thierry Chanelière. "Optical study of the anisotropic erbium spin flip-flop dynamics". In: *Physical Review B* 100.16 (2019), p. 165107.

[130] E Zambrini Cruzeiro, Alexey Tiranov, Imam Usmani, Cyril Laplane, Jonathan Lavoie, Alban Ferrier, Philippe Goldner, Nicolas Gisin, and Mikael Afzelius. "Spectral hole lifetimes and spin population relaxation dynamics in neodymium-doped yttrium orthosilicate". In: *Physical Review B* 95.20 (2017), p. 205119.

[131] Shobhit Gupta, Xuntao Wu, Haitao Zhang, Jun Yang, and Tian Zhong. "Robust millisecond coherence times of erbium electron spins". In: *Physical Review Applied* 19.4 (2023), p. 044029.

[132] Tian Xie, Jake Rochman, John G Bartholomew, Andrei Ruskuc, Jonathan M Kindem, Ioana Craiciu, Charles W Thiel, Rufus L Cone, and Andrei Faraon. "Characterization of Er 3+: YV O 4 for microwave to optical transduction". In: *Physical Review B* 104.5 (2021), p. 054111.

[133] Ruotian Gong, Guanghui He, Xingyu Gao, Peng Ju, Zhongyuan Liu, Bingtian Ye, Erik A Henriksen, Tongcang Li, and Chong Zu. "Coherent dynamics of strongly interacting electronic spin defects in hexagonal boron nitride". In: *Nature Communications* 14.1 (2023), p. 3299.

[134] Joonhee Choi, Soonwon Choi, Georg Kucsko, Peter C Maurer, Brendan J Shields, Hitoshi Sumiya, Shinobu Onoda, Junichi Isoya, Eugene Demler, Fedor Jelezko, et al. "Depolarization dynamics in a strongly interacting solid-state spin ensemble". In: *Physical review letters* 118.9 (2017), p. 093601.

[135] Emily J Davis, Bingtian Ye, Francisco Machado, Simon A Meynell, Weijie Wu, Thomas Mittiga, William Schenken, Maxime Joos, Bryce Kobrin, Yuanqi Lyu, et al. "Probing many-body dynamics in a two-dimensional dipolar spin ensemble". In: *Nature Physics* (2023), pp. 1–9.

[136] William K Schenken, Simon A Meynell, Francisco Machado, Bingtian Ye, Claire A McLellan, Maxime Joos, VV Dobrovitski, Norman Y Yao, and Ania C Bleszynski Jayich. "Long-lived coherences in strongly interacting spin ensembles". In: *arXiv preprint arXiv:2309.15444* (2023).

[137] Herman Y Carr and Edward M Purcell. "Effects of diffusion on free precession in nuclear magnetic resonance experiments". In: *Physical review* 94.3 (1954), p. 630.

[138] Joonhee Choi, Hengyun Zhou, Helena S Knowles, Renate Landig, Soonwon Choi, and Mikhail D Lukin. "Robust dynamic hamiltonian engineering of many-body spin systems". In: *Physical Review X* 10.3 (2020), p. 031002.

[139] Sergio Blanes, Fernando Casas, JA Oteo, and Javier Ros. "A pedagogical approach to the Magnus expansion". In: *European Journal of Physics* 31.4 (2010), p. 907.

[140] John S Waugh, Lee M Huber, and Ulrich Haeberlen. "Approach to high-resolution NMR in solids". In: *Physical Review Letters* 20.5 (1968), p. 180.

[141] Ulrich Haeberlen and John S Waugh. "Coherent averaging effects in magnetic resonance". In: *Physical Review* 175.2 (1968), p. 453.

[142] Georg Kucsko, Soonwon Choi, Joonhee Choi, Peter C Maurer, Hengyun Zhou, Renate Landig, Hitoshi Sumiya, Shinobu Onoda, Junich Isoya, Fedor Jelezko, et al. "Critical thermalization of a disordered dipolar spin system in diamond". In: *Physical review letters* 121.2 (2018), p. 023601.

[143] Alfred G Redfield. "Nuclear magnetic resonance saturation and rotary saturation in solids". In: *Physical Review* 98.6 (1955), p. 1787.

[144] MA Lephoto, OM Ntwaeaborwa, Shreyas S Pitale, HC Swart, JR Botha, and Bakang Moses Mothudi. "Synthesis and characterization of BaAl2O4: Eu2+ co-doped with different rare earth ions". In: *Physica B: Condensed Matter* 407.10 (2012), pp. 1603–1606.

[145] Amina El Fakir, Mouaad Sekkati, Guy Schmerber, Azzam Belayachi, Zineb Edfouf, Mohammed Regragui, Fouzia Cherkaoui El Moursli, Zouheir Sekkat, Aziz Dinia, Abdelilah Slaoui, et al. "Influence of Rare Earth (Nd and Tb) Co-Doping on ZnO Thin Films Properties". In: *physica status solidi c* 14.10 (2017), p. 1700169.

[146] Colin C Baker, Ashley Burdett, E Joseph Friebele, Daniel L Rhonehouse, Woohong Kim, and Jasbinder Sanghera. "Rare earth co-doping for increased efficiency of resonantly pumped Er-fiber lasers". In: *Optical Materials Express* 9.3 (2019), pp. 1041–1048.

[147] Andrei Ruskuc, Chun-Ju Wu, Jake Rochman, Joonhee Choi, and Andrei Faraon. "Nuclear spin-wave quantum register for a solid-state qubit". In: *Nature* 602.7897 (2022), pp. 408–413.

[148] Vedika Khemani, Achilleas Lazarides, Roderich Moessner, and Shivaji L Sondhi. "Phase structure of driven quantum systems". In: *Physical review letters* 116.25 (2016), p. 250401.

[149] Dominic V Else, Bela Bauer, and Chetan Nayak. "Floquet time crystals". In: *Physical review letters* 117.9 (2016), p. 090402.

[150] Curt W von Keyserlingk, Vedika Khemani, and Shivaji L Sondhi. "Absolute stability and spatiotemporal long-range order in Floquet systems". In: *Physical Review B* 94.8 (2016), p. 085112.

[151] Norman Y Yao, Andrew C Potter, I-D Potirniche, and Ashvin Vishwanath. "Discrete time crystals: Rigidity, criticality, and realizations". In: *Physical review letters* 118.3 (2017), p. 030401.

[152] Jiehang Zhang, Paul W Hess, A Kyprianidis, Petra Becker, A Lee, J Smith, Gaetano Pagano, I-D Potirniche, Andrew C Potter, Ashvin Vishwanath, et al. "Observation of a discrete time crystal". In: *Nature* 543.7644 (2017), pp. 217–220.

[153] J Randall, CE Bradley, FV van der Gronden, A Galicia, MH Abobeih, M Markham, DJ Twitchen, F Machado, NY Yao, and TH Taminiau. "Many-body–localized discrete time crystal with a programmable spin-based quantum simulator". In: *Science* 374.6574 (2021), pp. 1474–1478.

[154] Xiao Mi, Matteo Ippoliti, Chris Quintana, Ami Greene, Zijun Chen, Jonathan Gross, Frank Arute, Kunal Arya, Juan Atalaya, Ryan Babbush, et al. "Time-crystalline eigenstate order on a quantum processor". In: *Nature* 601.7894 (2022), pp. 531–536.

[155] Antonis Kyprianidis, Francisco Machado, William Morong, Patrick Becker, Kate S Collins, Dominic V Else, Lei Feng, Paul W Hess, Chetan Nayak, Guido Pagano, et al. "Observation of a prethermal discrete time crystal". In: *Science* 372.6547 (2021), pp. 1192–1196.

[156] William Beatrez, Christoph Fleckenstein, Arjun Pillai, Erica de Leon Sanchez, Amala Akkiraju, Jesus Diaz Alcala, Sophie Conti, Paul Reshetikhin, Emanuel Druga, Marin Bukov, et al. "Critical prethermal discrete time crystal created by two-frequency driving". In: *Nature Physics* 19.3 (2023), pp. 407–413.

[157] Hossein Taheri, Andrey B Matsko, Lute Maleki, and Krzysztof Sacha. "All-optical dissipative discrete time crystals". In: *Nature communications* 13.1 (2022), p. 848.

[158] Hans Keßler, Phatthamon Kongkhambut, Christoph Georges, Ludwig Mathey, Jayson G Cosme, and Andreas Hemmerich. "Observation of a dissipative time crystal". In: *Physical Review Letters* 127.4 (2021), p. 043602.

[159] Jared Rovny, Robert L Blum, and Sean E Barrett. "Observation of discrete-time-crystal signatures in an ordered dipolar many-body system". In: *Physical review letters* 120.18 (2018), p. 180603.

[160] Wen Wei Ho, Soonwon Choi, Mikhail D Lukin, and Dmitry A Abanin. "Critical time crystals in dipolar systems". In: *Physical review letters* 119.1 (2017), p. 010602.

[161] Florentin Reiter and Anders S Sørensen. "Effective operator formalism for open quantum systems". In: *Physical Review A* 85.3 (2012), p. 032111.

[162] Emily Davis, Gregory Bentsen, and Monika Schleier-Smith. "Approaching the Heisenberg limit without single-particle detection". In: *Physical review letters* 116.5 (2016), p. 053601.

[163] Anjun Chu, Peiru He, James K Thompson, and Ana Maria Rey. "Quantum enhanced cavity QED interferometer with partially delocalized atoms in lattices". In: *Physical Review Letters* 127.21 (2021), p. 210401.

Appendix A

ADIABATIC ELIMINATION OF CAVITY FIELD

In this appendix, we will discuss the adiabatic elimination of the cavity field, which we have been using frequently in chapter 3 and chapter 4. We will point out a potential confusion when performing adiabatic elimination, then present a rigorous derivation, and finally offer a simplified procedure — the formula that we use in chapter 3 and chapter 4.

A.1 Setting up the confusion

Starting with the Tavis-cumming model (Eq. 3.2), we rewrite the Hamiltonian here:

$$H = \Delta_c a^\dagger a + \frac{1}{2}\sum_{j=1}^{N} \Delta_j \sigma_j^z + \sum_{j=1}^{N} g_j (a^\dagger \sigma_j^- + \sigma_j^+ a) - i\frac{\kappa}{2}\sqrt{\mu}(a^\dagger - a). \tag{A.1}$$

We can write the quantum Langevin equation in the Heisenberg picture as in Eq. 3.5-3.7 (Equivalently, we can use the master equation to calculate the evolution of ρ and the expectation of the operators, and then drop the expectation symbol.):

$$\dot{a} = -(i\Delta_c + \frac{\kappa}{2})a - i\sum_{j=1}^{N} g_j \sigma_j^- - \frac{\kappa}{2}\sqrt{\mu} \tag{A.2}$$

$$\dot{\sigma}_j^- = -(i\Delta_j + \gamma)\sigma_j^- + i g_j \sigma_j^z a \tag{A.3}$$

$$\dot{\sigma}_j^z = 2i g_j (a^\dagger \sigma_j^- - \sigma_j^+ a) - \gamma_s (1 + \sigma_j^z). \tag{A.4}$$

We note that in Eq.A.4, some people write it as $(a^\dagger \sigma_j^- - \sigma_j^+ a)$ while others write it as $(a^\dagger \sigma_j^- - a\sigma_j^+)$, $(\sigma_j^- a^\dagger - a\sigma_j^+)$ or $(\sigma_j^- a^\dagger - \sigma_j^+ a)$. These four choices make no difference at this point since $[a, \sigma_j^-] = 0$. But we should remember that it implicitly contains the information $[a, \sigma_j^-] = 0$ (you will see it more clearly if you are deriving through master equation).

When the cavity field is adiabatically eliminated, we ignore the dynamics of the a operator by setting $\dot{a} = 0$, which gives

$$a = \frac{-i\sum_{j=1}^{N} g_j \sigma_j^- - \frac{\kappa}{2}\sqrt{\mu}}{i\Delta_c + \frac{\kappa}{2}}. \tag{A.5}$$

If we directly plug Eq. A.10 back to Eq. A.4, we will see that four choices give different results:

$$a^\dagger\sigma_j^- - \sigma_j^+ a = \frac{\sum_{k=1}^N g_k \left(i\frac{\kappa}{2}\left(\sigma_k^+\sigma_j^- + \sigma_j^+\sigma_k^-\right) - \Delta_c\left(\sigma_k^+\sigma_j^- - \sigma_j^+\sigma_k^-\right)\right)}{\Delta_c^2 + \frac{\kappa^2}{4}} + f(\mu) \tag{A.6a}$$

$$a^\dagger\sigma_j^- - a\sigma_j^+ = \frac{\sum_{k=1}^N g_k \left(i\frac{\kappa}{2}\left(\sigma_k^+\sigma_j^- + \sigma_k^-\sigma_j^+\right) - \Delta_c\left(\sigma_k^+\sigma_j^- - \sigma_k^-\sigma_j^+\right)\right)}{\Delta_c^2 + \frac{\kappa^2}{4}} + f(\mu) \tag{A.6b}$$

$$\sigma_j^- a^\dagger - a\sigma_j^+ = \frac{\sum_{k=1}^N g_k \left(i\frac{\kappa}{2}\left(\sigma_j^-\sigma_k^+ + \sigma_k^-\sigma_j^+\right) - \Delta_c\left(\sigma_j^-\sigma_k^+ - \sigma_k^-\sigma_j^+\right)\right)}{\Delta_c^2 + \frac{\kappa^2}{4}} + f(\mu) \tag{A.6c}$$

$$\sigma_j^- a^\dagger - \sigma_j^+ a = \frac{\sum_{k=1}^N g_k \left(i\frac{\kappa}{2}\left(\sigma_j^-\sigma_k^+ + \sigma_j^+\sigma_k^-\right) - \Delta_c\left(\sigma_j^-\sigma_k^+ - \sigma_j^+\sigma_k^-\right)\right)}{\Delta_c^2 + \frac{\kappa^2}{4}} + f(\mu). \tag{A.6d}$$

When $j \neq k$, the order of j and k in terms of operators is changeable. So, the difference between the four expressions occurs in those terms where $k = j$, and we use δ to represent this difference.

$$\delta(a^\dagger\sigma_j^- - \sigma_j^+ a) = \frac{ig\frac{\kappa}{2}\left(\sigma_j^z + I\right)}{\Delta_c^2 + \frac{\kappa^2}{4}} \tag{A.7a}$$

$$\delta(a^\dagger\sigma_j^- - a\sigma_j^+) = \frac{g\left(i\frac{\kappa}{2}I - \Delta_c\sigma_j^z\right)}{\Delta_c^2 + \frac{\kappa^2}{4}} \tag{A.7b}$$

$$\delta(\sigma_j^- a^\dagger - a\sigma_j^+) = \frac{ig\frac{\kappa}{2}\left(I - \sigma_j^z\right)}{\Delta_c^2 + \frac{\kappa^2}{4}} \tag{A.7c}$$

$$\delta(\sigma_j^- a^\dagger - \sigma_j^+ a) = \frac{g\left(i\frac{\kappa}{2}I + \Delta_c\sigma_j^z\right)}{\Delta_c^2 + \frac{\kappa^2}{4}} \tag{A.7d}$$

If we choose to plug Eq. A.10 back to Hamiltonian to get effective Hamitonian, we have similar issue

$$\Delta_c a^\dagger a + \sum_{j=1}^{N} g_j(a^\dagger \sigma_j^- + \sigma_j^+ a) = -\frac{\Delta_c}{\Delta_c^2 + \frac{\kappa^2}{4}} \sum_{k=1}^{N} g_k \sigma_k^+ \sum_{j=1}^{N} g_j \sigma_j^- + g_1 \tag{A.8a}$$

$$\Delta_c a^\dagger a + \sum_{j=1}^{N} g_j(a^\dagger \sigma_j^- + a\sigma_j^+) = \frac{i\kappa}{2\Delta_c^2 + \frac{\kappa^2}{2}} \sum_{j=1}^{N} g_j^2 \sigma_j^z - \frac{\Delta_c}{\Delta_c^2 + \frac{\kappa^2}{4}} \sum_{k=1}^{N} g_k \sigma_k^- \sum_{j=1}^{N} g_j \sigma_j^+ + g_1 \tag{A.8b}$$

$$\Delta_c a^\dagger a + \sum_{j=1}^{N} g_j(\sigma_j^- a^\dagger + a\sigma_j^+) = \frac{\Delta_c}{\Delta_c^2 + \frac{\kappa^2}{4}} \sum_{k=1}^{N} g_k \sigma_k^+ \sum_{j=1}^{N} g_j \sigma_j^- - \frac{2\Delta_c}{\Delta_c^2 + \frac{\kappa^2}{4}} \sum_{k=1}^{N} g_k \sigma_k^- \sum_{j=1}^{N} g_j \sigma_j^+ + g_1 \tag{A.8c}$$

$$\Delta_c a^\dagger a + \sum_{j=1}^{N} g_j(\sigma_j^- a^\dagger + \sigma_j^+ a) = -\frac{i\kappa}{2\Delta_c^2 + \frac{\kappa^2}{2}} \sum_{j=1}^{N} g_j^2 \sigma_j^z - \frac{\Delta_c}{\Delta_c^2 + \frac{\kappa^2}{4}} \sum_{k=1}^{N} g_k \sigma_k^- \sum_{j=1}^{N} g_j \sigma_j^+ + g_1. \tag{A.8d}$$

Note that we only keep the second-order terms (the product of two operators) since other terms do not have commutation issues. We can already see that Eq. A.8b and d are not Hermitian.

A.2 Effective Hamiltonian in the Schrödinger picture: Reiter and Sorenson's procedure

In this section, we will follow the procedure of Reiter and Sorenson [161]. Similar procedures have been applied to [162, 163].

To set up the problem more completely, we write down the Lindblad terms related to cavity decay as in Eqs. 4.1 in terms of Lindblad operator $\hat{L}_{\text{cav}}$

$$\begin{aligned} \mathcal{L}_{\text{cav}} &= \hat{L}_{\text{cav}} \rho \hat{L}_{\text{cav}}^\dagger - \frac{1}{2}(\hat{L}_{\text{cav}}^\dagger \hat{L}_{\text{cav}} \rho + \rho \hat{L}_{\text{cav}}^\dagger \hat{L}_{\text{cav}}) \\ &= \kappa(a\rho a^\dagger - \frac{1}{2} a^\dagger a \rho - \frac{1}{2} \rho a^\dagger a) \end{aligned} \tag{A.9}$$

where $\hat{L}_{\text{cav}} = \sqrt{\kappa} a$. Note that, unlike ρ_t used in section 4.5, here ρ represents the total density operator, consisting of both the cavity field and the atoms.

We should emphasize that, in order to use Reiter and Sorenson's procedure, the eliminated field has to be weakly excited (rather than just reaching the steady state).Due to the laser drive (μ), the photon occupation inside the cavity is not small, thus the weakly driven condition is not satisfied. However, we can subtract the classical term related to the external drive from the operator a to obtain a new operator b, which represents the quantum fluctuations. The relation between a and b is as follows:

$$a = b + \alpha \tag{A.10}$$

where $\alpha = -\frac{\frac{\kappa}{2}\sqrt{\mu}}{i\Delta_c + \frac{\kappa}{2}}$. Mathematically, b is just a displacement of a. We can rewrite the Hamiltonian Eq.A.1 in terms of b as

$$\begin{aligned} H = \Delta_c b^\dagger b + (\Delta_c \alpha - i\frac{\kappa}{2}\sqrt{\mu})b^\dagger + (\Delta_c \alpha^* + i\frac{\kappa}{2}\sqrt{\mu})b + \sum_{j=1}^{N} g_j(b^\dagger \sigma_j^- + b\sigma_j^+) \\ + \frac{1}{2}\sum_{j=1}^{N}\Delta_j\sigma_j^z + \sum_{j=1}^{N} g_j\left(\alpha^*\sigma_j^- + \alpha\sigma_j^+\right) + \Delta_c|\alpha|^2 - i\frac{\kappa}{2}\sqrt{\mu}(\alpha^* - \alpha) \end{aligned} \tag{A.11}$$

and plug Lindblad operators $\hat{L}_{\text{cav}} = \sqrt{\kappa}(b + \alpha)$ back to Eq. A.9. We find that:

$$\mathcal{L}_{\text{cav}} = \kappa(b\rho b^\dagger - \frac{1}{2}b^\dagger b\rho - \frac{1}{2}\rho b^\dagger b) - i\frac{\kappa}{2}[i\alpha^* b - i\alpha b^\dagger, \rho]]. \tag{A.12}$$

To simplify this, we know that master equation is:

$$\dot{\rho} = -i[H, \rho] + \mathcal{L}_{\text{cav}} \tag{A.13}$$

such that we can absorb the second term in Eq. A.12 into Hamiltonian. Using the equality $\Delta_c\alpha - i\frac{\kappa}{2}\sqrt{\mu} - i\frac{\kappa}{2}\alpha = 0$, we get know Hamiltonian and Lindblad operators:

$$\begin{aligned} H' = \Delta_c b^\dagger b + \sum_{j=1}^{N} g_j(b^\dagger\sigma_j^- + b\sigma_j^+) + \frac{1}{2}\sum_{j=1}^{N}\Delta_j\sigma_j^z + \sum_{j=1}^{N} g_j\left(\alpha^*\sigma_j^- + \alpha\sigma_j^+\right) \\ + \Delta_c|\alpha|^2 - i\frac{\kappa}{2}\sqrt{\mu}(\alpha^* - \alpha) \end{aligned} \tag{A.14}$$

and $\hat{L}'_{\text{cav}} = \sqrt{\kappa}b$.

Now, following reference [161], we will calculate the effective Hamiltonian H_{eff} and Lindblad operators $\hat{L}_{\text{eff}}$.

$$H'_{NH} = H'_e - \frac{i}{2}\hat{L}'^\dagger_{\text{cav}}\hat{L}'_{\text{cav}} = (\Delta_c - \frac{\kappa}{2}i)b^\dagger b \tag{A.15}$$

and

$$V_+ = \sum_{j=1}^{N} g_j b^\dagger \sigma_j^-. \tag{A.16}$$

Thus

$$
\begin{aligned}
H'_{\text{eff}} &= -\frac{1}{2}V_{-}\left(H'^{-1}_{NH} + (H'^{-1}_{NH})^{\dagger}\right)V_{+} + H'_{g} \\
&= -\frac{1}{2}\sum_{k=1}^{N} g_k \sigma_k^{+} b \left(\frac{b^{-1}(b^{\dagger})^{-1}}{\Delta_c - \frac{\kappa}{2}i} + \frac{b^{-1}(b^{\dagger})^{-1}}{\Delta_c + \frac{\kappa}{2}i}\right) b^{\dagger} \sum_{j=1}^{N} g_j \sigma_j^{-} + H'_{g} \\
&= -\frac{\Delta_c}{\Delta_c^2 + \frac{\kappa^2}{4}} \sum_{k=1}^{N} g_k \sigma_k^{+} \sum_{j=1}^{N} g_j \sigma_j^{-} + H'_{g}
\end{aligned} \tag{A.17}
$$

where $H'_g = \frac{1}{2}\sum_{j=1}^{N} \Delta_j \sigma_j^z + \sum_{j=1}^{N} g_j \left(\alpha^* \sigma_j^{-} + \alpha \sigma_j^{+}\right) + \Delta_c |\alpha|^2 - i\frac{\kappa}{2}\sqrt{\mu}(\alpha^* - \alpha)$. And

$$
\hat{L}'_{\text{eff}} = \hat{L}'_{\text{cav}} H'^{-1}_{NH} V_{+} = \frac{\sqrt{\kappa}}{\Delta_c - \frac{\kappa}{2}i} \sum_{j=1}^{N} g_j \sigma_j^{-}. \tag{A.18}
$$

A.3 Simplified procedure

Comparing Eq. A.8 and Eq. A.17, we can see that Eq. A.17 is the correct one. For Lindblad operators it is equivalent to replace quantum fluctuation b with $\frac{-i\sum_{j=1}^{N} g_j \sigma_j^{-}}{i\Delta_c + \frac{\kappa}{2}}$, and

$$
\mathcal{L}'_{\text{eff}} = \frac{\kappa}{\frac{\kappa^2}{4} + \Delta_c^2} \sum_{j,k}^{N} g_j g_k (\sigma_j^{-} \rho \sigma_k^{+} - \frac{1}{2}\sigma_j^{+}\sigma_k^{-}\rho - \frac{1}{2}\rho\sigma_j^{+}\sigma_k^{-}). \tag{A.19}
$$

Let us use the master equation to derive the evolution of $\langle \sigma_j^z \rangle$ after adiabatically eliminating the cavity field to determine the correct choice in Eq. A.6. For brevity, we drop the expectation symbol to show the equation of motion in the Heisenberg picture.

$$
\begin{aligned}
\dot{\sigma}_j^z &= -\frac{2ig_j\Delta_c}{\Delta_c^2 + \frac{\kappa^2}{4}} \sum_{k=1}^{N} g_k (\sigma_k^{+}\sigma_j^{-} - \sigma_j^{+}\sigma_k^{-}) - \frac{\kappa g_j}{\frac{\kappa^2}{4} + \Delta_c^2} \sum_{k=1}^{N} g_k (\sigma_k^{+}\sigma_j^{-} + \sigma_j^{+}\sigma_k^{-}) + f(\mu, \gamma_s) \\
&= 2ig_j \frac{\sum_{k=1}^{N} g_k \left(i\frac{\kappa}{2}(\sigma_k^{+}\sigma_j^{-} + \sigma_j^{+}\sigma_k^{-}) - \Delta_c(\sigma_k^{+}\sigma_j^{-} - \sigma_j^{+}\sigma_k^{-})\right)}{\Delta_c^2 + \frac{\kappa^2}{4}} + f(\mu, \gamma_s)
\end{aligned} \tag{A.20}
$$

We can see that Eq. A.6a is the correct one to use! Let us summarize the simple procedure here:

1. For the Hamiltonian, we write it in the this order: $a^{\dagger}\sigma_j^{-} + \sigma_j^{+} a$.

2. For the σ_j^z dynamics, we write it in the following order: $a^{\dagger}\sigma_j^{-} - \sigma_j^{+} a$.

3. We can see that the general rule is to keep the creation operator first, followed by annihilation operators, whether it is for the cavity field or the atom.

4. When adiabatic elimination of the cavity field is applied, we can substitute the operator a with its steady-state solution in the expressions that follow the above order.

5. For the Lindblad terms, we will also perform the same substitution, but the constant needs to be dropped.

Due to this reason, we maintain the order of operators as described above throughout the thesis.

Appendix B

ANALYTICAL SOLUTIONS FOR TWO AND THREE INTERACTING SPINS

In this appendix, we will include the full derivation for two and three interaction spins.

B.1 Two spins with interaction strength J and detuning Δ

For the two-atom case, we can theoretically solve the system's evolution under spin echo sequence. Let us transition to the toggling frame after the first $\pi/2$ pulse; the Hamiltonian in the first and second periods is as follows:

$$H_1 = \Delta S_2^z + J(S_1^x S_2^x + S_1^y S_2^y), \tag{B.1}$$

$$H_2 = -\Delta S_2^z + J(S_1^x S_2^x + S_1^y S_2^y). \tag{B.2}$$

We want to solve the eigenstates of the above Hamiltonians in the uncoupled basis $\{|\uparrow_1\uparrow_2\rangle, |\downarrow_1\uparrow_2\rangle, |\uparrow_1\downarrow_2\rangle, |\downarrow_1\downarrow_2\rangle\}$, where $\{|\uparrow_1\rangle, |\downarrow_1\rangle\}$ represent the eigenstates of S_1^z, and $\{|\uparrow_2\rangle, |\downarrow_2\rangle\}$ represent the eigenstates of S_2^z. It is easy to see that $|\uparrow_1\uparrow_2\rangle$ and $|\downarrow_1\downarrow_2\rangle$ are still the eigenstates of H_1 (H_2) with respective eigenenergies of $\pm\frac{1}{2}\Delta(\mp\frac{1}{2}\Delta)$. Therefore, we only need to deal with the evolution in the subspace $\{|\uparrow_1\downarrow_2\rangle, |\downarrow_1\uparrow_2\rangle\}$. Let us define new $\tilde{S_z} = \frac{1}{2}(|\downarrow_1\uparrow_2\rangle\langle\downarrow_1\uparrow_2| - |\uparrow_1\downarrow_2\rangle\langle\uparrow_1\downarrow_2|)$ such that the Hamiltonians can be written as

$$\tilde{H}_1 = \Delta\tilde{S}_z + J\tilde{S}_x \tag{B.3}$$

$$\tilde{H}_2 = -\Delta\tilde{S}_z + J\tilde{S}_x \tag{B.4}$$

where we have used the fact that

$$S_1^x S_2^x + S_1^y S_2^y = \frac{1}{2}\left(S_1^+ S_2^- + S_1^- S_2^+\right) = \frac{1}{2}\left(|\uparrow_1\downarrow_2\rangle\langle\downarrow_1\uparrow_2| + |\downarrow_1\uparrow_2\rangle\langle\uparrow_1\downarrow_2|\right) = \tilde{S}_x.$$

This is exactly the Rabi oscillation with detuning, and the sign of the detuning flips in the later half of the evolution time. We know that the eigenstates of these Hamiltonians are dressed states.

For $\tilde{H}_1$, the eigenstates and eigenenergies are as follows

$$E_\pm = \pm\frac{1}{2}\sqrt{\Delta^2 + J^2} \tag{B.5}$$

$$|+\rangle = \sin\theta\,|\uparrow_1\downarrow_2\rangle + \cos\theta\,|\downarrow_1\uparrow_2\rangle \tag{B.6}$$

$$|-\rangle = \cos\theta\,|\uparrow_1\downarrow_2\rangle - \sin\theta\,|\downarrow_1\uparrow_2\rangle \tag{B.7}$$

where θ is defined by

$$\tan 2\theta = \frac{J}{\Delta}\left(0 \le \theta < \frac{\pi}{2}\right). \tag{B.8}$$

The inverse solution is

$$|\uparrow_1\downarrow_2\rangle = \sin\theta\,|+\rangle + \cos\theta\,|-\rangle\,,$$

$$|\downarrow_1\uparrow_2\rangle = \cos\theta\,|+\rangle - \sin\theta\,|-\rangle\,.$$

For $\tilde{H}_2$, we just need to set $\Delta' = -\Delta$, and thus we obtain $\theta' = -\theta + \frac{\pi}{2}$, $E'_\pm = E_\pm$,

$$|+\rangle' = \cos\theta\,|\uparrow_1\downarrow_2\rangle + \sin\theta\,|\downarrow_1\uparrow_2\rangle\,,$$

$$|-\rangle' = \sin\theta\,|\uparrow_1\downarrow_2\rangle - \cos\theta\,|\downarrow_1\uparrow_2\rangle\,,$$

and the corresponding inverse solution as:

$$|\uparrow_1\downarrow_2\rangle = \cos\theta\,|+\rangle' + \sin\theta\,|-\rangle'\,,$$

$$|\downarrow_1\uparrow_2\rangle = \sin\theta\,|+\rangle' - \cos\theta\,|-\rangle'\,.$$

We get the relations between egenstates for $\tilde{H}_1$ and $\tilde{H}_2$ as:

$$|+\rangle = \sin 2\theta\,|+\rangle' - \cos 2\theta\,|-\rangle'\,, \tag{B.9}$$

$$|-\rangle = \cos 2\theta\,|+\rangle' + \sin 2\theta\,|-\rangle'\,. \tag{B.10}$$

The initial state in the full space after the first $\pi/2$ pulse around $\hat{x}$ axis is

$$\frac{1}{\sqrt{2}}(-i\,|\uparrow_1\rangle + |\downarrow_1\rangle)\frac{1}{\sqrt{2}}(-i\,|\uparrow_2\rangle + |\downarrow_2\rangle) = \frac{1}{2}\left(-|\uparrow_1\uparrow_2\rangle - i(|\downarrow_1\uparrow_2\rangle + |\uparrow_1\downarrow_2\rangle) + |\downarrow_1\downarrow_2\rangle\right). \tag{B.11}$$

After the total evolution time τ:

$$|\uparrow_1\uparrow_2\rangle \to |\uparrow_1\uparrow_2\rangle\, e^{-i\frac{1}{4}(\Delta-\Delta)\tau}$$

$$|\downarrow_1\downarrow_2\rangle \to |\downarrow_1\downarrow_2\rangle\, e^{-i\frac{1}{4}(-\Delta+\Delta)\tau}$$

and

$$|\downarrow_1\uparrow_2\rangle + |\uparrow_1\downarrow_2\rangle \to |\phi(\tau)\rangle$$

where $|\phi(\tau)\rangle$ is as follows

$$|\phi(\frac{\tau}{2})\rangle = (\sin\theta + \cos\theta)\,|+\rangle\, e^{-i\frac{E_+\tau}{2}} + (\cos\theta - \sin\theta)\,|-\rangle\, e^{-i\frac{E_-\tau}{2}} \tag{B.12}$$

$$
\begin{aligned}
|\phi(\tau)\rangle &= (\sin\theta+\cos\theta)(\sin 2\theta\,|+\rangle' e^{-iE_+\tau} - \cos 2\theta\,|-\rangle') \\
&\quad + (\cos\theta-\sin\theta)(\cos 2\theta\,|+\rangle' + \sin 2\theta\,|-\rangle' e^{-iE_-\tau}) \\
&= A_1\,|\uparrow_1\downarrow_2\rangle + A_2\,|\downarrow_1\uparrow_2\rangle
\end{aligned} \tag{B.13}
$$

where

$$
A_1 = \cos 2\theta(\cos 2\theta - \sin 2\theta) + \sin 2\theta(\sin 2\theta + \cos 2\theta)\cos(E_+\tau) - i\sin 2\theta\sin(E_+\tau) \tag{B.14}
$$

and

$$
A_2 = \cos 2\theta(\cos 2\theta + \sin 2\theta) + \sin 2\theta(\sin 2\theta - \cos 2\theta)\cos(E_+\tau) - i\sin 2\theta\sin(E_+\tau). \tag{B.15}
$$

The final $\pi/2$ rotation along $\hat{x}$ and measurement on the $\hat{z}$ basis is equivalent to measuring the expectation value of S_y.

$$
\begin{aligned}
P_1 &= \frac{1}{4}\left(-\langle\uparrow_1\uparrow_2| + i\,\langle\phi(\tau)| + \langle\downarrow_1\downarrow_2|\right) S_1^y \left(-|\uparrow_1\uparrow_2\rangle - i\,|\phi(\tau)\rangle + |\downarrow_1\downarrow_2\rangle\right) \\
&= \frac{1}{8}(A_2 + A_1^* + A_2^* + A_1) \\
&= \frac{\cos^2 2\theta}{2} + \frac{\sin^2 2\theta}{2}\cos\left(\frac{\sqrt{\Delta^2+J^2}}{2}\tau\right) \\
&= \frac{\Delta^2}{2(\Delta^2+J^2)} + \frac{J^2}{2(\Delta^2+J^2)}\cos\left(\frac{\sqrt{\Delta^2+J^2}}{2}\tau\right)
\end{aligned} \tag{B.16}
$$

It is easy to know that $P_1 = P_2$

B.2 Perturbation theory calculation for adding a third spin to a pair of strongly interaction spins

In this appendix, we provide the full derivation of second-order perturbation theory for the evolution of three resonantly interacting spins under an echo sequence. In the case without disorder, the three-atom Hamiltonian is given by

$$
H = H_0 + V = J_0(S_x^1 S_x^2 + S_y^1 S_y^2) + J_1(S_x^1 S_x^3 + S_y^1 S_y^3) + J_2(S_x^2 S_x^3 + S_y^2 S_y^3) \tag{B.17}
$$

where $H_0 = J_0(S_x^1 S_x^2 + S_y^1 S_y^2)$ and $|J_0| \gg |J_1|, |J_2|$, so V is a perturbation relative to H_0.

To begin, the eigenstates of $H_0 = \frac{J_0}{2}\left(S_+^1 S_-^2 + S_-^1 S_+^2\right)$ are as follows:

$$
|+\rangle = \frac{1}{\sqrt{2}}(|\uparrow_1\downarrow_2\rangle + |\downarrow_1\uparrow_2\rangle) \tag{B.18}
$$

$$|-\rangle = \frac{1}{\sqrt{2}}(|\uparrow_1\downarrow_2\rangle - |\downarrow_1\uparrow_2\rangle) \tag{B.19}$$

with eigenvalues of $\pm\frac{J_0}{2}$ and $|\uparrow_1\uparrow_2\rangle$, $|\downarrow_1\downarrow_2\rangle$ with eigenvalues of 0. The final eight eigenstates are formed by taking the direct product of these four eigenstates with the states of the third spin, $|\uparrow_3\rangle, |\downarrow_3\rangle$.

First-order correction

$$V = \frac{J_1}{2}(S^1_+S^3_- + S^1_-S^3_+) + \frac{J_2}{2}(S^2_+S^3_- + S^2_-S^3_+) \tag{B.20}$$

It is easy to see that the first-order correction to the eigenenergies is zero due to the fact that $\langle\uparrow_3| V |\uparrow_3\rangle = \langle\downarrow_3| V |\downarrow_3\rangle = 0$. Let us now calculate the first-order correction for the eigenstates.

$$|+\rangle |\uparrow_3\rangle^{(1)} = \frac{J_1 + J_2}{\sqrt{2}J_0} |\uparrow_1\uparrow_2\rangle |\downarrow_3\rangle \tag{B.21}$$

$$|+\rangle |\downarrow_3\rangle^{(1)} = \frac{J_1 + J_2}{\sqrt{2}J_0} |\downarrow_1\downarrow_2\rangle |\uparrow_3\rangle \tag{B.22}$$

$$|-\rangle |\uparrow_3\rangle^{(1)} = \frac{J_1 - J_2}{\sqrt{2}J_0} |\uparrow_1\uparrow_2\rangle |\downarrow_3\rangle \tag{B.23}$$

$$|-\rangle |\downarrow_3\rangle^{(1)} = \frac{J_2 - J_1}{\sqrt{2}J_0} |\downarrow_1\downarrow_2\rangle |\uparrow_3\rangle \tag{B.24}$$

$$|\downarrow_1\downarrow_2\rangle |\uparrow_3\rangle^{(1)} = -\frac{J_1 + J_2}{\sqrt{2}J_0} |+\rangle |\downarrow_3\rangle + \frac{J_1 - J_2}{\sqrt{2}J_0} |-\rangle |\downarrow_3\rangle \tag{B.25}$$

$$|\uparrow_1\uparrow_2\rangle |\downarrow_3\rangle^{(1)} = -\frac{J_1 + J_2}{\sqrt{2}J_0} |+\rangle |\uparrow_3\rangle + \frac{J_2 - J_1}{\sqrt{2}J_0} |-\rangle |\uparrow_3\rangle \tag{B.26}$$

$$|\downarrow_1\downarrow_2\rangle |\downarrow_3\rangle^{(1)} = |\uparrow_1\uparrow_2\rangle |\uparrow_3\rangle^{(1)} = 0 \tag{B.27}$$

Second-order correction

$$|+\rangle |\uparrow_3\rangle^{(2)} = \frac{(J_2^2 - J_1^2)}{4J_0^2} |-\rangle |\uparrow_3\rangle - \frac{(J_1 + J_2)^2}{4J_0^2} |+\rangle |\uparrow_3\rangle \tag{B.28}$$

$$|+\rangle |\downarrow_3\rangle^{(2)} = \frac{(J_1^2 - J_2^2)}{4J_0} |-\rangle |\downarrow_3\rangle - \frac{(J_1 + J_2)^2}{4J_0^2} |+\rangle |\downarrow_3\rangle \tag{B.29}$$

$$E^{(2)}_{|+\rangle|\uparrow_3\rangle} = E^{(2)}_{|+\rangle|\downarrow_3\rangle} = \frac{(J_1 + J_2)^2}{4J_0} \tag{B.30}$$

$$|-\rangle|\uparrow_3\rangle^{(2)} = \frac{(J_2^2 - J_1^2)}{4J_0^2}|+\rangle|\uparrow_3\rangle - \frac{(J_1 - J_2)^2}{4J_0^2}|-\rangle|\uparrow_3\rangle \tag{B.31}$$

$$|-\rangle|\downarrow_3\rangle^{(2)} = \frac{(J_1^2 - J_2^2)}{4J_0^2}|+\rangle|\downarrow_3\rangle - \frac{(J_1 - J_2)^2}{4J_0^2}|-\rangle|\downarrow_3\rangle \tag{B.32}$$

$$E^{(2)}_{|-\rangle|\uparrow_3\rangle} = E^{(2)}_{|-\rangle|\downarrow_3\rangle} = -\frac{(J_1 - J_2)^2}{4J_0} \tag{B.33}$$

$$|\downarrow_1\downarrow_2\rangle|\uparrow_3\rangle^{(2)} = -\frac{J_1^2 + J_2^2}{2J_0^2}|\downarrow_1\downarrow_2\rangle|\uparrow_3\rangle \tag{B.34}$$

$$|\uparrow_1\uparrow_2\rangle|\downarrow_3\rangle^{(2)} = -\frac{J_1^2 + J_2^2}{2J_0^2}|\uparrow_1\uparrow_2\rangle|\downarrow_3\rangle \tag{B.35}$$

$$E^{(2)}_{|\downarrow_1\downarrow_2\rangle|\uparrow_3\rangle} = E^{(2)}_{|\uparrow_1\uparrow_2\rangle|\downarrow_3\rangle} = -\frac{J_1 J_2}{J_0} \tag{B.36}$$

$$|\downarrow_1\downarrow_2\rangle|\downarrow_3\rangle^{(2)} = |\uparrow_1\uparrow_2\rangle|\uparrow_3\rangle^{(2)} = 0 \tag{B.37}$$

$$E^{(2)}_{|\downarrow_1\downarrow_2\rangle|\downarrow_3\rangle} = E^{(2)}_{|\uparrow_1\uparrow_2\rangle|\uparrow_3\rangle} = 0 \tag{B.38}$$

Thus, we have our eight new eigenstates and their eigenenergies to the second order.

Eigenstates	Eigenvalues
$\|1\rangle = (1 - \frac{(J_1+J_2)^2}{4J_0^2})\|+\rangle\|\uparrow_3\rangle + \frac{J_1+J_2}{\sqrt{2}J_0}\|\uparrow_1\uparrow_2\rangle\|\downarrow_3\rangle + \frac{(J_2^2-J_1^2)}{4J_0^2}\|-\rangle\|\uparrow_3\rangle$	$\frac{J_0}{2} + \frac{(J_1+J_2)^2}{4J_0}$
$\|2\rangle = (1 - \frac{(J_1+J_2)^2}{4J_0^2})\|+\rangle\|\downarrow_3\rangle + \frac{J_1+J_2}{\sqrt{2}J_0}\|\downarrow_1\downarrow_2\rangle\|\uparrow_3\rangle + \frac{(J_1^2-J_2^2)}{4J_0}\|-\rangle\|\downarrow_3\rangle$	$\frac{J_0}{2} + \frac{(J_1+J_2)^2}{4J_0}$
$\|3\rangle = (1 - \frac{(J_1-J_2)^2}{4J_0^2})\|-\rangle\|\uparrow_3\rangle + \frac{J_1-J_2}{\sqrt{2}J_0}\|\uparrow_1\uparrow_2\rangle\|\downarrow_3\rangle + \frac{(J_2^2-J_1^2)}{4J_0^2}\|+\rangle\|\uparrow_3\rangle$	$-\frac{J_0}{2} - \frac{(J_1-J_2)^2}{4J_0}$
$\|4\rangle = (1 - \frac{(J_1-J_2)^2}{4J_0^2})\|-\rangle\|\downarrow_3\rangle + \frac{J_2-J_1}{\sqrt{2}J_0}\|\downarrow_1\downarrow_2\rangle\|\uparrow_3\rangle + \frac{(J_1^2-J_2^2)}{4J_0^2}\|+\rangle\|\downarrow_3\rangle$	$-\frac{J_0}{2} - \frac{(J_1-J_2)^2}{4J_0}$
$\|5\rangle = (1 - \frac{J_1^2+J_2^2}{2J_0^2})\|\downarrow_1\downarrow_2\rangle\|\uparrow_3\rangle - \frac{J_1+J_2}{\sqrt{2}J_0}\|+\rangle\|\downarrow_3\rangle + \frac{J_1-J_2}{\sqrt{2}J_0}\|-\rangle\|\downarrow_3\rangle$	$-\frac{J_1 J_2}{J_0}$
$\|6\rangle = (1 - \frac{J_1^2+J_2^2}{2J_0^2})\|\uparrow_1\uparrow_2\rangle\|\downarrow_3\rangle - \frac{J_1+J_2}{\sqrt{2}J_0}\|+\rangle\|\uparrow_3\rangle + \frac{J_2-J_1}{\sqrt{2}J_0}\|-\rangle\|\uparrow_3\rangle$	$-\frac{J_1 J_2}{J_0}$
$\|7\rangle = \|\uparrow_1\uparrow_2\rangle\|\uparrow_3\rangle$	0
$\|8\rangle = \|\downarrow_1\downarrow_2\rangle\|\downarrow_3\rangle$	0

We can solve inversely up to second-order accuracy.

$$|\downarrow_1\downarrow_2\rangle|\uparrow_3\rangle = (1-\frac{J_1^2+J_2^2}{2J_0^2})|5\rangle + \frac{J_1+J_2}{\sqrt{2}J_0}|2\rangle + \frac{J_2-J_1}{\sqrt{2}J_0}|4\rangle \tag{B.39}$$

$$|\uparrow_1\uparrow_2\rangle|\downarrow_3\rangle = (1-\frac{J_1^2+J_2^2}{2J_0^2})|6\rangle + \frac{J_1+J_2}{\sqrt{2}J_0}|1\rangle + \frac{J_1-J_2}{\sqrt{2}J_0}|3\rangle \tag{B.40}$$

$$|+\rangle|\uparrow_3\rangle = (1-\frac{(J_1+J_2)^2}{4J_0^2})|1\rangle - \frac{J_1+J_2}{\sqrt{2}J_0}|6\rangle + \frac{J_2^2-J_1^2}{4J_0^2}|3\rangle \tag{B.41}$$

$$|+\rangle|\downarrow_3\rangle = (1-\frac{(J_1+J_2)^2}{4J_0^2})|2\rangle - \frac{J_1+J_2}{\sqrt{2}J_0}|5\rangle + \frac{J_1^2-J_2^2}{4J_0^2}|4\rangle \tag{B.42}$$

$$|-\rangle|\uparrow_3\rangle = (1-\frac{(J_1-J_2)^2}{4J_0^2})|3\rangle + \frac{J_2-J_1}{\sqrt{2}J_0}|6\rangle + \frac{J_2^2-J_1^2}{4J_0^2}|1\rangle \tag{B.43}$$

$$|-\rangle|\downarrow_3\rangle = (1-\frac{(J_1-J_2)^2}{4J_0^2})|4\rangle + \frac{J_1-J_2}{\sqrt{2}J_0}|5\rangle + \frac{J_1^2-J_2^2}{4J_0^2}|2\rangle \tag{B.44}$$

System evolution

Let us then look at the system evolution. The initial state after the $\pi/2$ rotation along $\hat{y}$[1] gives $|\phi(0)\rangle = \frac{1}{\sqrt{2}}(|\uparrow_1\rangle + |\downarrow_1\rangle)\frac{1}{\sqrt{2}}(|\uparrow_2\rangle + |\downarrow_2\rangle)\frac{1}{\sqrt{2}}(|\uparrow_3\rangle + |\downarrow_3\rangle)$, expressed in terms of the new eigenstates as

$$\begin{aligned}|\phi(0)\rangle = \frac{1}{2\sqrt{2}}\Bigg(&\left(\sqrt{2}+\frac{J_1+J_2}{\sqrt{2}J_0}-\frac{(J_1+J_2)^2}{2\sqrt{2}J_0^2}\right)(|1\rangle+|2\rangle)+\left(\frac{J_1-J_2}{\sqrt{2}J_0}+\frac{J_2^2-J_1^2}{2\sqrt{2}J_0^2}\right)(|3\rangle-|4\rangle)\\&+\left(1-\frac{J_1+J_2}{J_0}-\frac{J_1^2+J_2^2}{2J_0^2}\right)(|5\rangle+|6\rangle)+|7\rangle+|8\rangle\Bigg).\end{aligned} \tag{B.45}$$

Since there is no detuning, the middle π pulse will not change the final polarization along $\hat{x}$, so we can ignore it. After time t, the system state becomes:

$$\begin{aligned}|\phi(t)\rangle = \frac{1}{2\sqrt{2}}\Bigg(&\left(\sqrt{2}+\frac{J_1+J_2}{\sqrt{2}J_0}-\frac{(J_1+J_2)^2}{2\sqrt{2}J_0^2}\right)(|1\rangle+|2\rangle)e^{-i(\frac{J_0}{2}+\frac{(J_1+J_2)^2}{4J_0})t}\\&+\left(\frac{J_1-J_2}{\sqrt{2}J_0}+\frac{J_2^2-J_1^2}{2\sqrt{2}J_0^2}\right)(|3\rangle-|4\rangle)e^{i(\frac{J_0}{2}+\frac{(J_1-J_2)^2}{4J_0})t}\\&+\left(1-\frac{J_1+J_2}{J_0}-\frac{J_1^2+J_2^2}{2J_0^2}\right)(|5\rangle+|6\rangle)e^{i\frac{J_1J_2}{J_0}t}+|7\rangle+|8\rangle\Bigg).\end{aligned} \tag{B.46}$$

[1] In this derivation, note that we rotate relative to the $\hat{y}$ axis instead of the $\hat{x}$ axis to avoid using i. The results should be the same regardless of the choice of $\hat{x}$ and $\hat{y}$ axes.

Measure spin 1 at the end: $P_1 = \langle\phi(t)|\, 2S_x^1\, |\phi(t)\rangle$. The value should range from -1 to 1. Keep terms up to second order of J_1/J_0 and J_2/J_0.

$$2S_x^1(|1\rangle + |2\rangle) = \frac{J_1+J_2}{J_0}(|1\rangle + |2\rangle) + \frac{J_1}{J_0}(|3\rangle - |4\rangle) + \left(\frac{1}{\sqrt{2}} - \frac{4J_1^2 + J_2^2 + 3J_1J_2}{2\sqrt{2}J_0^2}\right)(|5\rangle + |6\rangle) + (\frac{1}{\sqrt{2}} - \frac{J_2^2 + J_1J_2}{2\sqrt{2}J_0^2})(|7\rangle + |8\rangle) \quad \text{(B.47)}$$

$$2S_x^1(|3\rangle - |4\rangle) = \frac{J_1}{J_0}(|1\rangle + |2\rangle) + \frac{J_1-J_2}{J_0}(|3\rangle - |4\rangle) + \left(\frac{1}{\sqrt{2}} - \frac{4J_1^2 + J_2^2 - 3J_1J_2}{2\sqrt{2}J_0^2}\right)(|5\rangle + |6\rangle) - (\frac{1}{\sqrt{2}} - \frac{J_2^2 - J_1J_2}{2\sqrt{2}J_0^2})(|7\rangle + |8\rangle) \quad \text{(B.48)}$$

$$2S_x^1(|5\rangle + |6\rangle) = \left(\frac{1}{\sqrt{2}} - \frac{4J_1^2 + J_2^2 + 3J_1J_2}{2\sqrt{2}J_0^2}\right)(|1\rangle + |2\rangle) + \left(\frac{1}{\sqrt{2}} - \frac{4J_1^2 + J_2^2 - 3J_1J_2}{4\sqrt{2}J_0^2}\right)(|3\rangle - |4\rangle) - \frac{2J_1}{J_0}(|5\rangle + |6\rangle) - \frac{J_2}{J_0}(|7\rangle + |8\rangle) \quad \text{(B.49)}$$

$$2S_x^1(|7\rangle + |8\rangle) = \left(\frac{1}{\sqrt{2}} - \frac{J_2^2 + J_1J_2}{2\sqrt{2}J_0^2}\right)(|1\rangle + |2\rangle) - \left(\frac{1}{\sqrt{2}} - \frac{J_2^2 - J_1J_2}{2\sqrt{2}J_0^2}\right)(|3\rangle - |4\rangle) - \frac{J_2}{J_0}(|5\rangle + |6\rangle) \quad \text{(B.50)}$$

Based on the orthogonality of different eigenstates, we can calculate the contribution from each eigenstate up to second order as follows:

$$P_1^{12} = \frac{1}{4}(\frac{2(J_1+J_2)}{J_0} + \frac{2(J_1+J_2)^2}{J_0^2} + \frac{J_1(J_1-J_2)}{J_0^2}e^{i(J_0 + \frac{J_1^2+J_2^2}{2J_0})t} + \left(1 - \frac{J_1+J_2}{2J_0} - \frac{13J_1^2 + 7J_2^2 + 12J_1J_2}{4J_0^2}\right)e^{i(\frac{J_0}{2} + \frac{J_1^2+J_2^2+6J_1J_2}{4J_0})t} + \left(1 + \frac{J_1+J_2}{2J_0} - \frac{J_1^2 + 3J_2^2 + 4J_1J_2}{4J_0^2}\right)e^{i(\frac{J_0}{2} + \frac{(J_1+J_2)^2}{4J_0})t}) \quad \text{(B.51)}$$

$$P_1^{34} = \frac{1}{4}\Big(\frac{J_1(J_1-J_2)}{J_0^2}e^{-i(J_0+\frac{J_1^2+J_2^2}{2J_0})t} + \left(\frac{J_1-J_2}{2J_0}+\frac{3(J_2^2-J_1^2)}{4J_0^2}\right)e^{-i(\frac{J_0}{2}+\frac{J_1^2+J_2^2-6J_1J_2}{4J_0})t} - \left(\frac{J_1-J_2}{2J_0}+\frac{J_2^2-J_1^2}{4J_0^2}\right)e^{-i(\frac{J_0}{2}+\frac{(J_1-J_2)^2}{4J_0})t}\Big) \quad \text{(B.52)}$$

$$P_1^{56} = \frac{1}{4}\Big(\left(1-\frac{J_1+J_2}{2J_0}-\frac{13J_1^2+7J_2^2+12J_1J_2}{4J_0^2}\right)e^{-i(\frac{J_0}{2}+\frac{J_1^2+J_2^2+6J_1J_2}{4J_0})t} + \left(\frac{J_1-J_2}{2J_0}+\frac{3(J_2^2-J_1^2)}{4J_0^2}\right)e^{i(\frac{J_0}{2}+\frac{J_1^2+J_2^2-6J_1J_2}{4J_0})t} - \frac{2J_1}{J_0}+\frac{4J_1(J_1+J_2)}{J_0^2}-\left(\frac{J_2}{J_0}-\frac{J_2(J_1+J_2)}{J_0^2}\right)e^{-i\frac{J_1J_2}{J_0}t}\Big) \quad \text{(B.53)}$$

$$P_1^{78} = \frac{1}{4}\Big(\left(1+\frac{J_1+J_2}{2J_0}-\frac{J_1^2+3J_2^2+4J_1J_2}{4J_0^2}\right)e^{-i(\frac{J_0}{2}+\frac{(J_1+J_2)^2}{4J_0})t} + \left(\frac{J_2-J_1}{2J_0}+\frac{J_1^2-J_2^2}{4J_0^2}\right)e^{i(\frac{J_0}{2}+\frac{(J_1-J_2)^2}{4J_0})t} - \left(\frac{J_2}{J_0}-\frac{J_2(J_1+J_2)}{J_0^2}\right)e^{i\frac{J_1J_2}{J_0}t}\Big). \quad \text{(B.54)}$$

And $P_1 = P_1^{12} + P_1^{34} + P_1^{56} + P_1^{78}$. We can list terms with different frequencies separately:

$$P_1^{DC} = \frac{J_2}{2J_0}+\frac{3J_1^2+J_2^2+4J_1J_2}{2J_0^2} \quad \text{(B.55)}$$

$$P_1^{\frac{J_1J_2}{J_0}} = -\frac{1}{2}\left(\frac{J_2}{J_0}-\frac{J_2(J_1+J_2)}{J_0^2}\right)\cos\frac{J_1J_2}{J_0}t \quad \text{(B.56)}$$

$$P_1^{J_0} = \frac{J_1(J_1-J_2)}{2J_0^2}\cos(J_0+\frac{J_1^2+J_2^2}{2J_0})t \quad \text{(B.57)}$$

$$P_1^{J_0/2,1} = \frac{1}{2}\left(1 - \frac{J_1 + J_2}{2J_0} - \frac{13J_1^2 + 7J_2^2 + 12J_1J_2}{4J_0^2}\right)\cos\left(\frac{J_0}{2} + \frac{J_1^2 + J_2^2 + 6J_1J_2}{4J_0}\right)t \tag{B.58}$$

$$P_1^{J_0/2,2} = \frac{1}{2}\left(1 + \frac{J_1 + J_2}{2J_0} - \frac{J_1^2 + 3J_2^2 + 4J_1J_2}{4J_0^2}\right)\cos\left(\frac{J_0}{2} + \frac{(J_1 + J_2)^2}{4J_0}\right)t \tag{B.59}$$

$$P_1^{J_0/2,3} = \frac{1}{2}\left(\frac{J_1 - J_2}{2J_0} + \frac{3(J_2^2 - J_1^2)}{4J_0^2}\right)\cos\left(\frac{J_0}{2} + \frac{J_1^2 + J_2^2 - 6J_1J_2}{4J_0}\right)t \tag{B.60}$$

$$P_1^{J_0/2,3} = \frac{1}{2}\left(\frac{J_2 - J_1}{2J_0} + \frac{J_1^2 - J_2^2}{4J_0^2}\right)\cos\left(\frac{J_0}{2} + \frac{(J_1 - J_2)^2}{4J_0}\right)t. \tag{B.61}$$